

# Magnetotransport properties of Topological Insulator thin films

THÈSE N° 6073 (2014)

PRÉSENTÉE LE 12 FÉVRIER 2014

À LA FACULTÉ DES SCIENCES DE BASE

LABORATOIRE DE SCIENCE À L'ÉCHELLE NANOMÉTRIQUE

PROGRAMME DOCTORAL EN SCIENCE ET GÉNIE DES MATÉRIAUX

ÉCOLE POLYTECHNIQUE FÉDÉRALE DE LAUSANNE

POUR L'OBTENTION DU GRADE DE DOCTEUR ÈS SCIENCES

PAR

Pascal GEHRING

acceptée sur proposition du jury:

Prof. P. Muralt, président du jury  
Prof. K. Kern, Dr M. Burghard, directeurs de thèse  
Prof. A. Fontcuberta i Morral, rapporteur  
Dr J. Honolka, rapporteur  
Prof. D. Van der Marel, rapporteur



ÉCOLE POLYTECHNIQUE  
FÉDÉRALE DE LAUSANNE

Suisse  
2014



Der Wissenschaftler findet seine Belohnung in dem,  
was Poincaré die Freude am Verstehen nennt,  
nicht in den Anwendungsmöglichkeiten seiner Erfindung.  
— Albert Einstein

---

*für Michaela...*

# Abstract

We are living in an era of digitalization. It is possible to permanently access knowledge of all kinds or even daily news without going to a library or buying newspapers. Furthermore, to access this data, we don't have to use our personal computer anymore, as high performance smartphones or tablet PCs are now available. Thus, nowadays a mobile phone needs to be a highly developed multi-media station rather than only a simple phone. Since high computing power is closely related to large power consumption, new power-saving transistors are needed. This task can be tackled for instance by spin-electronics (spintronics), where the spin information of an electron is used instead of its charge. Such devices promise fast and energy saving switching. However, suitable materials are needed that can convert conventional charge- into spin-currents. A new class of materials, namely *topological insulators (TIs)*, is predicted to exactly meet this demand. These materials are (conceptually) insulators in their inside, but conduct spin-polarized currents on their surfaces. However, in real TIs the bulk is intrinsically highly doped, resulting in a strong contribution of bulk currents to the total charge transport. On this basis, the aim of this thesis is to find fingerprints of the exotic surface states of three-dimensional TIs in electrical transport measurements. To this end, a chemical vapor deposition (CVD) system is set up to grow ultrathin films of  $\text{Bi}_2\text{Se}_3$  which possess a large surface-to-bulk ratio. These samples show a pronounced linear magnetoresistance (LMR) at low temperatures. Due to the very low film thickness we are able to alter the LMR into a classical parabolic magnetoresistance using a back-gate, which allows us to associate the LMR with the surface states of  $\text{Bi}_2\text{Se}_3$ . However, the electrical transport in this material is still dominated by the bulk. Thus, we use the same CVD method to grow  $\text{Bi}_2\text{Te}_2\text{Se}$  (BTS) nanostructures, a TI that is known to have the highest surface contribution to the total electrical transport reported so far. In low temperature magnetoconductance measurements a pronounced 2D weak anti-localization effect is observed, that is attributed to the topological surface states. In addition, by epitaxial growth of BTS on hexagonal boron nitride we are able to enhance its carrier mobility by a factor of 3 compared to samples grown on  $\text{Si}/\text{SiO}_x$  substrates. This enables the observation of pronounced, gate depended Shubnikov-de Haas oscillations for the first time in this material. The SdH oscillations have two-dimensional character and are likely to originate from the surface bands of BTS. However, despite the successfully increased mobility in the samples, the carrier density is still high. Therefore, we expand the quest for new TI materials to nature. Due to their geological age, the crystal structure of minerals should have reached thermodynamic equilibrium and accordingly an ultimately low defect concentration mainly given by their defect formation enthalpy. By angle-resolved photoemission measure-

---

ments on the two minerals Kawazulite and Aleksite, which both originate from former gold mines, we are able to proof their "topological" behavior. Both natural TIs possess high carrier mobilities and, in the case of Kawazulite, a comparatively low carrier density, which signifies a low defect density. In addition, both minerals show pronounced quantum coherence effects at low temperatures, where the phase coherence length in Aleksite exceeds 1  $\mu\text{m}$ .

**Keywords** Topological Insulators, Magnetotransport, Thin Films, Vapor-Solid Growth, Chemical Vapor Deposition, Natural Topological Insulators, Epitaxial Growth, Quantum Transport, Linear Magnetoresistance, Weak Anti-localization, Universal Conductance Fluctuations, Shubnikov-de Haas Oscillations, Bismuth Selenide, Kawazulite, Aleksite

# Zusammenfassung

Wir leben in einem Zeitalter der Digitalisierung. Neben der Möglichkeit ständig auf gespeichertes Wissen aller Art zugreifen zu können, finden nun auch tägliche Nachrichten ihren Weg zu uns ohne vorher den Umweg über eine Druckerpresse machen zu müssen. Zudem verlagert sich der Datenzugriff zunehmend vom heimischen Arbeitszimmer auf das Smartphone oder den Tablet-PC. Daher ist – in einer Welt ständiger Vernetzung – die Anforderung an Geräte, die diesen Ansprüchen gerecht werden sollen enorm hoch. Ein Mobiltelefon muss, neben seiner Eigenschaft als Telefon, auch als kompakte, leistungsstarke Multimedia Station dienen können. Dabei soll natürlich eine ausreichende Akkulaufzeit gewährleistet sein. Da schnelle Rechenleistung aber mit hohem Energieverbrauch einhergeht, ist eine neuartige Prozessortechnologie von Nöten damit, der technologische Fortschritt nicht zum Erliegen kommt. Einen Ausweg liefert die sogenannte Spin-Elektronik (engl. *Spintronic*), bei der der Spin einzelner Elektronen zur Datenspeicherung und –übertragung genutzt wird. Ein großer Vorteil: Spins lassen sich ohne großen Energieaufwand und auf sehr kleinen Zeitskalen manipulieren. Jedoch benötigt man hierfür aktive Komponenten/Materialien, die in der Lage sind, einen gewöhnlichen Ladungsstrom in einen Spin-Strom umzuwandeln. Eine neue Klasse von Quantenmaterialien, die sogenannten *Topologische Isolatoren*, erfüllt genau diese Eigenschaft. Diese Stoffe sind Isolatoren in ihrem Inneren, leiten jedoch einen spinpolarisierten Strom an ihrer Oberfläche. Auch wenn – zumindest von einem theoretischen Standpunkt aus – topologische Isolatoren direkt für Spintronik-Bauelemente eingesetzt werden könnten, sieht die Realität leider anders aus. Reale topologische Isolatoren sind in Wahrheit stark dotierte Halbleiter, dessen inneres den elektrischen Strom so gut leitet, dass Oberflächeneffekte gänzlich überschattet werden.

Ziel dieser Arbeit ist es daher, anhand elektrischer Leitfähigkeitsmessungen an dreidimensionalen topologischen Isolatoren Hinweise auf deren außergewöhnliche Oberflächenzustände zu erhalten. Für die Herstellung dünner Proben, welche ein hohes Oberflächen-zu-Volumen-Verhältnis aufweisen sollen, wird ein chemischer Gasphasenabscheidungs- (engl. *chemical vapor deposition (CVD)*) Reaktor aufgebaut. Nach Optimierung der Wachstumsbedingungen sind wir damit in der Lage,  $\text{Bi}_2\text{Se}_3$ -Schichten mit Schichtdicken im Bereich weniger nm zu wachsen. In elektrischen Leitfähigkeitsmessungen bei hohen Magnetfeldern und niedrigen Temperaturen können wir einen linearen Magnetowiderstand beobachten. Aufgrund der geringen Dicke unserer Proben sind wir in der Lage, diesen Effekt bei verschiedenen Gate-Spannungen zu untersuchen, was uns erlaubt, den linearen Magnetowiderstand mit den nicht-trivialen Oberflächenzuständen von  $\text{Bi}_2\text{Se}_3$  in Verbindung zu bringen.

---

Jedoch stammt der Hauptteil des Stromtransports von dem stark dotierten Inneren des Materials. Daher verwenden wir unseren CVD-Reaktor, um das weitaus vielversprechendere Material  $\text{Bi}_2\text{Te}_2\text{Se}$  herzustellen, dessen Oberflächenzustände einen hohen Beitrag zur Gesamtleitfähigkeit liefern sollen. Dieses zeigt eine ausgeprägte, zweidimensionale *schwache Lokalisierung* der Ladungsträger bei tiefen Temperaturen, welche wir den Oberflächenzuständen des Materials zuschreiben.

Indem wir dieses Material epitaktisch auf hexagonalem Bornitrid aufwachsen, sind wir in der Lage, dessen Ladungsträgermobilität um einen Faktor drei zu erhöhen. Das ermöglicht die Beobachtung ausgeprägter Shubnikov-de Haas (SdH) Oszillationen im Magnetowiderstand. Diese zeigen ein rein zweidimensionales Verhalten und stammen aller höchster Wahrscheinlichkeit nach von den Oberflächenkanälen des  $\text{Bi}_2\text{Te}_2\text{Se}$ . Dank der geringen Dicke unserer Schichten sind wir in der Lage, die SdH-Oszillationen durch Anlegen einer Gatespannung zu manipulieren und Rückschlüsse auf die Position der Fermienergie zu ziehen.

Das Problem der niedrigen Mobilität kann damit erfolgreich gelöst werden. Jedoch ist die Ladungsträgerdichte unserer Schichten nach wie vor vergleichsweise hoch, weshalb wir unsere Suche nach neuen Materialien in eine neue Richtung lenken. Dank ihres enormen Alters sollte sich das Kristallgitter von Mineralien im thermodynamischen Gleichgewicht befinden. Ihre Defektkonzentration ist daher auf ein absolutes Minimum, welches hauptsächlich von der Defektbildungsenthalpie abhängt, reduziert. Vor diesem Hintergrund untersuchen wir die Mineralien Kawazulit und Aleksit, welche beide aus ehemaligen Goldminen gewonnen wurden. Mittels winkelaufgelöster Photoelektronenspektroskopie (ARPES) sind wir in der Lage, diese Materialien als natürliche topologische Isolatoren zu identifizieren. Beide zeigen vergleichsweise hohe Mobilitäten und im Falle von Kawazulit auch eine sehr niedrige Ladungsträgerkonzentration, was auf eine geringe Defektdichte zurückgeführt werden kann. Außerdem zeigen die Mineralien bei niedrigen Temperaturen sehr ausgeprägte Quantenkohärenzeffekte mit einer Phasenkohärenzlänge, die einen Wert von bis zu  $1\text{ }\mu\text{m}$  erreichen kann.

**Schlagwörter** Topologische Isolatoren, Magnetotransport, Dünne Schichten, Vapor-Solid Wachstum, Chemische Gasphasenabscheidung, Natürliche Topologische Isolatoren, Epitaktisches Wachstum, Quanten Transport, Linearer Magnetowiderstand, Schwache Anti-Lokalisierung, Universelle Leitwertfluktuationen, Shubnikov-de Haas Oszillationen, Bismut Selenid, Kawazulit, Aleksit

# Contents

<b>Abstract (English/Deutsch)</b>	<b>v</b>
<b>1 Introduction</b>	<b>1</b>
<b>2 Theoretical Background of Topological Insulators</b>	<b>5</b>
2.1 Topological Insulators in a nutshell . . . . .	6
2.2 Why 'Topological'? . . . .	9
2.2.1 Berry-Phase . . . . .	9
2.2.2 Chern numbers . . . . .	10
2.2.3 Bulk-boundary correspondence . . . . .	12
2.3 Why 'Robust'? . . . .	13
2.3.1 Time-reversal symmetry . . . . .	13
2.3.2 Spin-Orbit Interaction . . . . .	15
2.3.3 Kramers theorem . . . . .	17
2.4 $Z_2$ Topological Insulators . . . . .	18
2.4.1 $Z_2$ invariants in three dimensions . . . . .	23
2.4.2 Theoretical prediction of real Topological Insulator materials . . . . .	25
<b>3 Magnetotransport phenomena</b>	<b>31</b>
3.1 Length scales . . . . .	32
3.2 Diffusive electrical transport . . . . .	33
3.2.1 Drude model with magnetic field . . . . .	33
3.2.2 Magnetoresistance . . . . .	35
3.2.3 Linear Magnetoresistance . . . . .	37
3.2.4 Shubnikov-de Haas oscillations . . . . .	38
3.3 Diffusive quantum transport . . . . .	40
3.3.1 Weak localization . . . . .	40
3.3.2 Weak anti-localization . . . . .	42
3.3.3 Decoherence . . . . .	44
3.4 Interference effects in quantum transport . . . . .	45
3.4.1 Aharonov-Bohm effect . . . . .	45
3.4.2 Universal conductance fluctuations . . . . .	48
3.5 Sample geometries in electrical transport measurements . . . . .	49

## Contents

---

<b>4</b>	<b>CVD growth and device fabrication</b>	<b>51</b>
4.1	How to grow Topological Insulators? . . . . .	52
4.2	Setting up a CVD system . . . . .	53
4.3	Results of the CVD growth . . . . .	54
4.4	Contacting topological insulator nanostructures . . . . .	62
<b>5</b>	<b>Gate-controlled linear magnetoresistance in thin <math>\text{Bi}_2\text{Se}_3</math> sheets</b>	<b>65</b>
5.1	Introduction . . . . .	66
5.2	Sample preparation and characterization . . . . .	66
5.3	Electrical transport measurements . . . . .	66
5.4	Quantum linear magnetoresistance? . . . . .	70
5.5	Summary . . . . .	71
<b>6</b>	<b>Two-dimensional magnetotransport in <math>\text{Bi}_2\text{Te}_2\text{Se}</math> nanoplatelets</b>	<b>73</b>
6.1	Introduction . . . . .	74
6.2	Sample preparation and characterization . . . . .	74
6.3	Electrical magnetotransport measurements . . . . .	75
6.4	Summary . . . . .	78
<b>7</b>	<b>Growth of High-Mobility <math>\text{Bi}_2\text{Te}_2\text{Se}</math> Nanoplatelets on hBN Sheets by van der Waals Epitaxy</b>	<b>79</b>
7.1	Introduction . . . . .	80
7.2	Sample preparation and characterization . . . . .	80
7.3	Electrical transport measurements . . . . .	82
7.4	Summary . . . . .	91
<b>8</b>	<b>Kawazulite: A natural Topological Insulator</b>	<b>93</b>
8.1	Introduction . . . . .	94
8.2	Sample characterization . . . . .	94
8.3	Electrical transport measurements . . . . .	97
8.4	Summary . . . . .	101
<b>9</b>	<b>A second example from the forge of nature: Aleksite</b>	<b>103</b>
<b>10</b>	<b>Summary and outlook</b>	<b>111</b>
10.1	Growth mechanism of BTS on hBN . . . . .	113
10.2	Anomalous Aharonov-Bohm oscillations in Kawazulite . . . . .	114
10.3	Graphene tunnel barrier . . . . .	114
<b>A</b>	<b>Supporting linear magnetoresistance data</b>	<b>119</b>
<b>B</b>	<b>Electrical transport data for 12 nm thin platelet grown on hBN</b>	<b>123</b>
<b>C</b>	<b>Details of XRD measurements on Kawazulite</b>	<b>125</b>
	<b>Bibliography</b>	<b>139</b>

<b>Danksagung</b>	<b>141</b>
-------------------	------------



# 1 Introduction

Isn't it fascinating that modern portable devices like mobile phones could be developed into high performance multi-media stations during the last decade? The computing power of up-to-date mobiles is comparable to that of personal computers from only about 10 years ago. Thus they have now advanced to the point where it is possible to play video games or watch high-definition movies on them. But the demand for faster, high-performance mobiles is increasing. This requires by implication energy saving processors to guarantee a certain period of use (since bigger batteries would unnecessarily increase the weight of the device). As an example, by reducing the size of conducting paths in a "system on a chip" (SoC) from 65 nm to 45 nm it was possible to reduce the electricity consumption by 30%.<sup>1</sup> But is there a superior strategy to fabricate power-saving and faster processors?

In nearly all semiconductor devices, electrical currents are needed to transport "information". This information is carried by the electron's charge. For example, to define the *on* or *off* state of a field-effect transistor the plates of a nanocapacitor have to be charged or discharged. Since electrons can be scattered by static defects or phonons their transport is dissipative. Hence, in the past decades researchers spent much effort to increase the crystal quality of semiconductor devices to reduce defects and thus energy dissipation.

However, it is also possible to use another intrinsic property of the electron instead of its charge: a property known as their spin which can be interpreted as the magnetic moment of a single electron. The emerging field of spin-electronics (*spintronics*) endeavors to use this spin to store and transport information. The advantage is that there is no external (charge) current needed to manipulate the spin information (*up* or *down*). In addition, typical spin relaxation times can be much higher than the lifetime of a charge state, which gets easily destroyed by defect scattering. Thus, spintronic devices are promising to reach much higher performance (fast switching) and consume less energy.<sup>2</sup>

Key components of spintronic devices are so-called spin-filters. These act like valves for one type of spin, thereby transforming charge into spin-currents. A common means to inject spins into materials is by ferromagnetic electric contacts. However, the typical spin polarization (that is the portion of spin-polarized electrons compared to all electrons flowing) reached is only several 10%.<sup>3</sup>

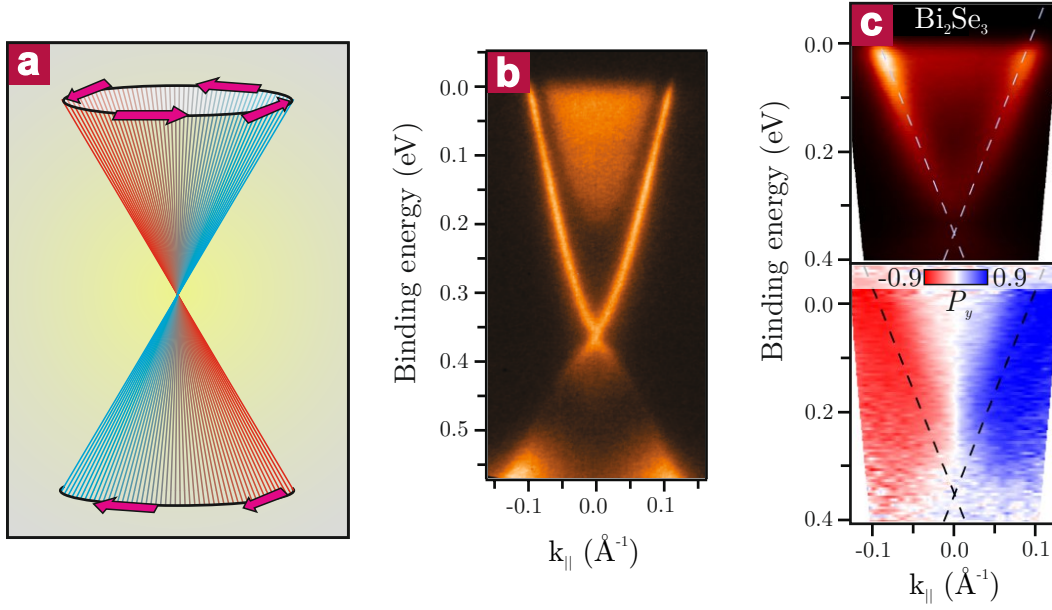


**Figure 1.1: The exotic band structure of topological insulators.** (a) Sketch of the spin-polarized Dirac cone associated with the surface of a topological insulator (TI). (b) Angle-resolved photoemission spectrum of the 3D TI Bi<sub>2</sub>Se<sub>3</sub>. The linear surface bands are clearly observable.<sup>4</sup> (c) Detailed ARPES spectrum of Bi<sub>2</sub>Se<sub>3</sub> (top) and the corresponding spin-polarized spectrum showing the helicity of the surface states (color denotes the spin-polarization in  $y$ -direction).<sup>5</sup>

A major leap forward in spintronics may be achieved by a new class of condensed matter recently discovered, namely *topological insulators* (TIs). These materials are insulators in their inside, but conduct electrical current on their surface. These surface channels emerge on the boundary between the material and its surrounding due to quantum mechanical principles, making them highly robust against almost any type of defects or chemical surface modification.<sup>6</sup> A special feature of these surface states is, that they form a so-called Dirac cone, i.e., the surface carriers' energy depends linearly on their momentum. Figure 1.1a and b depict a sketch and an experimental angle-resolved photoemission spectrum, respectively, of the surface Dirac cone of the topological insulator Bi<sub>2</sub>Se<sub>3</sub>. Another key feature of the surface channels is that the electrons' spin is locked to their direction of motion, as depicted by the spin-polarized ARPES data shown in Figure 1.1c. In particular, an electron moving in  $+k$  direction has a spin oriented in  $+y$  direction (blue), whereas an electron moving in the opposite direction ( $-k$ ) has a spin oriented in  $-y$  direction (red). Such spin-momentum coupling is also illustrated by the pink arrows in Figure 1.1a. Thus, topological insulators from a theoretical viewpoint are well-suited as an intrinsic spin filter with a spin-polarization of more than 50%.<sup>7</sup> Due to exceptionally low electron-phonon coupling they are promising for room temperature spintronic devices.<sup>8</sup> In addition, the helical surface states of TIs could provide access to novel, fascinating physical phenomena such as magnetic monopoles<sup>9</sup> or Majorana fermions.<sup>10</sup>

---

While in theory these characteristics renders the surface states promising for spintronic and quantum computing applications, as well as for fundamental research, their existence has been difficult to prove by electrical transport studies. One reason for that is the high conductivity of the intrinsically doped bulk of *real* topological insulators, making it difficult to distinguish between surface and volume effects. In case of the chalcogenides  $\text{Bi}_2\text{Se}_3$  (intrinsically n-doped) and  $\text{Sb}_2\text{Te}_3$  (intrinsically p-doped), there are two major origins of the doping reported in literature. Firstly, intrinsic point defects (vacancies or antisites) that form during the growth of the material can dope the bulk with extra charge carriers.<sup>11–13</sup> Secondly, upon exposure to ambient the surface may react with oxygen and create a surface oxide,<sup>14</sup> or react with water molecules to form positively charged surface vacancies as well as bismuth hydroxide.<sup>15</sup> For  $\text{Bi}_2\text{Se}_3$ , both types of chemical reactions are expected to result in strong n-doping of the sample.

Independent of the origin of intrinsic doping, the major problem remains that there are two possible transport channels in the sample, namely the (doped) bulk and the surface states. Hence, electrical transport measurement are generally dominated by the low resistive bulk. In addition, strong scatterers like point defects may destroy the protected Dirac surface state locally and create a virtual scattering channel from the surface to the bulk states.<sup>16,17</sup> To overcome this problem, several possible approaches have been followed. One option is to counter-dope the bulk,<sup>18,19</sup> or to combine (alloy) different topological insulators,<sup>20,21</sup> to compensate for the intrinsic doping. Both strategies result in a reduced carrier density, which has enabled the observation of an ambipolar effect, comprising a continuous crossover from n-type to p-type behavior by applying an external gate voltage, which is a hint for the existence of a state inside the bulk band gap of the material. However, the incorporation of doping atoms or the formation of a non-stoichiometric alloy often result in very low carrier mobilities. This is not only disadvantageous for device applications, but also low carrier mobilities prevent the observation of quantum oscillation effects which can be used to study details of the surface states.<sup>22</sup> Thus, another approach is to increase the crystal quality by improved synthesis methods or different growth conditions to decrease the amount of intrinsic defects. This can be achieved through evaporation techniques like molecular beam epitaxy (MBE) which also allows the growth of ultra-thin films to increase the surface-to-bulk ratio. In fact, high quality MBE films have enabled the observation of a crossover from topological to trivial insulating behavior by successively reducing the thickness of the sheets,<sup>23</sup> and the observation of the quantum anomalous Hall effect (QAHE) in magnetically doped TI films.<sup>24</sup> Although the high flexibility in selecting and combining materials and the good control over the film thickness renders MBE a valuable method for sample preparation, there are several drawbacks. Besides the fact that MBE machines are very expensive, the homogeneity of the obtained films is low. Thin films grown by MBE usually possess many step edges and terraces. Even though it has been experimentally demonstrated that surface electrons on TIs can transmit through step edges with a high transmission probability of about 50%,<sup>25</sup> terraces nevertheless can force the surface carriers to exotic quantum interference effects which might disturb the electrical transport measurements and render their interpretation difficult.<sup>26</sup> In addition, as-prepared MBE samples are much larger than the mean-free path and phase coherence length of the

material such that only the diffusive regime of the topological insulator is accessible.

On this basis, the present thesis aims to develop new strategies in crystal preparation and electrical characterization of TIs to explore the properties of the topological surface states. The synthesis method of choice is a comparatively simple and inexpensive chemical vapor deposition (CVD) technique reported recently.<sup>27</sup> By setting up a CVD system and optimizing the growth parameters, ultrathin  $\text{Bi}_2\text{Se}_3$  nanostructures with high surface-to-volume ratio are fabricated. These reveal novel electrical transport effects like gate-dependent linear magnetoresistance of  $\approx 100\%$ . The magnetoresistance can be changed from linear to classical parabolic behavior by applying an external gate voltage. Combined with the temperature dependence of resistance for different gate voltages, we are able to attribute the linear magnetoresistance to the non-trivial surface states.

Moreover, single-crystalline nanoplatelets of the ternary compound  $\text{Bi}_2\text{Te}_2\text{Se}$  are grown with thicknesses between 8 and 30 nm and lateral sizes of several micrometers. This compound is predicted to have superior properties compared to pure  $\text{Bi}_2\text{Se}_3$ .<sup>28</sup> Angle-dependent magnetconductance measurements on individual nanoplates reveal the presence of a two-dimensional weak anti-localization effect which might originate from the topologically protected surface states of the nanoplates. For the same TI, the structural quality of such nanoplatelets can be substantially improved by van der Waals epitaxial growth on thin hBN substrates. Thin films grown by this technique possess a surface state carrier mobility  $\mu_s$  up to  $20000 \text{ cm}^2/\text{Vs}$ . On average, epitaxial growth increases  $\mu_s$  by a factor of 3 compared to the samples grown on conventional  $\text{Si}/\text{SiO}_x$  substrates. This enables the gate-dependent study of well-developed Shubnikov-de Haas oscillations in this material for the first time.

Finally, we expand the quest for new TIs to nature. We identify the two minerals, Kawazulite and Aleksite, originating from former gold mines, as natural topological insulators with properties that compete well with their lab-made counterparts. Thin flakes with a thickness of a few tens of nanometers are obtained by mechanical exfoliation. They exhibit a sizable mobility of surface state carriers of the order of  $1000 \text{ cm}^2/\text{Vs}$  at low temperature in both cases. Whereas Kawazulite shows low intrinsic doping, Aleksite possesses a very high phase coherence length on the order of  $1 \mu\text{m}$ . Based on these findings, further minerals which due to their minimized defect densities display even better electronic characteristics may be discovered in the future.

## 2 Theoretical Background of Topological Insulators



This first chapter reviews the theoretical basics of topological insulators. Since the details are quite complicated, a short descriptive section will try to convey the basics necessary to understand the rest of this thesis to readers that are interested in a quick overview of the topic. The subsequent sections will then provide deeper insight into the matter by addressing the 'mysterious'  $Z_2$  *invariant*, the connection between topological insulators and donuts or oranges, and the *robustness* of this novel kind of quantum matter.

## **2.1 Topological Insulators in a nutshell**

Let's start with a definition:

A topological insulator is a material with a bulk electronic excitation gap generated by the spin–orbit interaction, which is topologically distinct from an ordinary insulator. This distinction, characterized by a  $Z_2$  topological invariant, necessitates the existence of gapless electronic states on the sample boundary. In two dimensions, the topological insulator is a quantum spin Hall insulator, [...] thus spin filtered, in the sense that the spin of the electron is correlated with its propagation direction.<sup>29</sup>

Since this definition is rather complicated, the intention of this chapter is to give a short overview of basics underlying the existence of topological insulators (TIs). In principle, a TI is nothing else than an electrical conductor on its surface but an insulator in its inside. In addition, the electrons propagating on the surface of the material are spin–polarized, this implies that the orientation of their spin is coupled to their direction of motion: an electron traveling from right to left will thus have the opposite spin orientation than an electron traveling from left to right. Thus, if an electron hits a non–magnetic impurity it cannot get scattered back (doing a U–turn) since it would need to flip its spin orientation. As a consequence, the electrical surface transport is nearly dissipationless.

But what is the origin of these extraordinary surface states? In most cases, surface states simply arise as a consequence of breaking the translational symmetry of a crystal, that is: making it finite by creating a surface. In semiconductors and insulators that have an energy gap separating their valence (highest occupied) and conduction (lowest unoccupied) band, the surface states could disperse such, that parts of their bands reach into the bulk band gap. Far away from the gap (at high/low energies) the surface states will overlap and hybridize with the bulk bands, so that it is impossible to distinguish between bulk and surface states anymore. Thus, in the simplest case, surface bands start and end in bulk bands and can disperse in a random way in between. To visualize that, imagine the bulk bands to be two rivers 1 and 2 that are flowing more or less parallel like depicted in Figure 2.1a. There are basically two different ways how to construct small creeks that start or end in one of the big rivers. As one possibility, the creek starts and ends in the same river. Alternatively, it may connect the two rivers. Now imagine, that from time to time some external parameters (like the topography of the landscape) smoothly change. As a result, the exact course of the creek may vary, too. For the creek that starts and ends in the same river this path disturbance could result in a case, where it completely vanishes in river 1. However, this is *impossible* for the other creek that starts in river 1 and ends in river 2. Hence, this creek is robust against smooth external changes of the landscape and cannot be pushed out of the gap between the two rivers.

To directly apply this idea to topological insulators we have to introduce two further ingredients, namely time–reversal symmetry and spin–orbit interaction. The first is easy to understand: just reverse the arrow of time by pressing the rewind button of the system and

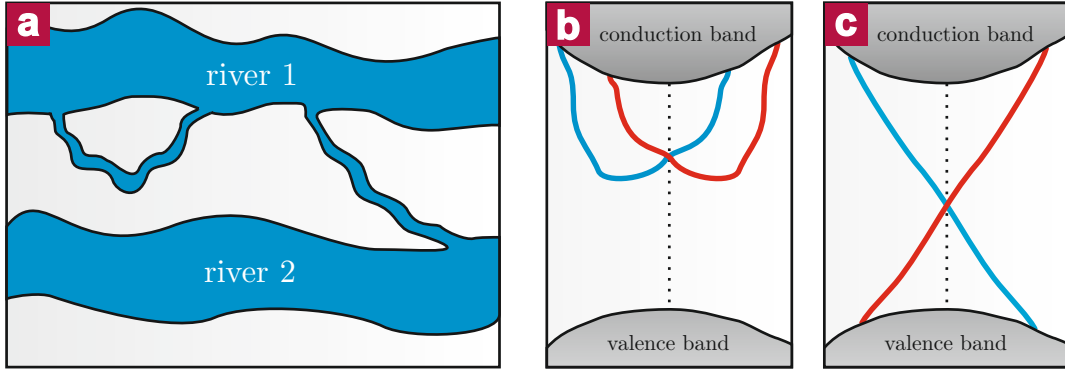


**Figure 2.1: Possible types of surface states.** (a) If a small creek has to fulfill only one boundary condition, that is to start and end in a big river, there are two ways such a creek could flow. In the left case the creek could be pushed out of the gap between the two big rivers by slightly changing the topography of the ground. By contrast, the right case, where the creek starts and ends in different rivers, is robust against perturbations. (b) A trivial insulator. The surface bands are spin-split and start and end in the same band (here: conduction band). (c) A topological insulator. Here, the surface bands connect conduction and valence band. Like for the connecting river arm, these bands cannot be pushed out of the band gap by smooth changes of the energy landscape describing the system.

look at its physical properties. Electrons that were moving in  $+\mathbf{k}$ -direction should now move in  $-\mathbf{k}$ -direction. But rewinding the system will also reverse the spinning direction of the electrons (e.g. their spin). Hence, for a system that is time-reversal symmetric, it follows for an electron with the energy  $E$ :

$$E(\mathbf{k}, \uparrow) = E(-\mathbf{k}, \downarrow). \quad (2.1)$$

For a "normal" material this requirement has little consequences, since every electronic state is two times degenerate (i.e. spin-up and spin-down have same energy). However, in materials consisting of heavy atoms, the electrons orbiting the atomic cores reach such high velocities (due to the very high potential of the positively charged core) that their magnetic orbital angular momentum (classical picture: a current flowing on a circular path induces a magnetic field) gets big enough to influence the orientation of the spin of the electron. This spin-orbit interaction leads to a breaking of the degeneracy of spin-up and -down states. As a consequence according to Equation 2.1 for every electron with, let's say spin-up, moving in  $+\mathbf{k}$  direction there must be a single state at  $-\mathbf{k}$  with opposite spin. Using the concept of connecting rivers, there are still only two possible ways to construct bands inside the gap that start and end in bulk bands. One way is shown in Figure 2.1b, comprising a "parabolic" surface dispersion for the spin-up case (red), which is mirrored at  $\mathbf{k} = 0$  to construct the spin-down band (blue). For the second case, shown in Figure 2.1c, the valence and conduction band are connected by a spin-up band, which is again just mirrored at  $\mathbf{k} = 0$ . One can directly see that Equation 2.1 is fulfilled in both cases.

## Chapter 2. Theoretical Background of Topological Insulators

These are the two possible surface states that can form on the surface of an insulating material with strong spin–orbit coupling, that is time–reversal symmetric. And like in the example of the rivers, the case shown in Figure 2.1b is trivial since the surface bands can be pushed out of the band gap by changes of the energy landscape, making this material a normal insulator. By comparison, Figure 2.1c represents the non–trivial case of a topological insulator, where the spin–polarized linear energy bands (called *Dirac cones*) on its surface cannot be destroyed by any (non–magnetic) disorder.

The last question we have to answer is: when is an insulator trivial and when is it "topological"? The answer is given by the topology of its band structure. Topology simply counts the number of holes in an object. A sphere can be smoothly deformed into a cube without destroying it. However it cannot be continuously deformed into a donut, since one would have to pinch through the surface and introduce a hole into the body. Thus, a sphere (zero holes) and a donut (one hole) are in different topological classes.

The concept of topology can also be applied to the electronic band structures of materi-

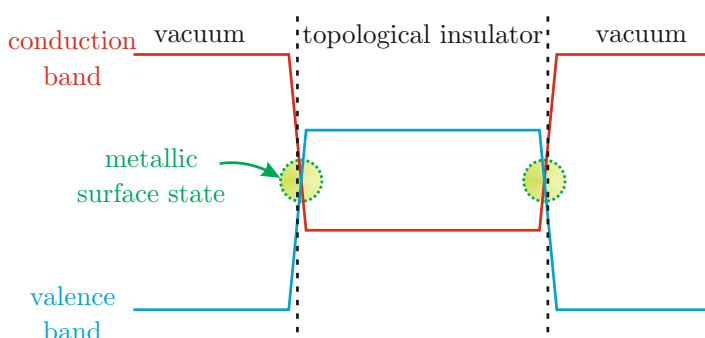


**Figure 2.2: Change in topology.** If a topological insulator is in contact with vacuum, the topology of the band structure changes upon crossing the interface. This results in a gap–closing and –reopening and thus metallic states at the interface.

als. Topological insulators exhibit so–called *inverted* band structures, that is, the order of conduction and valence band is switched, resulting in a "negative band gap" (drawing the band structure would look the same like in the normal case; the bands just have different symmetry and are thus called inverted per definition). These are topologically distinct from the normal band structure of trivial materials. By connecting a topological insulator and a normal insulator (for example vacuum) the topology of the band structure changes at their interface (see Figure 2.2). Thus, by going from the insulator to the topological insulator the band gap will close and re–open again (that's the change in topology; like cutting a hole in a sphere) resulting in a metallic state directly at the interface.

The above descriptions, although partially oversimplified, should provide a useful basis for the detailed mathematical derivation of the topological insulating phase in the next chapters.

## 2.2 Why 'Topological'?

### 2.2.1 Berry-Phase

To illustrate the idea behind a geometric phase, let us consider a gedankenexperiment proposed by Berry<sup>30</sup>: a pencil is placed at the north pole of a globe so that it points along one of the degrees of longitude (see Figure 2.3). It is then moved along this longitude (path 1 – 3) until

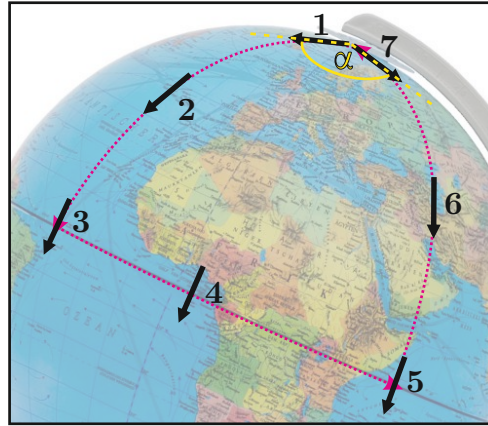


**Figure 2.3: Example of parallel transport.** A vector is moved on a sphere along the path 1 – 7. After a closed loop its angle has changed by  $\alpha$ .

it reaches the next degree of latitude where it makes a left turn and follows this latitude until reaching the next longitude (path 3 – 5). After another left turn, it should move back to the north pole (path 5 – 7). It can be directly seen, that (after returning to its original position) the pencil points in a different direction. This angle-shift  $\alpha$  is a fundamental and purely geometric result of parallel transport, i.e., moving a vector that is slaved to the local vertical along a curved surface. The anholonomy (=the angle shift, which formally equals the Berry-Phase) in this example is equal to the solid angle subtended at the globe's center by the area enclosed by the path the pencil was moved along. Another mechanical example where a Berry-Phase can be measured is the Foucault pendulum, where a vector (direction of swing) is parallel transported around a circle (due to the rotation of the earth). The concept of a geometric phase can also be used to describe phase shifts in electron wavefunctions, when a system in a certain eigenstate is adiabatically transferred to the same initial eigenstate by going along a closed circle in parameter space. This can be achieved by, for example, rotating the spin of an electron using an external magnetic field. The parameter space in this case is defined by a sphere that is spun by unit vectors representing the possible spins. The magnetic field direction is changed in such a way, that it follows a closed loop. Thus, although the electron reaches exactly the same state it had initially, its phase has changed. The geometric phase the electron acquires is given by the product of the spin-quantum number and the solid angle of the area the loop encloses on the parameter space sphere.

To find a general expression for the Berry phase in quantum systems we consider a system

## Chapter 2. Theoretical Background of Topological Insulators

---

with a Hamiltonian  $H(\mathbf{R})$  that changes in time.<sup>31</sup> The Hamiltonian depends on several time-dependent parameters (like the magnetic field, electric field, strain, ...) labeled by a vector  $\mathbf{R}(t) = (R_1(t), R_2(t), R_3(t), \dots)$ . Assume the system to be in its ground-state  $|n(\mathbf{R}(0))\rangle$ . If the state vector  $\mathbf{R}(t)$  is adiabatically (slowly) moved along a closed path  $C$ , the phase of the electron wavefunction changes by:

$$\gamma_n = i \oint_C \langle n(\mathbf{R}) | \nabla_{\mathbf{R}} | n(\mathbf{R}) \rangle d\mathbf{R}. \quad (2.2)$$

Here the Nabla operator  $\nabla_{\mathbf{R}} = \frac{\partial}{\partial \mathbf{R}}$  is the derivative with respect to the parameters. To further develop this equation we can (in analogy to electromagnetic fields) define the Berry vector potential  $\mathbf{A}_n(\mathbf{R}) = i \langle n(\mathbf{R}) | \nabla_{\mathbf{R}} | n(\mathbf{R}) \rangle$  and get

$$\gamma_n = \oint_C d\mathbf{R} \cdot \mathbf{A}_n(\mathbf{R}). \quad (2.3)$$

Since we assumed  $C$  to be a closed path that encloses the surface  $S$  (in parameter space) we can use Stokes theorem to get

$$\gamma_n = \oint_C d\mathbf{R} \cdot \mathbf{A}_n(\mathbf{R}) \stackrel{!}{=} \int_S dA \cdot (\nabla_{\mathbf{R}} \times \mathbf{A}_n(\mathbf{R})) = \int_S dA \cdot \Omega_n(\mathbf{R}). \quad (2.4)$$

In this equation we introduced the curl of the Berry vector potential which is called the Berry curvature  $\Omega_n(\mathbf{R})$ .<sup>i</sup> Like in electrodynamics, where the curl of the vector potential represents a magnetic flux density ( $\mathbf{B}(\mathbf{r}) = \nabla \times \mathbf{A}(\mathbf{r})$ ) the Berry curvature can be interpreted as a flux density in parameter space. The Berry phase is then simply the "flux" through any closed surface  $S$  in parameter space.

An effect that can be readily explained in this simple picture is the Aharonov–Bohm effect (see below). Here the parameter space through which the particle moves is not a complicated mathematical construct, but simply real space through which the particle moves on a circle. The Berry curvature is just the magnetic flux (in units of the flux quantum  $\phi_0 = h/e$ ) that is penetrating that circle.

### 2.2.2 Chern numbers

Before discussing quantum systems let us go back to basic geometry again. Imagine a 3-dimensional object—like a sphere—with a local Gaussian curvature  $K$ . Define a closed area  $S$  (with the boundary  $\partial S$  that may have a geodesic curvature  $k_g$ ) on the surface of the object. The boundary may also contain  $i$  angles  $\alpha_i$ . There is a theorem by Gauß and Bonnet that

---

<sup>i</sup>For the sake of completeness it can be shown, that Equation 2.4 can be used to solve the Foucault pendulum, too. If the Gauss curvature  $K = 1/r^2$  for a sphere with a radius  $r$  is used, the geometric phase  $\alpha(C)$  (in this case: the angle difference of the pendulum after one day) is simply given by  $\alpha(C) = \frac{S(C)}{r^2}$ , where  $S(C)$  is the area the path encloses on a sphere (= earth).

directly links the geometry of this object to its topology:

$$\int_S K dA + \int_{\partial S} k_g ds + \sum \alpha_i = 2\pi\chi(S). \quad (2.5)$$

Here, the Euler characteristic  $\chi(S) = 2 - 2g$  is defined by the genus  $g$  (= number of holes) of the 3-dimensional object. Thus, Equation 2.5 says, that the sum of all angles  $\alpha_i$  and the total curvatures of the surface  $S$  and its boundary  $\partial S$  is an integer number (given by the topology of the object) times  $2\pi$ . This formula simplifies for compact, boundaryless surfaces to

$$\int_S K dA = 2\pi\chi(S). \quad (2.6)$$

This equation states, that the total Gaussian curvature is independent of the exact shape of the surface and only given by the Euler characteristic of the object. Thus, if a sphere ( $g = 0 \rightarrow \chi(S) = 2$ ) is deformed in a completely random way, its local curvature may change drastically, but its total curvature remains constant, or in other words, it is topologically invariant.

These arguments also hold for quantum mechanical systems. Here, the right-hand side of Equation 2.6 is still an integer  $2\pi m$ , where  $m$  is called the Chern number. The importance of the Gauß–Bonnet theorem becomes apparent by comparing Equation 2.6 and Equation 2.4 for the Berry phase. This can be illustrated by the following example of the integer quantum Hall effect. Using the Kubo formula, Thouless, Kohmoto, Nightingale and den Nijs (TKNN) derived an expression for the Hall conductance:<sup>32</sup>

$$\sigma_{xy} = \frac{ie^2}{2\pi h} \sum_n \int_{BZ} d^2\mathbf{k} \left( \frac{\partial u_{n\mathbf{k}}^*}{\partial k_x} \frac{\partial u_{n\mathbf{k}}}{\partial k_y} - \frac{\partial u_{n\mathbf{k}}^*}{\partial k_y} \frac{\partial u_{n\mathbf{k}}}{\partial k_x} \right), \quad (2.7)$$

where the sum is over all occupied electron sub-bands (Landau levels<sup>ii</sup>) and the integration is over the Brillouin zone (BZ). Using the definition for the Berry vector potential (see above) for Bloch states  $\mathbf{A}_n(\mathbf{k}) = i \langle u_{n\mathbf{k}} | \nabla_{\mathbf{R}} | u_{n\mathbf{k}} \rangle$  reduces the Hall conductivity to

$$\sigma_{xy} = \nu \frac{e^2}{h} \quad (2.8)$$

where  $\nu = \sum_n \nu_n$  with

$$\nu_n = \int_{BZ} \frac{d^2\mathbf{k}}{2\pi} \left( \frac{\partial A_{n,y}}{\partial k_x} - \frac{\partial A_{n,x}}{\partial k_y} \right) \quad (2.9)$$

$$= \frac{1}{2\pi} \int_{BZ} d^2\mathbf{k} \cdot \Omega_n(\mathbf{k}) \quad (2.10)$$

$$= \frac{1}{2\pi} \gamma_n^{\partial BZ}. \quad (2.11)$$

<sup>ii</sup>By defining a unit cell with an area  $2\pi\hbar/eB$  (enclosing one flux quantum) Landau levels can be labeled with 2D crystal momenta  $\mathbf{k}$ . If there is in addition a periodic potential with lattice periodicity the energy levels disperse with  $\mathbf{k}$  and form sub-bands (like in an ordinary insulator).<sup>33</sup>

## Chapter 2. Theoretical Background of Topological Insulators

For the last step the definition of the Berry phase  $\gamma_n^{\partial BZ}$  (Equation 2.4) for an electron encircling the Brillouin zone boundary  $\partial BZ$  was used. This is an intriguing result, since it shows, that the Hall conductivity is governed by the phases the electrons in every sub-band  $n$  (=LL) accumulate upon encircling the BZ.

But how can the quantized nature of the quantum Hall effect be explained? The answer can be found using the Gauß–Bonnet theorem again. According to Equation 2.6 the Berry phase in Equation 2.10 should be an integer multiple of  $2\pi$ , where the integer  $m$  again is robust against external (continuous) changes to the system and only given by the topology of the BZ as long as there is a finite gap separating occupied and empty bands (= Landau levels).<sup>iii</sup> Thus, using  $\gamma_n^{\partial BZ} = 2\pi \cdot m$  ( $m$ : Chern numbers), it follows that the Hall conductivity  $\sigma_{xy}$  is quantized in integer values of  $e^2/h$ . In this context, the filling factor  $\nu$  is often referred to as the TKNN invariant.

### 2.2.3 Bulk–boundary correspondence

In the last section it was shown, that topology can be used to describe the quantized conductance in a quantum Hall insulator. But can it also give information on where the conduction actually takes place in the sample? Before answering that question, a simplified explanation for the formation of edge channels in quantum Hall systems shall be given. In a semi-classical

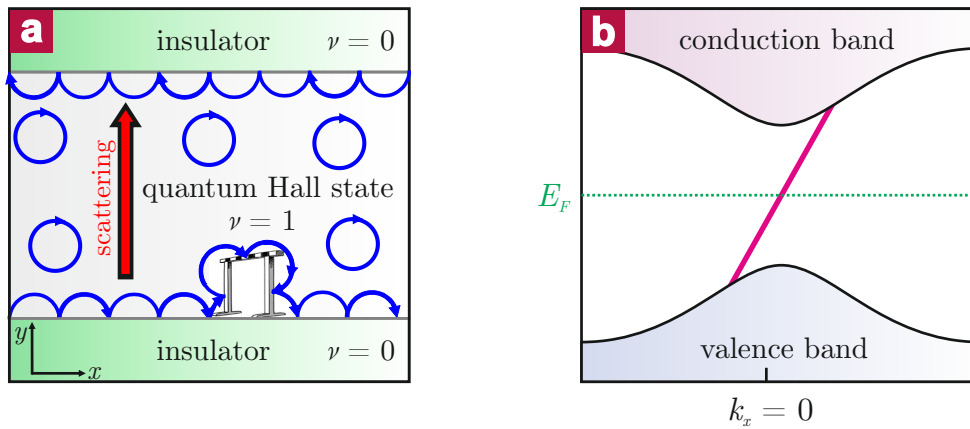


**Figure 2.4: Interface between a trivial insulator and a quantum Hall state.** (a) A system in the quantum Hall state (grey region) in direct contact to two trivial insulators (green region) in  $y$ -direction. An external magnetic field is applied out-of-plane. The electrons are forced on cyclotron orbits (blue circles). Electrons near the boundaries of the quantum Hall system form dissipationless edge channels (skipping orbits). (b) Sketch of the dispersion relation of a single edge state (purple) connecting the bulk conduction and valence band.

<sup>iii</sup>This is the reason why the Chern number is called topological invariant. The Hamiltonian describing the system is invariant under small deformations. Small deformations (external fields, forces, strain) may change the local curvature (= Berry curvature) but the total curvature remains constant, thus the system stays in the initial ground state. The only way to change the Chern number is a large deformation, so that higher energetic states become more favored.

picture, electrons in the quantum Hall state are forced on circular orbits due to the strong external magnetic field (see Figure 2.4a). Thus, electrons in the "bulk" are localized, corresponding to an insulating state. In contrast, electrons near the edges of the sample can probably not fulfill a whole cyclotron orbit but get reflected at the edge. This results in a so-called skipping orbit motion along the edges. Since the orbital motion of all electrons is clockwise or anti-clockwise (like in Figure 2.4a), depending on the orientation of the external magnetic field, there is only one possible direction the electrons can propagate along an edge. In addition, since there are no free states into which back-scattering can occur, the transport is dissipationless (the only possible back-scattering mechanism would be scattering from one edge to the other).

The formation of dissipationless edge states can also be understood on the basis of topology. For the case of a quantum Hall system in direct contact to an insulator (e.g., vacuum), as shown in Figure 2.4a, the topology, given by the TKNN invariant  $\nu$  changes from  $\nu = 0$  ( $\rightarrow \sigma_{xy} = 0$ , trivial insulator) to  $\nu = 1$  (quantum Hall state) upon moving perpendicular to the edges of the system ( $= y$ -direction). But, as stated above, a change in topology is only possible, when the energy gap closes and reopens again. Thus, there must be a gapless state, that is bound to the interface. The dispersion relation of such a state formed at one of the boundaries is sketched in Figure 2.4b. The state connecting the valence and conduction band of the bulk has a positive group velocity  $v_g = \frac{1}{\hbar} \frac{\partial E}{\partial k}$  at the Fermi level and represents a right-moving edge channel. Interestingly, by slightly changing the Hamiltonian near the interface, the shape of the dispersion of the edge state can vary. Imagine one would "deform" the Hamiltonian in such a way, that kinks are introduced in the edge band, such that it passes the Fermi level three times between the valence and the conduction band. This would result in two states with positive (right-mover) and one state with negative (left-mover) group velocity occupied at the Fermi level. In total, there would be one right-mover. The edge state dispersion can be deformed in an arbitrary manner, and the difference  $N_R - N_L$  between the number of right and left-mover will always remain constant and is determined by the topology of the bulk states. This is called the bulk-boundary correspondence

$$N_R - N_L = \Delta\nu, \quad (2.12)$$

where  $\Delta\nu$  is the difference in TKNN invariants across the interface.<sup>33</sup>

## 2.3 Why 'Robust'?

### 2.3.1 Time-reversal symmetry

It is intriguing to look what happens to physical systems, when the arrow of time is simply reversed:

$$T : t \rightarrow -t. \quad (2.13)$$

## Chapter 2. Theoretical Background of Topological Insulators

---

For the example of the quantum Hall effect, the picture of the skipping orbits illustrates how time-reversal changes the system: the electrons orbital motion is clockwise or anti-clockwise depending on the orientation of the external magnetic field. Thus, for a certain field, specific "one-way" channels are formed at the edges. By reversing time, electrons should in principle just go back the way they came from. But since the orientation of the external magnetic field is not changed, moving back along the same edge is impossible (backward moving is only allowed on the opposite edge, as can be seen in Figure 2.4). Accordingly, the Hall conductance would become zero when time is reversed—or in other words—the quantum Hall effect breaks time-reversal symmetry.

Although systems that are time-reversal invariant seem to be less interesting at first glance, some of them exhibit extraordinary topological properties, as will be demonstrated below. Before that, the details of the time-reversal operator shall be briefly explained. Since the time-reversal operator  $\Theta$  only changes the direction of time, the position operator will be unchanged. By contrast, the velocity of a particle and thus the momentum operator flip sign if the time is reversed:

$$\Theta \hat{x} \Theta^{-1} = \hat{x}, \quad \Theta \hat{p} \Theta^{-1} = -\hat{p}. \quad (2.14)$$

It is also possible to look at the action of the time reversal operator on the commutator of  $\hat{x}$  and  $\hat{p}$

$$\Theta [\hat{x}, \hat{p}] \Theta^{-1} = -[\hat{x}, \hat{p}], \quad (2.15)$$

where  $[\hat{x}, \hat{p}] = i\hbar$  (canonical commutation relation). Hence

$$\Theta i \Theta^{-1} = -i. \quad (2.16)$$

For particles without spin, the time reversal operator is equal to the operator of complex conjugation  $K$ . Since the spin  $\mathbf{S}$  of a particle can—in a classical picture—be seen as a kind of spinning-direction of the electron, the time reversal operator has to flip  $\mathbf{S}$ , when the time is reversed and the electron changes its spinning-direction:

$$\Theta \mathbf{S} \Theta^{-1} = -\mathbf{S}. \quad (2.17)$$

For a spin-1/2 particle  $\mathbf{S} = (\hbar/2)(\sigma_x, \sigma_y, \sigma_z)$  with the Pauli matrices

$$\sigma_x = \begin{pmatrix} 0 & 1 \\ 1 & 0 \end{pmatrix} \quad (2.18)$$

$$\sigma_y = \begin{pmatrix} 0 & -i \\ i & 0 \end{pmatrix} \quad (2.19)$$

$$\sigma_z = \begin{pmatrix} 1 & 0 \\ 0 & -1 \end{pmatrix}. \quad (2.20)$$

The operator of complex conjugation  $K$  alone cannot flip the spin of a particle, since  $K\sigma_x K^{-1} = \sigma_x$ ,  $K\sigma_y K^{-1} = -\sigma_y$  and  $K\sigma_z K^{-1} = \sigma_z$ . Thus, to fulfill Equation 2.17 the time-reversal operator has to be expanded by a unitary operator  $U$  with  $U\sigma_x U^{-1} = -\sigma_x$ ,  $U\sigma_y U^{-1} = \sigma_y$  and  $U\sigma_z U^{-1} = -\sigma_z$ . This can only be satisfied if  $U = i\sigma_y$ , hence the time-reversal operator for spin-carrying particles assumes the form:

$$\Theta = i\sigma_y K. \quad (2.21)$$

In classical systems, if the time is reversed twice one simply gets back to the starting point. But is this also true for quantum mechanical systems? Applying the time-reversal operator twice gives:

$$\Theta \cdot \Theta = i\sigma_y K \cdot i\sigma_y K = \begin{pmatrix} 0 & 1 \\ -1 & 0 \end{pmatrix} \begin{pmatrix} 0 & 1 \\ -1 & 0 \end{pmatrix} K^2 = \begin{pmatrix} -1 & 0 \\ 0 & -1 \end{pmatrix} = -I, \quad (2.22)$$

where  $I$  is the identity matrix. Thus, if the time is reversed twice, the spin of a particle is rotated by  $2\pi$ , however the system doesn't come back to its initial state but assumes a minus sign. This change is nothing else than the Berry phase the electron acquires when moving on a closed loop in parameter space (see chapter 2.2.1). A very important consequence of  $\Theta^2 = -1$  in time-reversal invariant systems is the Kramers theorem that will be introduced in chapter 2.3.3. Prior to that the phenomenon of spin-orbit interaction will be described in the following.

### 2.3.2 Spin-Orbit Interaction

A simple description of atoms is given by Bohr's model: electrons surround the positively charged atomic core on orbitals. Classically, an electric current along a closed path creates a magnetic field. Applying this concept to the case of electrons on orbitals, this magnetic field  $\mathbf{B}$  is proportional to their orbital angular momentum  $\mathbf{L}$ . The interaction between  $\mathbf{B}$  and the internal momentum of the electrons, their spin  $\mathbf{S}$ , leads to an energy increase in the case where  $\mathbf{B}$  and  $\mathbf{S}$  are parallel and a decrease in the anti-parallel case.

This picture can be generalized to spin-orbit effects in solids. Let us assume a crystal lattice

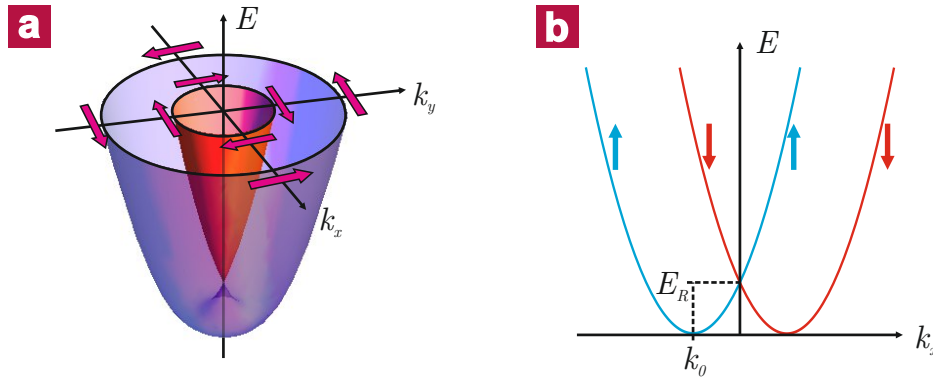


**Figure 2.5: Effect of the spin-orbit coupling on the band structure of a 2D material.** (a) Splitting of the bands into two energy paraboloids due to SOC. The arrows on the circles of constant energy indicate the orientation of the spin of the corresponding state in  $\mathbf{k}$  direction. (b) Cut through the dispersion relation along  $k_x$ . The color of the sub-bands indicates their spin. The shift  $k_0$  of the parabolas is given by the Rashba parameter  $\alpha_R$ .

with an internal electric field  $\mathbf{E} = \nabla V(\mathbf{r})$  due to the gradient of the potential  $V(\mathbf{r})$  of the atomic cores. If an electron moves with an velocity  $\mathbf{v}$  through this lattice, it will see a changing electric field which can be directly transformed (Lorentz transformation) into a  $\mathbf{B}$  field in the electrons rest frame.<sup>34</sup>

$$\mathbf{B} = -\frac{1}{c^2} \mathbf{v} \times \mathbf{E} = \frac{1}{mc^2} \mathbf{E} \times \mathbf{p}, \quad (2.23)$$

where terms of  $(v/c)^2$  or higher order are neglected. Thus, the moving electron "feels" a magnetic field normal to its direction of motion (and normal to the electric field) that can interact with its spin via the Zeeman interaction. The corresponding Hamiltonian is given by

$$H_{SO} = \frac{1}{2} \cdot g \mu_B \mathbf{B} \cdot \mathbf{S} = \frac{g \mu_B}{2mc^2} (\nabla V(\mathbf{r}) \times \mathbf{p}) \cdot \mathbf{S}, \quad (2.24)$$

where  $\mu_B = e/(2m)\hbar$  is the Bohr magneton and  $g$  is the spin gyromagnetic ratio of the electron. The factor  $1/2$  is a correction due to the Thomas precession.<sup>34</sup> Using Equation 2.24 we can also define the *Rashba Hamiltonian*

$$H_R = \alpha_R (\mathbf{S} \times \mathbf{p}) \cdot \mathbf{e} \quad (2.25)$$

where  $\alpha_R = \frac{g \mu_B E_0}{2mc^2}$  is the Rashba parameter, and  $\mathbf{e}$  is the unit vector of the electrical field  $E_0$ . As an example, the total Hamiltonian  $H = H_0 + H_R$  of a 2D electron gas can be diagonalized to

$$E_{\pm} = \frac{\hbar^2 k_{\parallel}^2}{2m^*} \pm \alpha_R k_{\parallel}, \quad (2.26)$$

with  $k_{\parallel} = \sqrt{k_x^2 + k_y^2}$ . It follows that SOC can split spin-degenerate levels since it directly couples the direction of motion to the orientation of the spin. This can be directly seen by plotting

Equation 2.26 (see Figure 2.5a). Figure 2.5b shows a cut in  $k_x$  direction through the dispersion relation. The two energy parabolas for different spins are shifted by  $k_0 = \alpha_R m^* / \hbar^2$ . This shift is most prominent if the electric field of the atomic cores is big. Since this field is directly related to the mass of the atoms, SOC is more relevant in compounds containing heavy elements.

### 2.3.3 Kramers theorem

In a time-reversal invariant system, the corresponding Hamilton operator  $H$  must commute with the time-reversal operator, meaning that  $[\Theta, H] = 0$ . Thus, the eigenstates  $|\psi\rangle$  and  $\Theta|\psi\rangle$  have the same energy  $E$ . But are  $|\psi\rangle$  and its time-reversed state  $\Theta|\psi\rangle$  simply the same quantum state or are they different? Assuming  $|\psi\rangle$  and  $\Theta|\psi\rangle$  were the same state and that they only differ by a phase  $\phi$ , then

$$\Theta|\psi\rangle = e^{i\phi} |\psi\rangle. \quad (2.27)$$

Calculating the time-reversed state yields

$$\Theta \cdot \Theta|\psi\rangle = \Theta \cdot e^{i\phi} |\psi\rangle = e^{-i\phi} \cdot \underbrace{\Theta|\psi\rangle}_{Eq. 2.27} = e^{-i\phi} \cdot e^{i\phi} |\psi\rangle = |\psi\rangle \quad (2.28)$$

$$\Rightarrow \Theta \cdot \Theta = +1. \quad (2.29)$$

This result is in contradiction with that derived from Equation 2.22, demonstrating that every quantum state  $|\psi\rangle$  is different from its time-reversed state  $\Theta|\psi\rangle$ . Therefore the Kramers

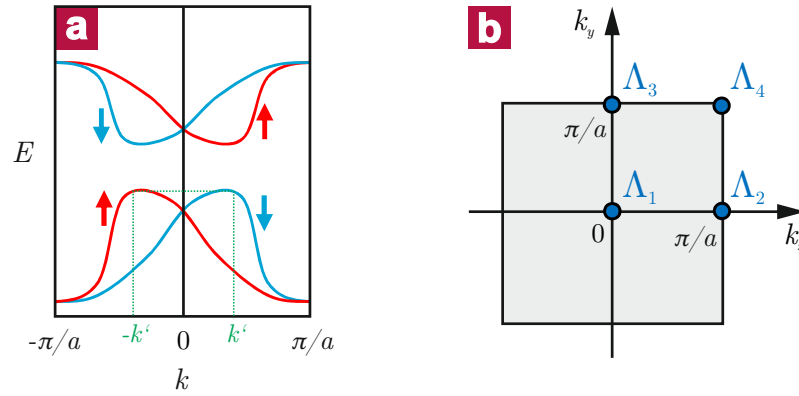


**Figure 2.6: Kramers pairs of bands and time-reversal invariant momenta (TRIMs).** (a) The degeneracy for spin-up (red) and -down (blue) bands is lifted due to spin-orbit coupling. For every wavevector  $k'$  there is a corresponding state  $-k'$  at the same energy (see dashed green line), forming a Kramers pair. Each pair of bands are degenerate at TRIM points. (b) Four TRIM points  $\Lambda_1$  to  $\Lambda_4$  for a 2D square BZ (grey shaded area).<sup>35</sup>

theorem states, that all eigenstates of a time-reversal invariant Hamiltonian  $H$  are at least

## Chapter 2. Theoretical Background of Topological Insulators

two-fold degenerate. In a system without spin–orbit interaction, this is *simply the degeneracy between spin–up and –down states* ( $E_{\uparrow}(\mathbf{k}) = E_{\downarrow}(\mathbf{k})$ ). But by switching on spin–orbit coupling, spin–degeneracy is lifted and the Kramers theorem has important consequences. A time–invariant Hamiltonian satisfies<sup>35</sup>

$$\Theta H(\mathbf{k}) \Theta^{-1} = H(-\mathbf{k}). \quad (2.30)$$

Thus, for every—for example spin–up—electron with a wavevector  $\mathbf{k}$  at a certain energy  $E$  there must be a corresponding time–reversed spin–down electron with  $-\mathbf{k}$  (see Figure 2.6a)

$$E_{\uparrow}(\mathbf{k}) = E_{\downarrow}(-\mathbf{k}). \quad (2.31)$$

These two states form a so–called *Kramers pair*. The Kramers pairs are degenerate at special time–reversal invariant momenta (TRIM) points due to the periodicity of the Brillouin zone (for example at  $\mathbf{k} = 0$  or  $\mathbf{k} = \pi/a$ , which is equal to  $\mathbf{k} = -\pi/a$ ). As an example the TRIM points of a 2D cubic BZ are depicted in Figure 2.6b.

### 2.4 $Z_2$ Topological Insulators

This section addresses the question, which materials are topological insulators and which ones are not. Imagine a 2D time–reversal invariant insulator whose valence and conduction bands

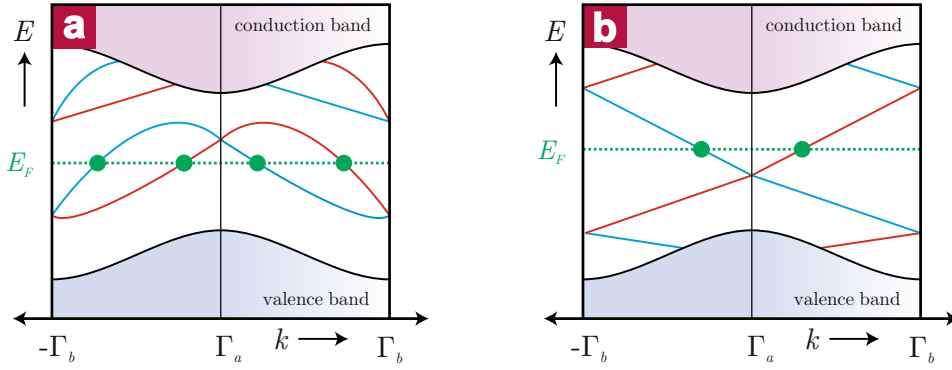


**Figure 2.7: Possible dispersion relations between two TRIM points  $\Gamma_a = 0$  and  $\Gamma_b = \pi/a$  at one edge of a 2D insulator.** (a) A trivial insulator, where an even number of edge states is crossing the Fermi energy  $E_F$  (green points). (b) The non–trivial case, where an odd number of edge states is crossing  $E_F$  (green points). This leads to topologically protected metallic boundary states.<sup>33</sup> To illustrate the concept of Kramers pairs, the band structure is plotted from  $-\Gamma_b$  to  $+\Gamma_b$  through  $\Gamma_a$ .

are separated by an energy gap (see Figure 2.7). Depending on the Hamiltonian describing the system, edge states may form within the bulk band gap. The Kramers theorem requires, that these states are two–fold degenerate at the TRIM points. If spin–orbit coupling is strong, this

degeneracy is lifted for all momenta  $k$  between the TRIM points ( $\Gamma_a = 0$  and  $\Gamma_b = \pi/a$  in Figure 2.7), such that the edge bands split into spin-down and spin-up bands. There are two possible ways how the TRIM points can be connected by the edge states. In Figure 2.7a, the TRIMs are connected by the same pair of spin-split bands. Thus, the edge states will cross the Fermi level an even number of times. This represents the case of a trivial insulator for two reasons: Firstly, back-scattering is allowed, since for every  $+k$  there are free states at certain  $-k'$  with the same spin-orientation. Thus, these states will be localized by weak disorder.<sup>36</sup> Secondly, by smoothly changing the Hamiltonian, it is possible to push the edge bands completely out of the band gap (imagine, the Kramers points at  $\Gamma_a$  and  $\Gamma_b$  are continuously pushed down to lower energies until they overlap with the bulk valence band).

But there is also a second way to connect the TRIMs. In Figure 2.7b, the edge bands cross the Fermi energy an odd number of times. This is a non-trivial case, i.e., of a topological insulator, since the edge states cannot be eliminated by slightly changing the Hamiltonian. Likewise, opening a gap in the crossing edge-states at the TRIM points is impossible, since they form Kramers doublets, whose degeneracy cannot be lifted by any perturbation that is not breaking time-reversal symmetry. This is an outstanding feature of topological insulators, involving robust, time-reversal symmetry protected boundary states which allow for example chemical modification of the material without destroying these boundary states.<sup>6</sup>

The band structure in Figure 2.7b closely resembles the one in Figure 2.4b for an edge channel in the quantum Hall phase. However there is an important difference: as a consequence of time-reversal invariance in the case of a topological insulator there are two counter-propagating channels per edge (the crossing bands possess different group velocities). But since the two bands form time-reversed Kramers pairs, their spin-orientation is opposite. Thus, the edge states are spin-filtered in the sense that electrons with opposite spins propagate in opposite directions.<sup>37</sup> Hence, like in the case of the quantum Hall effect, elastic back-scattering by a random potential is forbidden, and consequently electrical transport along an edge of a topological insulator is spin-filtered and dissipationless.

How can one distinguish between materials that behave trivial and those who are topological insulators? Unfortunately, the classification by TKNN invariants introduced in section 2.2.2 for the integer quantum Hall effect cannot directly be used for this purpose, since in time-reversal invariant systems the quantum Hall effect vanishes and thus the TKNN invariant  $\nu = 0$ . Thus, a new classification of time-reversal invariant systems by a so-called  $Z_2$  invariant  $\nu_{Z_2}$  has been introduced.<sup>36</sup> Since the number  $N_K$  of Kramers pairs that intersect the Fermi level directly tells us if the system is trivial ( $N_K = \text{even}$ ) or non-trivial ( $N_K = \text{odd}$ ), a new bulk-boundary correspondence (compare Equation 2.12) can be formulated:

$$\Delta\nu_{Z_2} = N_K \bmod 2, \quad (2.32)$$

where  $\Delta\nu_{Z_2}$  is the change in the  $Z_2$  invariant across the interface and  $\bmod 2$  is the modulo operation that finds the remainder of the division by 2. Thus, for example, if  $\nu_{Z_2}$  is the same on both sides of the interface,  $\Delta\nu_{Z_2} = 0$  and the edge states intersect the Fermi level an even number of times. By comparison—like in the case of the integer quantum Hall effect—the

## Chapter 2. Theoretical Background of Topological Insulators

---

"topology" changes when passing the boundary, an odd number of Kramers pairs cut the Fermi level and a non-trivial state is formed at the interface.

What is the physical meaning of the  $Z_2$  invariant and how can the value of  $\nu_{Z_2}$  be calculated? For the easiest case, a 2D system where the perpendicular spin  $S_z$  is conserved due to the absence of inter-band coupling, interactions or disorder, each spin component can be treated independently and is described by an individual TKNN integer  $n_\downarrow$  or  $n_\uparrow$ .<sup>36</sup> Time-reversal symmetry still requires, that the total TKNN integer  $n_\downarrow + n_\uparrow = 0$ , but their difference  $n_\sigma = (n_\downarrow - n_\uparrow)/2$  defines a quantized spin Hall conductivity. The  $Z_2$  variant is then given by

$$\nu_{Z_2} = n_\sigma \bmod 2. \quad (2.33)$$

It can be directly seen, that Equation 2.33 has only two possible solutions: the case of a trivial insulator ( $\nu_{Z_2} = 0$ ) and the case of a topological insulator ( $\nu_{Z_2} = 1$ ). For more realistic systems (where  $S_z$  is not conserved), however, the calculation of the  $Z_2$  invariant becomes more complicated. The basic principle to achieve this is to somehow "count" the number of Kramers pairs of the edge modes. One way to do so is to define an antisymmetric matrix  $w_{ij}(\mathbf{k})$  of overlaps of the  $i$ th occupied Bloch band wave function  $|u_i\rangle$  with the time-reversal of the  $j$ th eigenstate  $\Theta|u_j\rangle$ .<sup>31,36</sup>

$$w_{ij}(\mathbf{k}) = \langle u_i(\mathbf{k}) | \Theta | u_j(\mathbf{k}) \rangle. \quad (2.34)$$

There are two basic ways how a Bloch wave can change under application of the time-reversal operator: in the "even" case  $\Theta|u_j(\mathbf{k})\rangle$  is equal to  $|u_j(\mathbf{k})\rangle$ . This is, for example, fulfilled at the special TRIM points ( $k = 0, k = \pi/a$ ) in the BZ. In the "odd" case,  $\Theta|u_j(\mathbf{k})\rangle$  is orthogonal to  $|u_j(\mathbf{k})\rangle$ . This corresponds to the Kramers pairs we are interested in. The even and odd subspaces spanned by the Bloch waves can be identified by calculating the Pfaffian of  $w_{ij}(\mathbf{k})$ :

$$P(\mathbf{k}) = \text{Pf}[\langle u_i(\mathbf{k}) | \Theta | u_j(\mathbf{k}) \rangle]. \quad (2.35)$$

For the even subspace  $|P(\mathbf{k})| = 1$ , whereas for the (interesting) odd subspace  $P(\mathbf{k}) = 0$ . Thus, the strategy to calculate the  $Z_2$  invariant is to count the zeros of  $P(\mathbf{k})$  in half (time-reversal symmetry!) of the Brillouin zone. Depending on the symmetry of the system, these zeros can be at special symmetry points or lie on loops around TRIM points (where  $P(\mathbf{k}) = 1$ ). The  $Z_2$  index  $I$  is hence given by

$$I = \frac{1}{2\pi i} \int_C d\mathbf{k} \cdot \nabla \log(P(\mathbf{k})), \quad (2.36)$$

where the contour  $C$  is half the BZ.  $\nu_{Z_2} = I \bmod 2$  can be 0 for an even number of zeros (trivial insulator), or 1 for an odd number of zeros (topological insulator).

Before coming to real examples of TIs, a more physical interpretation of the  $Z_2$  index shall be given by introducing the model of time-reversal polarization ( $\Theta$ -polarization). In this model, the quantum spin Hall effect (topological insulator) is described by an *adiabatic spin pump*<sup>38</sup> similar to Laughlin's argument.<sup>39</sup> In the latter, the integer quantum Hall effect was thought as

an adiabatic charge pump within the following gedankenexperiment: Imagine a 2D electron

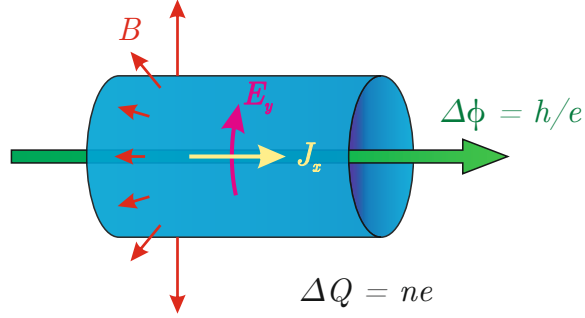


**Figure 2.8: Laughlin's gedankenexperiment.** For cylindrical 2D electron gas, a strong magnetic field  $B$  is applied normal to its surface to condensate all carriers in certain Landau levels. If the flux through the cylinder is changed, this charge pump generates an electrical field  $E_y$  in  $y$ -direction which induces a Hall current  $J_x$  in the  $x$ -direction. Changing the flux by one flux-quantum will transfer a charge  $ne$  from one side of the device to the other.<sup>40</sup>

gas that is rolled into cylindrical shape like depicted in Figure 2.8. Suppose that this system has an energy gap which is due to an external  $B$ -field normal to the surface, that condensates the density of states into Landau level and that the Fermi energy is located in this gap. If a magnetic flux  $\phi$  is penetrating through the cylinder and is slowly varied with time, an electrical field  $E_y$  will be induced on the cylinders surface (Faraday's law). This electric field is connected to the Hall current density  $J_x$  by  $J_x = \sigma_{xy} E_y$ , where  $\sigma_{xy}$  is the Hall conductance. The charge  $Q$  that is transported along  $x$  is related to the current density by the continuity equation:

$$\frac{dQ}{dt} = - \oint_C dl \cdot J_x = -\sigma_{xy} \oint_C dl \cdot E_y \stackrel{\text{Stokes}}{=} \sigma_{xy} \int_S dS \cdot \nabla \times E_y. \quad (2.37)$$

Using Faraday's law  $\nabla \times \mathbf{E} = -\frac{d\mathbf{B}}{dt}$  and the definition of magnetic flux  $\phi = \int_S dS \cdot \mathbf{B}$ , it can be written

$$\frac{dQ}{dt} = \int_S dS \cdot \frac{d\mathbf{B}}{dt} = \sigma_{xy} \frac{d\phi}{dt}. \quad (2.38)$$

Hence

$$\Delta Q = \sigma_{xy} \Delta \phi. \quad (2.39)$$

If the flux is changed by one flux quantum  $\Delta \phi = h/e$  the charge  $\Delta Q = n \cdot e$  is transferred from one side of the cylinder to the other, and the Hall conductance becomes  $\sigma_{xy} = n \frac{e^2}{h}$ . The number  $n$  of electrons corresponds to the so-called *charge polarization*  $P_\rho$ , which is given by Equation 2.10 (phase change of the electron when performing one orbit around the cylinder during one pump-cycle) and is equal to the TKNN invariant.

The above concept can be used to unravel the physical meaning of the  $Z_2$  invariant. If a

## Chapter 2. Theoretical Background of Topological Insulators

magnetic flux is threading a quantum *spin* Hall system that is rolled up into cylindrical shape, a certain *spin*  $\Delta S_z$  is transferred from one side of the cylinder to the other, when the flux is changed by one flux quantum (whereas the total *charge* that is transferred is zero due to time-reversal symmetry). In this case, the spin that is transported is given by  $\Delta S_z = v_{Z2} \hbar$ , where  $v_{Z2}$  is the  $Z_2$  invariant.<sup>38</sup> Following the idea of the charge pump, the total charge polarization  $P_\rho$  (that originally defined the number of electrons flowing during one pump cycle) can be redefined as a sum of *partial polarizations*  $P_i$  of every contributing band. Now let's have a look at time-reversal invariant systems. The contributing bands  $i$  should now be a Kramers pair, thus  $P_\rho = P_1 + P_2 \stackrel{!}{=} 0$ , since there is no charge polarization when the system is time-reversal invariant. But we can also define a new quantity called the  $\Theta$ -polarization  $P_\theta$  which is given by

$$P_\theta = P_1 - P_2 = 2P_1 - P_\rho. \quad (2.40)$$

This quantity represents the difference in charge polarization between spin-up and spin-down bands, since the bands 1 and 2 form a Kramers pair. The partial polarizations  $P_i$  can be calculated using Equation 2.10:

$$P_i = \frac{1}{2\pi} \int_{-\pi}^{\pi} dk \cdot A_i(k), \quad (2.41)$$

where  $A_i$  is the Berry vector potential (Berry connection) of the Kramers partner  $i$  and the integration is done from one TRIM at  $k = -\pi$  to  $k = \pi$  via the TRIM at  $k = 0$ . By using the matrix  $w_{ij}(k)$  (see Equation 2.34) it can be shown that:<sup>35,38</sup>

$$P_\theta = \frac{1}{i\pi} \log \left( \frac{\sqrt{\det[w(0)]}}{\text{Pf}[w(0)]} \cdot \frac{\text{Pf}[w(\pi)]}{\sqrt{\det[w(\pi)]}} \right), \quad (2.42)$$

or

$$(-1)^{P_\theta} = \frac{\sqrt{\det[w(0)]}}{\text{Pf}[w(0)]} \cdot \frac{\text{Pf}[w(\pi)]}{\sqrt{\det[w(\pi)]}}. \quad (2.43)$$

For a skew-symmetric matrix  $\text{Pf}[w]^2 = \det[w]$ . Thus,  $P_\theta$  can only assume the values 0 or 1. To expand this model to a 2D system (until now we were only integrating along one direction in the BZ), all TRIM points have to be included. For a cubic BZ, these are the points  $\Lambda_i$  with  $i = 1$  to 4 (see Figure 2.6). Therefore, the  $Z_2$  invariant is given by

$$(-1)^{v_{Z2}} = \prod_{i=1}^4 \delta_i \quad (2.44)$$

with

$$\delta_i = \frac{\text{Pf}[w(\Lambda_i)]}{\sqrt{\det[w(\Lambda_i)]}}. \quad (2.45)$$

The general idea behind this formula is the following: All TRIM points will be connected by two edge-bands (see TRIM points  $\Gamma_a$  and  $\Gamma_b$  in Figure 2.7). The expression  $\frac{\text{Pf}[w(\Lambda_i)]}{\sqrt{\det[w(\Lambda_i)]}}$  gives the  $\Theta$ -polarization at every TRIM point and can only be +1 or -1, since  $\text{Pf}[w]^2 = \det[w]$ . If the  $\Theta$ -polarization of two TRIM points is identical, then they share the same two spin-split edge bands (see Figure 2.7a). In contrast, if the  $\Theta$ -polarization of two TRIM points is different, there is a sign-change in between the points and thus there must be an edge mode crossing the Fermi level if situated in the gap.<sup>31</sup> This is the non-trivial case depicted in Figure 2.7b, where Kramers pairs "switch partners" (i.e., TRIM points).

It should be noted, that Equation 2.44 can be further simplified if the crystal has inversion symmetry. In that case only the eigenvalues  $\xi_m(\Lambda_i)$  of the space inversion operator  $\Pi$  have to be calculated at the TRIM points  $\Lambda_i$  using  $\Pi|u_m(\Lambda_i)\rangle = \xi_m(\Lambda_i)|u_m(\Lambda_i)\rangle$ . The  $Z_2$  invariant can then be simply obtained using

$$(-1)^{v_{Z_2}} = \prod_{i=1}^4 \prod_{m=1}^N \xi_m(\Lambda_i), \quad (2.46)$$

where the second product is over the Kramers pairs of  $2N$  occupied bands preserving inversion symmetry and time-reversal symmetry. This formalism is widely used to predict candidates of TI materials.<sup>41,42</sup>

### 2.4.1 $Z_2$ invariants in three dimensions

The concept of distinguishing trivial and non-trivial insulators using  $Z_2$  invariants can be easily generalized to three-dimensional (3D) systems.<sup>43</sup> In 3D, time-reversal invariant insulators are characterized by four  $Z_2$  invariants. Since every invariant can have the values 0 or 1, this leads to 16 classes of trivial/topological insulators. In a cubic-primitive Brillouin zone, the eight TRIM points  $\Gamma_i$  are located at the vertices of a cube (see Figure 2.9) and can be expressed in terms of a reciprocal lattice vector  $\Gamma_{i=n_1 n_2 n_3} = (n_1 \mathbf{b}_1 + n_2 \mathbf{b}_2 + n_3 \mathbf{b}_3)/2$ , with  $n_j = 0, 1$ . For every TRIM  $\Gamma_i$  a parameter  $\delta_i = \pm 1$  can be calculated using Equation 2.45 or 2.46 (if the crystal has inversion symmetry). The four  $Z_2$  invariants  $v_0; (v_1 v_2 v_3)$  describing the system are defined as

$$(-1)^{v_0} = \sum_{n_j=0,1} \delta_{n_1 n_2 n_3}, \quad (2.47)$$

$$(-1)^{v_{i=1,2,3}} = \sum_{n_{j \neq i}=0,1; n_i=1} \delta_{n_1 n_2 n_3}. \quad (2.48)$$

These equations shall be illustrated by an example. In the cubic BZ (blue) in Figure 2.9a, the  $\delta_i$  for every TRIM are:  $\delta_{000} = -1$ ,  $\delta_{100} = -1$ ,  $\delta_{010} = +1$ ,  $\delta_{001} = +1$ ,  $\delta_{110} = +1$ ,  $\delta_{011} = +1$ ,  $\delta_{101} = -1$  and  $\delta_{111} = +1$ . The invariant  $v_0$  can be calculated using Equation 2.47, as the product of *all* possible  $\delta_i$ , i.e.  $(-1) \cdot (-1) \cdot (+1) \cdot (+1) \cdot (+1) \cdot (+1) \cdot (-1) \cdot (+1) = -1$  and  $v_0 = 1$ . The index  $v_1$  can be calculated from the product of all  $\delta_{n_1 n_2 n_3}$  where  $n_1 = 1$  (see Equation

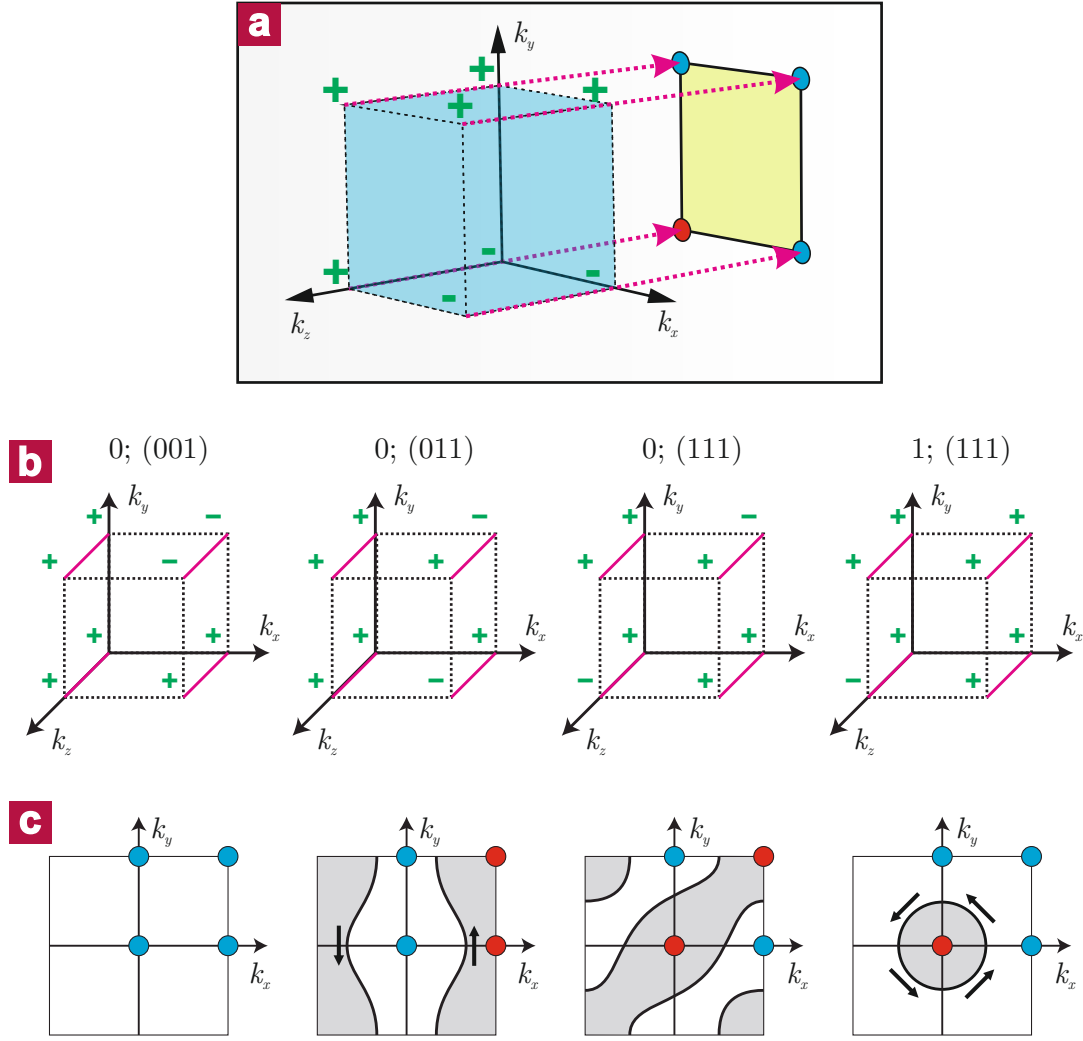


**Figure 2.9: Topological phases in three dimensions.** (a) Example of a (001) surface. The eight TRIM  $\Gamma_i$  are projected on the  $x$ - $y$  plane. The green + and - signs at the vertices of the cube depict the sign of  $\delta_i$ . The blue (+) and red (-) circles on the  $x$ - $y$  plane depict the sign of  $\pi_a = \delta_{i=a1}\delta_{i=a2}$ . (b) Four different phases indexed by  $v_0; (v_1 v_2 v_3)$ . (c) Corresponding projections on (001). The thick black lines and grey shaded areas indicate possible surface Fermi surface arcs.<sup>43</sup>

2.48), hence  $\delta_{100} \cdot \delta_{110} \cdot \delta_{101} \cdot \delta_{111} = (-1) \cdot (+1) \cdot (-1) \cdot (+1) = 1$  and  $v_1 = 0$ . The invariants  $v_2$  and  $v_3$  are obtained in the same manner yielding  $(-1)^{v_2} = \delta_{010} \cdot \delta_{011} \cdot \delta_{110} \cdot \delta_{111} = 1$  and  $(-1)^{v_3} = \delta_{001} \cdot \delta_{011} \cdot \delta_{101} \cdot \delta_{111} = -1$ , and finally:  $v_0; (v_1 v_2 v_3) = 1; (0, 0, 1)$ . Four other bulk phases are shown in Figure 2.9b.

Now let's come to the question what happens, if a boundary is introduced to a time-reversal invariant material. To investigate these boundaries (e.g. the surfaces), the TRIM points are projected along the direction normal to the surface that is formed. This is depicted in Figure 2.9a for a (001) surface, where the eight bulk TRIM points  $\Gamma_i$  are projected onto the  $x$ - $y$  plane

along the  $[00\bar{1}]$  direction. The four surface Kramers degenerate points  $\Lambda_a$  are projections of pairs  $\Gamma_{a1}\Gamma_{a2}$  and form 2D *Dirac points*. The pairs of  $\delta_i$  are combined to a new parameter  $\pi_a = \delta_{a1}\delta_{a2} = \pm 1$  which expresses the  $\Theta$ -polarization associated with every surface TRIM point  $\Lambda_a$ . The signs of  $\pi_a$  are depicted by blue (+) and red (−) circles in Figure 2.9a and c.

Importantly, the same arguments like in the 2D case can be used to describe the surface spectrum of the system: if two surface TRIM points  $\Lambda_a$  and  $\Lambda_b$  with different  $\Theta$ -polarization (given by the sign of  $\pi_a$  and  $\pi_b$ ) are connected, the  $\Theta$ -polarization has to change sign along that path resulting in a "partner switching" at the TRIM, as depicted in Figure 2.7b. Thus, this path intersects the Fermi surface once (non-trivial case). If there is no sign-change along a path connecting two TRIM points with the same  $\Theta$ -polarization, the surface band will intersect with the Fermi level an even number of times or not at all (see Figure 2.7a). Thus, for any path connecting two surface TRIM points  $\Lambda_a$  and  $\Lambda_b$ , the surface band structure will be equal to Figure 2.7a or b if  $\pi_a\pi_b = 1$  or  $-1$ . As a consequence, the Fermi surface will divide the surface BZ into two region: one region with Dirac points at TRIMs with  $\pi_a = -1$  and the other region with  $\pi_a = +1$ . This is shown in Figure 2.9c for the (001) surface of four different bulk phases. The thick black lines and grey shaded areas denote different surface Fermi arcs which enclose specific  $\Lambda_a$ . In the left panel all  $\pi_a$  are positive, thus no path connecting any TRIM will cut the Fermi surface. This is the case of a trivial insulator. In the second left panel the Fermi surface is intersected in  $k_x$  direction, although the path along  $k_y$  does not cut the Fermi surface (or is cutting it an even number of times). The second right panel shows a similar situation, since there is a path along the  $[110]$  direction where the surface Fermi surface is not cut. These phases with  $\nu_0 = 0$  are called *weak topological insulators* (WTI), since a weak periodic potential is able to open a gap at their Dirac points. They can be interpreted as a stack of 2D topological insulators in the direction given by the vector  $G_v = \nu_1\mathbf{b}_1 + \nu_2\mathbf{b}_2 + \nu_3\mathbf{b}_3$  defined by the  $Z_2$  invariants. This can be directly from Figure 2.9c, where  $G_v$  always points in the "trivial" direction, whereas planes normal to that vector would intersect the Fermi level once and thus behave non-trivial.

If the Fermi arc encloses either one or three Dirac points (like shown in the right panel) the phase is called a *strong topological insulator* (STI) described by  $\nu_0 = 1$ . These materials are robust and form Dirac points on all faces.<sup>43</sup> Like in the 2D case, time-reversal symmetry requires that states at  $\mathbf{k}$  and  $-\mathbf{k}$  have opposite spins making the surface states of a strong 3D topological insulator a so-called "helical metal" where the spin rotates with  $\mathbf{k}$  around the Fermi surface.<sup>33</sup> This leads to a non-trivial Berry-phase of  $\pi$  when an electron encircles the Fermi surface once. As a result, those states are immune against localization by weak disorder (see Chapter 3.3.2).

### 2.4.2 Theoretical prediction of real Topological Insulator materials

**2D Topological Insulators** Remarkably, the first topological insulator that was predicted theoretically was graphene, a  $sp^2$ -bonded monolayer of graphite.<sup>37</sup> It has been put forward that spin-orbit interaction should open a gap in the Dirac cones at the  $K/K'$  points of graphene. Interestingly, the signs of the gaps at  $K$  and  $K'$  are opposite. Thus, by connecting them, two edge

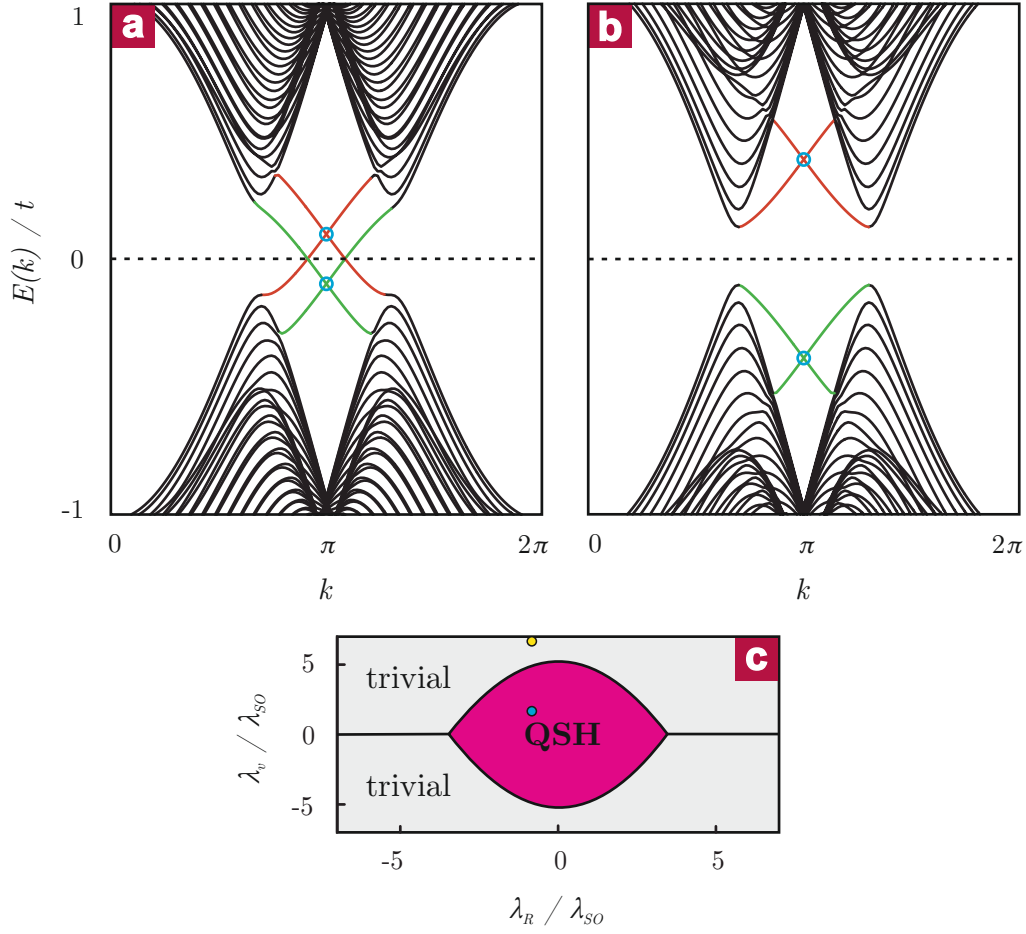


**Figure 2.10: Quantum spin Hall effect in a one-dimensional zigzag stripe of graphene.** (a) QSH phase. The dispersions of the different edges (green and red lines) cross at the TRIM point  $k = \pi$  (blue circles). (b) Trivial insulator case. (c) Phase diagram as a function of  $\lambda_v$ ,  $\lambda_R$  and  $\lambda_{SO}$ . The blue circle and yellow circle correspond to the QSH phase in (a) and the trivial case in (b), respectively.<sup>36</sup>

bands (per edge) will cross at the TRIM point  $k_x = \pi$  (see Figure 2.10a). The gap introduced by spin-orbit interaction is "topologically" different from a gap that could be introduced by, for example, breaking of inversion symmetry by a staggered sublattice potential (see Figure 2.10b). By smoothly changing the strength  $\lambda_v$  of the staggered sublattice potential, a transition between the two phases, the trivial and the non-trivial one, should occur. At the transition the bulk energy bandgap closes and reopens again, allowing the edge states to "switch partners". Thus, a phase diagram can be constructed, describing the occurrence of the different topological phases as a function of the strength of the spin-orbit coupling  $\lambda_{SO}$ , the strength of the staggered sublattice potential  $\lambda_v$ , and the strength of the Rashba effect  $\lambda_R$  (see Figure 2.10c).<sup>36</sup> Although from a theoretical point of view graphene should be a 2D topological insulator, an experimental proof is still lacking. This is mainly because the gap opened due to spin-orbit

interaction is on the order of  $10^{-3}$  meV, which is rather difficult to detect by spectroscopic or electrical transport measurements.

Nevertheless, the band-inversion (e.g., a "negative" bandgap) in graphene stimulated the identification of further TI materials. Such a band-inversion can be found at the  $\Gamma$ -point of quantum wells of HgTe.<sup>31</sup> Due to the heavy elements in that compound, the very strong spin-orbit interaction lifts the  $p$  orbitals above the  $s$  levels, resulting in an inverted band structure. However, bulk HgTe is a zero-gap semiconductor. A way to open up a gap in such systems is to reduce the dimensions of the material. Practically, for HgTe, that has been achieved by fabricating sandwich structures of CdTe/HgTe/CdTe.<sup>44</sup> Confining HgTe to two dimensions creates quantum well states parallel to the confinement direction. The band structure of the 2D electron gas (2DEG) formed normal to that direction can be tuned by the thickness of the well. For thick quantum wells ( $d > d_c$ ) the 2D bands have the same inverted order like the bulk material. By decreasing the well thickness the confinement energy for every subband increases. Below a critical thickness  $d_c$  the  $s$ -like subbands shift to higher energies than the  $p$ -like subbands and the band order is trivial again. Thus, by successively changing the thickness of the HgTe layer, its bandgap can be changed from inverted to normal band-order.<sup>45</sup> This quantum phase transition in turn comes along with a closing and opening of a bulk bandgap, and hence a change in the  $Z_2$  invariant of the system. For the inverted case, the  $Z_2$  invariant of the HgTe layer is  $\nu_{Z_2} = 1$ , whereas the CdTe layers are trivial insulators with  $\nu_{Z_2} = 0$ . The bulk-boundary correspondence leads to time-reversal protected edge states at the boundary. The existence of such spin-polarized edge-states in the 2D topological insulator HgTe could be verified by electrical transport measurements.<sup>46–48</sup>

**3D Topological Insulators** Like in the 2D case discussed above, the best strategy to find 3D TIs is to consider materials with strong spin-orbit interaction that may lead to an inverted band structure at certain points in their BZ. By investigating such compounds that additionally exhibit inversion symmetry (see Equation 2.46), Fu and Kane<sup>41</sup> were able to predict the first strong 3D topological insulators:  $\alpha$ -Sn and HgTe (both under uniaxial strain), as well as the  $\text{Bi}_{1-x}\text{Sb}_x$  alloy.  $\alpha$ -Sn and HgTe are zero-bandgap semiconductors with an inverted band-order at their  $\Gamma$  point. Small uniaxial strain lifts the degeneracy at  $\Gamma$  and opens up a band gap. Strained HgTe films have been successfully proven to be topological insulators using low- $T$  electrical transport measurements.<sup>49</sup>

Pure Bi is a semimetal with conduction band minima (separated from the valence band maxima by a small bandgap of several 10 meV) at the three equivalent L points overlapping with a valence band maximum at the T point. This leads to electron (hole) pockets at the L (T) point. By alloying Sb into Bi the valence band edge at the T point can be shifted to lower energies. Interestingly, at a concentration of about  $x \approx 0.04$ , the gap at the L point closes and reopens again in inverted order. At a concentration of about  $x \approx 0.09$ , the T band drops below the valence band at L and the system becomes a direct (inverted) semiconductor. This phase belongs to the 1;(111) class and is a strong TI.

## Chapter 2. Theoretical Background of Topological Insulators

Although it has been verified that  $\text{Bi}_{1-x}\text{Sb}_x$  alloy is a strong topological insulator by means of ARPES experiments<sup>50</sup> electrical transport experiments on this material are challenging. On the one hand, very good control of the composition  $x$  is needed, since the topological insulating phase only exists for the range  $0.07 < x < 0.22$ . In addition, alloys tend to form impurity bands inside their bandgap leading to an extra transport channel that screens surface effects. On the other hand, the electronic surface structure of  $\text{Bi}_{1-x}\text{Sb}_x$  is very complicated with five surface bands crossing the Fermi level. This complicates the interpretation of experimental results. Thus, the motivation to find materials with controlled stoichiometry and a simple surface band structure led to the discovery of the topological insulators  $\text{Bi}_2\text{Se}_3$ ,  $\text{Bi}_2\text{Te}_3$  and  $\text{Sb}_2\text{Te}_3$  by Zhang *et al.*<sup>42</sup>

The chalcogenides  $\text{Bi}_2\text{Se}_3$ ,  $\text{Bi}_2\text{Te}_3$  and  $\text{Sb}_2\text{Te}_3$  form rhombohedral (space group  $R\bar{3}m$ ) crystals consisting of hexagonally close-packed atomic layers of five atoms (quintuple layer) that are weakly bonded together by van der Waals interaction (see Figure 2.11a and b). In the case

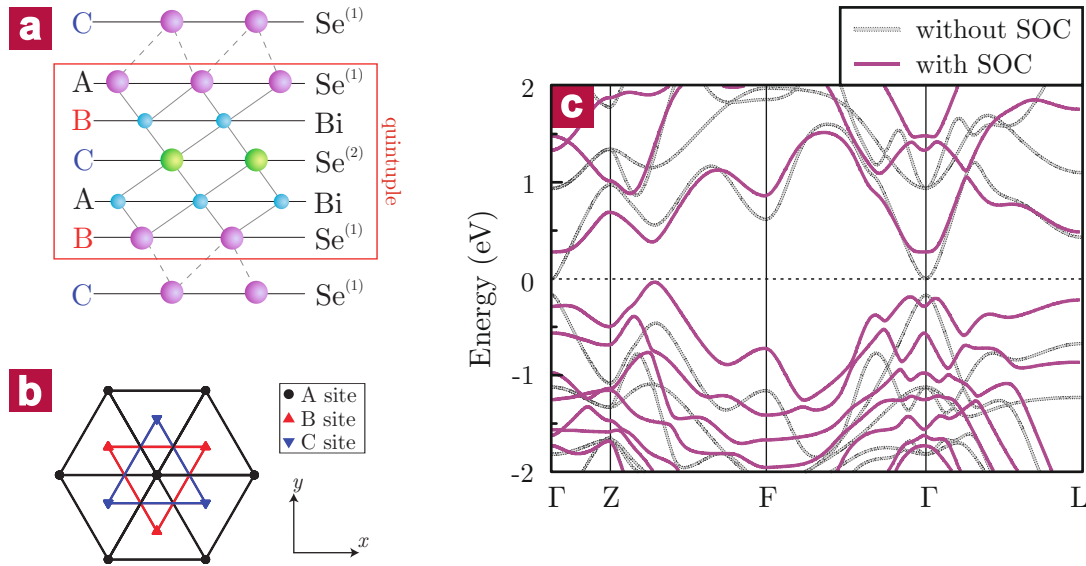


**Figure 2.11: Crystal and band structure of  $\text{Bi}_2\text{Se}_3$**  (a) Side view of the layer structure. Five covalently bond layers form one quintuple layer. The crystal has an inversion center at the  $\text{Se}^{(2)}$  positions. (b) View along the  $z$ -direction showing the stacking order of the crystal. (c) Calculated bulk band structure of  $\text{Bi}_2\text{Se}_3$  without (grey dashed line) and with (purple solid line) SOC. A camel's back feature appears at the  $\Gamma$  point when SOC is switched on.<sup>42</sup>

of  $\text{Bi}_2\text{Se}_3$ , for example, the stacking order is  $\text{Se}^{(1)}\text{--Bi--Se}^{(2)}\text{--Bi--Se}^{(1)}$ . These crystals have an inversion center at the  $\text{Se}^{(2)}$  site ( $\text{Te}^{(2)}$  site in the case of  $\text{Bi}_2\text{Te}_3$  and  $\text{Sb}_2\text{Te}_3$ ) which allows to use Equation 2.46 to calculate the  $Z_2$  invariant. However, the non-trivial character of these chalcogenides is already apparent from calculated band structures without and with spin-orbit interaction (see Figure 2.11c). By switching on SOC a pronounced anti-crossing feature at the  $\Gamma$  point emerges (camel's back like feature in the valence band) which is an indication for an inversion of the valence and conduction band, suggesting that  $\text{Bi}_2\text{Se}_3$  is a topological

**Table 2.1:** Parity of 14 occupied bands and the lowest unoccupied band at the  $\Gamma$  point of  $\text{Sb}_2\text{Te}_3$ ,  $\text{Bi}_2\text{Te}_3$  and  $\text{Bi}_2\text{Se}_3$ . The product of the parities of the occupied bands is given in brackets on the right hand side.

$\text{Sb}_2\text{Te}_3$	+ - + - + + - + - - - +; -	(-)
$\text{Bi}_2\text{Te}_3$	+ - + - + - + + - - - +; -	(-)
$\text{Bi}_2\text{Se}_3$	+ - + - + - + - + - - +; -	(-)

insulator. To verify that, a full parity analysis of all 14 occupied bands at the  $\Gamma$  point can be done. The results for  $\text{Bi}_2\text{Se}_3$ ,  $\text{Bi}_2\text{Te}_3$  and  $\text{Sb}_2\text{Te}_3$  are shown in Table 2.1. It can be seen, that the product of the parities of all occupied bands is  $-1$ , thus  $\nu_0 = 1$ , making these three materials strong TIs. To highlight the origin of band inversion, the effect of chemical binding, crystal field splitting and SOC on the atomic levels is shown in Figure 2.12. The parity of these levels is depicted in blue (even) and red (odd). Since the chemical bond in  $\text{Bi}_2\text{Se}_3$  is mainly via the

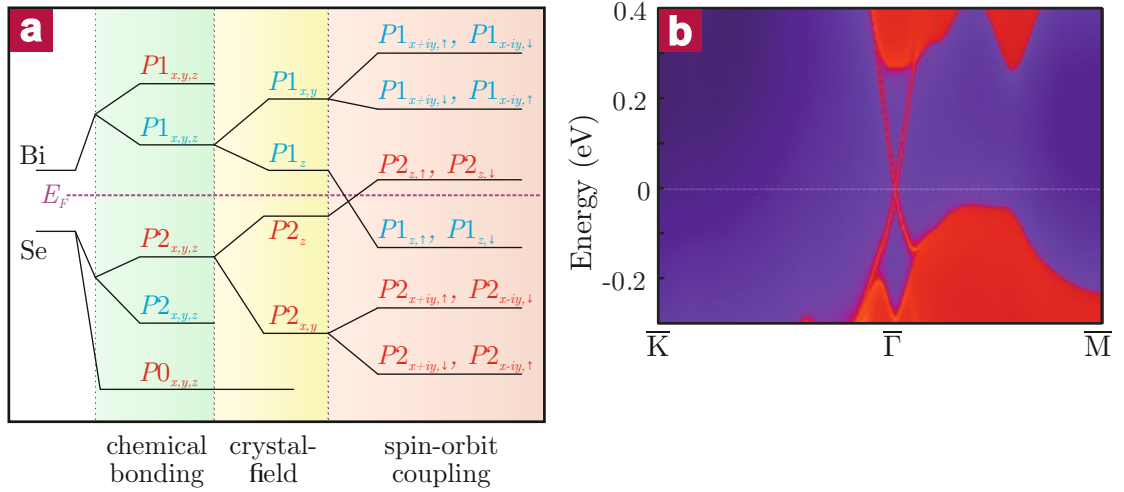


**Figure 2.12: Band sequence and surface states of  $\text{Bi}_2\text{Se}_3$**  (a) Evolution of the  $p$  atomic orbitals of Bi and Se into the valence and conduction band of  $\text{Bi}_2\text{Se}_3$  when forming a chemical bond, taking into account crystal field splitting and switching on SOC. (b) Numerical calculation of the energy and momentum dependence of the local density of states on a  $\text{Bi}_2\text{Se}_3$  (111) surface. The surface state can be seen at the  $\Gamma$  point.<sup>42</sup>

$p$  orbitals of Se ( $4s^24p^4$ ) and Bi ( $6s^26p^3$ ), effects of the  $s$  orbitals can be neglected. A simple chemical bond will result in a hybridization of the  $p$  orbitals which pushes down the three  $p$  orbitals (two of which have odd and one has even parity) of the Se atom and lifts the two  $p$  orbitals (one even, one odd) of the Bi atom. Crystal field splitting breaks the degeneracy of the  $p_z$  and the  $p_{xy}$  orbitals. Thus, after this splitting the two  $p$  orbitals closest to the Fermi level (purple) are the two  $p_z$  orbitals  $P1_z$  and  $P2_z$ . Switching on spin-orbit interaction, leads to a further level repulsion between the  $p_{xy}$  and the  $p_z$  components. If the SOC is strong enough, the  $P2_z$  orbitals of the Se can be lifted above the  $P1_z$  orbital of the Bi, imparting a switch in

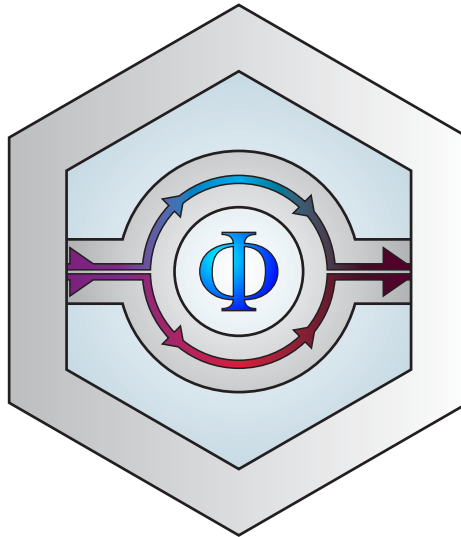
## Chapter 2. Theoretical Background of Topological Insulators

---

parity. This explains the band inversion of  $\text{Bi}_2\text{Se}_3$  at the  $\Gamma$  point.

Figure 2.12c shows the calculated surface band structure of the (111) surface of  $\text{Bi}_2\text{Se}_3$ .<sup>42</sup> It can be clearly seen, that a Dirac cone is formed inside the gap of the projected bulk bands. For all three chalcogenides  $\text{Bi}_2\text{Se}_3$ ,  $\text{Bi}_2\text{Te}_3$  and  $\text{Sb}_2\text{Te}_3$  only a single Dirac cone was observed. Thus, their surface band structure is much simpler than that of the  $\text{Bi}_{1-x}\text{Sb}_x$  alloy, making them ideal systems to study surface related phenomena.

### 3 Magnetotransport phenomena



In this chapter fundamental transport phenomena relevant for the investigation of topological insulator nanostructures will be presented. It covers classical diffusive electrical transport effects, as well as coherent and quantum transport phenomena. Which of these effects is predominantly manifested mainly depends the length scales of the sample under investigation.

### 3.1 Length scales

The strong interest in nano-electronics arises from the many fascinating electrical transport effects that can only be revealed when making the sample size  $L$  smaller than some special characteristic lengths. One of them is the carrier *mean free path*  $l_e$ . In disordered samples, electrons are scattered by impurities or phonons on a typical time scale  $\tau_e$ , and hence the mean free path defines which (average) distance  $l_e = v_F \tau_e$  (here  $v_F$  is the Fermi velocity) an electron can propagate between scattering events. If an electron is described quantum mechanically as a wave with a *Fermi wavelength*  $\lambda_F$ , its *phase*  $\phi$  changes after a certain time  $\tau_\phi$  due to various interactions. The resulting *phase coherence length*  $l_\phi = v_F \tau_\phi$  is crucial to understand the crossover between quantum mechanical and classical systems, since after a length  $l_\phi$  any interference phenomena will be lost. In a strongly disordered system, scattering is so strong that the carriers become localized on a certain length scale defined by the *localization length*  $\xi$  (see below). Comparing these length scales to the system size  $L$  allows to classify electrical transport phenomena as depicted in Figure 3.1:<sup>34</sup>

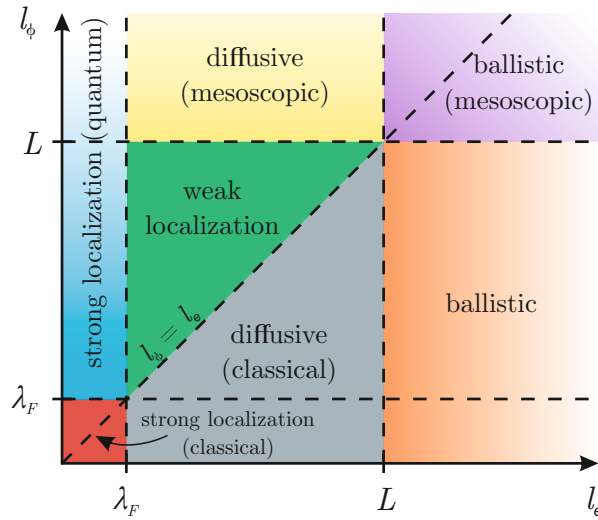


**Figure 3.1: Length scales.** Electrical transport regimes in dependence of the mean free path  $l_e$  and the phase coherence length  $l_\phi$  of an electron.  $L$  and  $\lambda_F$  denote the dimension of the sample and the Fermi wavelength, respectively.

1. **Diffusive classical transport** ( $L, \xi \gg l_e \geq l_\phi \gg \lambda_F$ ).

Due to pronounced scattering, the trajectories of individual electrons can be considered as random walks. Charge transport can be described by classical diffusion of an electron gas (Drude model).

2. **Weak localization regime** ( $L, \xi \gg l_\phi \gg l_e > \lambda_F$ ).

Carrier motion is still dominated by scattering and can be described by (semiclassical) quantum diffusion. The term semiclassical implies that the electrons follow essentially

classical trajectories, but carry a quantum phase information which allows for interference. Such interference can lead to enhanced back scattering and thus to localization (see below).

3. **Quantum regime of strong localization** ( $l_\phi > \xi \approx l_e \approx \lambda_F$ ).

Many (phase coherent) scattering events cause localization of electrons around the impurities. Electrical transport can be described by (occasionally coherent) hopping between localization sites.

4. **Regime of classical strong localization** ( $\xi \geq l_\phi \approx l_e \approx \lambda_F$ ).

Mainly dominated by classical, incoherent hopping transport without any quantum interference.

5. **Ballistic transport** ( $l_e > L$ ).

If the mean free path between two (elastic or inelastic) scattering events becomes larger than the sample size, the system acts like a waveguide for individual electron waves with a group velocity  $v_g$ .

6. **Mesoscopic systems** ( $l_\phi > L$ ).

The dimensionality of a system can be described by comparing the phase coherence length  $l_\phi$  to its size. If the width  $W$  of a 2D sample gets smaller than  $l_\phi$  it can be treated as a 1D mesoscopic system. Comparing the length  $L$  of that system to  $l_e$  allows to define a diffusive ( $l_e < L$ ) and a ballistic ( $l_e > L$ ) mesoscopic regime.

## 3.2 Diffusive electrical transport

### 3.2.1 Drude model with magnetic field

The simplest model to describe electronic transport in metallic systems is the Drude model. It considers that a solid contains a "gas" (in analogy to the kinetic gas theory) of non-interacting electrons. An external electric field  $\mathbf{E}$  will accelerate the electrons until they scatter with crystal defects, charged impurities or phonons within a mean free time  $\tau_e$ . After every scattering event the carriers will have *lost their memory* and move in a random direction. Thus, the paths of individual electrons are like a random walk movement. Although individual electrons move statistically, the whole electron gas drifts parallel to the external field  $\mathbf{E}$  with the drift velocity

$$\mathbf{v}_d = \frac{1}{N} \sum_i \mathbf{v}_i, \quad (3.1)$$

defined as the average carrier velocity of an electron gas containing  $N$  electrons with individual velocities  $\mathbf{v}_i$ .

An external magnetic field imports a Lorentz force on the electrons. As the direction of this force is always perpendicular to their direction of propagation, the electrons are forced onto circular orbits between two scattering events. This leads to the following classical equation of

### Chapter 3. Magnetotransport phenomena

motion:

$$m^* \dot{\mathbf{v}} = -e(\mathbf{E} + \mathbf{v}_d \times \mathbf{B}) - m^* \frac{\mathbf{v}_d}{\tau}. \quad (3.2)$$

For the stationary case  $\dot{\mathbf{v}} = 0$ , such that this equation simplifies to

$$\mathbf{v}_d = -\frac{e\tau}{m^*} (\mathbf{E} + \mathbf{v}_d \times \mathbf{B}). \quad (3.3)$$

For  $\mathbf{B} = 0$  the drift velocity is given by the general equation  $\mathbf{v}_d = \mu \mathbf{E}$ , where  $\mu = \frac{e\tau}{m^*}$  is the carrier mobility.

Upon application of a magnetic field  $\mathbf{B} = (0, 0, B_z)$  in  $z$ -direction, the components of  $\mathbf{v}_d$  in equation 3.3 can be written as

$$\begin{aligned} v_{d,x} &= -\frac{e\tau}{m^*} (E_x + v_{d,y} B_z) \\ v_{d,y} &= -\frac{e\tau}{m^*} (E_y - v_{d,x} B_z) \\ v_{d,z} &= -\frac{e\tau}{m^*} E_z. \end{aligned} \quad (3.4)$$

Inserting these equations into the general definition of the current density  $\mathbf{j} = en\mathbf{v}_d$  yields

$$\begin{pmatrix} j_x \\ j_y \\ j_z \end{pmatrix} = \frac{\sigma_0}{1 + (\omega_c \tau)^2} \begin{pmatrix} 1 & -\omega_c \tau & 0 \\ \omega_c \tau & 1 & 0 \\ 0 & 0 & 1 + (\omega_c \tau)^2 \end{pmatrix} \begin{pmatrix} E_x \\ E_y \\ E_z \end{pmatrix} = \underline{\underline{\sigma}} \mathbf{E}, \quad (3.5)$$

where  $\underline{\underline{\sigma}}$  is the conductivity tensor,  $\omega_c = \frac{eB_z}{m^*}$  is the cyclotron frequency, and  $\sigma_0 = ne^2\tau/m^*$  is the conductivity without external magnetic field.

For thin samples, it can be assumed that there is no current flowing in  $z$ -direction, thus  $j_z = 0$  and (by observing Equation 3.5)  $E_z = 0$ . Hence, Equation 3.5 simplifies to

$$\begin{pmatrix} j_x \\ j_y \end{pmatrix} = \frac{\sigma_0}{1 + (\omega_c \tau)^2} \begin{pmatrix} 1 & -\omega_c \tau \\ \omega_c \tau & 1 \end{pmatrix} \begin{pmatrix} E_x \\ E_y \end{pmatrix} = \begin{pmatrix} \sigma_{xx} & \sigma_{xy} \\ -\sigma_{xy} & \sigma_{xx} \end{pmatrix} \begin{pmatrix} E_x \\ E_y \end{pmatrix}. \quad (3.6)$$

The tensor of resistivity  $\underline{\underline{\rho}}$  is obtained by tensor inversion:

$$\begin{pmatrix} E_x \\ E_y \end{pmatrix} = \begin{pmatrix} \rho_{xx} & \rho_{xy} \\ -\rho_{xy} & \rho_{xx} \end{pmatrix} \begin{pmatrix} j_x \\ j_y \end{pmatrix} \quad (3.7)$$

with

$$\rho_{xx} = \frac{\sigma_{xx}}{\sigma_{xx}^2 + \sigma_{xy}^2} = \frac{1}{\sigma_0} = \frac{1}{ne\mu} \quad (3.8)$$

$$\rho_{xy} = \frac{\sigma_{xy}}{\sigma_{xx}^2 + \sigma_{xy}^2} = \frac{B}{ne}. \quad (3.9)$$

Thus, through measurement of the two components of the resistivity tensor as a function of the external  $B$ -field, the carrier density  $n$  and the mobility  $\mu$  can be calculated from

$$n = \left( e \frac{d\rho_{xy}}{dB} \Big|_{B=0} \right)^{-1} \quad (3.10)$$

$$\mu = \frac{1}{\rho_{xx}(B=0)} \cdot \frac{d\rho_{xy}}{dB} \Big|_{B=0}. \quad (3.11)$$

While the Drude model is able to predict the linear dependence of the *Hall resistivity*  $\rho_{xy}$  on  $B$ , it fails to describe the longitudinal component  $\rho_{xx}$ . In fact, the Drude model would predict that  $\rho_{xx}$  is independent of the magnetic field, and thus the magnetoresistance  $MR$

$$MR = \frac{\rho_{xx}(B) - \rho_{xx}(B=0)}{\rho_{xx}(B=0)} \quad (3.12)$$

is zero, in contradiction to experimental observations and will be topic of the next chapter.

#### 3.2.2 Magnetoresistance

The effect of a weak magnetic field  $|\omega_c| \tau \ll 1$  is to increase the magnetoresistance according to Kohler's rule by<sup>51, 52</sup>

$$MR \approx (\mu B)^2. \quad (3.13)$$

The absence of magnetoresistance in the Drude model results from the assumption of only one scattering time  $\tau_e$  and an average drift velocity  $v_d$  valid for all carriers. However, in reality  $\tau_e$  depends on the individual velocity  $v_i$  of every carrier. A simple expansion of this model is to take into account two types of carriers, which could be electrons and holes, electrons in  $s$  and  $d$  bands or open and closed orbits in the Fermi surface.<sup>52</sup> The steady state drift velocity in Equation 3.3 is then the sum  $\mathbf{v}_d = \mathbf{v}_1 + \mathbf{v}_2$  of the two individual velocities  $\mathbf{v}_1$  and  $\mathbf{v}_2$  with

$$\mathbf{v}_1 = \frac{e\tau_1}{m_1^*} (\mathbf{E} + \mathbf{v}_1 \times \mathbf{B}) \quad (3.14)$$

$$\mathbf{v}_2 = -\frac{e\tau_2}{m_2^*} (\mathbf{E} + \mathbf{v}_2 \times \mathbf{B}). \quad (3.15)$$

Here, we assume type 1 and type 2 to be electrons and holes with effective masses  $m_1^*$ ,  $m_2^*$  and scattering times  $\tau_1$ ,  $\tau_2$ , respectively. For high  $B$ -fields  $|\omega_{c1}| \tau_1 \gg 1$  and  $|\omega_{c2}| \tau_2 \gg 1$ , it follows

for the  $y$  components of the velocities in Equations 3.14 and 3.15:<sup>i</sup>

$$v_{1y} = \frac{E_x}{B_z} = v_{2y}. \quad (3.16)$$

Thus

$$j_y \equiv en_1 v_{1y} - en_2 v_{2y} = \frac{e(n_2 - n_1)}{B_z} E_x \quad (3.17)$$

and furthermore with  $j_y = E_x \sigma_{xx} + E_y \sigma_{xy}$

$$\sigma_{xy} = \frac{e(n_2 - n_1)}{B_z}. \quad (3.18)$$

This is a very important result, since it shows that for equal density of electrons and holes the Hall voltage becomes zero, and if  $\sigma_{xy} = 0$  then the resistivity becomes simply  $\rho_{xx} = (\sigma_{xx})^{-1}$ , with  $\sigma_{xx}$  given by Equation 3.6 (in the limit  $|\omega_c| \tau \gg 1$ ):

$$\rho_{xx} \cong (\mu_{eff} B_z)^2 \frac{1}{en\mu_{eff}}, \quad (3.19)$$

where  $n = n_1 = n_2$  and  $1/\mu_{eff} = 1/\mu_1 + 1/\mu_2$ . Thus, if  $n_1 = n_2$  the longitudinal magnetoresis-

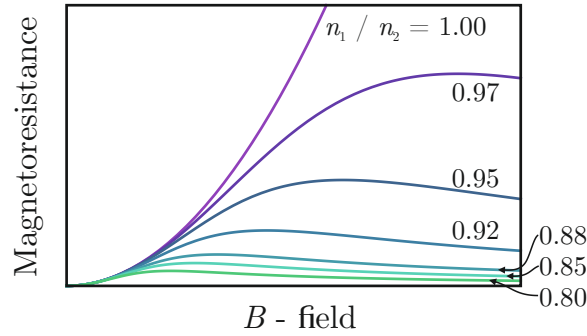


**Figure 3.2: Longitudinal magnetoresistance of a material containing electrons and holes.**  $\rho_{xx}$  was calculated using Equations 3.6 and 3.18 for different ratios  $n_1/n_2$ . It is apparent, that the magnetoresistance doesn't saturate for  $n_1 = n_2$ .

tance doesn't saturate. This is demonstrated in Figure 3.2 for different ratios  $n_1/n_2$ . Having the same concentration of different types of carriers is a special situation. Indeed, it has been observed, that in some materials the magnetoresistance doesn't saturate in special crystal orientations, although there is only one type of carriers contributing to the electrical transport.<sup>52</sup> Electrons in a magnetic field will move on orbits in real space. Such circular motion in real space corresponds to a likewise circular motion in reciprocal space. Correspondingly, the elec-

<sup>i</sup>Using Equation 3.4 we can write for the  $y$ -component of the velocity:  $v_y = -\frac{e\tau/m^*}{1+(\omega_c\tau)^2} (E_y + \omega_c\tau E_x)$ . In the high-field limit  $|\omega_c| \tau \gg 1$  this simplifies (with  $\omega_c = eB_z/m^*$ ) to  $v_y = -\frac{E_x}{B_z}$ .

trons will orbit the Fermi surface on paths normal to the external magnetic field. If the Fermi surface of a material lies entirely in the first BZ all these orbits will be closed. In comparison, if the Fermi surface extends the first BZ in some direction  $\mathbf{k}_{open}$ , then, due to the periodic zone scheme, a continuous surface forms in this direction. Accordingly, if an external magnetic field is applied normal to  $\mathbf{k}_{open}$  the orbits are called *open*. In strong magnetic fields currents can only be carried along open orbits. Thus, if there is an open orbit in  $k_x$  direction, the resistivity  $\rho_{xx}$  is<sup>52</sup>

$$\rho_{xx,open} = (\mu B)^2 \frac{1}{en\mu} \frac{s}{s+1}, \quad (3.20)$$

where  $s$  is defined by the conductivity in  $y$  direction  $\sigma_{yy} = sen\mu$ . This resistivity does not saturate and increases with  $B^2$ . If the crystal is oriented such that the transport is along a closed orbit, the resistivity becomes

$$\rho_{xx,closed} = \frac{en\mu}{s+1}, \quad (3.21)$$

implying that the magnetoresistance saturates at high fields.

In summary, for low  $B$ -fields the  $MR \propto (\mu B)^2$ , whereas in high fields, provided that there are open orbits, transport along these directions will result in non-saturating magnetoresistance. If the transport is normal to the open orbits the  $MR$  will saturate, unless there are two types of carriers with the same density.

#### 3.2.3 Linear Magnetoresistance

Some materials exhibit a non-saturating linear magnetoresistance (LMR) up to very high  $B$ -fields. Since the first observation of the LMR in 1928<sup>53</sup> numerous theoretical models have been proposed to account for this effect.<sup>54–61</sup> One simple explanation can be found for polycrystalline systems with an open Fermi surface. As shown in the previous section, for narrow intervals around these open directions the magnetoresistance should not saturate, but rather increase with  $B^2$ . It can be derived that the width of these intervals is proportional to  $1/B$ , rendering the average magnetoresistance in polycrystals proportional to  $B$ .<sup>62</sup>

Another classical model has been derived by Parish and Littlewood,<sup>63</sup> who calculated the magnetoresistance for macroscopically disordered semiconductors (e.g., non-stoichiometric  $\text{Ag}_{2+\delta}\text{Se}$ ) using a random resistor network model. In this model, a two-dimensional square lattice of four-terminal resistors is constructed, and an external magnetic field applied normal to the network. By calculating the current paths, they found that due to scattering, the current flows perpendicular to the applied voltage for a significant portion of time. Thus, a Hall resistance  $R_{Hall}$  contributes to the total longitudinal magnetoresistance which is linear in  $B$ , such that

$$MR \propto \langle \mu \rangle B, \quad (3.22)$$

### Chapter 3. Magnetotransport phenomena

for  $\Delta\mu < \langle\mu\rangle$  where  $\langle\mu\rangle$  is the average mobility and  $\Delta\mu$  is the mobility disorder. The crossover from the classical quadratic behavior at low  $B$ -fields to the linear  $MR$  occurs at a crossover field  $B_{crossover} \approx \langle\mu\rangle^{-1}$ .

For isotropic metals in the extreme quantum limit (all carriers occupy the first Landau level) that fulfill

$$n_0 \ll \frac{eB^{3/2}}{\hbar} \quad \text{and} \quad T \ll \frac{eB\hbar}{m^*} \quad (3.23)$$

a *quantum linear magnetoresistance* has been theoretically proposed by Abrikosov.<sup>62,64</sup>

$$\rho_{xx} = \rho_{yy} = \frac{N_i B}{\pi n_0^2 e}, \quad (3.24)$$

where  $n_0$  is the electron density at  $T = 0$  and  $N_i$  is the concentration of static scattering centers. This model can be slightly modified for inhomogeneous materials that are not in the quantum limit. They might consist of regions with high carrier density that are surrounded by a medium with very low carrier density (which can reach the quantum limit). If these materials display in addition a *linear dispersion relation* (like graphene or topological insulators), the magnetoresistance is given by

$$\rho_{xx} = \rho_{xy} = \frac{1}{2\pi} \left( \frac{e^2}{\epsilon_\infty \hbar v_F} \right) \frac{N_i}{e n_0^2} B \ln(\epsilon_\infty), \quad (3.25)$$

where  $\epsilon_\infty$  is the background dielectric constant due to the ion cores, and  $v_F$  is the Fermi velocity (for a dispersion relation  $E = \hbar v_F k$ ). The crossover from quadratic to LMR then occurs at the  $B$ -field where all carriers in the areas of low carrier density condense into the first LL.

#### 3.2.4 Shubnikov–de Haas oscillations

**Landau quantization** Let's start with a simple, semi-classical picture. As already mentioned, a magnetic field curves the trajectories of electrons. As a consequence, they move on orbits with a cyclotron frequency  $\omega_c = eB/m^*$  in the plane normal to this field. If  $\omega_c > 1/\tau_e$  an electron can fulfill an orbit without experiencing a scatter event. Thus, it can "interfere with itself" forming a standing wave if the phase it accumulates (= Aharonov-Bohm phase, which is given by the flux inside the cyclotron orbit) during its orbit is  $n \cdot 2\pi$ . This leads, like in the Bohr-Sommerfeld model for atoms, to a quantization of energy for different orbits described by a quantum number  $n$  (= *Landau quantization*).

Deriving the quantized energy states requires an exact solution of Schrödinger's equation. The Hamiltonian describing this problem is very similar to the 1D quantum mechanical harmonic oscillator of an electron that "oscillates" (circular) with a frequency  $\omega_c$ . The corresponding energy eigenvalues are

$$E_n = \hbar\omega_c \left( n + \frac{1}{2} \right). \quad (3.26)$$

Thus, the energy spectrum of the system consists of discrete *Landau levels* (LL) whose energy is determined by the strength of the external magnetic field  $B$ . As a natural consequence, also the density of states (DOS) becomes discrete and can be described by delta functions located at every  $E_n$ .

In real samples, carriers will have a finite lifetime  $\tau_q$ , and therefore this discrete DOS broadens due to carrier scattering events. The lifetime broadening leads to a Lorentzian-shaped DOS at every  $E_n$ , where the full-width-at-half-maximum of the Lorentzian  $L_n$  is given by  $\hbar/\tau_q$ :

$$DOS_{2D} = 2 \cdot n_L \sum_n L_n(E - E_n), \quad (3.27)$$

where  $n_L$  is the degeneracy of a LL and the factor 2 accounts for the spin. Calculating the limit of this sum for  $n \rightarrow \infty$  yields<sup>34</sup>

$$DOS_{2D} = \frac{m^*}{\pi \hbar^2} \left[ 1 - 2e^{-\pi/(\omega_c \tau_q)} \cos\left(2\pi \frac{E}{\hbar \omega_c}\right) \right]. \quad (3.28)$$

It follows that firstly, at constant energy the DOS oscillates with a period of  $1/B$ , and secondly, the so-called *Dingle factor*  $\exp[-\pi/(\omega_c \tau_q)]$  leads to an exponential increase in the amplitude of the DOS modulation when the  $B$ -field is increased.

**Magnetoresistance oscillations** By involving the Fermi-Dirac distribution function, Equation 3.28, and Drude's model (see Equation 3.6) the component  $\rho_{xx}$  of the resistivity tensor is obtained as<sup>34, 65</sup>

$$\rho_{xx}(B, T) = \frac{m^*}{e^2 n_s \tau_0} \left[ 1 - 2e^{-\pi/(\omega_c \tau_q)} \frac{\lambda(T)}{\sinh \lambda(T)} \cos\left(2\pi \frac{\hbar n_s}{2eB}\right) \right]. \quad (3.29)$$

The resistivity hence oscillates around the  $B$ -field independent prefactor  $\rho_0 = m^*/(e^2 n_s \tau_0)$ , which corresponds to the classical Drude resistivity. These magnetoresistance oscillations are called *Shubnikov-de Haas* (SdH) oscillations. Minima in the longitudinal resistivity arise as a result of minima in DOS at  $E_F$ . If the temperature  $T$  is increased, the amplitude of the oscillations decreases due to the prefactor

$$\lambda(T) = \frac{2\pi^2 kT}{\hbar \omega_c}. \quad (3.30)$$

The exponential increase of the amplitude with increasing  $B$ -field accounts for the finite carrier lifetime. Since the argument of the oscillation factor is  $E_F/(\hbar \omega_c) = \hbar n_s/(2eB)$ , similar oscillations emerge if Fermi level is varied at a constant  $B$ -field.

**Determination of  $n_s$ ,  $\tau_q$ , and  $m^*$  from SdH oscillations** Minima in the SdH oscillations are periodic in  $1/B$  and occur at

$$\hbar n_s/(2eB) = i + \gamma_O, \quad (3.31)$$

where  $\gamma_O$  is the Onsager phase (see below) and  $i$  is an integer. Thus, plotting the positions  $1/B$  of the minima versus the index  $i$  gives a straight line with a slope of  $2e/(hn_s)$ .

For a circular Fermi surface,  $k_F$  can be calculated from the carrier density  $n_s$  using  $k_F = \sqrt{4\pi n_s}$ . According to Equation 3.29 the envelope of the oscillations can be written as

$$\frac{\rho_{xx} - \rho_0}{\rho_0} = \pm 2e^{-\pi/\omega_c \tau_q} \frac{\lambda(T)}{\sinh \lambda(T)}. \quad (3.32)$$

This can be rewritten as

$$\ln \left( \frac{\rho_{xx} - \rho_0}{\rho_0} \frac{\sinh \lambda(T)}{\lambda(T)} \right) = -\frac{\pi m^*}{e\tau_q} \frac{1}{B} + \text{const.} \quad (3.33)$$

Thus, by plotting the left-hand side of this equation versus  $1/B$ , the carrier lifetime  $\tau_q$  can be extracted from the slope of the resulting straight line. Moreover, using  $l_e = v_F \tau_q$  and  $\mu = e\tau_q/m^*$  the mean free path and the carrier mobility can be calculated, respectively.

To obtain the effective mass  $m^*$ , the SdH oscillations have to be measured at different temperatures. From a fit to the plot of the amplitude of one particular maximum/minimum at different  $T$  using

$$\frac{\rho_{xx} - \rho_0}{\rho_0} = \frac{\lambda(T)}{\sinh \lambda(T)} \quad (3.34)$$

$m^*$  can then be extracted.

It should furthermore be mentioned, that the Onsager phase is closely related to the Berry phase via (see Equation 2.4 and 2.10)

$$\gamma_O = \frac{1}{2} - \frac{1}{2\pi} \oint_C d\mathbf{k} \cdot \mathbf{A}_n(\mathbf{k}). \quad (3.35)$$

In conventional metals, the Onsager phase  $\gamma_O = 1/2$ . However, topological insulators possess a non-trivial Berry phase of  $\pi$ , and hence the Onsager phase becomes  $\gamma_O = 0$ .<sup>22</sup> Thus, by plotting the position  $1/B$  of the minima of the SdH oscillations as a function of the filling factor and extrapolating to  $B \rightarrow \infty$ , the intersect with the abscissa allows to extract the Berry phase.<sup>28</sup>

## 3.3 Diffusive quantum transport

### 3.3.1 Weak localization

In a diffusive system, the mean free path  $l_e$  of an electron is much smaller than the system size  $L$ . Thus, the electron motion will be dominated by scattering, equivalent to a random walk movement. In the previous section, electrons were treated as classical particles which only interact by scattering. If, by contrast, the phase coherence length  $l_\phi$  of the electrons becomes sufficiently long, they will keep their quantum phase information over many scattering events. This can lead to interesting interference phenomena like *localization* effects.

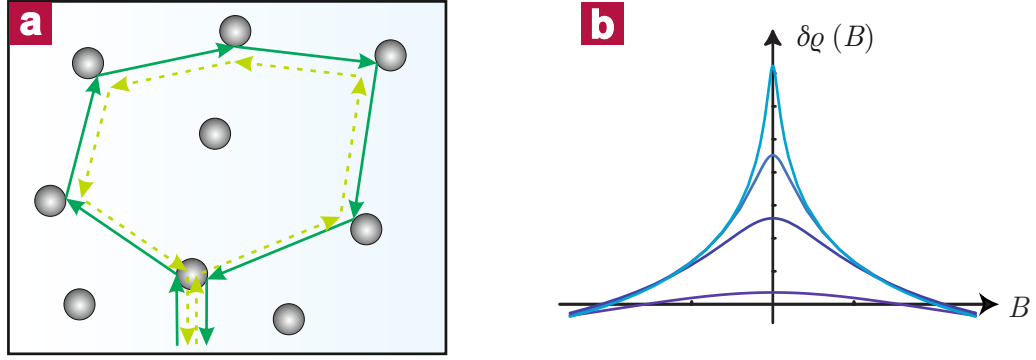


**Figure 3.3: Weak localization.** (a) Time-reversed paths in a diffusive sample. Without external magnetic field the two paths  $|A^+\rangle$  (dark green solid) and  $|A^-\rangle$  (light green dashed) are always interfering constructively. (b) Magnetoresistance correction for different ratios  $l_\phi/l_e$ . The larger this ratio, the sharper are the maxima around zero field.<sup>34</sup>

Imagine an electron that is scattered such that it follows a closed path, as depicted by the green solid line in Figure 3.3a. If we treat the electron quantum mechanically, this path may have a certain complex amplitude  $|A^+\rangle = Ae^{i\varphi^+}$ , where  $A$  is a positive real number between zero and one, and  $\varphi$  is a real-valued phase. Correspondingly, we consider the time-reversed path described by  $|A^-\rangle = Ae^{-i\varphi^-}$  of the electron simply moving the same path back. The classical probability  $P_{cl}$  for an electron returning to its starting point would then simply be

$$P_{cl} = \langle A^+ | A^+ \rangle + \langle A^- | A^- \rangle = 2A^2, \quad (3.36)$$

that is the sum of the two individual probabilities for getting scattered clockwise or anti-clockwise. However, in quantum mechanics the total probability is given by the scalar product of the two probabilities, thus

$$\langle A^+ | A^- \rangle = 2A^2 + 2A^2 \cos(\varphi^+ - \varphi^-). \quad (3.37)$$

Here, the second term on the right hand side represents the interference of the two paths. Without external magnetic field, time-reversal symmetry requires  $|A^+\rangle = |A^-\rangle$  (hence  $\varphi^+ = \varphi^-$ ) and the time-reversed paths always interfere constructively. As an important consequence, the probability for backscattering is enhanced by  $2A^2$  due to interference effects, and hence, the conductivity of the sample is decreased compared to the classical value obtained by the Drude model. This effect is called *weak localization*, since the probability distribution of electrons is enhanced in regions where their trajectories form closed loops.

Applying a magnetic field  $B$  normal to the area  $S$  enclosed by the paths can suppress this effect since it adds an Aharonov-Bohm phase  $\varphi_{AB} = 2\pi BS/\phi_0$  to the electron wavefunctions (see Section 3.4.1). The sign of the phase depends on the direction of the path. Specifically, the clockwise moving electron will acquire a phase  $\varphi^+ = +\varphi_{AB}$ , the anti-clockwise moving one a phase  $\varphi^- = -\varphi_{AB}$ . Thus, the constructive interference between time-reversed paths will be

destroyed and the conductance approaches its classical value (see Figure 3.3b). The shape of the conductance minimum is determined by the ratio of  $l_\phi/l_e$ : the higher this ratio, the sharper is the minimum around zero  $B$ -field. It is noteworthy, that by inserting the AB-phases in Equation 3.37, one may expect an oscillatory modulation of the quantum interference correction for every area  $S$  enclosed by random scattering paths. However, in a macroscopic diffusive sample, there are so many individual paths contributing to this effect that different oscillations average out completely. Close to zero  $B$ -field, all oscillations have the same phase and add up to the weak localization effect and the conductance minimum survives the averaging.

For the sake of completeness, it should be mentioned that by increasing the density of scattering centers in a sample, there will be a crossover to *strong localization* if  $k_F l_e < 1$ . In that case the electrons are localized on a length scale  $\xi \approx l_e e^{k_F l_e/2}$  (localization length) around scattering centers. As a consequence, at low temperatures electronic transport can only occur by electron hopping from one impurity site to another.

### 3.3.2 Weak anti-localization

The weak localization effect described in Section 3.3.1 is fundamentally different in diffusive systems with strong spin-orbit coupling. Upon getting scattered along a closed path, the spin of the electron will be slightly rotated between every scattering event. After one loop, all these rotations add up to a total rotation  $R$  and the spin  $|s\rangle$  (before the rotation) will change into<sup>66</sup>

$$|s'\rangle = R|s\rangle. \quad (3.38)$$

The spin on the time-reversed path will get rotated exactly in the opposite way:

$$|s''\rangle = R^{-1}|s\rangle, \quad (3.39)$$

where  $R \cdot R^{-1} = 1$ .

If the spin-orbit time  $\tau_{SO}$  of the system, i.e., the typical time required to randomize the spin orientation due to SOC, is very small (= strong SOC) the spin of the electron will be completely randomized after performing the closed loop. By comparison, the spin of the electron taking the time-reversed path has experienced the opposite rotation. Toward calculating the total probability for backscattering, it follows in analogy to Equation 3.37:

$$|\langle s' | s'' \rangle|^2 = 2 + 2 \langle s'' | s' \rangle = 2 + 2 \langle s | R^2 | s \rangle. \quad (3.40)$$

Interestingly, calculating the expectation value of  $R^2$  for all possible rotation angles (averaging is possible if  $\tau_{SO}$  is small enough and the spin orientation after one loop is completely random) gives  $\langle s | R^2 | s \rangle = -1/2$ .<sup>ii</sup> Thus, in the case of strong SOC the destructive interference between

<sup>ii</sup>For  $\tau_{SO} \gg \tau_\phi$  the spin will essentially not change during scattering events. Thus,  $R$  becomes 1. This is the case of weak localization discussed above. Using the spin-orbit length  $l_{SO} = \sqrt{D\tau_{SO}}$  we can say: for  $l_{SO} > l_\phi > l_e$  we expect to see weak localization. If we reduce  $l_{SO}$  (increase SOC) until  $l_{SO} = l_e < l_\phi$  we expect to see a cross over to

time-reversed paths dominates and the quantum correction to the classical conductance is negative (and half of the value valid for weak localization). Like for weak localization, this effect can be destroyed by an external magnetic field. An analytical expression to describe localization in 2D diffusive systems has been derived by Hikami, Larkin and Nagaoka (HLN):<sup>67</sup>

$$\Delta\sigma(B) = \alpha \frac{e^2}{h} \left[ \ln\left(\frac{B_\phi}{B}\right) - \Psi\left(\frac{1}{2} + \frac{B_\phi}{B}\right) \right], \quad (3.41)$$

where  $\Psi$  is the digamma function,  $l_\phi = \sqrt{D\tau_\phi}$  the phase coherence length,  $B_\phi = \hbar/(4el_\phi^2)$ , and the constant  $\alpha$  is 1 for weak localization and  $-0.5$  for weak anti-localization.

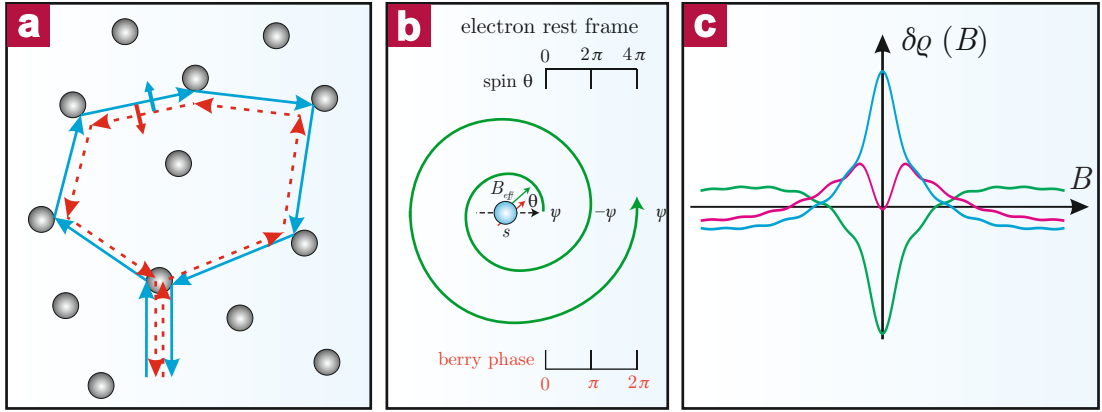


**Figure 3.4: Weak anti-localization.** (a) Time-reversed paths in a topological insulator have opposite spin orientation, which results in a phase difference of  $\pi$  due to the anomalous Berry phase in TIs. (b) If the spin of an electron on the surface of a TI is rotated by  $2\pi$ , the electrons phase changes by  $\pi$ .<sup>68</sup> (c) Magnetoresistance correction calculated for different strengths of the spin-orbit coupling, i.e.,  $l_{SO}/l_e = 30$  (blue), 3 (pink) and 1 (green). The ratio  $l_\phi/l_e = 5$  is kept constant.<sup>34</sup>

It should be noted that in exotic Dirac systems like topological insulators, the weak anti-localization effect can be explained in a simpler way. Specifically, since in TIs the spin of an electron is locked to its momentum, the two time-reversed paths will always have opposite spin (see Figure 3.4a), hence at every point on the loop the spin-rotation between the two paths is  $\pi$ . As a full orbit around the Fermi surface of a TI results in a Berry phase of  $\pi$ , the spin-rotation of  $\pi$  corresponds to a Berry phase of  $\pi/2$  (see Figure 3.4b). Therefore, the time-reversed paths moving clockwise and anti-clockwise acquire a phase of  $+\pi/2$  and  $-\pi/2$ , respectively. The resulting phase difference of  $\pi$  which leads to destructive interference. On this basis, the factor  $\alpha$  is often used to determine the number of transport channels contributing to the total conductance; for a bulk sample with a single conductive surface state  $\alpha = -1/2$ . Previous studies on various types of TIs have found  $\alpha$  values between  $-0.3$  and  $-1.1$ , which were interpreted as evidence for transport through a single surface state,<sup>69,70</sup> two decoupled surface channels with comparable phase coherence length,<sup>71</sup> or intermixing of bulk and

weak anti-localization (see Figure 3.4c).

surface conductance.<sup>72</sup>

It is also possible to modulate these interference effects. In particular, by using magnetic impurities, a gap  $\Delta$  can be opened in the topological surface states. The resulting Berry phase is then given as<sup>73</sup>

$$\gamma = \pi \left( 1 + \frac{\Delta}{2E_F} \right), \quad (3.42)$$

where  $E_F$  is measured from the middle of the gap. In the strongly doped regime  $2E_F$  can reach  $\Delta$ . Thus, in dependence of the doping level, the Berry phase will change from  $\pi$  (weak anti-localization) to  $2\pi$  (weak localization). Such a transition is illustrated in Figure 3.4c, where the magnetoresistance correction is calculated using Equation 15.4 in Ref [34, pp.270 & 283] for  $k_F = 0.2 \text{ \AA}^{-1}$ ,  $l_\phi = 50 \text{ nm}$ ,  $l_e = 10 \text{ nm}$ , and  $l_{SO} = 300 \text{ nm}$  (blue),  $30 \text{ nm}$  (pink), or  $10 \text{ nm}$  (green)

#### 3.3.3 Decoherence

As already mentioned, there are scattering processes that destroy the quantum phase information of an electron, such as inelastic scattering by phonons. As at temperatures below 4.2K lattice vibrations are frozen out, electron-electron scattering becomes the dominant dephasing mechanism. As an electron wave is surrounded by a sea of randomly moving other electrons, randomly fluctuating electromagnetic fields (photons) are created, which can scatter with the electron and destroy its phase. The decoherence rate  $1/\tau_\phi$  can usually be described by a power law:

$$\frac{\hbar}{\tau_\phi} \propto (kT)^p. \quad (3.43)$$

where  $p = 3/2$  for 3D,  $p = 1$  for 2D and  $p = 2/3$  for 1D systems.<sup>74,75</sup> Thus, for decreasing temperature the phase coherence time increases and localization effects become more pronounced (i.e., more paths enclosing an area  $S < l_\phi^2$  can contribute). This has a very important consequence at very low  $T$ , namely that disordered systems without SOC will be in an insulating state when reaching the zero-temperature limit, whereas systems with SOC will remain metallic.

### 3.4 Interference effects in quantum transport

#### 3.4.1 Aharonov–Bohm effect

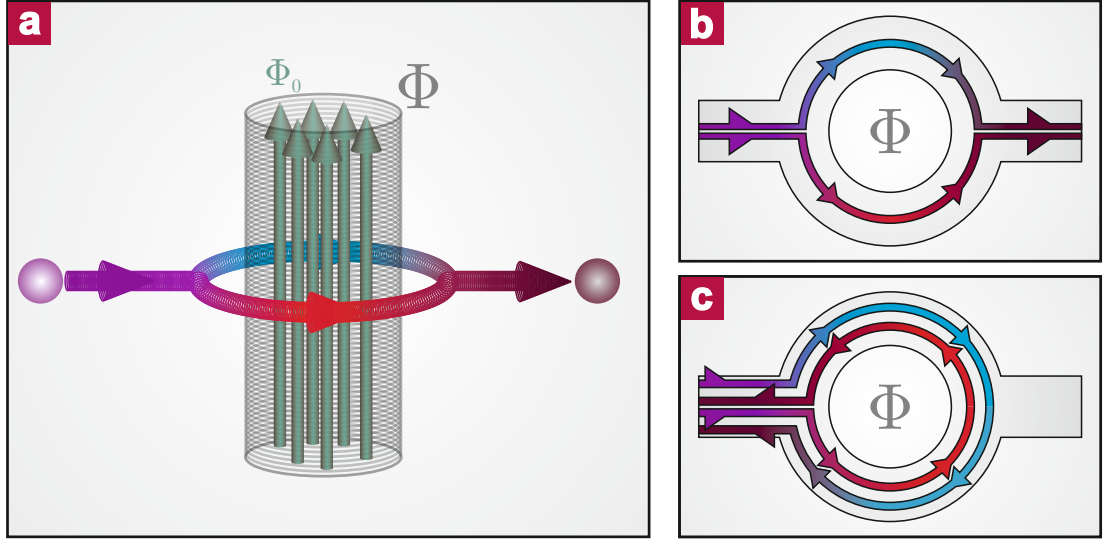


**Figure 3.5: Aharonov-Bohm effect.** (a) An electron beam is split and passing around a solenoid containing a total flux  $\Phi$  (consisting of quantized flux-quanta  $\phi_0$ , gray green arrows). When the two individual paths interfere after passing the flux, their quantum phase may change depending on  $\Phi$ . (b) Schematic illustration of the AB-effect (top view). A metallic ring is connected to two electrical contacts. The incoming electron wave is split into a component moving clockwise and a component moving counter-clockwise. Upon increasing  $\Phi$  the resistance of the device will oscillate with a period given by Equation 3.47. (c) AAS-effect, involving the interference of waves that travel around the ring completely in different directions. This results in resistance oscillations with a period half of that of the AB-effect.

**General basics** In quantum mechanical systems potentials can have an effect on charged particles even when they move in regions without any fields and thus no external forces are acting on them. Aharonov and Bohm<sup>76</sup> predicted that an electron which is passing around a long solenoid that is enclosing a **B**-field will acquire a phase of

$$\Delta\varphi_{AB} = -\frac{e}{\hbar} \oint_C \mathbf{A} d\mathbf{s} = -\frac{e}{\hbar} \phi = -2\pi \frac{\phi}{\phi_0}. \quad (3.44)$$

Here,  $\phi = \oint_C \mathbf{A} d\mathbf{s}$  is the magnetic flux trapped in the solenoid. Interestingly, this phase shift is solely due to the vector potential **A** since the **B**-field outside the solenoid is zero. Now imagine the situation depicted in Figure 3.5a: an electron wave is split into two components  $|\psi\rangle = |\psi_1\rangle + |\psi_2\rangle$ , where  $|\psi_1\rangle$  is going around the solenoid clockwise and  $|\psi_2\rangle$  is passing around it anti-clockwise. Thus,  $|\psi_1\rangle$  travels an angle  $-\pi$  and acquires a phase of  $-\pi\phi/\phi_0$ , whereas  $|\psi_2\rangle$  travels an angle  $\pi$  and acquires a phase  $\pi\phi/\phi_0$ . After passing the solenoid the two partial

waves interfere. Thus, the total transmission probability is given by

$$T = |\langle \psi_1 | \psi_2 \rangle|^2 \propto \cos\left(2\pi \frac{\phi}{\phi_0}\right). \quad (3.45)$$

Consider an experiment where a metallic ring structure with an area  $S$  is connected to two contacts, as depicted in Figure 3.5b. By applying an external magnetic field  $B$  normal to the ring, the flux  $\phi$  inside the ring will change by

$$\phi = B \cdot S. \quad (3.46)$$

Based upon Equation 3.45 the conductance of the device should oscillate when the  $B$ -field is swept. The period of these oscillations is given by

$$\Delta B = \frac{h/e}{S}. \quad (3.47)$$

It should be mentioned that by applying an external magnetic field a Lorentz force will act on the electrons. However, when the field is small enough, that the cyclotron radius  $R_c = \hbar k_F / (eB)$  is large compared to the radius of the ring, these forces are negligible.

In experiments, oscillations with a periodicity of

$$\Delta B = \frac{h/(2e)}{S}, \quad (3.48)$$

half of the periodicity of the AB oscillations are observed. These are the Altshuler-Aronov-Spivak (AAS) oscillations, which result from (constructive) interference of time-reversed paths, associated with electrons traveling around the ring completely either clockwise or anti-clockwise. Since both the AB and AAS effect depend on the interference of electron waves with different phases, the phase coherence length  $l_\phi$  needs to be at least on the order of the diameter of the ring structure. Accordingly, this effect vanishes at high temperatures due to the onset of decoherence effects (see Section 3.3.3).

**AB effect in Topological Insulators** The Landauer-Büttiker formalism can be used to describe the AB and the AAS effect.<sup>34</sup>

In this framework, the conductance of the ring-like structure is given by

$$G = \frac{2e^2}{h} T(E_F) = \frac{2e^2}{h} [1 - R(E_F)], \quad (3.49)$$

where  $T(E_F)$  and  $R(E_F)$  are the transmission and reflection probability at the Fermi energy, respectively. There are three possible electron paths, as depicted in Figure 3.6. In (a) an electron is simply reflected at the entrance of the ring with a probability amplitude  $r_0$ . In (b) and (c) the electron is reflected after traveling around the ring clockwise and counterclockwise, respectively, (probability amplitude  $r_1$ ) where upon it acquires an AB-phase. If we ignore paths

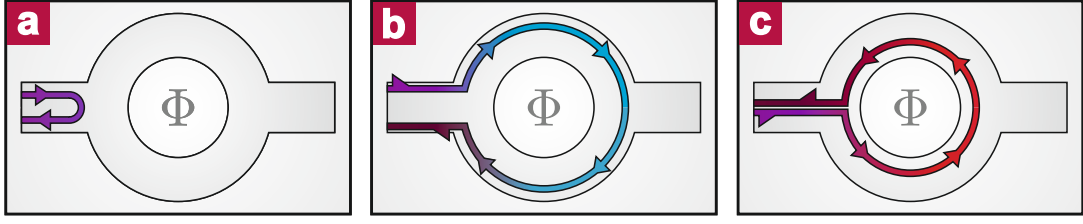


**Figure 3.6: Paths considered in the Landauer-Büttiker description of the Aharonov-Bohm effect.** (a) An electron is reflected at the entrance of the ring structure. (b) An electron is reflected after moving around the ring once clockwise. (c) An electron is reflected after moving around the ring counter-clockwise.<sup>34</sup>

where the electron moves around the ring more than once, the total reflection probability can be written as

$$R = \left| r_0 + r_1 e^{i \cdot 2\pi\phi/\phi_0} + r_1 e^{-i \cdot 2\pi\phi/\phi_0} \right|^2 \quad (3.50)$$

$$= \underbrace{|r_0|^2 + 2|r_1|^2}_{\text{classical}} + \underbrace{4|r_0||r_1|\cos(\delta)\cos\left(2\pi\frac{\phi}{\phi_0}\right)}_{AB} + \underbrace{2|r_1|^2\cos\left(4\pi\frac{\phi}{\phi_0}\right)}_{AAS}. \quad (3.51)$$

Thus, the AB-effect can be visualized as the interference of an electron moving around the ring once with an electron that is reflected at the entrance. The AAS oscillations originate from the interference of electrons moving once around the ring clockwise and counter-clockwise. In this model, a phase  $\delta$  is introduced to account for the phase an electron acquires when it moves once around the ring at zero magnetic field (= Berry phase). In a TI wire, the spin of an electron moving once around the circumference rotates by  $2\pi$  and the electrons phase changes by  $\pi$ . This non-trivial Berry phase in topological insulators has intriguing consequences. Unlike for normal metals, one would expect the magnetoconductance to oscillate with a period of  $\phi_0$ , but with a *maximum* at integers of  $\phi = \phi_0/2$  and a minimum at  $B = 0$  for ballistic undoped TIs. The physical reason for this is, that in a wire-like structure the Berry phase of an electron orbiting the wire diameter would open a gap in the energy spectrum.<sup>iii</sup> However, for a flux of  $\phi = \phi_0/2$  the Berry phase is exactly compensated by the AB-phase, and hence a gap-less and perfectly transmitting state can exist. Numerical simulations furthermore show, that for small disorder the position of the conductance maximum should vary between  $\phi = 0$  and  $\phi = \phi_0/2$  when the Fermi level is continuously shifted to higher energies.<sup>77,78</sup>

<sup>iii</sup>If  $x$  and  $y$  are the direction along the wire axis and around the wires circumference, respectively, then for a wire with an circumference  $W$  the periodic boundary conditions  $\phi(x, y + W) = e^{i\pi}\phi(x, y)$  get anti-periodic due to the Berry phase  $\pi$ . This leads to a gapped energy spectrum with many sub-bands for different transverse momenta  $q_n = 2\pi n/W$ .

### 3.4.2 Universal conductance fluctuations

In low temperature magnetoresistance experiments on small metallic systems it is often observed that the signal gets more "noisy" the lower the temperature is. Interestingly, this non-periodic noise is perfectly reproducible and symmetric in  $B$ -field. Moreover, at very low  $T$  the amplitude of these oscillations is found to be of the order of  $e^2/h$ , independent of the sample size, shape and defect concentration. This is the reason why this effect is called *universal conductance fluctuations* (UCF).

Imagine a metal bar that is connected to two electrical contacts. To estimate its conductance, Equation 3.49 can provide the reflection probabilities for all possible paths starting and ending (getting back-reflected) in one of the contacts. Summing up all paths (with slightly different probabilities) gives a certain conductance value for a certain arrangement of scattering centers. Changing the defect configuration will change the trajectories of the electrons, and thus result in a slightly different conductance. Thus, by measuring the conductance as a function of different scattering distributions one would expect a fluctuating behavior. If all scattering paths would be *uncorrelated*, the root-mean-square (rms) of the conductance signal (i.e., the *power* of its fluctuations) would be<sup>75</sup>

$$\text{rms}(G_u) \approx \frac{l_e}{L}. \quad (3.52)$$

This result suggests, that the variation of the conductance measured for a wide range of different statistical defect configurations averages out if the system size  $L$  gets big enough. However, such scenario is in contradiction to the universal amplitude of  $e^2/h$  found in diffusive materials at very low  $T$  for all system sizes. Instead of assuming uncorrelated paths, the UCF can be explained by considering that the phase coherence length  $l_\phi$  of the electrons in a diffusive metal is larger than the system size  $L$ , and hence electrons can propagate through the whole sample without losing their phase information. Thus, there can be many pairs of paths connecting the contacts that form closed loops. Like in the case of weak localization (see Section 3.3.1), closed loops can lead to interference effects that change the total conductance by about  $e^2/h$  and thus survive averaging. By changing the impurity configuration the specific phases of the paths will be modified in an arbitrary manner, causing the interference terms to vary randomly. The same effect can be achieved by an external magnetic field which introduces a further arbitrary relative phase to each pair of paths that form a closed loop (AB-phase). The effect of finite temperatures will be to reduce both, the phase coherence length and conductance fluctuations. For example, if the phase coherence length becomes smaller than the length of a 2D sample ( $W < l_\phi < L$ ), then one can consider  $L/l_\phi$  segments of the channel fluctuating independently.<sup>34</sup> The UCF amplitude then reduces to

$$\text{rms}(G) \propto \frac{e^2}{h} \left( \frac{l_\phi}{L} \right)^{(4-d)/2} \quad (3.53)$$

where  $d$  is the dimension of the electron system (in our quasi-1D example  $d = 1$ ). This makes the effect sensitive to averaging if the sample size is increased (*finite size effect*)<sup>iv</sup>. The average spacing between two conductance spikes corresponds to  $\Delta B_c \propto \frac{\phi_0}{W l_\phi}$  since every small segment with a size  $l_\phi W$  can be considered as an individual Aharonov-Bohm ring (see Equation 3.47). This is the so-called *field correlation range*, which provides access to the phase coherence length. It represents the decay length of the autocorrelation function of the conductance signal (since an autocorrelation function always decays on the time scale a measured quantity fluctuates).

### 3.5 Sample geometries in electrical transport measurements

In an electrical transport experiment typically either the *resistance* or the *conductance* of a device is measured, which both depend on the geometry and dimension of the sample. However, for the physical interpretation of the results, often specific values like *resistivity* or *conductivity* are needed. Two possible device geometries that can be used to avoid geometric errors are *Hall bars* and *van der Pauw structures* (see Figure 3.7).

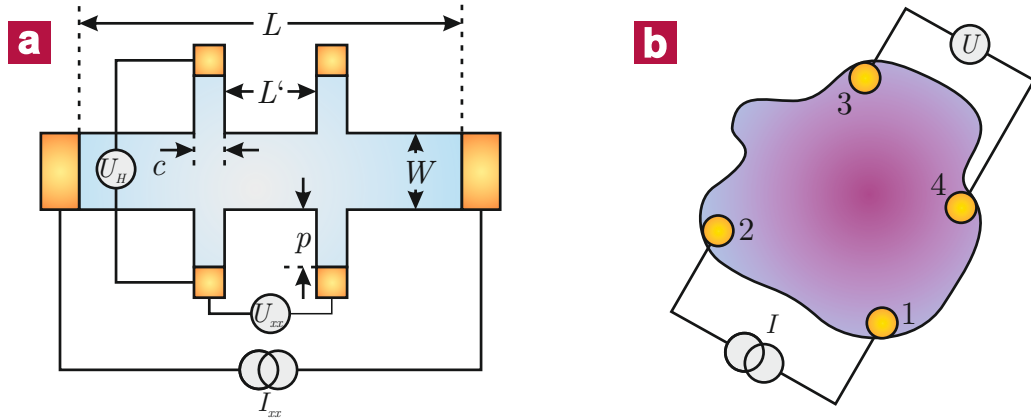


**Figure 3.7: Hall bar and van der Pauw contact configuration.** (a) The geometry of a Hall bar is defined by its length  $L$ , width  $W$  and the separation  $L'$  of the side arms that have length  $p$  and width  $c$ . (b) Sketch of the van der Pauw method.

A typical Hall bar is depicted in Figure 3.7a. The sample is electrically contacted by a source and a drain contact, complemented by several (in this case four) voltage probes. The components of the resistivity tensor of a 2D sample are given by

$$\rho_{xx} = \frac{U_{xx}}{I_{xx}} \frac{W}{L'}, \quad (3.54)$$

$$\rho_{xy} = \frac{U_H}{I_{xx}}. \quad (3.55)$$

<sup>iv</sup>Remark: Keep in mind that this is only valid for finite temperatures.

### Chapter 3. Magnetotransport phenomena

---

To minimize geometric errors, the Hall bar should have an aspect ratio  $L/W \geq 3$ . By contacting simple rectangular samples (length of side arms  $p = 0$ ) the error in the Hall mobility can be fairly large and is given by:<sup>79</sup>

$$\frac{\Delta\mu_H}{\mu_H} = 1 - \left(1 - e^{-\frac{\pi}{2W}}\right) \left(1 - \frac{2c}{\pi W}\right). \quad (3.56)$$

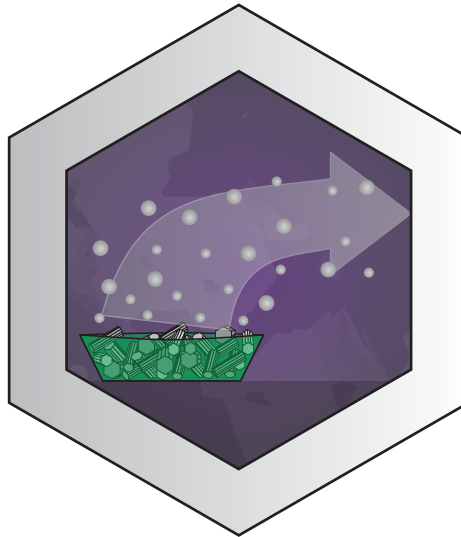
Thus, to reduce the contact size error the following aspect ratios are ideal:  $p \approx c$  and  $c \leq W/3$ .<sup>79</sup> For arbitrary shaped samples, an alternative is the use of the van der Pauw method. Here, in the ideal case, four point contacts are attached to the edges of the sample (see Figure 3.7b). If a current is applied between contacts 1 and 2, the voltage drop measured between contacts 3 and 4 can be used to calculate the resistance  $R_{12,34} = U_{34}/I_{12}$ . The sheet resistance  $R_s = \rho_{xx}/t$  (where  $t$  is the thickness of the sample) can be determined by measuring two different contact configurations and numerically solving the equation

$$e^{-\pi R_{12,34}/R_s} + e^{-\pi R_{23,41}/R_s} = 1. \quad (3.57)$$

The Hall resistance can also be measured using the van der Pauw method. For this purpose, a current is applied between contacts 1 and 3, and the voltage drop between contacts 2 and 4 is measured during a full  $B$ -field sweep (from  $-B$  to  $+B$ ). Two resistance components  $R_{13,24}^P$  (measured at positive  $B$ ) and  $R_{13,24}^N$  (measured at negative  $B$ ) can be calculated. This has to be repeated for  $R_{24,31}^{P(N)}$ . The Hall resistance can then be calculated from

$$R_H = \frac{(R_{13,24}^P - R_{13,24}^N) + (R_{24,31}^P - R_{24,31}^N)}{4}. \quad (3.58)$$

## 4 CVD growth and device fabrication



To fabricate ultrathin platelets and ribbons of topological insulators which possess a high surface-to-bulk ratio, chemical vapor deposition is a valuable method. In this chapter the relevant parameters that influence the morphology of the as-grown material are discussed. It will be shown that not only the growth conditions but also the growth substrate strongly influences the resulting films. The last part of this chapter outlines how to identify thin TI platelets and the approach to electrically contact them.

## 4.1 How to grow Topological Insulators?

**General methods** After the discovery of the 3D topological insulator behavior of  $\text{Bi}_2\text{Se}_3$  and  $\text{Bi}_2\text{Te}_3$  many groups have used these materials in their research. This choice has a physical reason. Both chalcogenides have a band gap of  $E_g \approx 0.3$  eV, big enough for room temperature applications, and possess a single Dirac cone at their surfaces.<sup>11,42,80</sup> The latter feature renders them into ideal model systems to study topologically protected surface states. Moreover, these compounds have been studied for many decades as very promising thermoelectric materials. Thus, many fabrication techniques are available, several of which can be easily repeated in any lab. One of them is the widely-used Bridgman method,<sup>81,82</sup> in which ultrapure elements (for example Bi and Se in the proper stoichiometry) are sealed in a quartz tube and put into a horizontal or vertical furnace. The furnace is then heated to a temperature above the melting points of the elements. After the material melted, the quartz tube is pulled out of the furnace at a defined rate (in furnaces with many heating zones this can be also done by appropriate temperature programs) to achieve controlled solidification of the desired compound. Although the stoichiometry of the formed crystals should be controllable, there is still a high degree of intrinsic doping (vacancies), so that the growth of undoped crystals of good quality is difficult.<sup>81</sup> Nonetheless, this method allows to reduce the carrier density by co-alloying the compounds with dopants. For instance, by using a small amount ( $< 2\%$ ) of Ca, negatively charged substitutional defects ( $\text{Ca}_{\text{Bi}}'$ ) are created that generate holes to compensate the electrons introduced by the Se vacancies.<sup>83,84</sup> As a result, the Fermi level can be lowered by about 400 meV towards the valance band making the material p-type with a carrier density of about  $1 \times 10^{17} \text{ cm}^{-3}$ .<sup>84,85</sup> The same effect can be achieved by doping  $\text{Bi}_2\text{Se}_3$  with Sb.<sup>86,87</sup> Besides doping, the Bridgman method can also be used to form alloys of different topological insulators. In many cases these alloys are TIs themselves. For example, the system  $(\text{Bi}_x\text{Sb}_{1-x})_2\text{Te}_3$  has been demonstrated to show topological surface states for the entire mixing range  $x$ .<sup>20</sup>

Another way to increase the influence of the topological surface states is to fabricate samples with a high surface-to-bulk ratio by using vapor phase processes. Molecular beam epitaxy (MBE) allows to grow single crystalline films of, for example,  $\text{Bi}_2\text{Se}_3$  with any desired thickness and high crystal quality.<sup>88</sup> By successively decreasing the thickness of the sample, a transition between a non-trivial and a trivial insulating state could be observed.<sup>23</sup> For films thinner than 6 "quintuple layers" (see below) the interaction between the top and the bottom surface is strong enough to open a gap in the surface states. The same conclusion has been drawn from electrical transport measurements on exfoliated  $\text{Bi}_2\text{Se}_3$  films, revealing an purely insulating behavior when their thickness is below 6.5 nm.<sup>89</sup>

Since the chalcogenides  $\text{Bi}_2\text{Se}_3$ ,  $\text{Bi}_2\text{Te}_3$  and  $\text{Sb}_2\text{Te}_3$  are quasi-2D layered compounds, wherein covalently bond quintuple layers composed of 5 atomic layers are held together by van der Waals interaction (see Figure 2.11a) with no dangling bonds between the individual quintuple layers, it is possible to grow high quality films by van der Waals epitaxy (VDWE). In VDWE, passivation of the dangling bonds at the surface of the growth substrate is necessary to ensure that the interactions during growth are purely van der Waals forces. In this technique the

lattice matching conditions are drastically relaxed, allowing epitaxial growth even for lattice misfits of more than 50%.<sup>90</sup> Bismuth selenide films grown with VDWE on Si(111)<sup>91</sup> or double-layer graphene<sup>92</sup> show low intrinsic doping of  $1 - 3 \times 10^{18} \text{ cm}^{-3}$  and bulk insulating behavior. It is also possible to grow  $\text{Sb}_2\text{Te}_3$  films on graphene substrates with MBE.<sup>93</sup> In this case, the defect concentration could be minimized and there is transfer doping between the n-doped graphene growth substrate and the intrinsically p-doped  $\text{Sb}_2\text{Te}_3$  films grown on top which results in high quality layers with the Fermi level in the bulk band gap.

V–VI binary and ternary compounds containing Bi, Sb, Te and Se can also be synthesized by solvothermal methods by mixing the metal oxides with a reducing organic solvent and heating in an autoclave for several hours.<sup>94,95</sup> The thickness of thus obtained, mostly hexagonal shaped nanoplates ranges from 4–30 QL, rendering them highly interesting for gate dependent electrical transport studies. However, their intrinsic doping is also relatively high due to both, the low growth temperatures (about 200 K), and possibly the incorporation of organic traces into the crystal lattice during growth.

**CVD growth** Thin films and nanowires of 3D TIs can also be grown by a chemical vapor deposition (CVD) method. Kong *et al.* reported an elegant approach to  $\text{Bi}_2\text{Se}_3$  and  $\text{Bi}_2\text{Te}_3$  nanostructures using an Au-catalyzed vapor–liquid–solid<sup>96</sup> or a catalyst-free vapor–solid<sup>27</sup> mechanism. In the latter method, ultrapure  $\text{Bi}_2\text{Se}_3$  or  $\text{Bi}_2\text{Te}_3$  crystals are placed in the hot zone of a horizontal tube furnace, while the growth substrates are placed several cm away in the colder down-stream zone. A carrier gas (Argon) with defined flow rate is used to transport the evaporated material to the substrates. Depending on the source temperature, gas flow, substrate temperature, pressure in the tube, growth time, and the growth substrates nanostructures with different lateral size and thickness can be obtained. It is noteworthy, that it is also possible to use catalytic particles to grow wires or ribbons and to in situ incorporate traces of the particles into the lattice of the nanostructures. In this manner, Sb particles can impart p-doping of  $\text{Bi}_2\text{Se}_3$ ,<sup>97</sup> while Ni particles can dope the material magnetically which is expected to open up a gap in the surface states.<sup>98</sup>

## 4.2 Setting up a CVD system

Figure 4.1 shows the CVD system that was set up during this work. A quartz tube (diameter 2.5 cm, CF flanges) is put inside a horizontal tube furnace (Gero + Eurotherm 818 temperature controller). The left end of the tube is connected to a flow controller (red-y smart, Vögtlin instruments) which can regulate the flow of ultrapure Ar gas (6.0) in the tube in the range of 1 – 150 sccm. To increase the speed of the venting process, a bypass is installed to bridge the flow controller.

The right end of the tube is connected to a pumping station (HiCube 80 Eco, Pfeiffer Vacuum, equipped with a oil-free membrane pump and a turbo pump) via a  $\text{LN}_2$  cold trap and a needle valve. A pressure gauge (active capacitive gauge CMR 361, 0.1 – 1100 mbar, Pfeiffer Vacuum) is connected to the exhaust of the cold trap. The cold trap serves to avoid contamination of

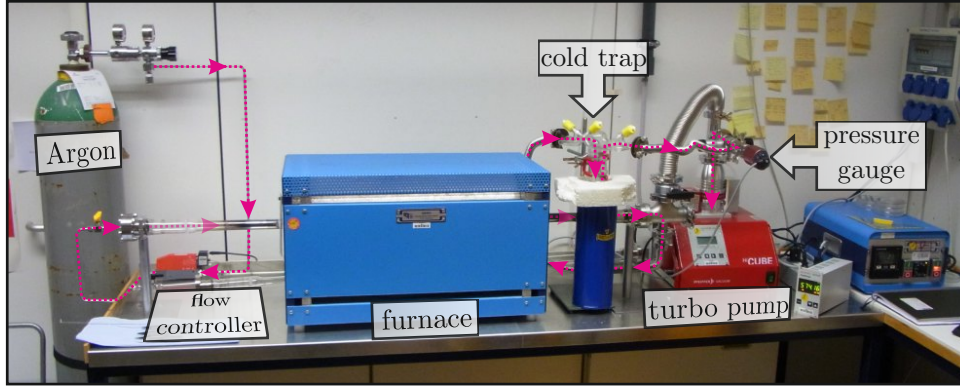


**Figure 4.1: Image of the CVD system.** The pink arrows illustrate the Ar flow direction in the system. For details see main text.

the turbo pump. The needle valve allows precise regulation of the pressure inside the tube. To allow faster evacuation, a bypass is connecting the pump directly with the glass tube via a butterfly valve. Figure 4.5a shows the temperature gradient along the furnace at the typical growth temperature of 582 K. This gradient can be used to control the source and substrate temperatures individually.

### 4.3 Results of the CVD growth

In a typical growth process, ultrapure source material ( $\text{Bi}_2\text{Se}_3$  and/or  $\text{Bi}_2\text{Te}_3$  crystalline powders) are placed in the hot zone of the tube furnace, with growth substrates positioned several cm away within the colder downstream region. To exclude residual oxygen, the tube is repeatedly evacuated to a pressure of  $p < 1$  mbar and flushed with ultrapure argon (at least three times). Subsequently, the carrier gas flow rate and the pressure inside the tube are adjusted. The furnace is then heated to the growth temperature, at which it is kept for a growth time of several min, followed by natural cool down without gas flow at a constant pressure. The deposited material appears as a gray film on the growth substrate. The final morphology, size and thickness of the nanostructures strongly depends on the growth parameters like the growth temperature, time and pressure, the flow rate, the temperature of the growth substrates (i.e. their position) and the heating rate. Before discussing the influence of these parameters in detail the possible growth morphologies will be presented.

**Possible morphologies** In most cases, the vapor–solid growth of platelets starts with the formation of triangles as depicted in Figure 4.2a. The ratio of the growth rates in  $\langle 10\bar{1}0 \rangle$ ,  $\langle 11\bar{2}0 \rangle$  or  $\langle 0001 \rangle$  directions mainly governs the morphology of the nanostructures. If the growth rate in  $\langle 10\bar{1}0 \rangle > \langle 11\bar{2}0 \rangle (> \langle 0001 \rangle)$ , thin hexagonal or trigonal platelets will grow (see Figure 4.2b and c). If the rate in  $\langle 11\bar{2}0 \rangle > \langle 10\bar{1}0 \rangle (> \langle 0001 \rangle)$ , which is normally favored in the vapor–liquid–solid mechanism<sup>99</sup> when using catalysts (Au nanoparticles or "catalytic dirt"

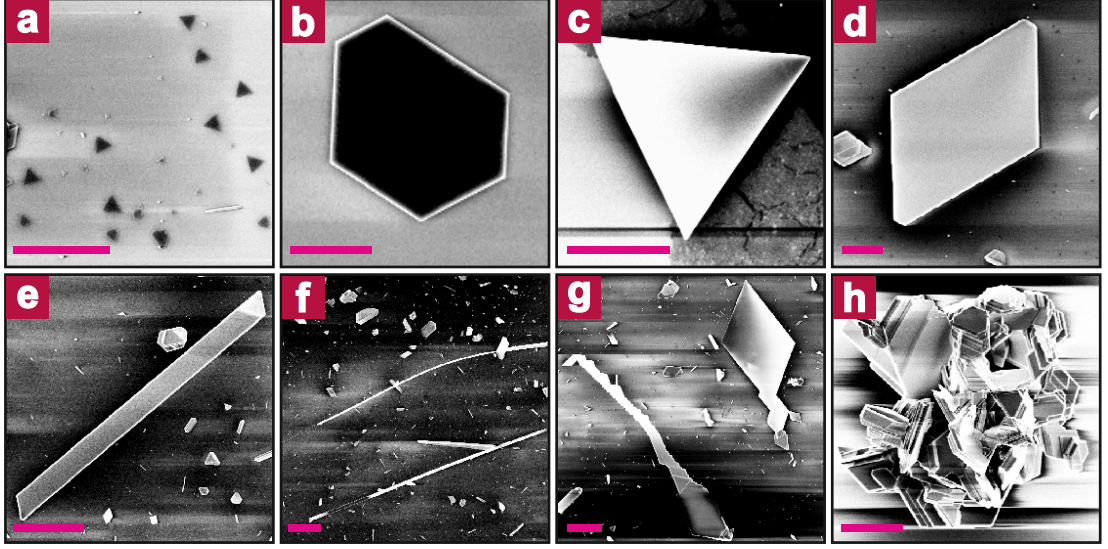


**Figure 4.2: Growth morphologies of topological insulators.** (a) VS-growth of nanoplatelets typically starts with the formation of nanotriangles. If the growth rate in  $\langle 10\bar{1}0 \rangle$  direction is higher than in  $\langle 11\bar{2}0 \rangle$  direction, hexagonal (b) or triangular (c) platelets form. In the opposite case, trapezoidal (d) platelets, nanoribbons (e), nanowires (f) or saw-tooth shaped nanostructures (g) can form. (h) Bulk-like crystals form at elevated substrate temperatures. Scale bars: (a)–(d): 1  $\mu\text{m}$ , (e)–(h): 4  $\mu\text{m}$ .

like metallic Se/Te melt droplets that can form spontaneously), trapezoidal (Figure 4.2d) or quasi 1D (Figure 4.2e and f) nanoribbons/wires or saw tooth-like (Figure 4.2g) structures are obtained. If the rate in  $\langle 0001 \rangle$  becomes sufficiently large (at elevated substrate temperatures) bulk-like crystals will be formed (Figure 4.2h).

**Growth rate-dominating parameters** The growth rate-dominating steps of a typical CVD process are depicted in Figure 4.3. Source material (for example  $\text{Bi}_2\text{Se}_3$ ) with mass  $m$  and a total surface area  $A_{\text{Bi}_2\text{Se}_3}$  will sublime due to the difference in vapor pressure  $p_{\text{vap}}^{\text{Bi}_2\text{Se}_3}$  and partial pressure  $p_{\text{par}}^{\text{Bi}_2\text{Se}_3}$ , with a rate given by the Knudsen–Langmuir equation

$$\Phi_{\text{Bi}_2\text{Se}_3} = \frac{p_{\text{vap}}^{\text{Bi}_2\text{Se}_3} - p_{\text{par}}^{\text{Bi}_2\text{Se}_3}}{\sqrt{2\pi mkT}}. \quad (4.1)$$

Here, the saturation vapor pressure  $p_{\text{vap}}^{\text{Bi}_2\text{Se}_3} = A \exp\left(-\frac{\Delta H_{\text{subl}}^{\text{Bi}_2\text{Se}_3}}{kT}\right)$  can be estimated using the Clausius–Clapeyron equation, and depends on the sublimation enthalpy  $\Delta H_{\text{subl}}^{\text{Bi}_2\text{Se}_3}$  and the temperature  $T$ . Since sublimated material is continuously transported away from the surface by the Ar gas flow (flow rate  $J_{\text{Ar}}$ ) the partial pressure of  $\text{Bi}_2\text{Se}_3$  in the gas phase can be calculated

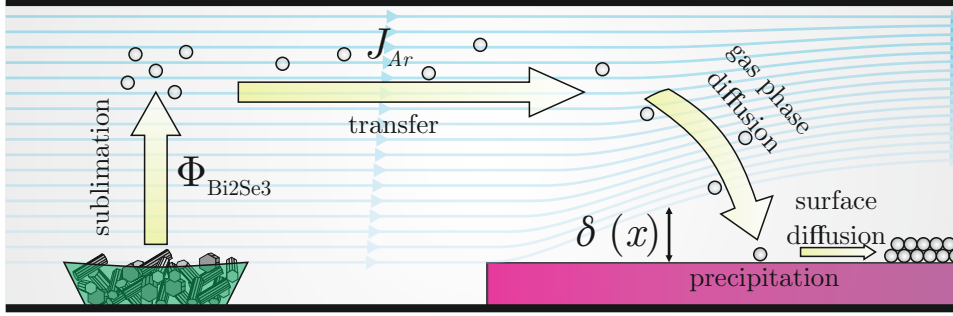


**Figure 4.3: Material transport in an CVD growth process.** Source material sublimates with a rate  $\Phi_{Bi_2Se_3}$  and is transported by the Ar gas (flow rate  $J_{Ar}$ ) to the colder substrates in the down-stream zone. The gas flow in the tube is assumed to be laminar, such that different stream lines (blue) do not cross or mix. A boundary layer with the thickness  $\delta(x)$  forms on the substrate surface. Material has to diffuse through this layer to reach the substrate. Adsorbed material can diffuse on the surface and agglomerate to form a stable cluster that is able to grow further.

using<sup>100</sup>

$$p_{par}^{Bi_2Se_3} = \frac{\Phi_{Bi_2Se_3} A_{Bi_2Se_3}}{\Phi_{Bi_2Se_3} A_{Bi_2Se_3} + J_{Ar}} p_{total}. \quad (4.2)$$

The material will be transported to the substrates in the down-stream region by the Ar gas. For sufficiently low gas flow rates, the flow is laminar, thus material is transported in different *gas layers* that do not mix. The velocity distribution of the gas inside a glass tube is restricted by two boundary conditions:  $v = 0$  at the walls of the tube (and at the surface of the substrates inside the tube) and  $v = v_0$ , where  $v_0$  is the velocity of the undisturbed incoming gas, far away from the walls. This results in the formation of a *boundary layer* with a thickness  $\delta(x)$  given by

$$\delta(x) = 5 \frac{x}{\sqrt{Re}}. \quad (4.3)$$

The Reynolds number is given by  $Re = \frac{vd}{\nu}$ , where  $v$  is the mean velocity of the gas,  $d$  is the diameter of the quartz tube and  $\nu$  is the kinematic viscosity. Transported material has to diffuse through the depleted boundary layer to reach the substrate surface. The driving force for precipitation on the substrates is again the difference between the partial pressure of the material in the gas phase and the equilibrium vapor pressure of Bi<sub>2</sub>Se<sub>3</sub> in the solid phase at the substrate temperature  $T_s$  (cold substrates → enhanced precipitation). Adsorbed material has to diffuse to supercritical clusters to form a crystal (warm substrates → enhanced diffusion).

**Source temperature** According to literature<sup>27,96,99</sup> typical source temperatures range between 450 and 700 °C. In contrast to observations by other groups, the influence of the source temperature on the morphology of the nanostructures deposited on the growth substrates in this study was found to be small. In general, the source temperature influences the sublimation rate of the source material according to Equation 4.1. For growth temperatures lower than 450 °C there is hardly any deposition occurring on the substrates, whereas for  $T > 600$  °C the amount of deposited material is so large, that it is not possible to find individual and isolated nanostructures that are suitable for electrical contacting. It also turned out, that at elevated temperatures ( $T \gg 600$  °C) deposition of metallic Se occurs at colder substrates and the colder parts of the quartz tube. This observation indicates that  $\text{Bi}_2\text{Se}_3$  is decomposed into its metallic components.

**Pressure and gas flow rate** The pressure has two important effects: firstly, the sublimation rate of the source material and the deposition rate of evaporated material on the growth substrates depends on the partial pressure of this material (see Equation 4.1), which in turn depends on the pressure in the tube (Equation 4.2). Thus, lower system pressures facilitate sublimation of material. Secondly, the interplay between pressure and gas flow defines the thickness of the boundary layer formed at the substrate surface (see Equation 4.3). In the ideal

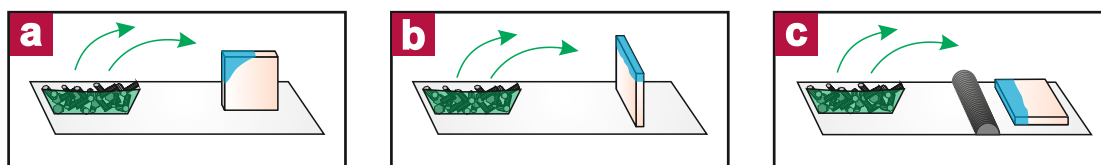


**Figure 4.4: Control experiments to exclude diffusion controlled growth.** If the growth is diffusion controlled, the deposition is inhomogeneous if the substrate is mounted vertically (a), (b) or placed behind a barrier (c).

case, the diffusion through the boundary layer should be much faster than the precipitation and diffusion on the surface, such that the total CVD process is *reaction-controlled*. In this case, the morphology of the nanostructures can be controlled by the substrate temperature. To check if the system is diffusion or reaction controlled, the growth substrates were placed horizontally behind barriers, or mounted vertically with their faces parallel or perpendicular to the Ar flow direction (see Figure 4.4). An indication for diffusion controlled growth was the inhomogeneous deposition of material at the edges of the substrate. By reducing the pressure inside the tube, and/or increasing the flow rate, it should be possible to render the growth reaction-controlled. Indeed, such cross-over was found to occur at a flow rate of about 80 sccm for a pressure of 80 mbar in a tube with a diameter of 2.5 cm. For lower flow rates there is no deposition of material on the substrates, except when barriers are introduced (that probably cause turbulent flow) or the substrates are tilted into the material stream. For the sake of completeness it should be mentioned, that decreasing the tube diameter  $d$  has a similar effect on the size of the boundary layer, since in Equation 4.3  $\delta(x) \propto (\nu d)^{-0.5}$ . As the

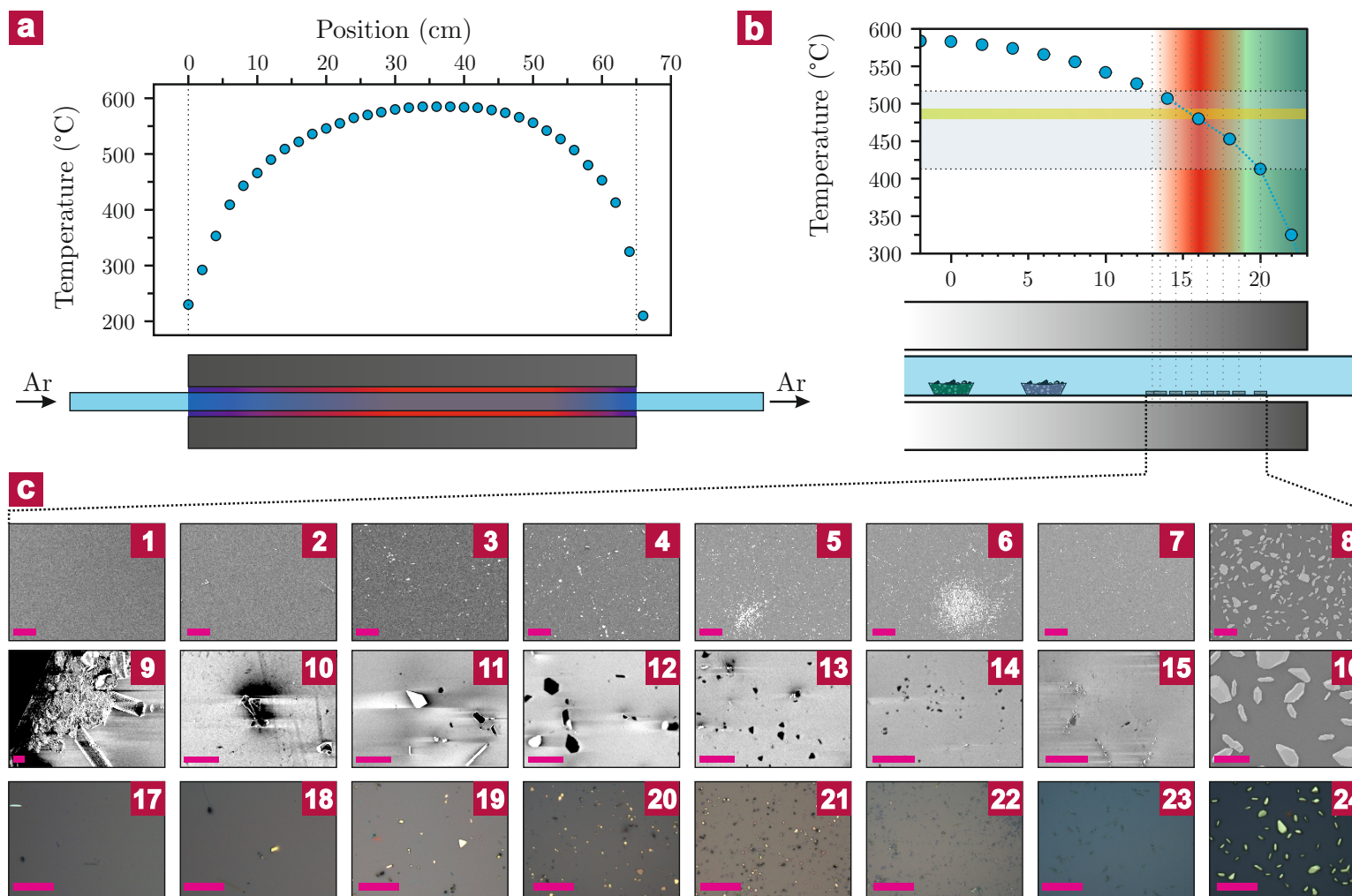
velocity of the gas is proportional to the flow  $f$  divided by the cross-sectional area  $(d/2)^2\pi$  of the tube,  $\delta(x) \propto d/f$ . Or in other words: if the flow is constant the gas atoms have to move faster to transport the same volume when the diameter of the tube is reduced.

**Heating rate** Although the heating rate strongly influences the CVD growth and morphology of the nanostructures, the underlying mechanism is unclear. Best growth results were obtained by following heating rates:  $20 \rightarrow 100^\circ\text{C}$  with  $25^\circ\text{C}/\text{min}$ ,  $100 \rightarrow 510^\circ\text{C}$  with  $80^\circ\text{C}/\text{min}$  and  $510 \rightarrow 582^\circ\text{C}$  with  $25^\circ\text{C}/\text{min}$ . It was found, that the third ramp is the most important one. Tests using different heating rates between  $20^\circ\text{C}/\text{min}$  and  $70^\circ\text{C}/\text{min}$  for the third ramp revealed, that only in a small window of  $25 - 30^\circ\text{C}/\text{min}$  regular and thin nanoplatelets can be grown. Outside this parameter window, the substrates are mainly covered with irregular, polycrystalline nanocrystals.

**Substrate temperature/position** The substrate temperature strongly influences the morphology of the deposited material. Figure 4.5 illustrates this dependency for a typical growth of  $\text{Bi}_2\text{Te}_2\text{Se}$  (see Chapter 6)<sup>i</sup> using  $T_{\text{Bi}_2\text{Se}_3} = 582^\circ\text{C}$ ,  $\text{Bi}_2\text{Se}_3$  source at 0 cm,  $\text{Bi}_2\text{Te}_3$  source at 6 cm,  $p = 80$  mbar,  $f = 150$  sccm and  $t = 1$  min.

---

<sup>i</sup>The results would be qualitatively the same for  $\text{Bi}_2\text{Se}_3$ .



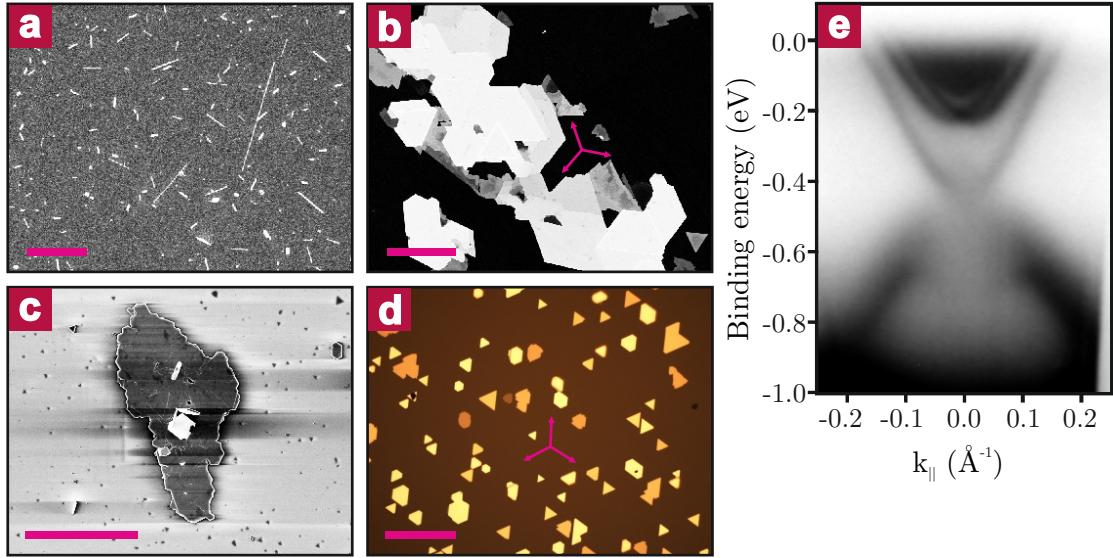
**Figure 4.5: Influence of the substrate position.** (a) Temperature profile of the furnace at 80 mbar and 150 sccm Ar flow rate. (b) Magnification of (a) (Red area: region of BTS growth, green area: deposition of metallic Te and Se). The position of the Bi<sub>2</sub>Se<sub>3</sub> source (42 cm in (a)) is chosen as 0 cm. The Bi<sub>2</sub>Te<sub>3</sub> source is located at 6 cm. Substrates are placed between 13 and 20 cm. The growth results are shown in (c). The three images in every column correspond to one substrate position and comprise two SEM images (secondary electron and in-lens detector) and an optical micrograph (scale bars 1–8: 100  $\mu$ m, 9–16: 5  $\mu$ m, 17–24: 20  $\mu$ m).

Figure 4.5b shows the relevant temperature gradient of the furnace under growth conditions. The substrates are placed 13 – 20 cm away from the  $\text{Bi}_2\text{Se}_3$  source material. The size and morphology of the deposited material is determined by the interplay of nucleation and growth. If some adsorbed atoms on the substrate surface randomly aggregate, the cluster they form is stable, if its size is bigger than the critical cluster size given by the substrate temperature. The cooler the substrate, the smaller is the critical cluster size and the higher is the chance that a stable cluster is formed. This can be directly seen in the Figures 4.5c (panels 1 – 7), where the substrate temperature is reduced from approximately 520 °C to 440 °C. The amount of material is increasing when the substrate temperatures decreases. In order that a cluster is growing, more and more atoms have to diffuse to it. Thus, crystal growth is faster at higher temperatures. Comparison of the SEM images in Figures 4.5c (panels 9 – 15) or the optical micrographs in panels 17 – 23 supports that model. For very hot substrates a few very big crystals form (mainly at defects like the substrate edge, see also Figure 4.2h). The colder the substrates get, the smaller the nanostructures become. In addition, the temperature also influences the thickness of the platelets. In general, the layer-by-layer growth of the chalcogenides investigated in this work is very anisotropic and lateral growth is always favored compared to growth normal to the layers. However, at elevated substrate temperatures growth usually gets more and more isotropic due to the higher thermal energy, and the platelets become thicker. In conclusion, the optimal growth conditions are found by trading the lateral size of the structures against their thickness. In our experiments, flakes with a lateral size of about 1 – 10  $\mu\text{m}$  and a thickness down to 5 nm are obtained at substrate temperatures between 480 – 490 °C (yellow region in Figure 4.5b).

For the sake of completeness two things have to be added. First, at very low substrate temperatures pure metals (Te and Se) can deposit and form small hexagonal crystals (see Figure 4.5c panels 8, 16 and 24). Another interesting finding is, that the amount of wire-like structures (quasi 1D growth) increases upon increasing the substrate temperature (see the typical area depicted in Figure 4.5c panel 18). This behavior is in contrast to the reports of Yan *et al.*<sup>99</sup>

**Growth time** The growth time mainly influences the density of structures and their size. Long growing times result in big and thick flakes. Again, the best growth time can be found by trading the lateral size of the structures against their thickness.

**Growth substrate type** In this work we mainly used Si substrates with a 300 nm thick layer of  $\text{SiO}_x$ . An advantage of these substrates is, that the interaction between the  $\text{SiO}_x$  layer and the nanostructures is weak and that they often grow out of the surface under a small angle. This arrangement facilitates the transfer of as-grown material to other substrates (like marker substrates suitable for e-beam lithography). However, by modifying these substrates or by using substrates that strongly interact with the deposited material, interesting changes in the morphology can be observed. For example, when a small amount of metal (Au, Bi) is thermally evaporated onto Si/ $\text{SiO}_x$  substrates it forms small clusters instead of a closed film. These metal particles can dissolve  $\text{Bi}_2\text{Se}_3$  at elevated temperatures until the metal- $\text{Bi}_2\text{Se}_3$  alloy



**Figure 4.6: Influence of the growth substrate.** (a) VLS growth of  $\text{Bi}_2\text{Se}_3$  nanowires and –ribbons on  $\text{Si}/\text{SiO}_x$  covered with 5 nm Bi. (b) Van der Waals epitaxy of  $\text{Bi}_2\text{Se}_3$  on HOPG. The arrows indicate the rotation angles of  $0^\circ$ ,  $60^\circ$  and  $120^\circ$ . (c) Van der Waals epitaxy of  $\text{Bi}_2\text{Se}_3$  on graphene oxide (GO). (d) Van der Waals epitaxy of  $\text{Bi}_2\text{Te}_2\text{Se}$  on mica.  $\text{Bi}_2\text{Se}_3$  can be grown similar and forms closed single-crystalline films suitable for ARPES investigation (e).

gets supersaturated, and  $\text{Bi}_2\text{Se}_3$  precipitates again. This well-known vapor–liquid–solid (VLS) process results in the growth of nanowires or –ribbons with a diameter that is influenced by the metal particle size.<sup>96</sup> Figure 4.6a shows a typical growth using a  $\text{Si}/\text{SiO}_x$  substrate covered with 5 nm of Bi. The ribbons have a length ranging from about 100 nm to 20  $\mu\text{m}$  with a thickness on the order of 50 – 200 nm and a typical width of 100 nm – 1  $\mu\text{m}$ . Almost no platelets can be found.

Using substrates with a layered crystal structure allows for epitaxial growth (*van der Waals epitaxy*, for details see Chapter 7) which provides access to high quality TI crystals.<sup>93</sup> One possible layered substrate is highly oriented pyrolytic graphite (HOPG).<sup>101</sup> Figure 4.6b shows a SEM image of  $\text{Bi}_2\text{Se}_3$  grown on HOPG. It is apparent that the material grows in an oriented manner with platelets parallel or rotated by  $60^\circ$  or  $120^\circ$ . Since HOPG is a good conductor, it is rather difficult to perform electrical transport experiments on structures grown on it. Instead, insulating substrates with similar lattice structure, like hexagonal boron nitride (see Chapter 7) or graphene oxide (GO) have to be used for epitaxial growth. To test the latter, a GO solution<sup>102</sup> was spin-coated on a  $\text{Si}/\text{SiO}_x$  substrate. Figure 4.6c shows the resulting growth of  $\text{Bi}_2\text{Se}_3$  as a closed film on the underlying GO flake. Another insulating layered material useful for epitaxial growth is mica. As depicted in Figure 4.6d, the growth on this substrate is highly oriented which is again an indication for epitaxial growth. By increasing the growth time, individual nanoplatelets merge together and form a closed, single-crystalline film with lateral size of up to several mm. Such single-crystalline films can be directly investigated with angle-resolved photoemission spectroscopy (ARPES).<sup>103</sup> Figure 4.6e shows the ARPES band structure

of a 300 – 400 nm thick  $\text{Bi}_2\text{Se}_3$  film grown on mica. One can clearly observe the linear surface states inside the bulk band gap. Additionally, a Rashba split parabolic surface band is visible near by the Fermi level. Such detailed information is comparable to ARPES measurements on grown bulk single crystals (whose preparation is quite demanding) making this CVD method an elegant approach to produce high quality samples for ARPES experiments.

### 4.4 Contacting topological insulator nanostructures

As a first step toward electrical contacting, individual nanostructures were identified by optical microscopy. The optical contrast can be used to estimate the thickness of the crystals. Figure

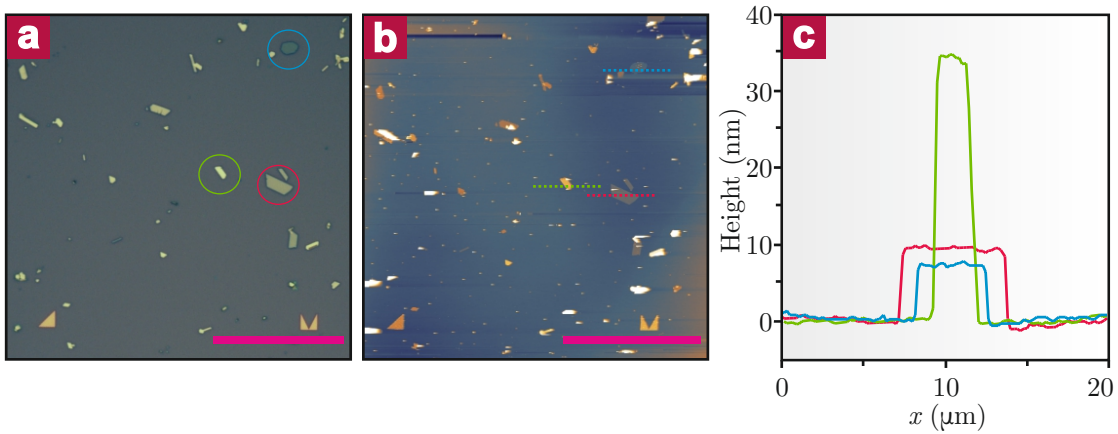


**Figure 4.7: Influence of the growth substrate.** (a) Optical image of  $\text{Bi}_2\text{Se}_3$  nanoplatelets transferred onto a marker substrate. The optical contrast of the flakes can be used to estimate their thickness. (b) AFM scan of the same area shown in (a). The corresponding height profiles are shown in (c). Fitting these profiles reveals the following thickness values: 7 nm (blue), 9 nm (pink) and 34 nm (green). Scale bars: 40  $\mu\text{m}$ .

4.7a shows an optical image of thin  $\text{Bi}_2\text{Se}_3$  nanoplatelets transferred onto a marker substrate. Three flakes with different contrast are highlighted by colored circles. By comparing their contrast to the AFM image of the same area (Figure 4.7b) and the corresponding height profiles (Figure 4.7c) it can be concluded, that the darker the flakes appear under the optical microscope, the thinner they are.

The process of electrical contacting using e-beam lithography (EBL) is depicted in Figure 4.8. Initially, an e-beam resist is spin-coated onto the substrates bearing the structures to be contacted. As resist, we typically use a double layer of PMMA (a layer of PMMA with a degree of polymerization of 950K on top of a layer with 200K) to facilitate the lift-off process. During EBL, an electron beam exposes the intended contact areas and destroys bonds in the PMMA polymer (positive resist). Since the polymer chains become shorter their solubility is

#### 4.4. Contacting topological insulator nanostructures

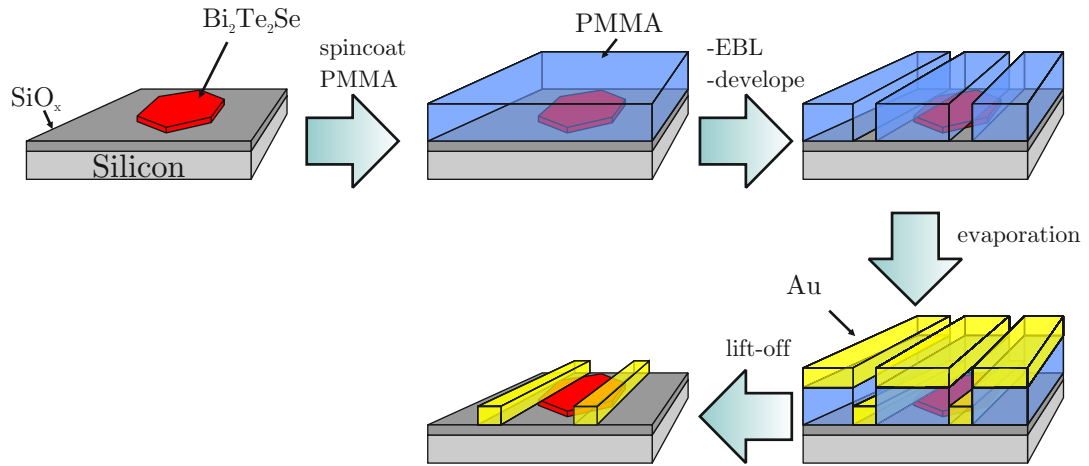


**Figure 4.8: Electrical contacting of nanostructures.** Flakes are transferred to a marker substrate and e-beam resist (PMMA) is spin-coated on top. After e-beam lithography and development, the contact material is thermally evaporated, followed by lift-off that leaves metal only in the developed regions.

increased.<sup>ii</sup> In the development step a weak solvent is used to dissolve the (shortened) PMMA in the exposed areas.

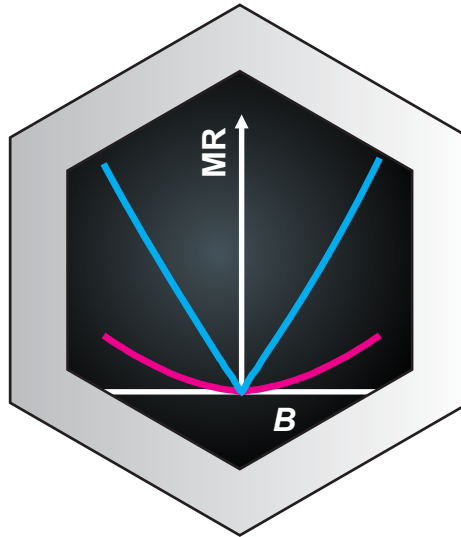
Deposition of the contact material is typically done by thermal evaporation, since this is a very anisotropic deposition technique which ensures, that no contact material is deposited on the side-walls of the developed PMMA trenches. In our studies we mainly used a combination of a very thin adhesion layer (< 5 nm Ti) and a gold film with a thickness about twice the thickness of the contacted nanoplatelets (30 – 150 nm). The gold on top of the PMMA is removed during the lift-off process, during which the substrate is immersed into warm acetone for several hours.

We observed, that it is not possible to attain ohmic contacts by directly evaporating the contact material on the as-grown structures. The reason for that could be the formation of a (insulating) native oxide layer<sup>14</sup> when the nanoplatelets are exposed to air and/or humidity. To remove this layer, we used two different techniques, either a 6 min "dip" in 36% HCl, or a 50 s Ar-plasma treatment right before loading the sample to the evaporation chamber. Both methods ensured good ohmic contacts.

<sup>ii</sup>Since the shorter chains get destroyed easier this results in a so-called *undercut* which prevents the evaporated contact material touching the walls of the PMMA film.



## 5 Gate-controlled linear magnetoresistance in thin $\text{Bi}_2\text{Se}_3$ sheets



We explore the emergence of linear magnetoresistance in thin  $\text{Bi}_2\text{Se}_3$  sheets upon tuning the carrier density by a back gate. With increasingly negative gate voltage, a pronounced magnetoresistance of  $\approx 100\%$  is observed, while the associated  $B$ -field dependence changes from quadratic to linear. Concomitantly, the resistance vs. temperature-curves evolve from metallic to semiconductor-like, and increasingly strong weak anti-localization behavior is manifested. Analysis of the magnetoresistance data reveals two contributions, namely from the bulk conduction band and from a state inside the bulk gap. The latter is responsible for the linear magnetoresistance and likely represents the topologically protected surface state.

## 5.1 Introduction

Linear magnetoresistance (LMR), first discovered about 100 years ago in Bi,<sup>53</sup> has been observed in a wide range of materials, albeit the underlying mechanism can be quite different (see Section 3.2.3). Examples of *topological* materials in which LMR has been detected are Bi<sub>2</sub>Se<sub>3</sub> and Bi<sub>2</sub>Te<sub>3</sub>,<sup>22,104</sup> semi-metallic YPtBi,<sup>105</sup> as well as the silver-based compounds Ag<sub>2+δ</sub>Te and Ag<sub>2+δ</sub>Se.<sup>106</sup> In case of the prototypical TI Bi<sub>2</sub>Se<sub>3</sub>, LMR has been observed under high magnetic fields applied to 100 nm thick nanoribbons and attributed to the topological surface states (TSS).<sup>104</sup> Furthermore, it has been found that Bi<sub>2</sub>Se<sub>3</sub> thin films are able to exhibit LMR down to a thickness of 6 nm below which a weak negative magnetoresistance emerges.<sup>107</sup> In this chapter, we demonstrate the possibility to tune the magnetoresistance characteristics of Bi<sub>2</sub>Se<sub>3</sub> by electrostatically tuning the carrier concentration. Under large negative gate potential, a MR on the order of 100% can be obtained in this manner, a finding that is relevant for magnetic field sensor applications. We assign the LMR observable under such condition to predominant charge transport through TSS. This suggests LMR as a possible fingerprint of TSS in charge transport experiments, thus complementing the widely employed ARPES measurements.

## 5.2 Sample preparation and characterization

Thin plates of Bi<sub>2</sub>Se<sub>3</sub> were synthesized by a catalyst-free vapor transport method (see Chapter 4). The chemical composition of the product was confirmed by transmission electron microscopy (TEM) and Raman spectroscopy. The TEM analysis revealed the top and bottom surface of the Bi<sub>2</sub>Se<sub>3</sub> platelets to be (0001) facets, while their side faces correspond to (01 $\bar{1}$ 0) facets (see Figure 5.1a and b). The Raman spectra of a thin sheet and a Bi<sub>2</sub>Se<sub>3</sub> bulk crystal are compared in Figure 5.1c and were acquired with a 633 nm laser beam. They display modes at 131 and 173 cm<sup>-1</sup>, which can be attributed to the E<sub>g</sub> and A<sub>1g</sub> modes of bulk Bi<sub>2</sub>Se<sub>3</sub>, respectively.<sup>108</sup> The lower intensity in the bulk sample is due to multiple reflections in the crystal that is suppressed for thin sheets.<sup>109</sup> Figure 5.1d and e show the reflection image and the corresponding Raman E<sub>g</sub> map of an electrically contacted nanoplatelet, respectively. Raman intensity can only be observed in the region of the platelet.

For the electrical transport studies, Cr/Au electrodes were defined using standard e-beam lithography. To reduce the contact resistance, the exposed contact regions were etched for 6 min in diluted HCl directly prior to the metal deposition, with the aim of removing the surface oxide (mainly Bi<sub>2</sub>O<sub>3</sub>).

## 5.3 Electrical transport measurements

The two- and four-terminal MR of an approximately 10 nm thick platelet is shown as a function of applied (negative) gate voltage in Figures 5.2a and b, respectively. At the measurement temperature of  $T = 40$  K, the most pertinent features could be observed. For the highest negative gate voltage ( $V_g = -100$  V), a significant MR of  $\approx 80\%$  is reached. The same MR mag-

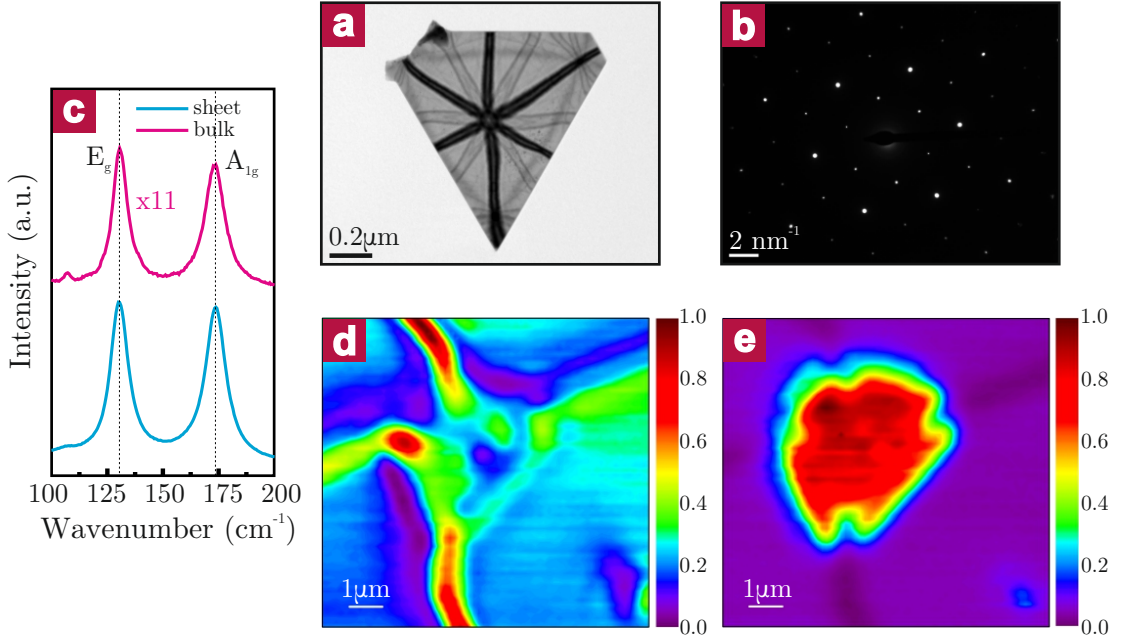


**Figure 5.1: Sample characterization.** (a) Real space TEM image of a Bi<sub>2</sub>Se<sub>3</sub> nanosheet. (b) Corresponding selected area diffraction pattern. (c) Raman spectra of a Bi<sub>2</sub>Se<sub>3</sub> bulk crystal (used for synthesis, pink line) and a synthesized nanosheet (blue line). The bulk signal is amplified by a factor 11 for comparison. (d) Optical reflection image and (e) Raman E<sub>g</sub> map of an electrically contacted sheet.

nitude was reproducibly observed for nine other samples with thicknesses ranging between 10 and 30 nm. In the lower gate voltage regime ( $|V_g| < 40$  V), the MR curves display a quadratic  $B$ -field dependence, in accordance with previous reports.<sup>69</sup> This dependence is characteristic of Lorentz deflection of charge carriers, which can be described by Kohler's rule (see Section 3.2.2)

$$\frac{R(B)}{R(B=0)} \approx 1 + (\mu B)^2, \quad (5.1)$$

where  $\mu$  is the carrier mobility. With increasingly negative gate voltage, a transition from quadratic to linear  $B$ -field dependence occurs. It is noteworthy that at all gate voltages, the region around  $B = 0$  deviates from the linear dependence as a consequence of the weak anti-localization effect (see Section 3.3.2), which is most pronounced at  $V_g = -100$  V. The trend from quadratic to linear  $B$ -field dependence is obvious from both the two- and four-terminal data, excluding that the LMR originates from the contact resistance. In order to unravel its origin, we measured the temperature dependence of resistance at different gate voltages. As exemplified in the inset of Figure 5.2b for the above sample, with increasingly negative gate voltage the resistance increases, which can be attributed to reduced carrier concentration. It is furthermore evident that the  $R$  vs.  $T$  curves exhibit metallic behavior up to  $V_g = -40$  V, while a resistance peak appears at more negative gate voltages. A reasonable explanation for the

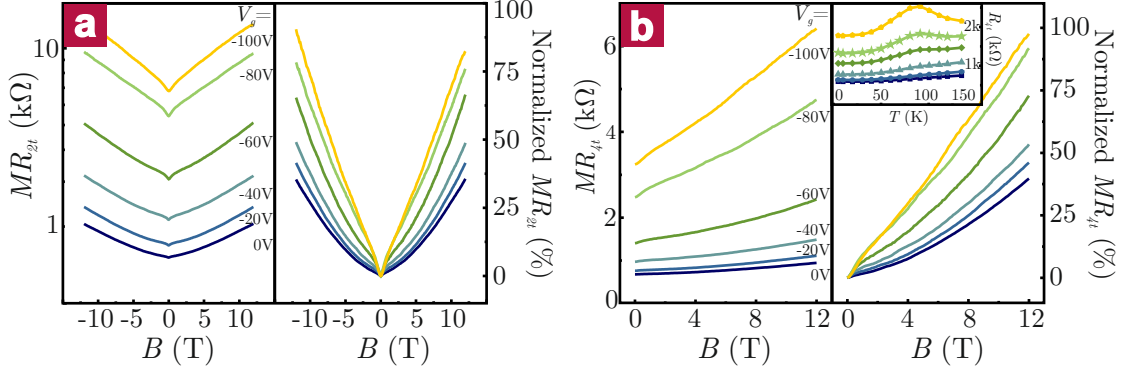


**Figure 5.2: Gate-dependent magnetoresistance.** (a) Two-terminal magnetoresistance of a 10 nm thick Bi<sub>2</sub>Se<sub>3</sub> sheet at 40 K and different back gate voltages. The left panel shows the absolute values, and the right the relative magnetoresistance. (b) Four-terminal magnetoresistance of the sample at 40 K for different back gate voltages. In left panel, the absolute values are plotted, in the right panel the relative values. In all cases, the Hall contribution was removed from the raw data. Inset: Resistance vs. temperature curves of the sample measured at different gate voltages.

peak is that two components contribute to the charge transport, with the first one showing normal metallic behavior and the second one thermally activated behavior.<sup>110</sup> While the latter behavior likely stems from the thermal excitation of carriers to the bottom of the conduction band, the metallic component can be ascribed to a state inside the bulk gap. Although there is convincing evidence that this state is the topological surface state (see further below), it is termed “gap state” in the following analysis of the resistance peak.

Figure 5.3a depicts a set of MR curves measured on the above sample at different temperatures and fixed  $V_g = -100$  V. It is apparent that with decreasing temperature, the curves become more linear. In Figure 5.3b, the corresponding zero-field resistance is plotted as a function of temperature. For fitting the curves, we write the total conductance  $G_t$  of the sample as

$$G_t(T) = G_i(T) + G_b(T), \quad (5.2)$$

where  $G_i$  is the conductance of the gap state, and  $G_b$  is the conductance associated with the bulk conduction band.<sup>51</sup> We furthermore assume that  $G_i$  is given by

$$G_i(T) = \frac{1}{A + BT}, \quad (5.3)$$

where  $A$  accounts for the static disorder scattering and  $B$  introduces electron-phonon coupling.<sup>111</sup> The thermally activated bulk conductance can be written as

$$G_b(T) = e\mu n_{b0} \exp\left(-\frac{\Delta}{T}\right) = \frac{1}{R_{b0}} \exp\left(-\frac{\Delta}{T}\right), \quad (5.4)$$

where the fitting parameter  $\Delta$  defines the energy gap between the Fermi level and the bottom of the bulk conduction band, and  $G_{b0}$  is the high temperature conductance of the bulk state. The fit of the data in Figure 5.3b yields  $\Delta = 369.9$  K,  $R_{b0} = 290.7 \Omega$ ,  $A = 2665.3 \Omega$  and  $B = 18.42 \Omega/\text{K}$ . The extracted gap size  $\Delta$  is significantly larger than the measurement temperature in Figures 5.2 ( $T = 40$  K), indicating that under this condition, the bulk conduction band contribution to the transport is strongly suppressed. In fact, based upon the above fitting values, one obtains  $R_b(T = 40 \text{ K}) = 3.0 \text{ M}\Omega$  and  $R_i(T = 40 \text{ K}) = 3.4 \text{ k}\Omega$ . It follows that the bulk resistance exceeds the gap state resistance by approximately three orders of magnitude and is even larger than the total magnetoresistance measured at the highest  $B$ -field (12 T). Accordingly, at low temperature, the gap state is expected to dominate the charge transport and thus impart the observed linear magnetoresistance behavior. The poor agreement between the fit and measured data at lowest temperatures ( $T < 20$  K) is attributable to electron–electron interaction.<sup>112</sup> Under the

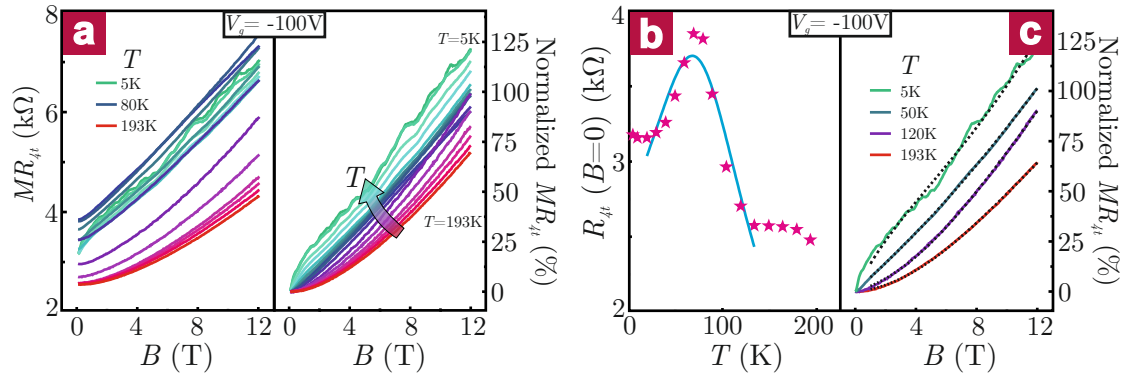


**Figure 5.3: Temperature-dependent magnetoresistance.** (a) Four-terminal magnetoresistance of the same sample as in Figure 5.2 measured between 5 and 193 K at fixed  $V_g = -100$  V. Left panel: absolute values; right panel: relative values. (b) Resistance at zero  $B$ -field measured as a function of temperature with  $V_g$  fixed at  $-100$  V. Fitting (solid line) of the raw data (stars) reveals a thermally activated behavior. (c) Fits (dashed lines) of the raw magnetoresistance curves (solid lines) recorded at four different temperatures. Fitting was performed using the parallel conduction model involving a bulk conduction band and a topological surface state contribution.

assumption that the gap state and the bulk conduction band are characterized by a linear and quadratic  $B$ -field dependence, respectively, the total magnetoresistance is given by

$$R_t(B) = \frac{R_i(B)R_b(B)}{R_i(B) + R_b(B)}, \quad (5.5)$$

where  $R_b(B)$  and  $R_i(B)$  are the bulk and gap state resistance, respectively. The two components can be expressed by

$$R_b(B) = R_b(0) + \alpha B^2 \quad (5.6)$$

and

$$R_i(B) = R_i(0) + \beta B. \quad (5.7)$$

As  $R_i(0)$  and  $R_b(0)$  are interrelated fitting parameters, only three fitting parameters remain. The fits yield the mobility of the bulk charge carriers  $\mu_b = \sqrt{\alpha/R_b(0)}$  and the bulk carrier density  $n_b = 1/(R_b(0)e\mu_b F)$ , where  $F = W/L = 3$  represents the sample width divided by length. The curve fits in Figure 5.3c (for  $V_g = -100$  V) describe well the measured data for temperatures roughly above 70 K (see Appendix A). At lower temperatures, by comparison, there is a notable deviation at low  $B$ -fields, which is due to the fact that the model does not include the weak anti-localization effect. From the fits, bulk carrier densities of  $5.3 \times 10^{23} \text{ m}^{-3}$  at 193 K and  $4.7 \times 10^{22} \text{ m}^{-3}$  at 70 K were calculated. This decrease upon cooling is in qualitative agreement with the assumed thermally activated behavior, and the absolute values are similar to those reported for Bi<sub>2</sub>Se<sub>3</sub> nanostructures.<sup>110</sup> Moreover, the obtained gap and bulk state resistance values are consistent with the fitting results based upon Equations 5.2 to 5.4 (see Appendix A). In order to characterize the gap state, we further analyze the weak anti-localization (WAL) effect around zero  $B$ -field, which is notably enhanced with increasingly negative gate voltage (see Figure 5.2). The low field anomaly in the magnetoconductivity of Bi<sub>2</sub>Se<sub>3</sub> is well described by the Hikami-Larkin-Nagaoka (HLN) model introduced in Section 3.3.2 (see Equation 3.41). The 2D magnetoconductivity is obtained by multiplying the conductance with the geometric factor  $L/W = 1/3$ . Previous magnetotransport studies on Bi<sub>2</sub>Se<sub>3</sub>/Bi<sub>2</sub>Te<sub>3</sub> grown by MBE have concluded that only the top surface of the layer conducts.<sup>69,113</sup> By contrast, magnetotransport data gained from exfoliated Bi<sub>2</sub>Se<sub>3</sub> sheets have pointed toward both surfaces contributing to the transport.<sup>110</sup> In Figure 5.4a,  $\Delta\sigma(B)$  is plotted for the above sample under different applied gate voltages. The data can be well fitted using the HLN equation, which underscores that the gap state is the topological surface state of Bi<sub>2</sub>Se<sub>3</sub>. Moreover,  $\alpha$  decreases from  $-0.6$  at  $V_g = 0$  V to  $-1.2$  at  $V_g = -80$  V, as seen in Figure 5.4b, suggesting that under the latter condition, charge transport occurs through both surfaces. The fact that  $\alpha$  slightly exceeds the value of  $-1$  might be due to a residual contribution of the bulk state or to the rough estimation of sample geometry. The dephasing length  $l_\phi$  shows an initial increase upon changing the gate voltage from 0 V to  $-40$  V, which likely reflects the suppression of the bulk conduction band contribution. The subsequent decrease of  $l_\phi$  when the gate voltage is made more negative is ascribable to enhanced electron-electron interaction with decreasing electron density.<sup>113</sup>

## 5.4 Quantum linear magnetoresistance?

The finding of gate-controllable LMR in Bi<sub>2</sub>Se<sub>3</sub> has implications for related materials such as Ag<sub>2+ $\delta$</sub> Te and Ag<sub>2+ $\delta$</sub> Se, which according to theory are likely candidates as TIs.<sup>106</sup> The MR in these compounds shows a transition from quadratic to linear  $B$ -field dependence at a certain crossover field.<sup>57,58</sup> The physical meaning of this field has not yet been fully clarified. Specifically, within the quantum magnetoresistance model by Abrikosov<sup>62,64</sup> it corresponds to the  $B$ -field above which all the electrons condense into the first Landau level, while the

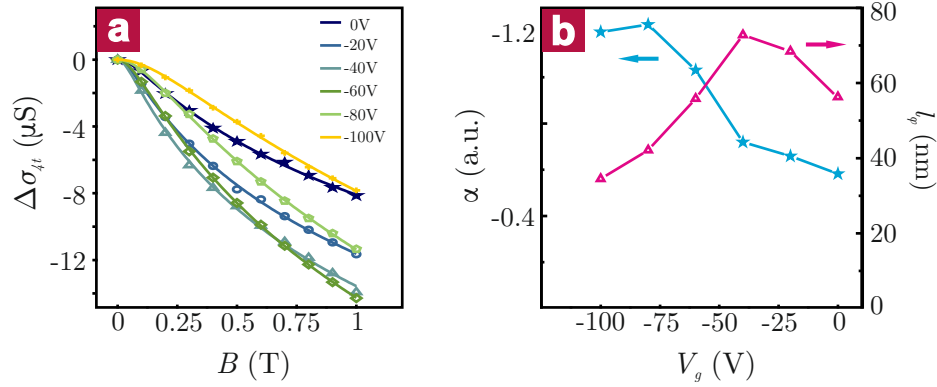


**Figure 5.4: Weak anti-localization in a  $\text{Bi}_2\text{Se}_3$  nanosheet.** (a) Anomaly in the two-dimensional magnetoconductivity, defined as  $\Delta\sigma_{4t}(B) = \sigma_{4t}(B) - \sigma_{4t}(0)$ , for different gate voltages applied to the same sample as in Figures 5.2 and 5.3. The raw data is represented by symbols and the fitting curves by solid lines. (b) Fitting parameter  $\alpha$  and dephasing length  $l_\phi$  as a function of gate voltage, both extracted from the line fits in (a).

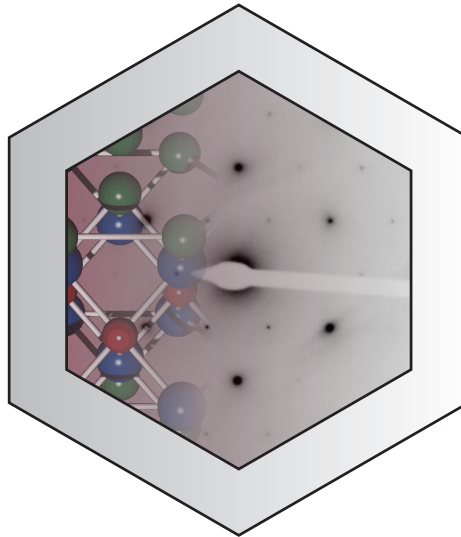
classical Parish–Littlewood model<sup>63</sup> considers it as a measure of average mobility or mobility disorder (see Chapter 3.2.3). Based upon the above analysis, the crossover field may well reflect the competition between the bulk and topological surface state contributions.

## 5.5 Summary

In conclusion, we have demonstrated that by the application of high negative gate voltages to thin  $\text{Bi}_2\text{Se}_3$  plates, the  $B$ -field dependence of magnetoresistance can be tuned from quadratic to linear. This transition is accompanied by a notable enhancement of the weak anti-localization effect, while the temperature dependence of the sample resistance changes from metallic to semiconductor-like. Our data analysis suggests that the quadratic  $B$ -field dependence originates from the bulk conduction band, while the linear  $B$ -field dependence is most likely associated with the topologically protected surface state of the sheets. The possibility of gate control over the magnetotransport characteristics of thin topological insulator sheets could prove useful for the development of magnetic sensors.



## 6 Two-dimensional magnetotransport in $\text{Bi}_2\text{Te}_2\text{Se}$ nanoplatelets



Single-crystalline  $\text{Bi}_2\text{Te}_2\text{Se}$  nanoplatelets with thickness between 8 and 30 nm and a lateral size of several micrometers were synthesized by a vapour-solid growth method. Angle-dependent magnetoconductance measurements on individual nanoplatelets revealed the presence of a two-dimensional weak anti-localization effect. In conjunction with gate-dependent charge transport studies performed at different temperatures, evidence was gained that this effect originates from the topologically protected surface states of the nanoplatelets.

## 6.1 Introduction

Although the LMR observed in Chapter 5 gives hints toward the existence of a topologically protected surface state, the contribution of the highly n-doped bulk still dominates the total electrical transport in Bi<sub>2</sub>Se<sub>3</sub>. One approach to overcome this problem is to enhance the surface transport contribution by using materials with low bulk mobility. One of the most promising candidates for this purpose is Bi<sub>2</sub>Te<sub>2</sub>Se that has been theoretically predicted<sup>114</sup> and experimentally confirmed by ARPES<sup>115</sup> to be a TI. According to recent magnetotransport studies, Bi<sub>2</sub>Te<sub>2</sub>Se has indeed a high bulk resistivity of 6 Ωcm, and hence a strong surface contribution to the total conductance of about 6%, which is one of the largest values thus far reported for TIs.<sup>28</sup> In this chapter, we investigate thin platelets of this compound, in particular the possibility to control the position of the Fermi level in the bulk band gap via electrostatic gating. Such capability is needed to compensate for the fact that most established synthesis procedures yield samples wherein the bulk dominates the electrical transport.

## 6.2 Sample preparation and characterization

Bi<sub>2</sub>Te<sub>2</sub>Se (BTS) nanoplatelets were synthesized by a catalyst-free vapour-solid (VS) method, similar to that used for the synthesis of Bi<sub>2</sub>Se<sub>3</sub> nanostructures. The details of BTS growth are provided in Chapter 4. It was found that the stoichiometry Bi<sub>2</sub>(Se<sub>x</sub>Te<sub>1-x</sub>)<sub>3</sub> of the product depends sensitively on the position of the Bi<sub>2</sub>Se<sub>3</sub> and Bi<sub>2</sub>Te<sub>3</sub> sources and the molar ratio of the two compounds. In order to obtain Bi<sub>2</sub>Te<sub>2</sub>Se, 266 mg of Bi<sub>2</sub>Se<sub>3</sub> powder (hot zone) and 355 mg of Bi<sub>2</sub>Te<sub>3</sub> powder (6 cm away) had to be used. According to atomic force microscopy (AFM) and scanning electron microscopy (SEM) analysis, thus obtained Bi<sub>2</sub>Te<sub>2</sub>Se nanoplatelets have a lateral size of 1 – 10 μm and thickness of 8 – 30 nm. In Figure 6.1a and b, a transmission electron microscopy (TEM) image and a corresponding selected area diffraction pattern of a typical Bi<sub>2</sub>Te<sub>2</sub>Se platelet are shown, respectively. Bi<sub>2</sub>Te<sub>2</sub>Se forms rhombohedral (space group  $R\bar{3}m$ ) crystals that consist of hexagonally close-packed atomic layers of five atoms (quintuple layer) which arrange along the c-axis as follows: Se<sup>(1)</sup>/Te<sup>(1)</sup> – Bi – Se<sup>(2)</sup>/Te<sup>(2)</sup> – Bi – Se<sup>(1)</sup>/Te<sup>(1)</sup> (see Chapter 2.4.2 and Figure 2.11a and b). All flakes investigated by TEM were found to be single-crystalline, exhibiting {0001} and {11 $\bar{2}$ 0} crystal facets. Toward determining their chemical composition, the Bi<sub>2</sub>Te<sub>2</sub>Se platelets were investigated by Raman microscopy. The chalcogenides Bi<sub>2</sub>Se<sub>3</sub> and Bi<sub>2</sub>Te<sub>3</sub> are strongly Raman active and can be identified by their characteristic A<sub>1g</sub><sup>1</sup>, E<sub>g</sub><sup>2</sup>, and A<sub>1g</sub><sup>2</sup> Raman peaks in the low wavenumber region.<sup>116</sup> In the corresponding alloys Bi<sub>2</sub>(Se<sub>x</sub>Te<sub>1-x</sub>)<sub>3</sub>, these peaks shift with changing composition.<sup>108</sup> For  $x < 1/3$  this shift is small, since only the Te<sup>(2)</sup> atoms are replaced by Se atoms and the Bi–Te<sup>(2)</sup> and Bi–Se<sup>(2)</sup> bonds are of similar strength. In contrast, when  $x$  exceeds 1/3 also Te<sup>(1)</sup> atoms get replaced by Se, which causes a notable shift of the A<sub>1g</sub><sup>1</sup> mode, as well as a splitting of the A<sub>1g</sub><sup>2</sup> mode due to out-of-phase movements of the outer Bi and Te<sup>(1)</sup>/Se<sup>(1)</sup> atoms. Figure 6.1c compares the Raman spectra acquired from the Bi<sub>2</sub>Se<sub>3</sub>/Bi<sub>2</sub>Te<sub>3</sub> starting materials and a representative Bi<sub>2</sub>Te<sub>2</sub>Se nanoplatelet. The experimentally accessible range of 80 – 200 cm<sup>-1</sup> contains the E<sub>g</sub><sup>2</sup> and A<sub>1g</sub><sup>2</sup> peaks, but not the A<sub>1g</sub><sup>1</sup> peak. The nanoplatelets spectrum displays

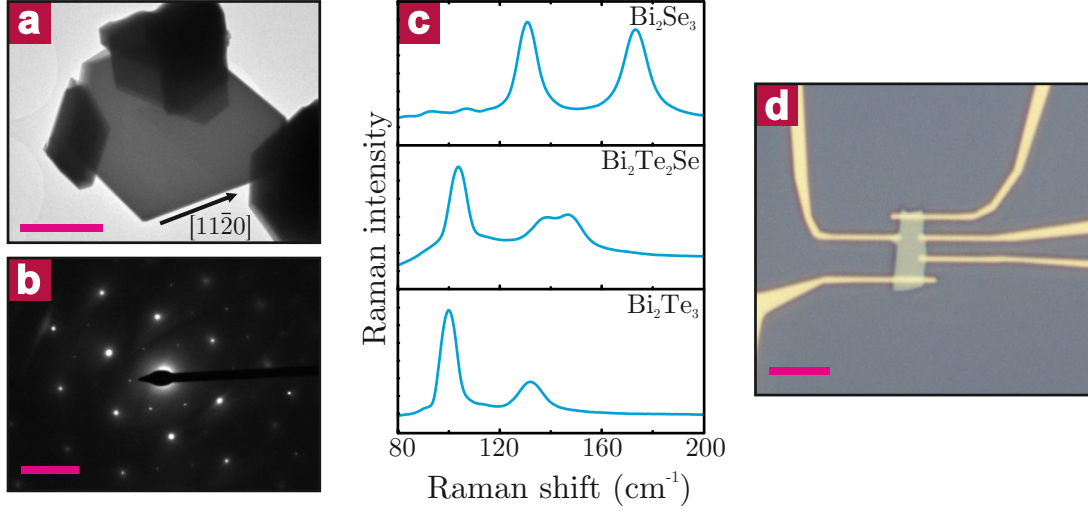


**Figure 6.1: Characterization of Bi<sub>2</sub>Te<sub>2</sub>Se nanoplatelets.** (a) Transmission electron microscopy (TEM) image and corresponding selected area diffraction pattern (b) of a Bi<sub>2</sub>Te<sub>2</sub>Se nanoplatelet. Scale bar corresponds to 1 μm (b): 5 nm<sup>-1</sup> (c) Raman spectra of a Bi<sub>2</sub>Se<sub>3</sub> flake (top), a Bi<sub>2</sub>Te<sub>2</sub>Se nanoplatelet synthesized by the CVD method (middle), and a Bi<sub>2</sub>Te<sub>3</sub> flake (bottom). (d) Optical image of a 15 nm thick flake contacted in Hall bar geometry (scale bar: 5 μm).

three distinct features, namely the  $E_g^2$  peak at 105.2 cm<sup>-1</sup>, and the  $A_{1g}^2$  peak which is split into two components at 138.8 cm<sup>-1</sup> and 148.9 cm<sup>-1</sup>, respectively. The latter two peak positions are in good agreement with the corresponding values of  $139.7 \pm 1$  cm<sup>-1</sup> and  $148.5 \pm 1$  cm<sup>-1</sup>, as reported by Richter and Becker<sup>108</sup> for Bi<sub>2</sub>Te<sub>2</sub>Se bulk samples, from which  $x = 0.34$  can be concluded for the present samples.

### 6.3 Electrical magnetotransport measurements

In order to determine the charge transport mechanism and dimensionality of the involved transport channels in the nanoplatelets, we performed magnetotransport studies. To this end, the Bi<sub>2</sub>Te<sub>2</sub>Se nanoplatelets were mechanically transferred onto Si substrates covered with a 300 nm thick SiO<sub>2</sub> layer. Individual platelets were provided with Ti(4 nm)/Au(40 nm) contacts in Hall bar or van der Pauw geometry using e-beam lithography (as exemplified in Figure 6.1d). Prior to metal evaporation, the exposed regions were subjected to Ar-plasma (50 s at 250 W) in order to reduce the contact resistance. Low temperature Hall measurements on several devices revealed an average electron density  $n_{3D}$  of about 10<sup>25</sup> m<sup>-3</sup>, a value comparable to typical Bi<sub>2</sub>Se<sub>3</sub> crystals.<sup>27</sup> The average Hall mobility  $\mu_H$  of our samples was determined to be on the order of 100 – 400 cm<sup>2</sup>/Vs, which is lower than in pure Bi<sub>2</sub>Se<sub>3</sub> or Bi<sub>2</sub>Te<sub>3</sub> nanostructures.<sup>14, 117</sup> Figure 6.2a presents the low field magnetoconductance signal  $\Delta\sigma = \sigma(B) - \sigma(B = 0)$  of a 15 nm thick Bi<sub>2</sub>Te<sub>2</sub>Se platelet at  $T = 1.5$  K as a function of the tilting angle  $\theta$  between the  $z$ -axis and the  $B$ -field direction. The prominent peak around  $B = 0$  T can be attributed to

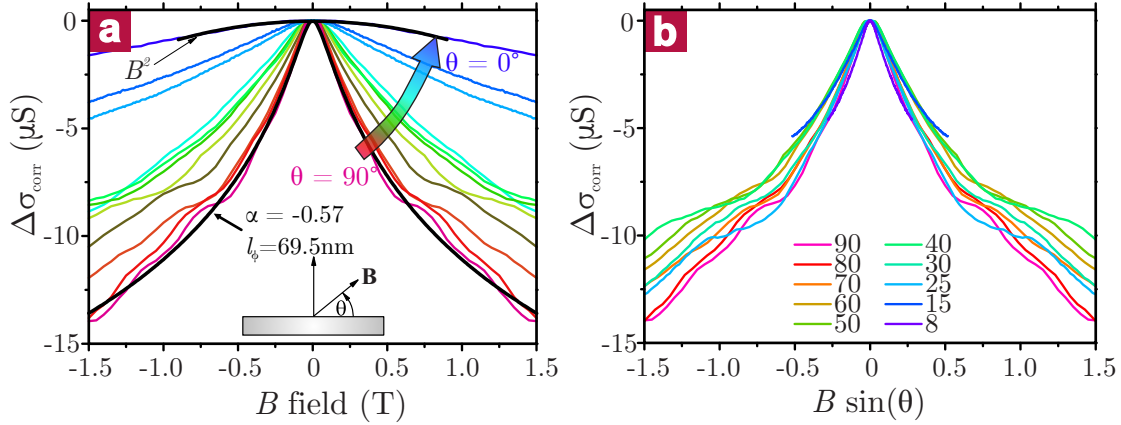


**Figure 6.2: Weak anti-localization of  $\text{Bi}_2\text{Te}_2\text{Se}$  nanoplatelets.** (a) Corrected low field magnetoconductance signal acquired from a 15 nm thick  $\text{Bi}_2\text{Te}_2\text{Se}$  nanoplatelet for different angles  $\theta$  as a function of the magnetic field, and (b) as a function of the magnetic field component  $B_z = B \sin(\theta)$  normal to the surface. The fitting result for the WAL curve recorded at  $\theta = 90^\circ$  is shown in black. The data at  $\theta = 0^\circ$  was fitted with a  $B^2$  model (panel (a)).

the weak anti-localization (WAL) effect (see Section 3.3.2). This effect is not limited to 2D systems, but can also have a contribution from the 3D bulk. To test whether the observed WAL effect is a pure 2D effect, the sample was tilted in the external magnetic field, since in this case the signal should depend only on the magnetic field component  $B_z = B \sin(\theta)$  normal to the sample surface. For the present samples, the WAL effect vanishes at  $\theta = 0^\circ$  ( $B$  in plane,  $B_z = 0$ ), under which condition the magnetoconductance shows a simple parabolic behavior like in conventional semiconductors. The 2D character of the WAL is further illustrated by Figure 6.2b, where  $\Delta\sigma$  is plotted as a function of  $B_z$ . It can be seen that all curves coincide for different angles  $\theta$ . The observed angular dependence of  $\Delta\sigma$  signifies the 2D character of the WAL, suggesting that this effect originates from the topologically protected 2D surface states. A similar conclusion based upon angle-dependent magnetotransport measurements has recently been drawn for thin  $\text{Bi}_2\text{Te}_3$  films grown by MBE.<sup>69</sup> The magnetoconductance data can be well fitted by the Hikami-Larkin-Nagaoka (HLN) model for 2D localization (Equation 3.41). Fitting the magnetoconductance curve at  $\theta = 90^\circ$  yields  $\alpha = -0.57$  and  $l_\phi = 69.5 \text{ nm}$ . The value of  $\alpha = -0.57 \approx -0.5$  indicates that either only one surface is contributing to the 2D WAL effect, or that the top and the bottom surfaces are strongly coupled, in analogy to observations made for  $\text{Bi}_2\text{Se}_3$ <sup>113</sup> and  $\text{Bi}_2\text{Te}_3$ <sup>69</sup> thin films. It is noteworthy that the  $\Delta\sigma(B)$  signal in Figure 6.2a shows a notable oscillatory behavior. This feature could be explained by quantum interference phenomena like universal conductance fluctuations<sup>18</sup> or the Aharonov-Bohm effect<sup>97</sup> which have been observed in various TI materials (for details see Chapter 3).

Having demonstrated the pure 2D magnetotransport in very thin BTS nanoplatelets, we explored the possibility of using an external gate to tune the Fermi level in such manner as to favor charge transport through the surface state also in thicker platelets. Such samples still show WAL at zero angle,<sup>69</sup> and their Fermi level position is expected near the conduction band (CB) edge. Along these lines, we measured the temperature dependence of resistance

at different back gate voltages for several platelets with a thickness above 20 nm. The aim of these experiments was to determine the Fermi level position from the observed thermal activation barriers. The electrical behavior is exemplified in Figure 6.3 for a  $\approx 20$  nm thick

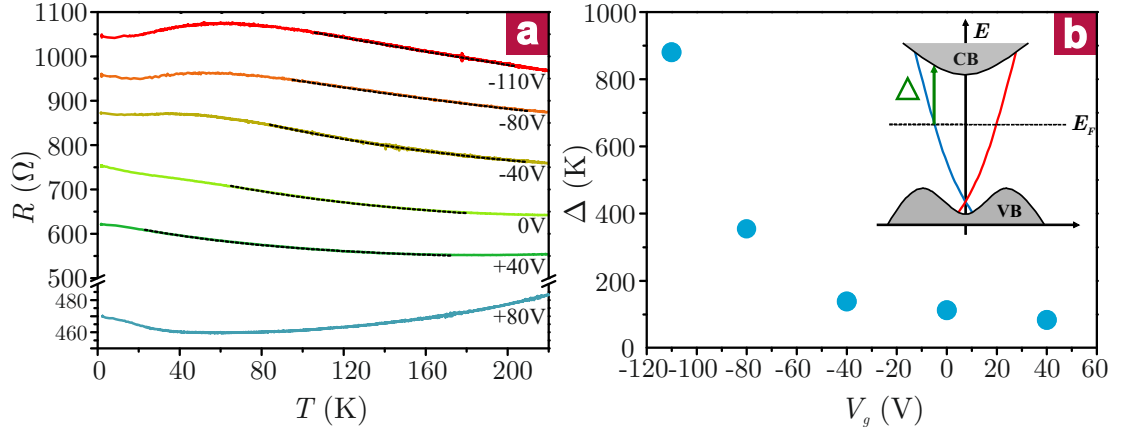


**Figure 6.3: Temperature dependent electrical transport behavior of  $\text{Bi}_2\text{Te}_2\text{Se}$  nanoplatelets.** (a) Temperature dependent resistance recorded at different backgate voltages applied to a  $\text{Bi}_2\text{Te}_2\text{Se}$  nanoplatelet with a thickness of  $\approx 20$  nm. Dotted lines: Arrhenius fits to the curves. (b) Energy gap  $\Delta$  between Fermi level and bulk conduction band edge for different gate voltages, as obtained from Arrhenius-type fitting. The inset shows the definition of  $\Delta$ .

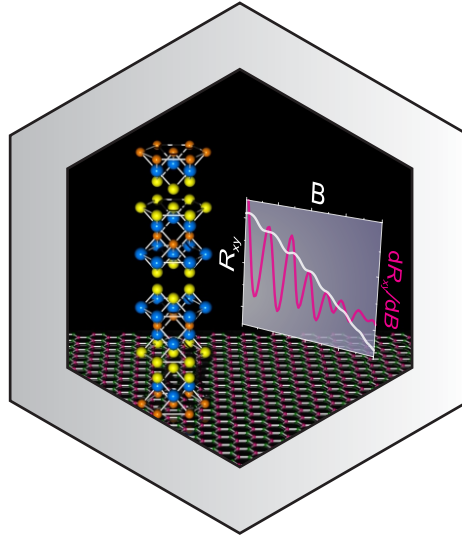
$\text{Bi}_2\text{Te}_2\text{Se}$  nanoplatelet. While at zero gate voltage, purely thermally activated behaviour can be discerned, at highest negative gate voltage ( $-100$  V) a resistance maximum emerges at approximately 50 K. At moderate temperatures, the mobility of the surface electrons is expected to be low due to strong electron–phonon scattering,<sup>111</sup> and correspondingly the charge transport through the bulk should dominate over the surface state. On this basis, the thermal activation behaviour can be attributed to the excitation of surface state electrons nearby the Fermi level into the bulk CB, with the excitation energy being equal to the energy gap  $\Delta$  between the Fermi level and the CB edge.<sup>110</sup> We extracted the energy gap  $\Delta$  by fitting the  $R(T)$  curves in the high  $T$  range (80 – 180 K) with an Arrhenius formula  $R(T) = R_0 + A \cdot \exp(-\Delta/T)$  (black, dotted curves in Figure 6.3a). Thus obtained values are plotted in Figure 6.3b as a function of gate voltage. It is apparent that the application of increasingly negative gate voltages results in the expected increase of the energy gap. The maximum in the  $R(T)$  curves at negative gate voltages can be explained by an interplay between two effects. The first one comprises a resistance increase due to the reduced carrier concentration at lower temperatures. The second effect, which counteracts the aforementioned resistance increase, involves the reduction of electron–phonon scattering of the surface electrons upon cooling, owing to the metallic character of surface state electrons.<sup>110</sup> As distinguished from the behavior under negative gate voltages, the temperature characteristic can be changed into purely metallic by applying a strong positive gate voltage ( $+80$  V). In this gating regime, the Fermi level is located within the bulk conduction band, similar to quasi-metallic  $\text{Bi}_2\text{Se}_3$  crystals without compensation

doping.<sup>84</sup>

### 6.4 Summary

In summary, we have demonstrated the presence of a 2D WAL effect in thin nanoplatelets of  $\text{Bi}_2\text{Te}_2\text{Se}$ , which points toward the participation of the topologically protected surface states in the charge transport. The samples are amenable to gate control, as proven by gate- and temperature-dependent resistance measurements, enabling the manifestation of surface state transport also for thicker platelets. Our results establish  $\text{Bi}_2\text{Te}_2\text{Se}$  as a valuable material for further studies of the fundamental properties of topological surface states.

## 7 Growth of High-Mobility $\text{Bi}_2\text{Te}_2\text{Se}$ Nanoplatelets on hBN Sheets by van der Waals Epitaxy



The electrical detection of the surface states of topological insulators is strongly impeded by the interference of bulk conduction, which commonly arises due to pronounced doping associated with the formation of lattice defects. As exemplified by the topological insulator  $\text{Bi}_2\text{Te}_2\text{Se}$ , we show that via van der Waals epitaxial growth on thin hBN substrates the structural quality of such nanoplatelets can be substantially improved. The surface state carrier mobility of nanoplatelets on hBN is increased by a factor of about 3 compared to platelets on conventional  $\text{Si}/\text{SiO}_x$  substrates, which enables the observation of well-developed Shubnikov–de Haas oscillations. We furthermore demonstrate the possibility to effectively tune the Fermi level position in the films with the aid of a back gate.

## **7.1 Introduction**

Strategies that have been pursued to minimize the contribution of the bulk transport include compensation doping,<sup>85,118</sup> alloying of differently doped TIs,<sup>20,115</sup> or increasing the surface to bulk ratio by using ultrathin samples.<sup>27</sup> However, doping or alloying typically results in a concomitant drastic decrease in carrier mobility due to the introduction of defects. One possibility to avoid such decrease in the structural quality of the crystals involves the epitaxial growth of TI thin films on graphene (see Section 4.3), which has been demonstrated to significantly reduce the defect density and hence the bulk interference.<sup>93</sup> At the same time, the lowered defect concentration in epitaxially grown films ensures enhanced carrier mobilities.<sup>119</sup> The suitability of graphene as a substrate for epitaxial growth of TI materials derives from its layered structure with hexagonal lattice symmetry, combined with its C–C bonding length of 1.42 Å corresponding to a small lattice mismatch of only 2.9% versus  $\text{Bi}_2\text{Se}_3$ .<sup>93,101</sup> However, due to its high electrical conductivity, graphene rules out as underlying substrate if electrical transport studies are desired on the grown TIs.

In this chapter, we report the van der Waals epitaxial growth and electrical characterization of high quality  $\text{Bi}_2\text{Te}_2\text{Se}$  thin films on electrically insulating hexagonal boron nitride (hBN) sheets (band gap of about 6 eV<sup>120</sup>).  $\text{Bi}_2\text{Te}_2\text{Se}$  has emerged as one of the most promising TIs due to its simple surface band structure, large bulk band gap, and low bulk contribution to the total charge transport.<sup>28,115,121</sup>

Our  $\text{Bi}_2\text{Te}_2\text{Se}$  films grown by van der Waals epitaxy are sufficiently ordered to display Shubnikov–de Haas (SdH) oscillations that provide access to important quantities such as the cyclotron mass, the Fermi velocity, or Fermi energy.<sup>22</sup> This capability is in contrast to previously investigated  $\text{Bi}_2\text{Te}_2\text{Se}$  films grown by chemical vapor deposition (CVD) on Si/SiO<sub>x</sub> substrates in which case the relatively low surface state mobility<sup>122</sup> has prevented the observation of SdH oscillations (see Chapter 6). As another advantage, the present  $\text{Bi}_2\text{Te}_2\text{Se}$  films are sufficiently thin to permit tuning the Fermi level position over a sizable range by applying a back gate voltage.

$\text{Bi}_2\text{Te}_2\text{Se}$  forms rhombohedral (space group  $R\bar{3}m$ , see Figure 7.1a) crystals with the lattice constants  $a = 4.283$  Å and  $c = 29.846$  Å.<sup>123</sup> Thus, hexagonal boron nitride (hBN), which likewise forms a layered crystal with hexagonal symmetry and has a B–N bonding length of 1.45 Å (close to that of the C–C bonding length of graphene) is a suitable insulating substrate for van der Waals epitaxy. The alignment of  $\text{Bi}_2\text{Te}_2\text{Se}$  on hBN proposed in Figure 7.1b is characterized by a small lattice mismatch of 1.5%. In addition, the layered crystal structures of  $\text{Bi}_2\text{Te}_2\text{Se}$  and hBN are expected to favour epitaxial growth by van der Waals epitaxy. Herein, the weak van der Waals interaction between the two materials relaxes the lattice–mismatch condition.<sup>101</sup>

## **7.2 Sample preparation and characterization**

Thin  $\text{Bi}_2\text{Te}_2\text{Se}$  (BTS) films were grown by a catalyst-free vapor solid method as described in Chapter 4. The hBN sheets were prepared by micromechanical cleavage of hBN powder. To this end, a tiny amount of the powder was placed on a stripe of scotch tape, which was then

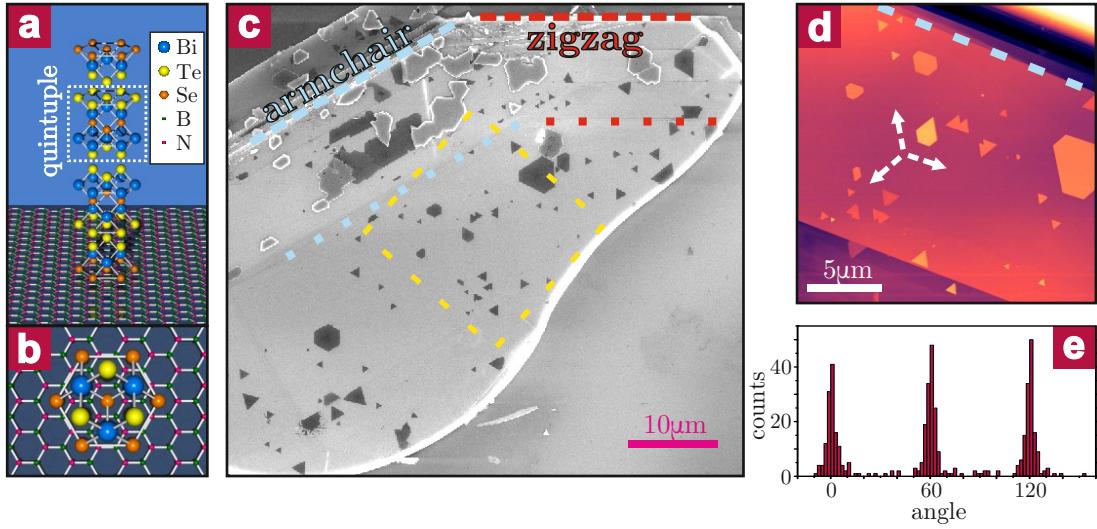


**Figure 7.1: Van-der-Waals epitaxy of  $\text{Bi}_2\text{Te}_2\text{Se}$  on hBN.** (a) Schematic illustration of the crystal structure of  $\text{Bi}_2\text{Te}_2\text{Se}$ , and (b) the proposed epitaxial growth mode on hBN. (c) SEM image of  $\text{Bi}_2\text{Te}_2\text{Se}$  nanoplatelets grown on hBN. The armchair and zigzag edges of the hBN sheet are marked in blue and red, respectively. (d) AFM image of the square area marked in (c). (e) Histogram of the orientation distribution of the  $\text{Bi}_2\text{Te}_2\text{Se}$  nanoplatelets grown on hBN.

repeatedly folded onto itself. Subsequently, a  $\text{Si}/\text{SiO}_x$  substrate was pressed onto the tape and then removed, followed by ultrasonication of the substrate in 2-propanol to remove thick hBN flakes. In this manner, hBN flakes with a thickness down to 7 nm were obtained. The growth substrates were mounted in the quartz tube 15 cm away from the hot zone within the colder downstream region. Finally, the furnace was heated to approximately  $590^\circ\text{C}$  and held at this temperature for 30 s to 6 min, followed by natural cool down without gas flow. Morphology and thickness of the BTS films were found to sensitively depend on the position of the growth substrates and the growth time. The accessible film thickness was determined to range between 4 and 500 nm.

As exemplified by the SEM image in Figure 7.1c, as well as the AFM image in Figure 7.1d,  $\text{Bi}_2\text{Te}_2\text{Se}$  grows on top of the hBN in the form of regular platelets with hexagonal symmetry. The  $\text{Bi}_2\text{Te}_2\text{Se}$  growth mechanism proposed in Figure 7.1b is supported by the observation that the crystal faces in all platelets are oriented parallel or rotated by  $60^\circ$  or  $120^\circ$  (see Figure 7.1d, e). Moreover, it can be seen in Figure 7.1c that the nanoplatelets preferably grow parallel to one of the sharp edges of the hBN sheet that are formed during exfoliation. Since the edges of the hBN flake enclose an angle of precisely  $30^\circ$ , they can be assigned to armchair or zigzag edges. Assuming that the edges marked in blue in Figure 7.1c are the armchair edges of the hBN flakes, the growth mechanism suggested in Figure 7.1b gains further support (if these edges were the zigzag edges instead, the resulting misfit would be unrealistically high, specifically 26% in case that the  $\text{Bi}_2\text{Te}_2\text{Se}$  flakes would be compressed, and 47% if they would be expanded). Evidence for the formation of  $\text{Bi}_2\text{Te}_2\text{Se}$  could be gained by Raman spectroscopy. The chalcogenides  $\text{Bi}_2\text{Se}_3$ ,  $\text{Bi}_2\text{Te}_3$ , and their alloys  $\text{Bi}_2(\text{Se}_x\text{Te}_{1-x})_3$  are highly Raman active in the low wavenumber

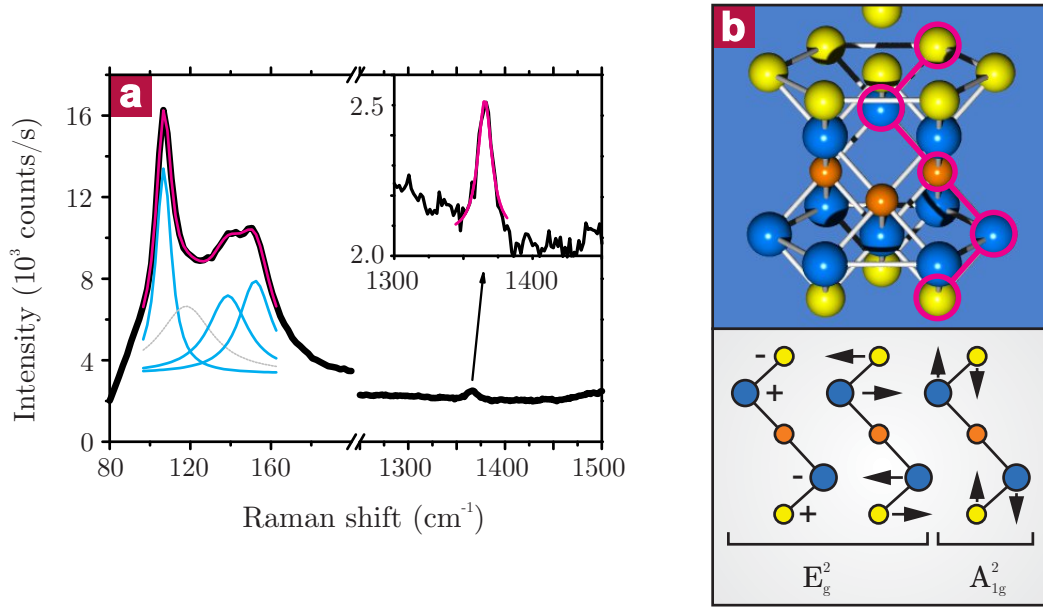


**Figure 7.2: Raman measurements of  $\text{Bi}_2\text{Te}_2\text{Se}$  on hBN.** (a) Raman spectrum of  $\text{Bi}_2\text{Te}_2\text{Se}$  on hBN, acquired with  $\lambda_{exc} = 633$  nm. The low wavenumber region can be fitted (pink curve) using three Lorentzians (blue curves). The inset amplifies the wavenumber region 1300 – 1450  $\text{cm}^{-1}$ , with a Lorentzian fit to the peak (pink curve). (b) Sketch of the  $E_g^2$  and the  $A_{1g}^2$  Raman modes.

region.<sup>108</sup> The Raman spectrum in Figure 7.2a, acquired with a laser wavelength of 633 nm, displays three peaks at 105.0, 139.1, and 149.6  $\text{cm}^{-1}$ , respectively. They can be identified as the  $E_g^2$  and the  $A_{1g}^2$  peak (which is split into two components) of  $\text{Bi}_2\text{Te}_2\text{Se}$  (see Figure 7.2b).<sup>108</sup> The additional peak at 1365.5  $\text{cm}^{-1}$  (see Figure 7.2a, inset) corresponds to the  $E_g^2$  mode of the underlying hBN flake.<sup>124</sup>

It is noteworthy that besides  $\text{Bi}_2\text{Te}_2\text{Se}$ , also  $\text{Bi}_2\text{Se}_3$  could be grown on hBN by van der Waals epitaxy (see Figure 7.3a). The growth conditions were as follows:  $\text{Bi}_2\text{Se}_3$  source material was placed in the hot zone, and Si/SiO<sub>x</sub> substrates covered with hBN flakes 14 cm away from the source in the down-stream zone. The pressure, flow, temperature and time were  $p = 80$  mbar,  $f = 150$  sccm,  $T = 590$  °C and  $t = 6$  min, respectively. The thickness of thus-prepared  $\text{Bi}_2\text{Se}_3$  nanoplatelets ranged between 5 nm and several hundreds of nm (see Figure 7.3b). As the growth preferentially occurred on thick hBN flakes ( $d > 400$  nm), subsequent electrical contacting of the  $\text{Bi}_2\text{Se}_3$  nanoplatelets proved very difficult.

### 7.3 Electrical transport measurements

For electrical transport studies, standard e-beam lithography was performed to provide individual  $\text{Bi}_2\text{Te}_2\text{Se}$  platelets with Ti(4 nm)/Au(200 nm) contacts in Hall bar or van der Pauw geometry. Figure 7.4a displays the high field part of the sheet resistance  $R_s$  and the Hall resis-

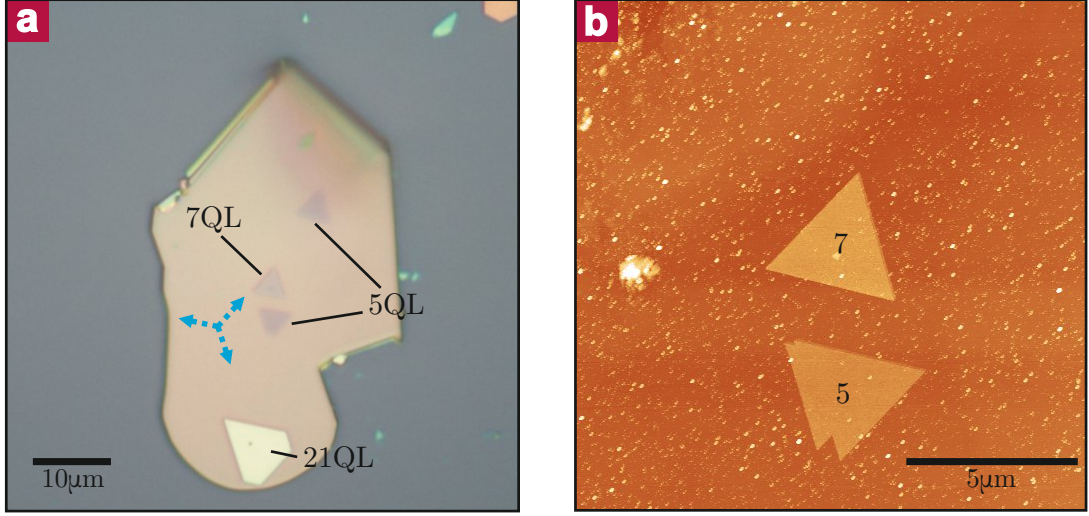


**Figure 7.3: Epitaxial growth of  $\text{Bi}_2\text{Se}_3$  nanoplatelets on hBN.** (a) Optical micrograph. The thickness of the platelets ranges from 5 QL to 21 QL. In general, the flakes were found to be oriented parallel or tilted by  $120^\circ$  (indicated by the blue arrows) with respect to each other. (b) AFM image of the two  $\text{Bi}_2\text{Se}_3$  platelets close to the center of the hBN sheet in panel (a).

tance  $R_{xy}$  as a function of the magnetic field  $B$  at  $T = 1.5$  K for a 19 nm thick  $\text{Bi}_2\text{Te}_2\text{Se}$  platelet on a 17 nm thick hBN sheet. Here the sheet resistance is calculated via the standard procedure applied to samples contacted in van der Pauw geometry (see Section 3.5), specifically by solving Equation 3.57 for each contact pair. It is apparent that both signals feature Shubnikov–de Haas (SdH) oscillations. Subtraction of the background (different ways of smoothing were tested, which gave an identical oscillation period) yields the oscillatory signal depicted in Figure 7.4b, where  $\Delta R / \langle R \rangle$  is plotted to highlight the different signal-to-noise ratio in the two cases.<sup>i</sup> Importantly,  $R_s$  and  $R_{xy}$  show the same oscillation frequency, while there is a phase shift of about  $\pi/2$  between them (see also the fan diagrams in Figure 7.4c). Such phase shift is expected by theory (see Section 3.2.4) and consistent with experimental observations on bulk  $\text{Bi}_2\text{Te}_3$  samples.<sup>22</sup>

In a prototypic two-dimensional (2D) electron gas, SdH oscillations are periodic in  $1/B$ , with a periodicity given by<sup>22</sup>

$$2\pi n = A_F \frac{\hbar}{eB}, \quad (7.1)$$

where  $n$  is the Landau level (LL) index, and  $A_F$  is the external cross-section of the Fermi surface (see also Section 3.2.4). Such periodicity is evident by plotting the  $1/B$  values of the maxima/minima of the  $R_s$  and  $R_{xy}$  data as a function of the LL index (see fan diagram in Figure 7.4c). We determined the position  $1/B$  of the LL using the minima of the  $R_s$  signal.<sup>22, 28</sup> The maxima are shifted by  $\pi$  with respect to the minima, which results in a shift of  $n + 1/2$

<sup>i</sup>Since the signal-to-noise ratio for the  $R_{xy}$  signal is much higher than that for  $R_s$ , the former will be used for further analysis.

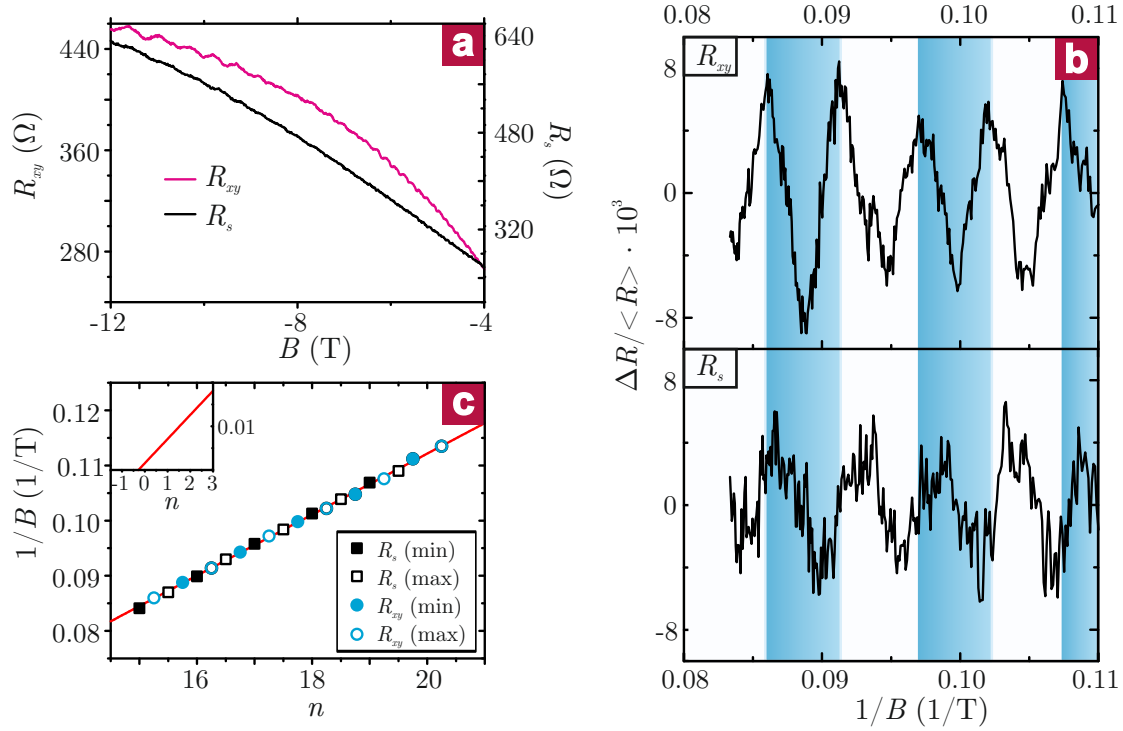


**Figure 7.4: Shubnikov–de Haas oscillations in epitaxially grown Bi<sub>2</sub>Te<sub>2</sub>Se nanoplatelets.** (a) Comparison between the  $R_{xy}$  (green) and  $R_s$  (black) signal. (b) The same data shown in (a) subtracted by a smoothed background ( $\langle R \rangle$ ). To compare the signal-to-noise ratio,  $\Delta R$  was divided by the smoothed background. The period of the SdH oscillations in the  $R_{xy}$  signal is highlighted by grey shades. (c) Fan diagram using the data shown in (b). The inset shows the extrapolation to  $1/B \rightarrow 0$ .

in the fan diagram. Since the  $R_{xy}$  signal is shifted by a phase of  $\pi/2$ , the maxima/minima are corrected by  $n + 1/4$  and  $n + 3/4$ , respectively. By extrapolating to  $1/B \rightarrow 0$  we find an intersection with the abscissa at  $-0.28$  (see inset of Figure 7.4c). This value is at least close to  $-0.5$ , which would be expected for SdH oscillations originating from Dirac fermions (see Section 3.2.4 and Equation 3.31). To further test whether the observed oscillations originate from the topological surface states, their dimensionality has to be determined. Figure 7.5a displays the high field part of the Hall resistance  $R_{xy}$  as a function of the magnetic field  $B$  at  $T = 1.5$  K for a 45 nm thick Bi<sub>2</sub>Te<sub>2</sub>Se platelet on a 50 nm thick hBN sheet. The  $R_{xy}$  signal clearly features SdH oscillations, as highlighted by the first derivative  $dR_{xy}/dB$  (green curve). For 2D electron systems, the formation of LLs depends only on the  $B$ -field component  $B = B \cos(\theta)$  normal to the surface. Accordingly, if the observed quantum oscillations originated from the topological 2D surface states, the maxima/minima of the SdH oscillations should shift by  $1/[B \cos(\theta)]$  upon tilting the sample in the magnetic field  $B$ . In the plot of the amplitude of the SdH oscillations  $\Delta R_{xy} (= R_{xy} - \langle R_{xy} \rangle$ , where  $\langle R_{xy} \rangle$  is a smoothed background) as a function of  $B$  in Figure 7.5b, indeed all curves coincide up to an angle of  $50^\circ$ . To further underscore the 2D character, the inset of Figure 7.5b demonstrates that the dependence of the

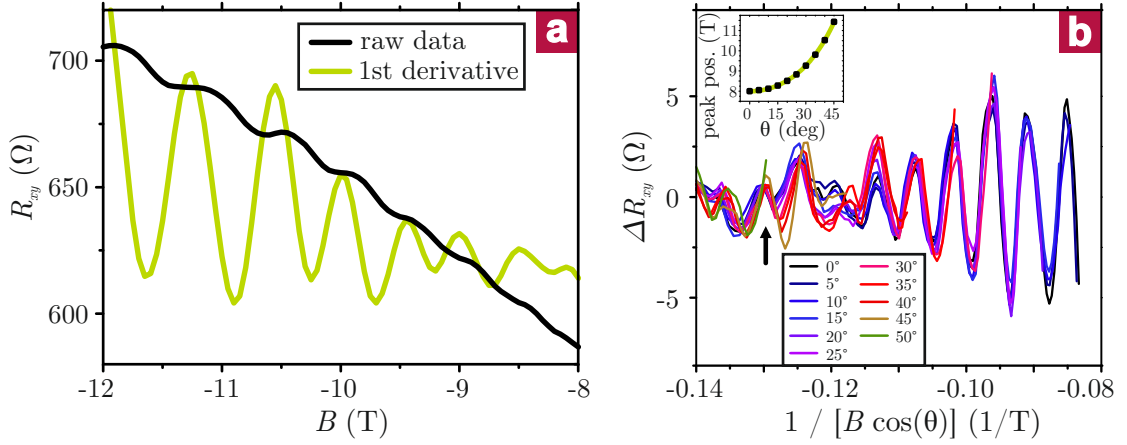


**Figure 7.5: Shubnikov–de Haas oscillations in epitaxially grown nanoplatelets.** (a) High-field Hall resistance (black curve) and its first derivative (green curve) as a function of the magnetic field, featuring pronounced Shubnikov–de–Haas (SdH) oscillations. (b) Amplitude of the SdH oscillations as a function of  $1/[B \cos(\theta)]$  for different tilting angles  $\theta$  (between surface normal and magnetic field). The inset shows the position  $1/B$  of the SdH peak with the LL index  $n = 22$  (arrow) for different angles  $\theta$ , combined with a  $1/\cos(\theta)$  fit (green curve) to the data.

position of the  $n = 22$  peak at  $B = 7.7$  T (for  $\theta = 0^\circ$ ) on the tilting angle  $\theta$  can be smoothly fitted with a  $1/\cos(\theta)$  function.

Having confirmed the 2D nature of the SdH oscillations, we now address the position of the Fermi level in our samples. The Fermi energy can be calculated from

$$E_F = m_{cyc} v_F^2 \quad (7.2)$$

where  $m_{cyc}$  is the cyclotron mass and  $v_F$  is the Fermi velocity. According to the Lifshitz–Kosevich (LK) theory<sup>65</sup> the thermal damping of the SdH oscillations provides a suitable estimate for the cyclotron mass  $m_{cyc}$  (see Equation 3.34). From the plot of  $\Delta R_{xy}$  versus  $1/B$  at different temperatures in Figure 7.6a, the oscillation amplitude is seen to decrease with increasing temperature. Figure 7.6b displays the amplitude of the  $n = 15$  peak at  $B = 11$  T, normalized according to Equation 3.34

$$\frac{\Delta\sigma_{xy}(T)}{\Delta\sigma_{xy}(0)} = \frac{\lambda(T)}{\sinh \lambda(T)}, \quad (7.3)$$

where  $\lambda(T) = 2\pi^2 k_B T m_{cyc} / (\hbar e B)$ . Fitting of the data yields a value of  $m_{cyc}/m_0 = 0.15$ , which agrees well with previous reports on  $\text{Bi}_2\text{Te}_2\text{Se}$  bulk crystals.<sup>28</sup> Furthermore, in order to access the Fermi vector  $k_F$  we plot the position  $1/B$  of the SdH maxima as a function of the LL index  $n$  (see Figure 7.7b below). The LL index is obtained by plotting the SdH maxima as a function of  $n + 1/4$  (since we are using the  $R_{xy}$  signal, see above) and extrapolating to  $1/B \rightarrow 0$  (i.e.,  $B \rightarrow \infty$ ). The intersection with the abscissa defines the first LL. By fitting the data with the Onsager

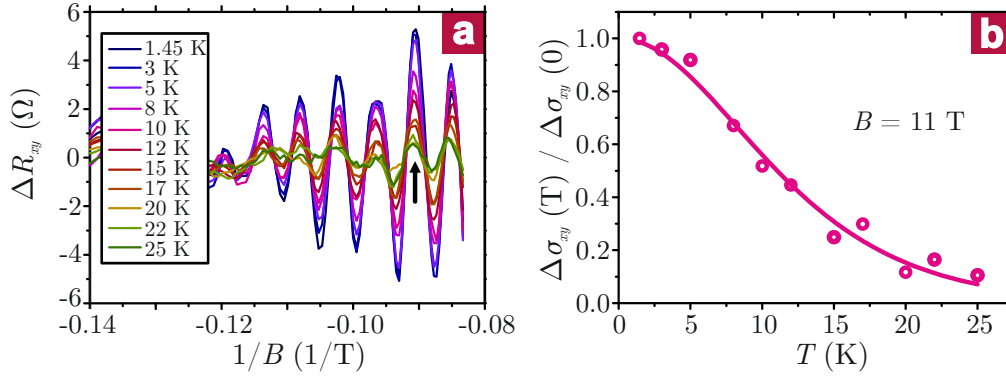


**Figure 7.6: Shubnikov-de Haas oscillations at different temperatures.** (a) Amplitude of the SdH oscillations as a function of  $1/B$  for different temperatures and (b) the normalized amplitude of the SdH maximum with the LL index  $n = 15$  (arrow) as a function of temperature. The data fit (solid line) was obtained using the Lifshitz-Kosevich theory (see Section 3.2.4).

relation (Equation 7.1) and assuming a circular 2D Fermi surface with  $A_F = \pi k_F^2$ , one obtains a value of  $k_F = 0.073 \text{ \AA}^{-1}$ . On this basis, a surface carrier density of  $4.2 \times 10^{16} \text{ m}^{-2}$  is calculated from  $n_s = k_F^2/4\pi$ . This value agrees well with the surface carrier density of  $5.4 \times 10^{16} \text{ m}^{-2}$ , as derived from Hall measurements (see below), thus further supporting the 2D nature of the SdH oscillations.

Toward determining the Fermi energy using Equation 7.2, we assume Dirac fermions with linear dispersion relation and a Fermi velocity of  $v_F = k_F/m_{cyc} = 5.7 \times 10^5 \text{ m/s}$ , which is close to the value of  $v_F = 4.6 \times 10^5 \text{ m/s}$  determined by ARPES.<sup>115</sup> This yields a Fermi energy of  $E_F = 272 \text{ meV}$  above the Dirac point. By comparison, a value of  $E_F = 223 \text{ meV}$  is calculated from  $k_F = 0.073 \text{ \AA}^{-1}$ , as derived from the ARPES-derived band structure.<sup>115</sup> We have furthermore tested the possibility to tune the Fermi level in the samples through the action of a back gate. As can be discerned from Figure 7.7a, which displays the extracted SdH oscillations for different back gate voltages  $V_G$ , the period  $\Delta 1/B$  rises with increasing  $V_G$ . In Figure 7.7b, the peak positions of the SdH oscillations are plotted as a function of the LL index  $n$ . As discussed above, the slopes directly yield values for the Fermi vector  $k_F$  via Equation 7.1. The corresponding  $E_F$  values can then be determined with the aid of the ARPES-derived band structure of Bi<sub>2</sub>Te<sub>2</sub>Se, see Figure 7.7c.<sup>115</sup> In this manner, the error associated with the assumptions made to calculate the cyclotron mass can be avoided. For comparison, Figure 7.7c also includes the  $E_F$  values derived from the cyclotron mass. The sketch in Figure 7.7d evidences that  $E_F$  (of the bottom surface which is influenced by the back gate, see arguments below) can be shifted by approximately 160 meV through the back gate voltage. Similar Fermi level shifts have been attained in case of considerably thicker hBN sheets ( $\approx 200 \text{ nm}$ ), which is in accordance with the following estimation: In a simple capacitor model, the charge carrier density  $n(V_G)$  induced at the interface between TI and gate dielectric by applying a gate voltage  $V_G$  can be written as

$$n(V_G) = \frac{\epsilon_0 \epsilon_d}{t \cdot e} V_G, \quad (7.4)$$

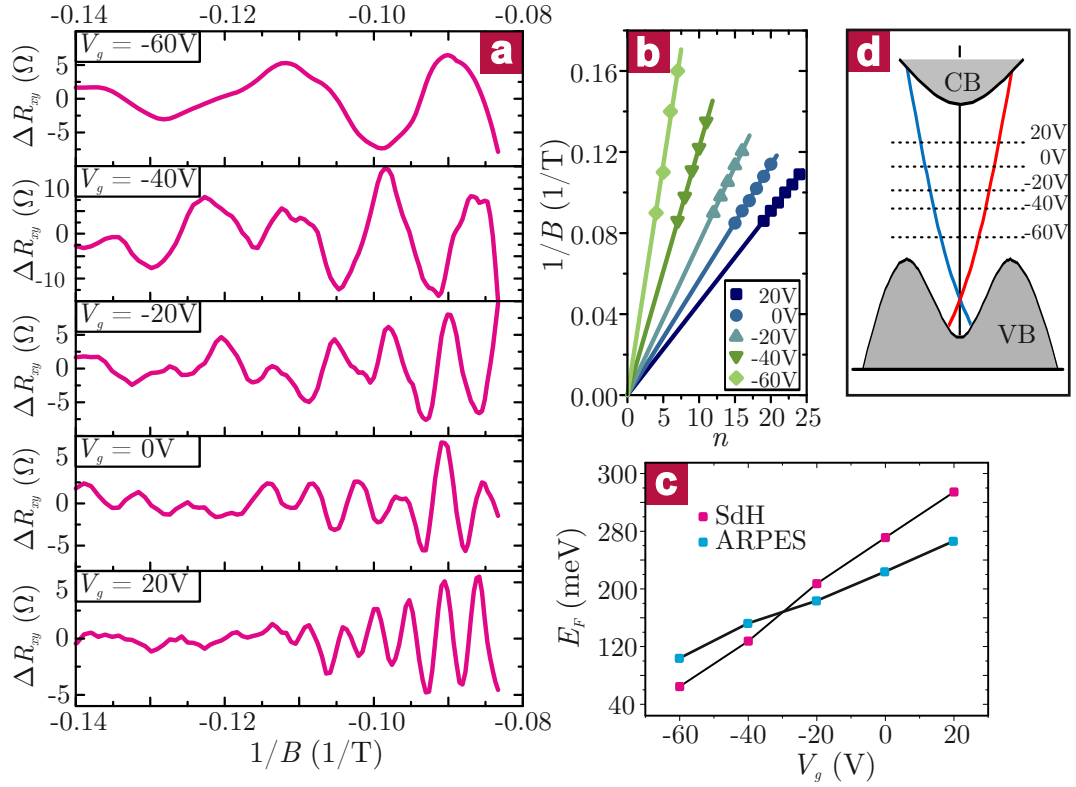


**Figure 7.7: Gate-dependent Shubnikov-de Haas oscillations.** (a) Amplitude of the SdH oscillations as a function of  $1/B$  for different back gate voltages. (b) Plot of position  $1/B$  of the SdH maxima versus LL index for different gate voltages. The data fits (solid lines) were performed using Equation 7.1. (c) Comparison of the Fermi energy in  $\text{Bi}_2\text{Te}_2\text{Se}$  nanoplatelets, calculated from the cyclotron mass obtained by SdH analysis (pink rectangles), and from the ARPES-derived band structure (blue rectangles). (d) Sketch of the position of the Fermi level of the bottom surface in the  $\text{Bi}_2\text{Te}_2\text{Se}$  samples for different back gate voltages.

where  $\epsilon_0$  is the vacuum permittivity,  $e$  is the elementary charge, and  $\epsilon_d$  and  $t$  are the dielectric constant and the thickness of the dielectric, respectively. Assuming a linear dispersion relation for the surface states, the Fermi energy can be calculated from

$$E_F(k_F) = \hbar v_F k_F, \quad (7.5)$$

where  $v_F$  is the Fermi velocity and  $k_F$  is the Fermi wave vector. For a circular Fermi surface,  $k_F$  is related to the 2D surface carrier density  $n_s$  (per spin) via  $k_F = 2\sqrt{\pi n_s}$ . Based on these equations, the gate-induced Fermi level shift is given by  $E_F(V_G) \propto \sqrt{\frac{\epsilon_d}{t}} V_G$ . While the dielectric constants of  $\text{SiO}_2$  and hBN are similar,<sup>125</sup> the gate effect depends on the total thickness of the dielectric. By using a 200 nm thick hBN substrate instead of a 50 nm thick one, the gate efficiency is only changing by a factor of 0.84, which explains the efficient gating of  $\text{Bi}_2\text{Te}_2\text{Se}$  nanoplatelets grown on relatively thick hBN sheets.

The application of a gate voltage is expected to cause bending of the bands at the interface

between dielectric (hBN) and semiconductor (Bi<sub>2</sub>Te<sub>2</sub>Se), and thereby to create a depletion layer. The thickness of the latter, which corresponds to the penetration depth of the electric field in the semiconductor, is of the order of only 10 nm.<sup>19</sup> Accordingly, the bulk and the top surface of the platelet should be only little affected by gating.

The fact that the SdH oscillations display only a single period for all gate voltages (see Figure 7.7), points toward the contribution of only one surface state. A similar conclusion has been drawn from the magnetotransport behavior of Bi<sub>2</sub>Te<sub>2</sub>Se nanoplatelets on Si/SiO<sub>x</sub> (see Chapter 6).<sup>70</sup> We attribute this finding to a deterioration of the surface state at the top surface due to long exposure to air, an explanation which is in accordance with previous charge transport studies on Bi<sub>2</sub>Se<sub>3</sub>.<sup>14, 118</sup>

Evaluation of the SdH oscillations also enables the determination of the carrier mobility (see

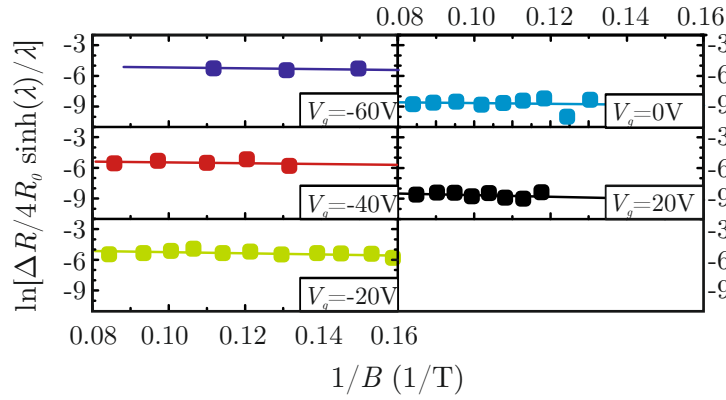


**Figure 7.8: Dingle plots for different gate voltages.** Straight lines are linear fits to the data using Equation 3.33.

Section 3.2.4). The amplitude of the SdH oscillations is given by Equation 3.29. By a Dingle plot (Equation 3.33) of  $\ln \left[ \frac{\Delta R_{max/min}}{4R_0} \left( \frac{\sinh \lambda}{\lambda} \right) \right]$  versus  $1/B$  (see Figure 7.8), where  $\Delta R_{max/min}$  is the amplitude of the maxima/minima of the SdH oscillations, the transport lifetime  $\tau$  can be extracted from a linear data fit. This in turn yields the mean-free path  $l_e = v_F \tau$  and the mobility  $\mu = \frac{ev_F \tau}{\hbar k_F}$ .

To further explore the gate effect in our devices, we performed low temperature Hall measurements at different back gate voltages. Figure 7.9a presents such data for the sample discussed above (see also Appendix B for Hall data of a different device). Consistent with the n-doped character of our samples,<sup>28, 121, 122</sup> all curves show negative slopes up to the highest negative gate voltages. Another notable feature is the pronounced non-linearity of the curves, which can be explained by the contribution of two types of charge carriers to the total electrical transport. Assuming parallel conduction of bulk electrons (described by a bulk carrier density  $n_b$  and a bulk mobility  $\mu_b$ ) and bottom-surface electrons (described by  $n_s$  and  $\mu_s$ ), a two band model<sup>28</sup> can be used to fit the Hall data according to

$$\rho_{xy} = \frac{(R_s \rho_b^2 + R_b \rho_s^2) B + R_s R_b (R_s + R_b) B^3}{(\rho_s + \rho_b)^2 + (R_s + R_b)^2 B^2}, \quad (7.6)$$

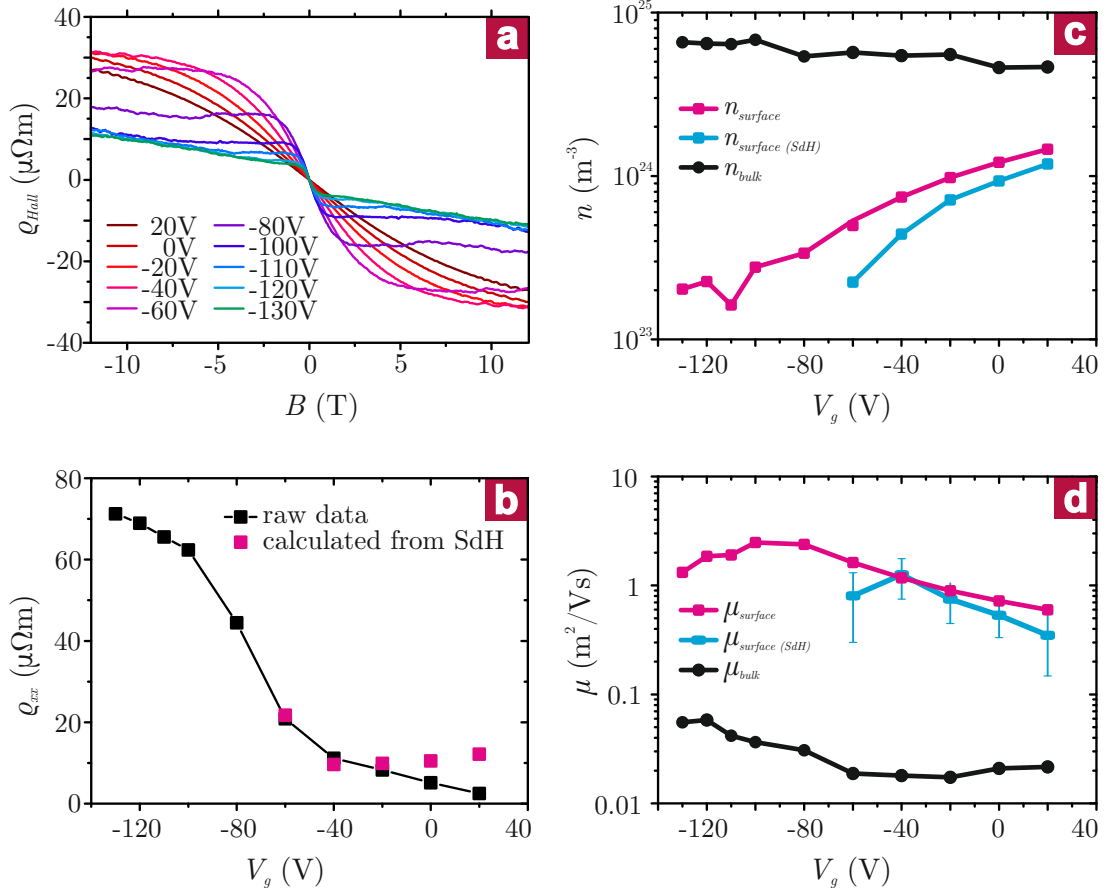


**Figure 7.9: Hall measurements of epitaxially grown  $\text{Bi}_2\text{Te}_2\text{Se}$  films on hBN.** (a) Hall resistivity as a function of  $B$ -field for different back gate voltages ( $T = 1.5$  K). (b) Comparison of the bulk- (black curve) and surface- (pink curve) carrier density for different gate voltages, as obtained by fitting the data in panel (a) using the two-band model. The blue curve corresponds to the surface carrier density derived by analysis of the SdH oscillations. (c) Plot of the measured resistivity  $\rho_{xx}$  as a function of gate voltage. For comparison, resistance values calculated from the SdH oscillations are shown. (d) Comparison of the bulk- (black) and surface state- (pink) mobility for different gate voltages, as obtained using the two-band model for fitting. The blue points are the values obtained by the Dingle analysis.

where  $R_s$ ,  $R_b$  are the Hall constants of the surface/bulk, and  $\rho_s$ ,  $\rho_b$ , is the surface/bulk resistivity. The four fitting parameters contained in this equation can be reduced to three<sup>126</sup> by using  $\rho_s = \rho_b \rho_{xx} / (\rho_b - \rho_{xx})$ , with  $\rho_{xx} = R_{sheet} d$ , where  $d$  is the thickness of the sample and  $R_{sheet}$  is the sheet resistance measured separately (see Figure 7.9b). The fitting results are shown in Figure 7.9c and d in dependence of gate voltage. As apparent from Figure 7.9c, the surface carrier density  $n_s$  is decreasing with increasingly negative gate voltage, a trend consistent with the above described downshift of the Fermi level. Comparison with the corresponding values obtained from the SdH analysis reveals a very good agreement, thereby consolidating the surface nature of the oscillations at different gate voltages. In contrast to the surface carriers,

the bulk carrier density remains almost unaffected over the complete voltage range. This behavior can again be explained by assuming that the gating is effective only for the bottom surface of the Bi<sub>2</sub>Te<sub>2</sub>Se sheet. Accordingly, the bulk of the platelet should be only little affected by gating, while the surface carrier density at the bottom increases by roughly one order of magnitude upon applying the highest negative gate voltage.

The reason why despite the high bulk carrier density of almost  $10^{25} \text{ m}^{-3}$  the bulk is not dominating the total transport can be gleaned from Figure 7.9d, which shows that the mobility of the topological surface state is one to two orders of magnitude higher than the bulk value over the entire gate voltage range. The Hall mobilities agree well (within a factor of 2) with the values extracted from the SdH oscillations for  $-60 \text{ V} < V_g < 20 \text{ V}$  (see Figure 7.9d).<sup>ii</sup>

To further test the reliability of the latter values, we calculated the sample resistivity from  $\rho_{xx} \approx (\sigma_{xx})^{-1} = e(n_s^{SdH}\mu_s^{SdH} + n_b\mu_b)^{-1}$ , where  $n_s^{SdH}$  and  $\mu_s^{SdH}$  are the surface carrier density and mobility derived from the SdH analysis, respectively, and  $n_b$  and  $\mu_b$  are the corresponding values for the bulk, as obtained from the Hall data. In Figure 7.9b, thus gained resistivity is compared to  $\rho_{xx}$  measured at different gate voltages.

Figure 7.9d furthermore evidences that upon lowering the electron density the surface carrier mobility first increases, and then decreases again. One reasonable explanation for the initial increase involves reduced electron–electron interaction at lower electron concentration. The relevance of such interaction has been documented recently.<sup>112,127</sup> If we assume, that for highly negative gate voltages (low electron density) electron–electron interaction dominates the total scattering of electrons, then the scattering rate is expected to be proportional to the square-root of the electron density, according to  $\frac{1}{\tau_{e-e}} \propto \sqrt{n_s}$  (electron–electron Coulomb scattering in 2D systems).<sup>128</sup> In conjunction with  $\mu = \frac{e\tau}{m_{eff}}$ , where the effective mass  $m_{eff}$  to a first approximation is independent of the carrier density, it follows that the surface mobility  $\mu_s$  should be proportional to  $1/\sqrt{n_s}$ . In order to test this hypothesis, we plot  $1/\sqrt{n_s}$  versus the surface state mobility  $\mu_s$  (see Figure 7.10a). The good quality of the line fit proves the validity of this model for electron densities above  $1.5 \times 10^{16} \text{ m}^{-2}$ . The subsequent decrease of mobility at lower electron densities may originate from the opening of a new scattering channel from the surface states into the bulk VB when the Fermi level position approaches the valence band (VB) edge, which in Bi<sub>2</sub>Te<sub>2</sub>Se is located above the Dirac point.<sup>115</sup> A similar model has recently been used to account for scattering effects in scanning tunneling microscopy (STM) on Bi<sub>2</sub>Se<sub>3</sub>.<sup>16</sup> To consolidate this assertion, we calculate the Fermi energy for different surface carrier densities by using the equations  $n_s = k_F^2/(4\pi)$  and  $E_F = m_{cyc}v_F^2$  (with  $v_F = \hbar k_F/m_{cyc}$  and  $m_{cyc} = 0.15m_0$ ), and plot the surface mobility as a function of the Fermi energy, as depicted in Figure 7.10b together with a sketch of the band structure of Bi<sub>2</sub>Te<sub>2</sub>Se. The arrow in the band diagram indicates a scattering event from the surface states into the bulk VB. Alternatively, such scattering may occur into an acceptor band, which has been reported to

<sup>ii</sup>The mobility obtained from SdH analysis is approximately two times smaller than the Hall mobilities. This difference originates from the fact that  $\tau$  obtained from the Dingle analysis reflects scattering events in all directions, with backscattering as the dominant contribution. However, as in topological insulators backscattering is prohibited,  $\tau$  will be underestimated.<sup>28</sup> It should be noted that the Dingle analysis becomes more and more difficult for higher negative gate voltages due to the limited number of maxima/minima in this regime. This leads to considerable error bars in Figure 7.8.

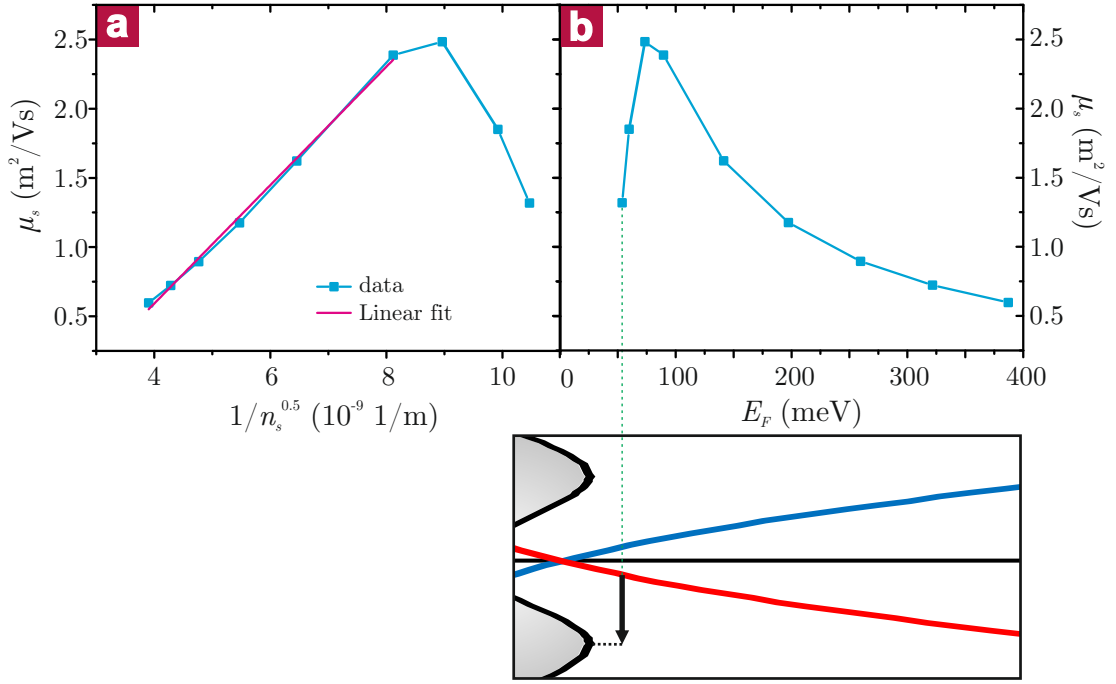


**Figure 7.10: Models to describe the change in mobility.** (a) Surface mobility as a function of the surface carrier density. The linear fit (pink line) confirms the assumed electron–electron scattering mechanism, as discussed in the text. (b) Surface mobility as a function of the Fermi energy (with respect to the Dirac point).

be about 33 meV above the VB edge.<sup>28</sup> A fully quantitative analysis would require detailed knowledge of the energy dispersion and transition probabilities, which is, however, difficult to achieve.

The question why SdH oscillations are observable in nanoflakes epitaxially grown on hBN, whereas the same flakes grown on normal Si/SiO<sub>x</sub> substrates do not show this effect, can be resolved by comparing the obtained mobility values. For the Bi<sub>2</sub>Te<sub>2</sub>Se on hBN sample discussed above, very high surface state carrier mobilities in the range of 8000 to 20000 cm<sup>2</sup>/Vs were found, most likely owing to the reduced defect density in the films grown by van der Waals epitaxy. This assertion gains support by comparing Bi<sub>2</sub>Te<sub>2</sub>Se thin films grown on hBN or Si/SiO<sub>x</sub> substrates (see Chapter 6). Specifically, an average surface state mobility of 4900 cm<sup>2</sup>/Vs was observed on hBN, approximately three times larger than the value of 1600 cm<sup>2</sup>/Vs obtained in case of the Si/SiO<sub>x</sub> substrates.

## 7.4 Summary

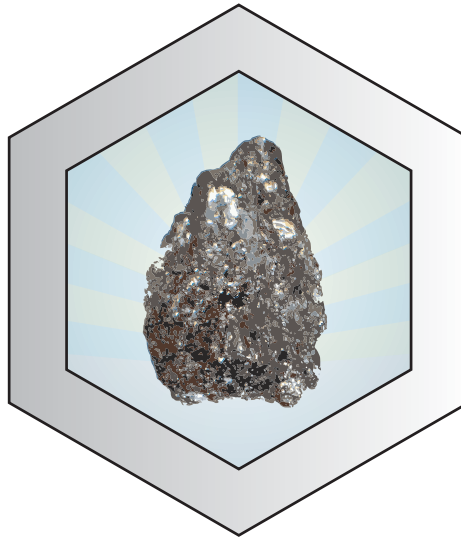
In summary, we have successfully grown the topological insulator Bi<sub>2</sub>Te<sub>2</sub>S on hBN in an oriented manner by van der Waals epitaxy. Thus obtained thin films show enhanced surface mobilities, which enable the study of gate-dependent quantum oscillations for the first time in this material. The unique combination of high mobility surface charge transport with an

## **Chapter 7. Growth of High-Mobility $\text{Bi}_2\text{Te}_2\text{Se}$ Nanoplatelets on hBN Sheets by van der Waals Epitaxy**

---

efficient tunability of the Fermi level provides a suitable basis for studying novel, spin-related charge transport phenomena in such devices.

## 8 Kawazulite: A natural Topological Insulator



The earth's crust and outer space are rich sources of technologically relevant materials which have found application in a wide range of fields. Well-established examples are diamond, one of the hardest known materials, or graphite as a suitable precursor of graphene. The ongoing drive to discover novel materials useful for (opto)electronic applications has recently drawn strong attention to topological insulators. Here, we report that Kawazulite, a mineral with the approximate composition  $\text{Bi}_2(\text{Te,Se})_2(\text{Se,S})$ , represents a naturally occurring topological insulator whose electronic properties compete well with those of its synthetic counterparts. Kawazulite flakes with a thickness of a few tens of nanometers were prepared by mechanical exfoliation. They exhibit a low intrinsic bulk doping level and a sizable mobility of surface state carriers of more than  $1000 \text{ cm}^2/\text{Vs}$  at low temperature. Based on these findings, further minerals which due to their minimized defect densities display even better electronic characteristics may be identified in the future.

### 8.1 Introduction

The extraordinary properties and architecture of naturally occurring compounds have inspired the synthesis of numerous biomimetic materials, a field that has attracted tremendous interest in the past few years.<sup>129</sup> Nature's ability to serve as a valuable blueprint for modern synthetic compounds is owed to the fact that it houses a wide variety of materials which have been forged over geological periods of time under extreme conditions that are difficult to simulate in the laboratory. Many of these naturally occurring materials are finding use in fields like optics, electronics, mechanics, or materials science. A most intriguing example is diamond, which is formed in the lithosphere at considerable depth, supplying the required high pressure and temperature.<sup>130</sup> Furthermore, quasi-crystals, of which the discovery was awarded by the Nobel Prize in 2011,<sup>131</sup> were very recently found in sky-fallen meteorites,<sup>132</sup> although they were hitherto believed to be only synthetically accessible. A further notable natural compound is graphite as a source for graphene, the thinnest atomic sheet isolated to date.<sup>133</sup> Owing to its linear energy dispersion relation at low carrier energies, graphene has emerged as one of the most promising components of future electronic devices. In this chapter we demonstrate that it is also possible to find another interesting class of materials closely related to graphene in nature, i.e., natural topological insulators.

Quartz veins, which have a long history in gold mining, represent a promising location to encounter TIs in nature. In fact, chalcogenides have been shaped in such veins over billions of years via hydrothermal deposition at high temperatures ( $> 300\text{ }^{\circ}\text{C}$ ).<sup>134</sup> Some of these compounds contain heavy elements like bismuth or antimony which are a necessary ingredient for the strong spin-orbit coupling (SOC) operative in TIs. One prospective candidate is Kawazulite, a metallic gray mineral with the general chemical composition  $\text{Bi}_2(\text{Te,Se})_2(\text{Se,S})$ , which is named after the Kawazu mine in Japan, where it was first discovered. It belongs to the Tetradymite group (rhombohedral, space group  $R\bar{3}m$ ) featuring a crystal structure composed of quintuple layers  $(\text{VI}^{(1)}-\text{V}-\text{VI}^{(2)}-\text{V}-\text{VI}^{(1)})$ , where  $\text{VI} = (\text{Se, Te, S})$  and  $\text{V} = \text{Bi}$  that are held together through van der Waals bonds. Its crystal structure was first reported by Bland and Basinski in 1961.<sup>135</sup>

### 8.2 Sample characterization

The samples investigated in this work originate from a former gold mine in Jílové u Prahy, Czech Republic. Figure 8.1a shows an optical micrograph of one of the investigated specimens (purchased from Mineralienkontor, Germany), comprising Kawazulite crystals as metallic-like inclusions in a quartz matrix. Chemical analysis of mechanically extracted, tiny Kawazulite pieces by inductively coupled plasma mass spectrometry (ICP) revealed a composition of  $(\text{Bi}_{2.12}\text{Sb}_{0.06})\text{Te}_2(\text{Se}_{0.14}\text{S}_{0.32})$ . Besides these major elements, fourteen additional trace elements could be identified (see Table 8.1).<sup>i</sup> Powder diffractometry (see Figure 8.1b) indicated that

---

<sup>i</sup>For supporting XPS data, see Appendix C.

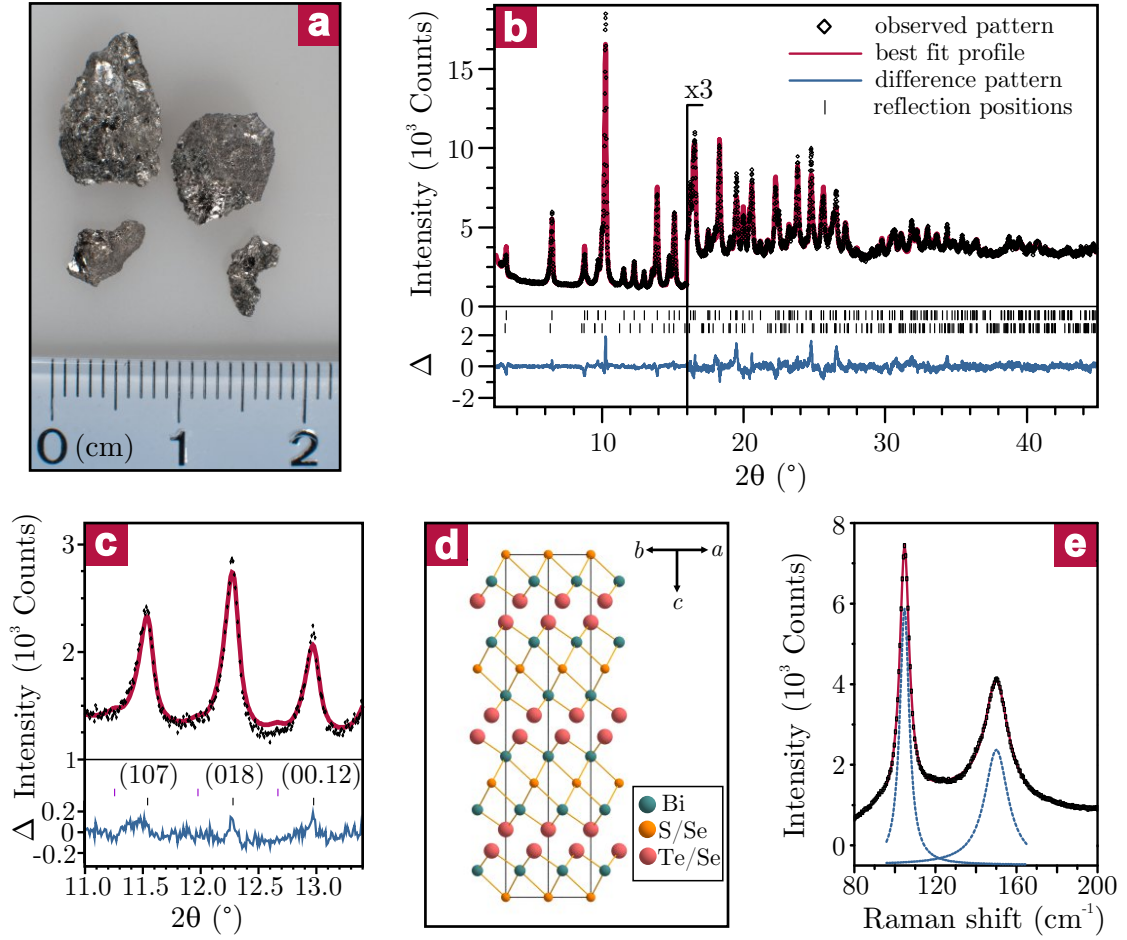


**Figure 8.1: X-ray and Raman characterization of Kawazulite.** (a) Optical micrograph of the investigated specimens with a size between 3 and 10 mm. (b) Rietveld plots for the two Kawazulite phases. (c) Magnified plot of the X-ray diffraction (XRD) data within the range of 11° to 13.4°. (d) Sketch of the unit cell of the mineral, as derived from the XRD analysis. (e) Raman spectrum recorded from a Kawazulite crystallite ( $\lambda_{exc} = 633$  nm). The two blue lines are Lorentzian fits, while the red line corresponds to the total fit.

the Kawazulite is composed of two different crystalline phases, which both crystallize in rhombohedral ( $3\bar{R}m$ ) structure and exhibit slightly different lattice constants (see Appendix C for details). While the major phase (89.6 wt %) is characterized by the lattice parameters  $a = 4.25$  Å and  $c = 29.70$  Å (Se rich), with a stoichiometry of  $\text{Bi}_2(\text{Se}_{0.2}\text{S}_{0.74})(\text{Te}_{0.61}\text{Se}_{0.39})_2$ , values of  $a = 4.37$  Å and  $c = 30.42$  Å (Te rich) and a stoichiometry of  $\text{Bi}_2(\text{Se}_{0.59}\text{Te}_{0.41})\text{Te}_2$  were found for the minor phase (10.4 wt %). These lattice parameters are smaller than for  $\text{Bi}_2\text{Te}_3$ , consistent with the fact that S and Se atoms are smaller than Te. Moreover, the observation of (107) and (00.12) peaks (see Figure 8.1c) testifies a sizable extent of chalcogen ordering and correspondingly the presence of an ordered layer structure<sup>136</sup> (see sketch of the unit cell in Figure 8.1d). In addition to the two Kawazulite phases, some spectra also contain

**Table 8.1:** List of the trace elements determined by semi-quantitative ICP analysis.

Element	wt %	Element	wt %	Element	wt %
Al	1.28	Cr	0.02	Ni	0.05
As	0.73	Cu	0.02	Ti	0.02
Au	0.11	Fe	0.23	Zn	0.01
Ba	0.01	Mg	0.58	Zr	0.04
Co	0.12	Na	0.18		

peaks originating from the surrounding matrix of the mineral, which could be identified as Clinocllore ( $\text{Mg,Fe,Al})_6(\text{Si,Al})_4\text{O}_{10}(\text{OH})_8$  (in good agreement with the determined elemental composition, see Table 8.1).

The layered structure of the Kawazulite is confirmed by its Raman spectrum, which displays two pronounced peaks located at  $105\text{ cm}^{-1}$  and  $151\text{ cm}^{-1}$  (Figure 8.1e). Similar to the layered chalcogenides  $\text{Bi}_2\text{Se}_3$ ,  $\text{Bi}_2\text{Te}_3$ ,  $\text{Sb}_2\text{Te}_3$ , and their alloys, these two peaks can be assigned to the  $E_g^2$  and the  $A_{1g}^2$  peak, respectively, which originate from the opposite phase motion of the outer V and VI<sup>(1)</sup> atoms of the quintuple layers. Based upon the dependence of the  $E_g^2$  peak position on the chemical composition of the alloys,<sup>108</sup> it can be concluded that the Kawazulite comprises a Te-rich  $\text{Bi}_2(\text{Te}_{1-x}\text{Se}_x)_3$  matrix, with a Se content  $x < 0.6$ . Further clues regarding the composition derive from the absence of a split of the  $A_{1g}^2$  peak. Replacing the heavy Te atoms by Se atoms is documented to shift this peak from  $134\text{ cm}^{-1}$  in pure  $\text{Bi}_2\text{Te}_3$  to higher energy, with a split into two components at  $139\text{ cm}^{-1}$  and  $150\text{ cm}^{-1}$  upon reaching  $\text{Bi}_2\text{Te}_2\text{Se}$  stoichiometry.<sup>108</sup> It hence follows that the Se concentration in Kawazulite is slightly below  $x = 1/3$ . The quite high energy of the  $A_{1g}^2$  peak ( $151\text{ cm}^{-1}$ ) can be explained by the Sb content of the sample, in close correspondence to the up-shift detected upon replacing the heavy Bi atoms in  $\text{Bi}_2\text{Te}_3$  by lighter Sb atoms.<sup>108</sup>

The electronic structure of the (111)-surface near the  $\Gamma$ -point ( $k_{\parallel} = 0$ ), determined by angle-

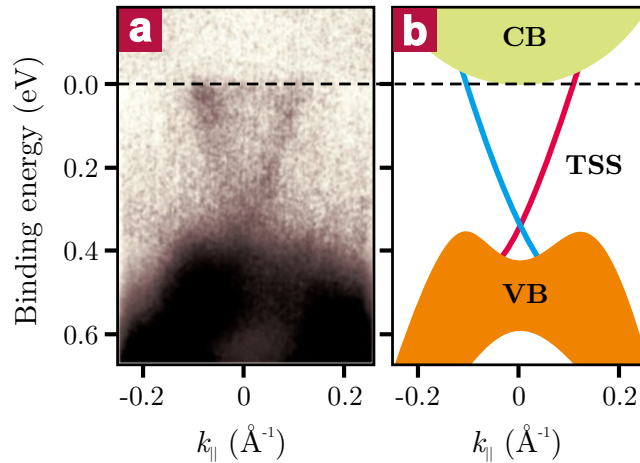


**Figure 8.2: ARPES of Kawazulite.** Raw data (a) and sketch of the electronic band structure derived from the measurement (b).

resolved photoemission spectroscopy (ARPES) of a tiny ( $0.7 \times 0.7 \text{ mm}^2$ ) Kawazulite crystal, is displayed in Figure 8.2a. A surface state with the typical Dirac-like conical dispersion can be seen in the center, which verifies the natural Kawazulite to be a TI. In Figure 8.2b, the corresponding electronic band structure is schematically illustrated. The general dispersion closely resembles that of the thoroughly investigated Bi chalcogenide family.<sup>11,42,83,137–139</sup> While the area of enhanced intensity above a binding energy of 0.4 eV can be attributed to the bulk valence band, the bulk conduction band is difficult to discern near the Fermi level presumably due to a suppression of the spectral intensity through matrix element effects or sample/surface quality. If the Fermi level actually resides within the occupied states, comparison with similar compounds suggests that it is less than 0.1 eV away from the band edge.<sup>138,139</sup> In any case, it can be concluded that the size of the band gap is at least 0.25 eV if the conduction band is slightly occupied, or above 0.35 eV assuming that it is completely unoccupied. The latter value exceeds the band gap reported for pure  $\text{Bi}_2\text{Te}_3$ ,<sup>138</sup> which may be explained by the higher electronegativity of sulfur vs. tellurium.<sup>139</sup>

The appreciable sulfur content of the Kawazulite is remarkable in view of the finding that the replacement of Se by S atoms in  $\text{TlBi}(\text{S}_{1-x}\text{Se}_x)_2$  weakens the spin–orbit interaction in these compounds, which causes a topological quantum phase transition from a topological state (Se rich) to a trivial insulating state (S rich).<sup>137</sup> In the topological insulators  $\text{Bi}_2\text{X}_3$  ( $X = \text{Se}, \text{Te}$ ), a similar transition takes place, which is, however, coupled to a structural phase transition. For increasing sulfur content in  $\text{Bi}_2\text{Se}_3$  a change from rhombohedral  $R\bar{3}m$  (Se rich) to orthorhombic crystal structure  $Pnma$  (S rich) occurs, resulting in a trivial band insulator with a large gap.<sup>138</sup> In  $\text{Bi}_2(\text{Te}_{1-y}\text{S}_y)_3$ , by contrast, the heavier Te stabilizes the rhombohedral structure up to high sulfur contents of  $y = 0.5$ .<sup>138</sup> As natural Kawazulite contains a sizable amount of Te, a similar stabilization can be expected, consistent with the rhombohedral crystal structure revealed by XRD analysis.

Evaluation of the ARPES data yields a Fermi vector of  $k_F = 0.091 \pm 0.002 \text{ \AA}^{-1}$ , a Fermi velocity of  $v_F = 8.63 \times 10^5 \text{ m/s}$ , and (by assuming a circular Fermi surface) a surface electron density of  $n_s = k_F^2/4\pi = 6.45 \times 10^{16} \text{ m}^{-2}$ .

### 8.3 Electrical transport measurements

Furthermore, we determined the electrical conductivity of individual thin Kawazulite flakes prepared by micromechanical cleavage of the extracted crystals (see inset of Figure 8.3a for an optical image of a typical device in Hall bar configuration, or Figure 8.3b for an AFM image of a ribbon-like device). Thus obtained microflakes (see TEM image in Figure 8.3c) exhibit the bulk crystal structure, as evidenced by the selected area diffraction (SAD) data in Figure 8.3d. From the SAD pattern, it furthermore follows that they reproducibly comprise (111) crystal faces which are oriented parallel to the substrate surface. In Figure 8.3a, the Hall resistance of a 12 nm thick flake is plotted as a function of the applied  $B$ -field. From low temperature ( $T = 1.5 \text{ K}$ ) Hall measurements on a range of different flakes, a Hall mobility between 300 and  $1300 \text{ cm}^2/\text{Vs}$ , and an average electron density of  $n = 1 \times 10^{17} \text{ m}^{-2}$  (normalized by the

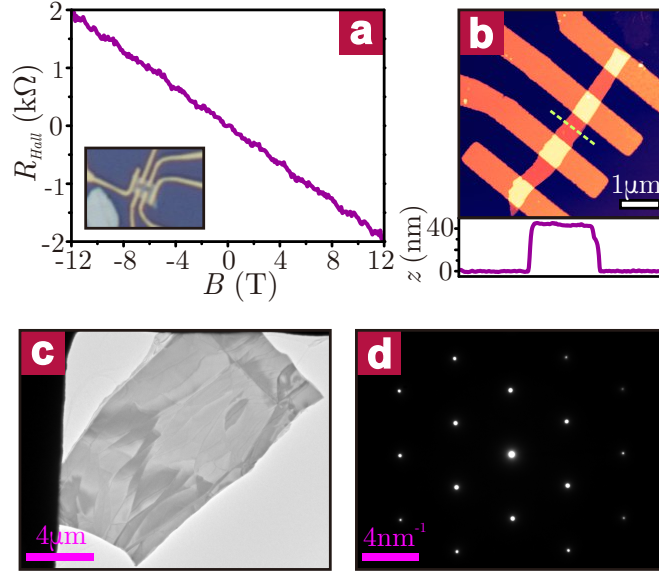


**Figure 8.3: Hall and TEM measurements on Kawazulite flakes.** (a) Hall data gained from the device shown in the inset (optical micrograph). (b) Atomic force microscopy image of the device discussed in the main text. The height profile is taken along the dashed line. (c) TEM image and (d) SAD pattern of a typical microflake.

sample thickness) could be derived (see Table 8.2 for details). The latter density is only slightly

**Table 8.2:** Sheet thickness, sheet resistance, carrier density and mobility values for several devices.

Sample-#	$d$ (nm)	$R_s$ ( $\Omega$ )	$n$ ( $\text{m}^{-2}$ )	$\mu$ ( $\text{cm}^2 / (\text{Vs})$ )
1	7	–	$1.72 \times 10^{17}$	–
2	70	1277	$1.88 \times 10^{17}$	260
3	17	2437	$1.24 \times 10^{17}$	393
4	17	2013	$1.81 \times 10^{17}$	270
5	12	2047	$3.80 \times 10^{16}$	1272
6	46	3641	$5.20 \times 10^{16}$	934

higher than the value gained from the ARPES data, indicative of a dominant contribution of the surface state to the total charge transport. To further consolidate this assertion, we evaluated the low-temperature magnetoresistance of the samples at different tilting angles  $\theta$ . As apparent from Figure 8.4a, where data gained from the device in Figure 8.3b are shown, there emerges a pronounced weak anti-localization (WAL) peak in the sheet conductance  $\Delta\sigma = \sigma(B) - \sigma(B = 0)$  (see Section 3.3.2). When  $\Delta\sigma$  is plotted in dependence of  $B \cos(\theta)$ , that is, the  $B$ -field component normal to the surface, all curves coincide (see Figure 8.4b), signifying the 2D character of the effect.<sup>69</sup> In addition, the low-field magnetoconductance data can be well-fitted by the Hikami–Larkin–Nagaoka (HLN) model for 2D localization, according to Equation 3.41. By fitting the low-field magnetoconductance of the above sample at different

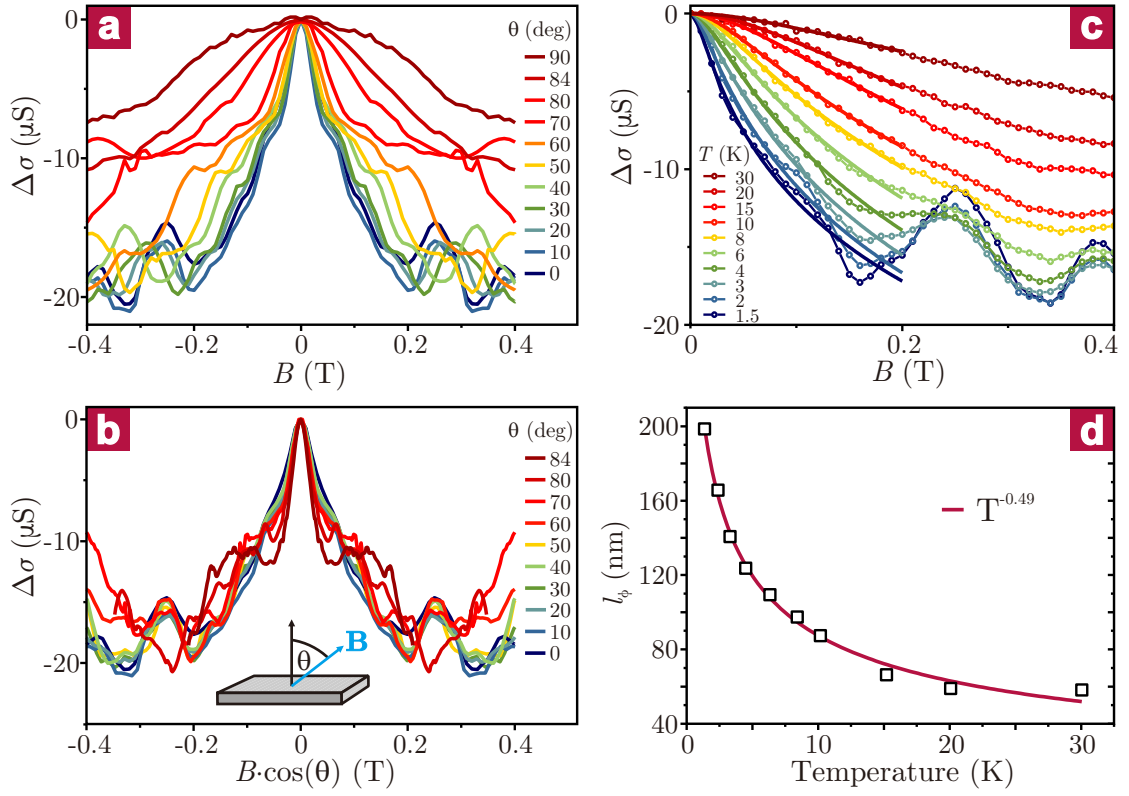


**Figure 8.4: Weak anti-localization in Kawazulite.** (a) Low  $B$ -field range of the magnetoconductance recorded at tilting angles  $\theta$ . (b) The same data shown in panel (a), after normalization to the  $B$ -field component normal to the surface. (c) Low field magnetoconductance data at different temperatures. The solid lines in the range  $0 < B < 0.2$  T represent data fits obtained by the HLN equation. (d) Temperature dependence of the phase coherence length extracted from the fits in panel (c). The curve fit (red line) indicates scaling of the phase coherence length with  $T^{-0.49}$ .

temperatures (see Figure 8.4c), a phase coherence length of 200 nm at 1.5 K and 60 nm at 30 K was obtained. In addition, the fits yielded an average value of  $\alpha = -0.92$ , which suggests electrical transport through two decoupled surface channels, that is, the top and bottom surface with comparable phase coherence length. As apparent from Figure 8.4d, the phase coherence length displays a pronounced decrease with increasing temperature, which is attributable to enhanced electron–phonon and electron–electron interactions.<sup>140</sup> Assuming that electron–electron scattering is the dominant mechanism, we fit the data by a simple power law, where  $l_\phi$  is proportional to  $T^{-1/2}$  for a 2D system, and  $T^{-2/3}$  in the 3D case.<sup>74</sup> From such a fit, we obtain an exponent very close to  $-1/2$ , thus further corroborating the 2D nature of the WAL in the present samples.

Another intriguing observation is the emergence of pronounced universal conductance fluctuations (UCF) in the magnetoconductance curves (see Section 3.4.2), as exemplified in Figure

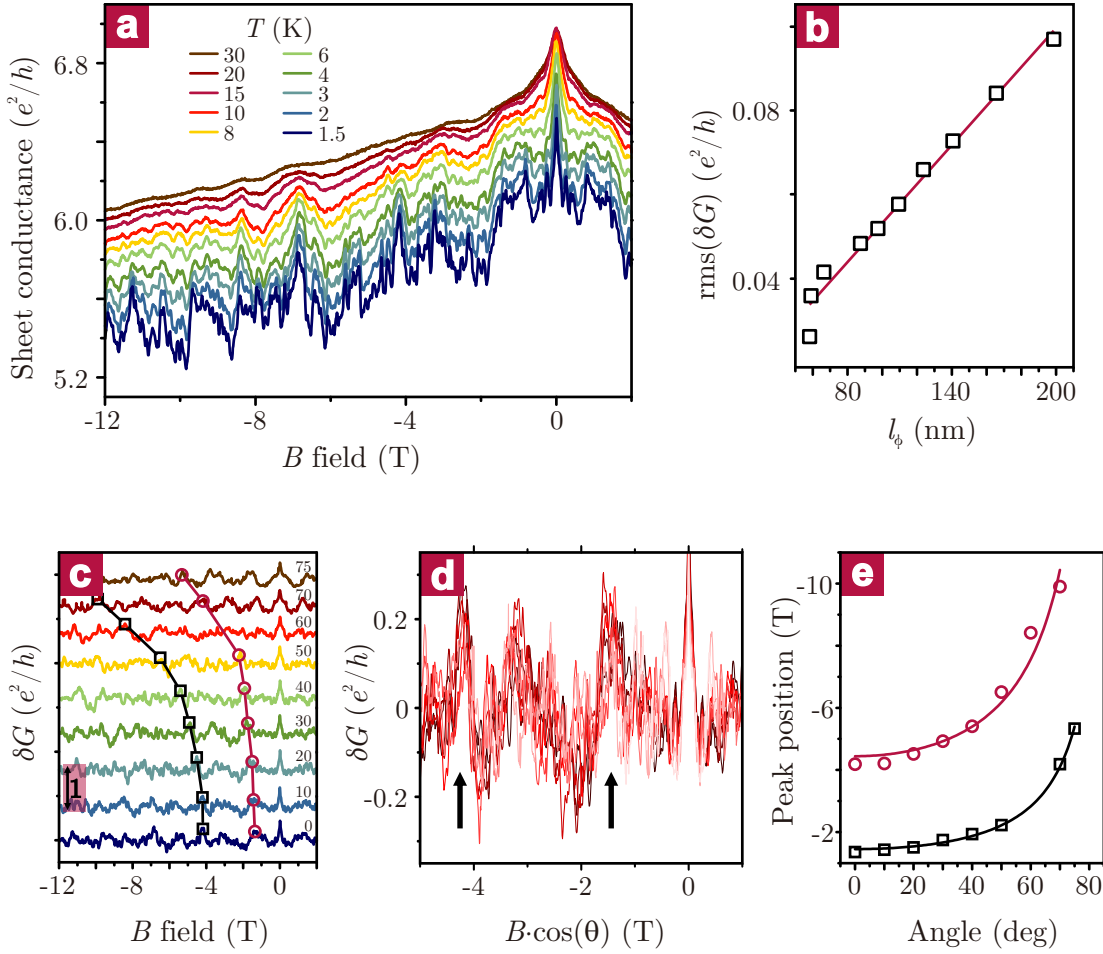


**Figure 8.5: Universal conductance fluctuations in Kawazulite.** (a) Magnetoconductance recorded at different temperatures. (b) Root-mean-square of the UCF as a function of the phase coherence length calculated from the WAL fits (see Figure 8.4). The red line is a linear fit to the data. (c) UCF at different angles. The squares/circles mark the  $B$ -field position of the two characteristic features (marked with arrows in (d)) of the UCF at different angles. (d) UCF as a function of the  $B$ -field component normal to the sample surface. (e)  $B$ -field position of the two characteristic features of the UCF in dependence of the tilting angle of the sample. The solid lines are  $(1/\cos\theta)$  fits to the data.

8.5a. These oscillations are non-periodic, but perfectly reproducible and symmetric in  $B$ -field, and provide valuable information about the defect distribution. It is evident from the magnetoconductance plot in Figure 8.5a that the UCF amplitude decreases substantially with increasing temperature. According to Equation 3.53, the root-mean-square (rms) of the UCF is related to the phase coherence length of the electrons via  $\text{rms}(\delta G) \propto (l_\phi/L)^{(4-2)/2}$ , where  $L$  is the typical edge length of the sample and  $d$  is the dimensionality of the electronic system. On this basis, the dimensionality of the observed UCF can be determined by plotting  $\text{rms}(\delta G)$  as a function of  $l_\phi$  derived from the WAL measurements (see Figure 8.5b). The very good quality of the fit by a straight line ( $d = 2$ ) signifies a 2D character of the UCF. To further consolidate this

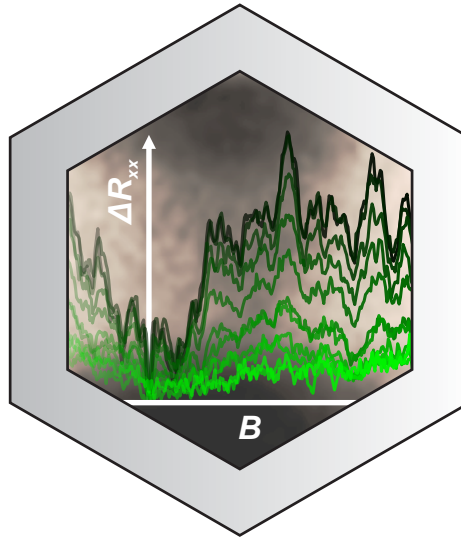
conclusion, we studied the angle dependence of the magnetoconductance. In Figure 8.5c the UCF amplitude, obtained by subtracting a smoothed background, is depicted as a function of the  $B$ -field. Plotting the UCF amplitude as a function of the  $B$ -field component normal to the surface (see Figure 8.5d) reveals several features that shift in  $B$  by tilting the sample. In Figure 8.5e, the position of two selected peaks (see guideline to the eye in Figure 8.5d) is plotted versus the tilting angle  $\theta$ . That the data can be well fitted by a  $1/\cos(\theta)$  function indicates that the peak positions depend only on the  $B$ -field component normal to the substrate plane, thus confirming the 2D character of the charge transport.

## 8.4 Summary

The discovery of Kawazulite as a natural TI whose electrical properties are comparable to those of state-of-the-art synthetic compounds renders it likely that further minerals belonging to this fascinating class of materials can be located in nature. Prospective candidates are, for instance, the members of the Tetradyomite and Aleksite group which together comprise more than 20 compounds. One useful search guideline may be established on the basis of theoretical predictions, making use of, for example, high-throughput robustness descriptors.<sup>141</sup> This could involve sorting out those compounds which occur as minerals, and further select those exhibiting high defect formation energies. Due to their geological age, the crystal structure of these minerals should have reached thermodynamic equilibrium and therefore an ultimately low defect concentration. In this manner, it may be possible to spot natural TIs which display further reduced bulk doping and accordingly even better accessible surface state transport, as compared to Kawazulite. In addition, the very recent visualization of topological phases in photonic quasi-crystals<sup>142</sup> suggests that also their natural counterparts can display "topological" properties.



## 9 A second example from the forge of nature: Aleksite



The discovery of the natural topological insulator Kawazulite strongly motivates the search for a new "non-trivial" mineral with even better properties. ARPES studies on Aleksite, a lead containing mineral with the composition  $\text{PbBi}_2\text{Te}_2\text{S}_2$ , allow us to identify a second natural TI. Low temperature Hall measurements reveal the existence of two transport channels with a significant average Hall mobility of  $943 \text{ cm}^2/\text{Vs}$  and a high carrier density of  $n = 3.9 \times 10^{25} \text{ m}^{-3}$ . Thin Aleksite nanoribbons display a 1D weak anti-localization effect from which a high Nyquist dephasing length on the order of  $1 \text{ }\mu\text{m}$  can be extracted. In addition very pronounced 1D universal conductance fluctuations with an amplitude close to the theoretical value of  $1e^2/h$  are observed. Interestingly, a cross-over to 2D behavior is found for a ribbon width above approximately  $200 \text{ nm}$ .

In Chapter 8 we successfully demonstrated, that it is possible to find topological insulators in nature. However, the crystal structure and electronic properties of Kawazulite are comparable with TI materials grown in the lab. Thus, we now address the question if also more exotic TIs with unique properties occur in nature. Our work<sup>143</sup> (and a theoretical work published recently by Silkin *et al.*<sup>144</sup>) suggested that minerals belonging to the Aleksite group may be novel natural topological insulators.

Aleksite, with a composition  $\text{PbBi}_2\text{Te}_2\text{S}_2$ , is a promising candidate for several reasons: firstly, theoretical calculations predict it to have a relatively large band gap of the order of 0.3 eV. Secondly, most TIs investigated so far are materials closely related to Tetradymite which has a crystal structure (space group  $R\bar{3}m$ ) that forms quintuple layers separated by a van der Waals gap. Aleksite, by contrast, belongs to the space group  $P\bar{3}m1$  comprising seven-layer blocks that are also separated by van der Waals gaps (see Figure 9.1). In addition, it is interesting to investigate the influence of Pb and S on the topological insulating behavior, which both can lead to a phase transition from TI to a trivial insulator.<sup>137,145</sup> The Aleksite microcrystals

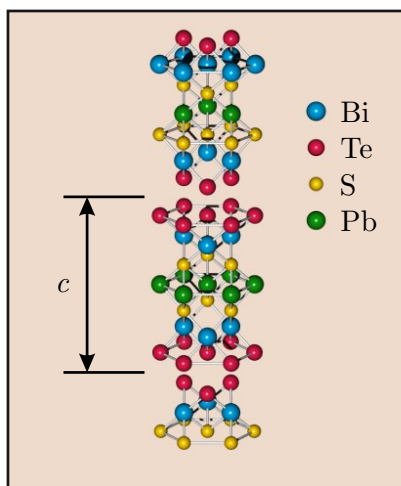


**Figure 9.1: Crystal structure of Aleksite.** Seven atoms form a block. The covalently bond blocks are held together by van der Waals interaction. Bismuth, Tellurium, Sulfur and Lead atoms are shown in blue, red, yellow and green, respectively.<sup>144</sup>

investigated in this work were purchased from Mineralienkontor and originate from the Kochkar district in southern Urals, Russia. Unfortunately, the size of the specimen was only about 200  $\mu\text{m}$ . This small amount of material (most of the material was needed for ARPES and electrical characterization) hampered the investigation of the crystal structure of the mineral. In particular, single crystal X-ray diffraction (SC-XRD) and powder XRD measurements did not provide reliable results. Thus, lattice constants  $a$  and  $c$  could not be determined, and also a Rietveld fit to the data was impossible.

To test whether Aleksite is a natural topological insulator we need to know its surface band structure. To this end, we performed ARPES measurements on a tiny single crystalline domain of the mineral. After cleaving the Aleksite crystal in air to clean its surface, it was directly

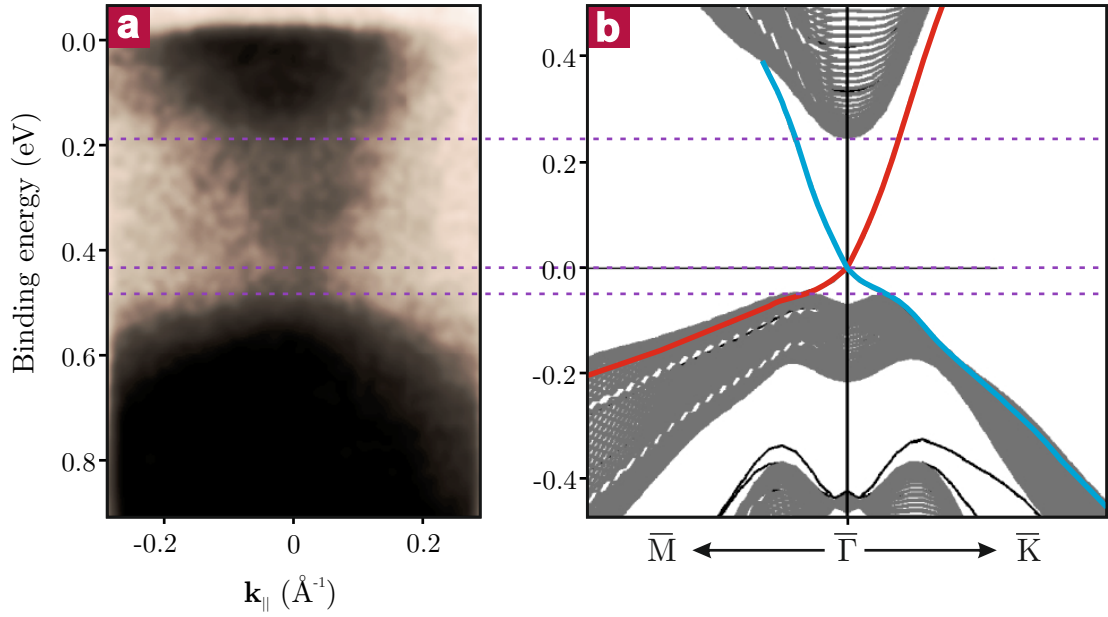


**Figure 9.2: ARPES of Aleksite.** (a) ARPES spectrum of Aleksite. (b) Calculated band structure of Aleksite.<sup>144</sup> The theoretical and calculated band structures are aligned in such a way, that the valence band edges are at the same energy value.

transferred to UHV. Figure 9.2a shows the ARPES spectrum obtained at about 100 K. Despite the weak signal, a cone-like shaped band can be observed inside the band gap. This result can be compared to theoretical calculations<sup>144</sup> of the band structure of Aleksite (see Figure 9.2b). The two band structures are aligned such that the valence band edge (which is the clearest feature in the experiment) is at the same energy. Thus, if the dark region in Figure 9.2a close to the Fermi energy is attributed to the bulk conduction band, the experimental ARPES spectrum is in good agreement with the theoretical prediction ( $E_g = 307$  meV).<sup>144</sup> The band gap value is significantly larger than the gaps found in  $\text{PbBi}_2\text{Te}_4$  and  $\text{PbBi}_4\text{Te}_7$  (below 200 meV).<sup>35</sup> This difference may be due to the replacement of heavy Te atoms by lighter S which weakens the SOC and thus lowers the splitting of the states forming the valence and conduction band of the material. As a result the band gap is expected to increase.<sup>144</sup> It can be further concluded from Figure 9.2 that the Fermi energy is located deep inside the bulk conduction band. Such high n-doping was also found experimentally in the compound  $\text{PbBi}_4\text{Te}_7$ .<sup>146</sup>

After having gained convincing evidence for Aleksite to be natural topological insulator we further investigated its electronic properties. For this purpose, we used micromechanical cleaving (see Chapter 8) to prepare thin flakes and ribbons. Figure 9.3a shows a 19 nm thin (see Figure 9.3b) and about 130 nm wide ribbon randomly formed during exfoliation. We were also able to find thin platelets with a thickness down to 10 nm. Individual thin nanostructures were identified by their optical contrast, and then electrically contacted using standard e-beam lithography, followed by thermal evaporation of contact metals (4 nm Ti / 60 nm Au). To ensure

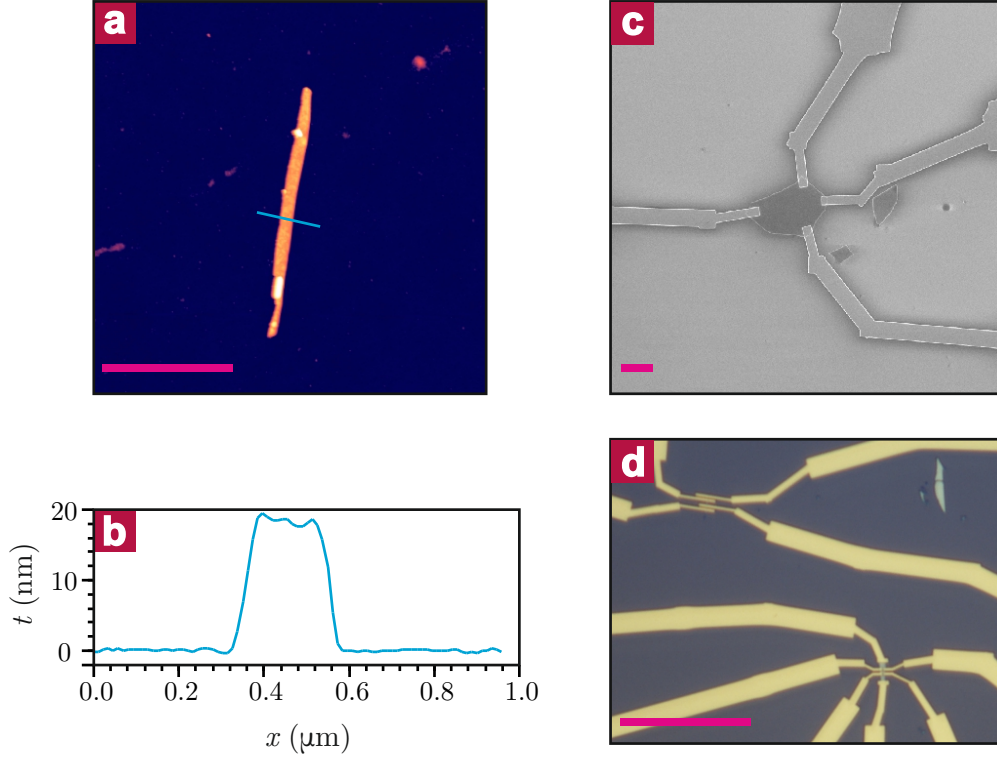


**Figure 9.3: Electrical contacting of Aleksite.** (a) AFM image of a ribbon that randomly formed during mechanical exfoliation (electrical transport data of this ribbon are shown in Figure 9.5 and 9.6). (b) Height profile of the ribbon along the blue line in panel (a). (c) SEM image of a typical thin flake contacted in van der Pauw geometry. (d) Optical image of the ribbon shown in panel (a) contacted with electrode fingers (top), and a thin flake contacted in Hall geometry (bottom). Scale bars: (a),(c) 2  $\mu\text{m}$ , (d) 20  $\mu\text{m}$ .

Ohmic contacts, the contact regions were pre-treated with Ar plasma for 50 s. Figure 9.3c and d show typical devices defined in van der Pauw (Figure 9.3c), "finger-like" (9.3d, top) and Hall bar (9.3d, bottom) geometry, respectively.

To determine the carrier density and mobility we performed DC Hall measurements at 1.4 K. A typical Hall curve is depicted in Figure 9.4a. Using a linear fit to the data (see Equation 3.10), an average carrier density of  $n = 3.9 \times 10^{25} \text{ m}^{-3}$  was found. This comparatively high value agrees with the ARPES results, and indicates that (as usual) the Fermi level is located within the bulk conduction band. Application of Equation 3.11 yielded an average mobility of  $943 \text{ cm}^2/\text{Vs}$ , slightly higher than the value found for Kawazulite. It should be noted, that all measured Hall curves were slightly non-linear. This non-linearity is highlighted by plotting  $\Delta\rho_{xy} = \rho_{xy} - \rho_{Hall}^{linear}$ , where  $\rho_{Hall}^{linear}$  is the linear background subtracted from the measured data (see Figure 9.4b). If we assume parallel conduction of two different transport channels, a two-band model (see Equation 7.6) can be used to fit the data. Fits to the data using a linear fit (blue) and the two-band model (pink) are depicted in Figure 9.4a and b, respectively. Interestingly, the curvature of the Hall curves is opposite from those found for  $\text{Bi}_2\text{Te}_2\text{Se}$

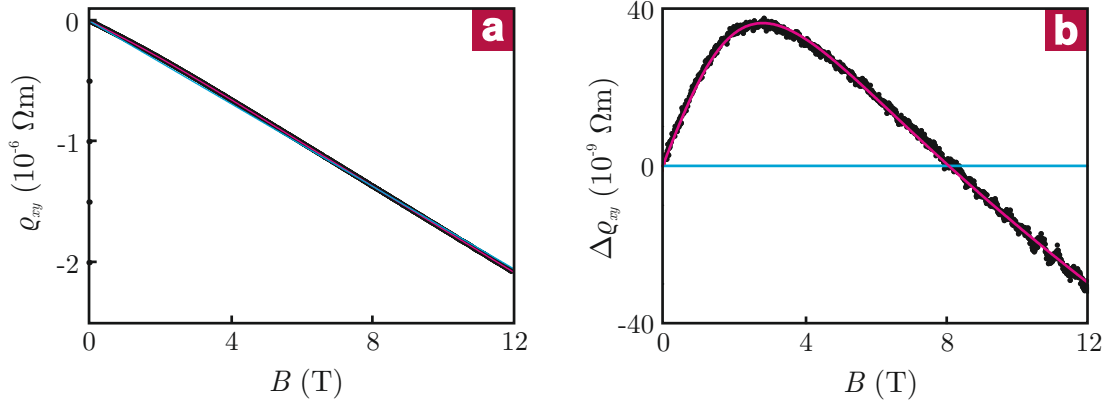


**Figure 9.4: Hall measurements of Aleksite.** (a) Hall resistivity as a function of the external magnetic field, recorded at 1.4 K. (b) Non-linearity of the Hall curve in panel (a). The blue and pink curves represent a linear fit and a fit based upon the two-band model, respectively.

(see Figure 7.9a), and can only be explained assuming both an electron- and a hole-like transport channel. The results of the fits using the two-band model are  $\mu_{electron} = 943 \text{ cm}^2/\text{Vs}$ ,  $n_{electron} = 3.9 \times 10^{25} \text{ m}^{-3}$ ,  $\mu_{hole} = 2972 \text{ cm}^2/\text{Vs}$  and  $n_{hole} = 2.7 \times 10^{23} \text{ m}^{-3}$ . The origin of this high-mobility hole channel is not evident. Although the sign of the carriers could be explained by transport through an impurity band located closely above the valence band edge which is formed by acceptors like in the case of  $\text{Bi}_2\text{Te}_2\text{Se}$ ,<sup>28</sup> the high mobility would still be unexpected.

The four-terminal resistance of thin Aleksite flakes at low temperatures is on the order of several Ohms. This low value impeded a careful analysis of the magnetotransport behavior, since the changes in resistance were only several 100 m $\Omega$  at the highest external magnetic fields. Therefore, we investigated thin ribbon-like devices with a typical resistance of several 100  $\Omega$ . The corrected low-field magnetoresistance  $\Delta R_{xx}(B) = R_{xx}(B) - R_{xx}(B=0)$  of a 19 nm thick, 138 nm wide and 1.6  $\mu\text{m}$  long ribbon (see Figure 9.3a and d top) recorded at different temperatures is depicted in Figure 9.5a. Around zero magnetic field a very pronounced WAL (see Section 3.3.2) resistance minimum can be observed. To investigate the dimensionality of the WAL the sample is tilted in the external magnetic field. It can be seen in Figure 9.5b that the WAL only depends on the  $B$ -field component  $B \cos(\theta)$  normal to the sample surface. Fitting the data with the 2D Hikami-Larkin-Nagaoka model (see Equation 3.41) yielded unphysically high values for the parameter  $\alpha$  in the range of  $-3$  to  $-5$ .<sup>69,71,72</sup> For an estimation we assume an extended 2D system with two decoupled and parallel transport channels by fixing  $\alpha = -1$ . Fitting the data yields a phase coherence length of about  $l_\phi \approx 700 \text{ nm}$ . This value is much larger than the width  $W$  of the ribbon pointing toward a lower dimensionality than 2. That assumption is further supported by the fact that the WAL correction is on the order of  $e^2/h$  and thus much higher than the value found in typical 2D systems. Accordingly, we attribute the WAL to 1D diffusive transport in the device.

To analyze our data along this line, we use a 1D localization model developed by Altshuler *et*

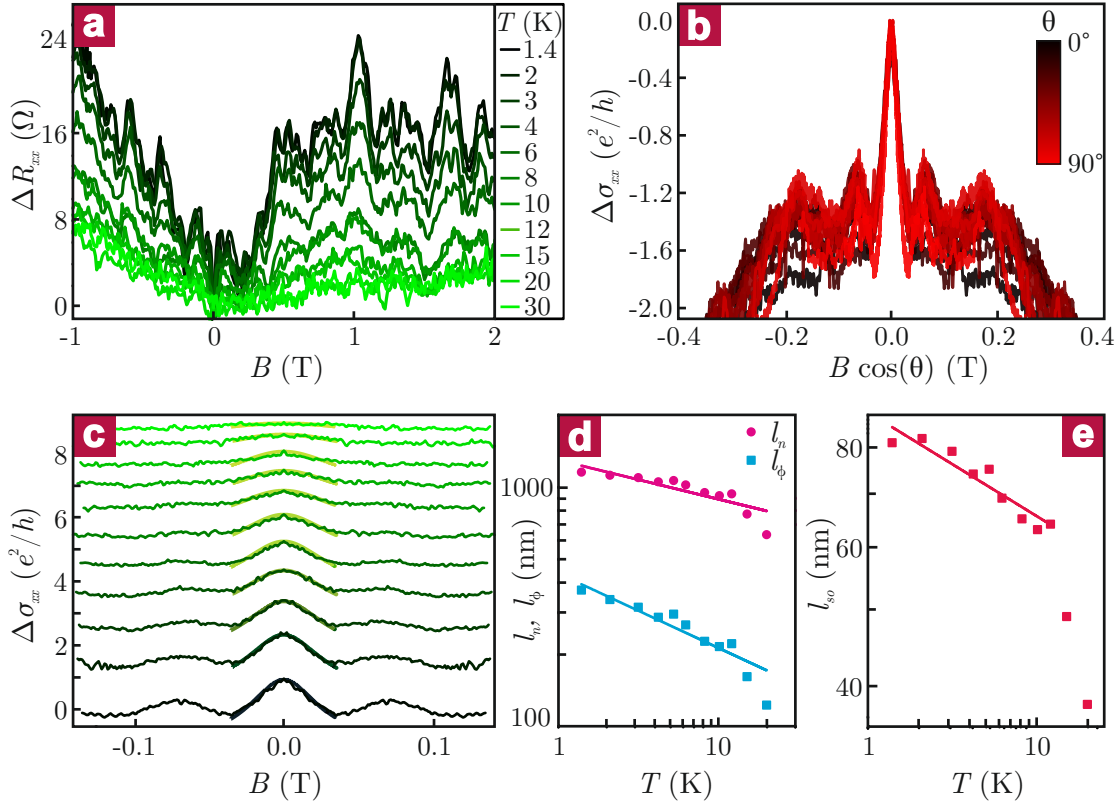


**Figure 9.5: Weak anti-localization in Aleksite.** (a) Corrected magnetoresistance at different temperatures. (b) Corrected magnetoconductance as a function of the  $B$ -field component  $B \cos(\theta)$  normal to the sample surface. Since all curves coincide it can be concluded that the WAL is 2D or 1D. (c) Fits of the magnetoconductances recorded at different temperatures (colors are the same like in panel (a)) using Equation 9.2. (d) Nyquist (pink) and phase coherence length (blue) extracted from the fits in panel (c) as a function of  $T$ . The solid lines are fits to the data, specifically  $l_n \propto T^{-0.13}$  and  $l_\phi \propto T^{-0.31}$ . (e) Spin-orbit length  $l_{so}$  calculated from the conductance correction  $\delta\sigma$  using the results of panel (d) and Equation 9.1. The solid line is a linear fit the last two data points (where the estimation of  $l_{so}$  is obscured by the very weak WAL).

*al.*:<sup>147–149</sup>

$$\delta\sigma = \frac{\sqrt{2}e^2}{\pi\hbar} \frac{l_n}{W} \left\{ \frac{3}{2} \cdot \mathcal{F} \left[ \frac{8}{3} \frac{l_n^2}{l_{so}^2} \right] - \frac{1}{2} \cdot \mathcal{F} \left[ 2 \frac{l_n^2}{l_\phi^2} + \frac{2}{3} l_n^2 \left( \frac{eWB}{\hbar} \right)^2 \right] \right\}, \quad (9.1)$$

where  $\delta\sigma$  is the conductance correction,  $\mathcal{F}[x] = \frac{\text{Ai}(x)}{\text{Ai}'(x)}$ , with Ai and Ai' as the Airy Ai function and its derivative, respectively,  $l_n$  is the dephasing length governed by low energy Nyquist scattering,  $l_\phi$  is the phase coherence length associated with other phase-breaking mechanisms other than the Nyquist one, and  $l_{so}$  is the spin-orbit length. This model can be slightly modified

by calculating  $\Delta\sigma(B) = \delta\sigma(B) - \delta\sigma(B = 0)$ :

$$\Delta\sigma = \frac{e^2}{\sqrt{2\pi\hbar}} \frac{l_n}{W} \left\{ \mathcal{F} \left[ 2 \frac{l_n^2}{l_\phi^2} \right] - \mathcal{F} \left[ 2 \frac{l_n^2}{l_\phi^2} + \frac{2}{3} l_n^2 \left( \frac{eWB}{\hbar} \right)^2 \right] \right\}, \quad (9.2)$$

which is independent of  $l_{so}$ . The corresponding fits of the magnetoconductivity data recorded at different temperatures using Equation 9.2 are depicted in Figure 9.5c. Their excellent quality supports the validity of the 1D model. The fits yield a Nyquist length  $l_n = 1152$  nm and a phase coherence length  $l_\phi = 370$  nm at  $T = 1.4$  K. Furthermore, by assuming the conductance correction  $\delta\sigma$  to be the difference between the conductance maximum at  $B = 0$  and the flat background at higher magnetic fields (see Figure 9.5c) a spin–orbit length  $l_{so} = 81$  nm can be estimated using Equation 9.1. The low spin–orbit length reflects the strong spin–orbit interaction in Aleksite.

The temperature dependences of these characteristic lengths are shown in Figure 9.5d and e. All lengths decrease with increasing temperature. Curve fits revealed a  $l_n \propto T^{-0.13}$  dependence for the Nyquist length and a  $l_\phi \propto T^{-0.31}$  dependence for the phase coherence length. According to theory, the dephasing length should decay with  $T^{-1/2}$  if the system is 2D and  $T^{-1/3}$  if it is 1D (see Equation 3.43 with  $l = \sqrt{D\tau}$ ). Both exponents,  $-0.13$  and  $-0.31$  are close to  $-1/3$ , which further underscores that the WAL observed in the samples is of 1D nature. The

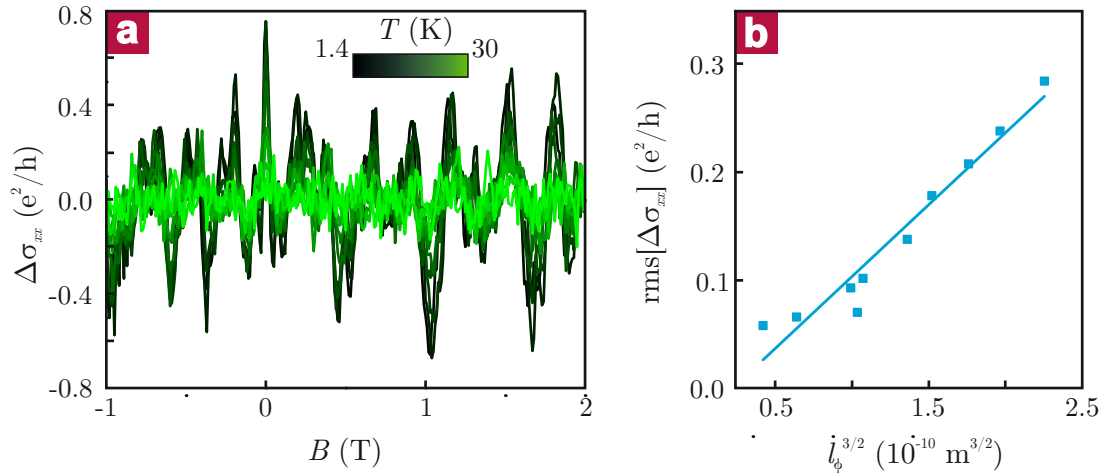


**Figure 9.6: Universal conductance fluctuations in Aleksite.** (a) UCF amplitude obtained by subtracting a smoothed background from the magnetoconductance for different temperatures. (b) Root–mean–square of the oscillations as a function of phase coherence length obtained from the 1D fits to the WAL data (see Figure 9.5d).

quite large phase coherence lengths observed in Aleksite ribbons give rise to pronounced universal conductance fluctuations (UCF, see Section 3.4.2), which are clearly observable in Figure 9.5a. This is further illustrated in Figure 9.6, where a smoothed background is subtracted from the magnetoconductance at different temperatures. It can be seen that the amplitude of the oscillations is on the order of  $0.3e^2/h$ , close to the theoretically predicted (universal)

value of  $1e^2/h$ . This finding again reflects the high phase coherence length in this material. With increasing temperature, the phase coherence length decreases and the UCF get less pronounced. The analytical relation between the root-mean-square of the oscillations and the phase coherence length is given by  $\text{rms}(\Delta\sigma) \propto l_\phi^{(4-d)/2}$  (see Chapter 8), where  $d$  is the dimensionality of the system. Thus, for a 1D system  $\text{rms}(\Delta\sigma) \propto l_\phi^{3/2}$ , which is confirmed by the plot in Figure 9.6b (a linear fit to  $\text{rms}(\Delta\sigma)$  vs.  $l_\phi$  failed), where the phase coherence lengths were taken from Figure 9.5d.

It is noteworthy that for a slightly wider ribbon ( $W = 300$  nm,  $d = 13$  nm,  $L = 1.7$   $\mu\text{m}$ ) it was possible to fit the data using the 2D HLN theory giving the expected  $\alpha = -1$ , and  $l_\phi = 195$  nm ( $< W$ !) at 1.4 K. The amplitude of the UCF in this sample is on the order of  $0.1e^2/h$ , slightly smaller than the value found in the narrow ribbon. In addition,  $\text{rms}(\Delta\sigma)$  scales linear with the phase coherence length indicating 2D behavior. On this basis, we conclude a cross-over from 2D to 1D diffusive transport if the ribbon width falls below approximately 200 nm. However, to verify this scenario, additional ribbon-like devices need to be investigated in the future. Unfortunately, the chance to find ribbons formed during exfoliation is very low, since most quasi-1D structures tend to break into small pieces which cannot be electrically contacted. It should again be emphasized that the observation of low-dimensional WAL and UCF alone is no direct proof for the contribution of topological surface states to the electrical transport. Nonetheless, the existence of a low-dimensional transport channel with relatively large coherence length (which is presumably associated with the high mobility channel observed in the Hall experiments) makes Aleksite a very interesting topological insulator for future studies.

## 10 Summary and outlook

The central topic of this work was a quest for novel topological insulating materials with outstanding properties. A main focus was on the key problem in this field of research, namely the interference of the conducting bulk with the electrical transport through the exotic surface states. To address this issue, a CVD system was set up to grow ultrathin platelets of  $\text{Bi}_2\text{Se}_3$  with an enhanced surface-to-bulk ratio. This allowed us to reveal a novel electrical transport fingerprint of the topological surface states, the linear magneto-resistance (LMR). By applying a back gate voltage to these devices we were able to switch on and off the contribution of the transport channel that is responsible for the LMR. The temperature dependent study of the resistance combined with the observation of pronounced weak anti-localization in these samples provided strong evidence that this LMR channel can be related to the non-trivial surface states of  $\text{Bi}_2\text{Se}_3$ .

However, the contribution of bulk states to the total transport in  $\text{Bi}_2\text{Se}_3$  is very high. This problem is mainly caused by the spontaneous formation of Se vacancies during growth, which results in strong n-doping of the material. Therefore, we synthesized thin structures of a novel material,  $\text{Bi}_2\text{Te}_2\text{Se}$ , which was known from experiments on bulk crystals to have the highest surface contribution to the total electrical transport reported so far. For the first time we were able to grow this TI using the same CVD technique that we used for the fabrication of  $\text{Bi}_2\text{Se}_3$  nanostructures. After having verified the stoichiometry of  $\text{Bi}_2\text{Te}_2\text{Se}$  (BTS) using TEM and Raman studies we investigated its low temperature magnetoconductance behavior. Standard Hall measurements provided an average carrier density on the order of  $10^{25} \text{ m}^{-3}$  and a carrier mobility of about  $100 - 400 \text{ cm}^2/\text{Vs}$ . The magneto-conductance showed a purely 2D weak anti-localization, evidencing the existence of a 2D electrical transport channel on the surface of the material. By investigating the thermally activated temperature behavior of the four-terminal resistance of the devices we were able to estimate the position of the Fermi level. It was found, that the Fermi energy is located inside the bulk band gap even without applying any external gate voltage. Using different back gate voltages, we were able to tune the Fermi level in the BTS sheets.

After having demonstrated that it is possible to grow thin BTS platelets with electronic properties superior to those of pure  $\text{Bi}_2\text{Se}_3$ , we aimed at optimizing the carrier mobility in these

samples. Our strategy was to grow BTS on layered hBN in an oriented manner by van der Waals epitaxy. An epitaxial growth mode was suggested based on SEM and AFM studies of the films. The surface state mobility of thus obtained thin platelets was increased by a factor of 3 compared to platelets grown on Si/SiO<sub>x</sub>. This enabled the study of gate-dependent Shubnikov–de Haas oscillations for the first time in this material. Analysis of the non-linear Hall effect using a two-band model suggested the existence of a high mobility transport channel which can be attributed to the topological surface state of BTS, and is located at the interface between the Bi<sub>2</sub>Te<sub>2</sub>Se and hBN.

Although BTS on hBN exhibits very high surface carrier mobility, the total carrier density, and thus the influence of the bulk conduction channel, still remains appreciable. This stimulated us to search for new materials with lower bulk defect density. But materials science is not only restricted to materials made in the lab. Due to their geological age, the crystal structure of minerals should have reached thermodynamic equilibrium and therefore an ultimately low defect concentration. This raises the question whether there are natural topological insulators. By investigating Kawazulite, a mineral with the approximate composition Bi<sub>2</sub>(Te,Se)<sub>2</sub>(Se,S), originating from a former gold mine in Czech Republic, we were able to demonstrate the first natural occurring topological insulator. Its Hall mobility is on the order of 300 – 1300 cm<sup>2</sup>/Vs and it shows pronounced 2D coherence effects like universal conductance fluctuations and weak anti-localization at low temperature. Thus, Kawazulite can readily compete with its synthetic counterparts made in the lab. Since the equilibrium defect concentration of minerals is mainly governed by their defect formation energies, it may be possible to spot new TIs in nature that display even better electronic performance than Kawazulite. One such candidate provided by nature is the mineral Aleksite. According to recent theoretical predictions<sup>144</sup> Aleksite should also be a natural TI that furthermore has a large band gap (> 300 meV) making it suitable for room temperature electronic device applications. We were able to demonstrate topological insulating properties in an Aleksite crystal originating from a former gold mine in the Ural, Russia. ARPES revealed that the band gap energy is indeed in the order of 300 meV. Hall measurements revealed an average carrier mobility of the order of 943 cm<sup>2</sup>/Vs, 1.5 times larger than the value found for Kawazulite. Low temperature magnetoconductance measurements of thin Aleksite ribbons yielded very pronounced UCF and WAL, both on the order of the theoretical limit of  $e^2/h$ . By analyzing these diffusive transport effects with a 1D model, very high coherence lengths up to 1 μm were found.

In summary, we were able to contribute important pieces to the big puzzle of the ongoing research on topological insulators. While ARPES measurements have been well-established to prove the existence of topological surface states, this goal has not yet been achieved for electrical transport experiments. Numerous publications have tried to associate low-dimensional transport phenomena to the surface states of TIs. However, most 3D TI materials are layered (and thus possess a highly anisotropic resistivity) semiconductor crystals and naturally tend to form a trivial 2D electron gas on their surface.<sup>15</sup> Moreover, as experimentalists often use ultrathin samples wherein the 'bulk' itself is subjected to confinement into 2D, strong caution has to be exercised when interpreting the results. Nevertheless, the strategies to increase the performance of existing materials or to discover new TIs in nature, as described in this thesis,

are promising to stimulate future research.

In the following some unanswered questions that came up during this work will be presented. Based upon these ideas, the long-awaited bullet proof electrical transport experiments to verify the existence of helical surface states in topological insulators may be attainable.

### 10.1 Growth mechanism of BTS on hBN

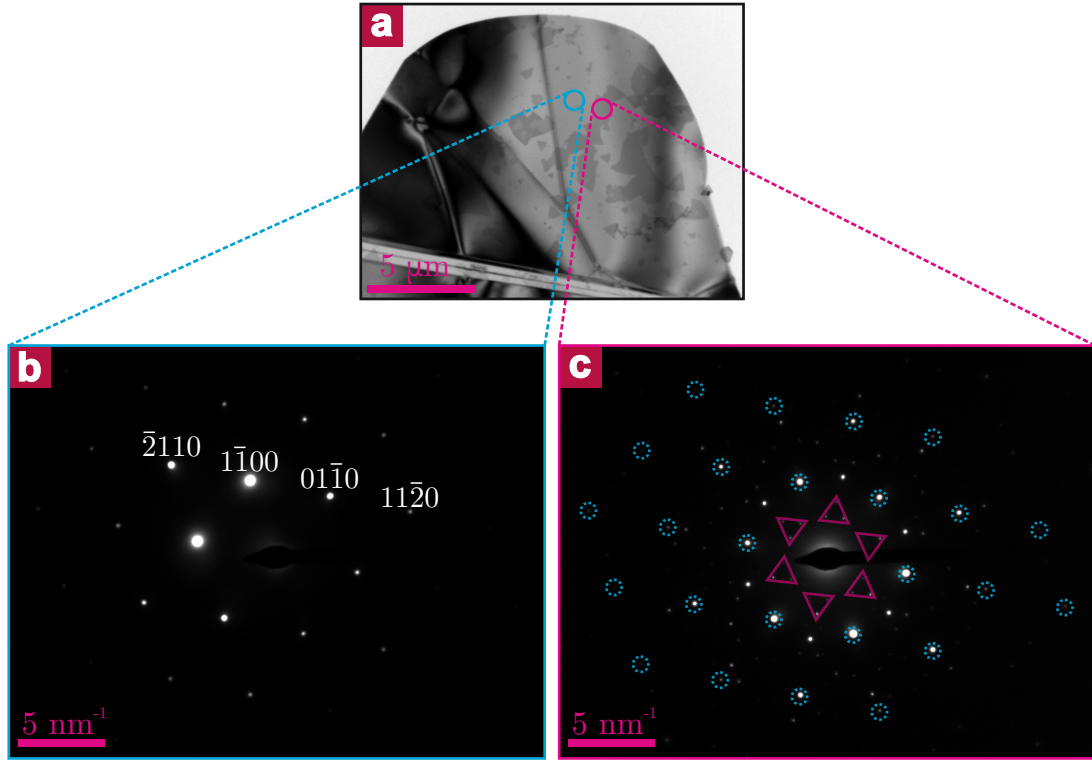


**Figure 10.1: TEM study of  $\text{Bi}_2\text{Te}_2\text{Se}$  on hBN.** (a) TEM image of a hBN flake with BTS flakes grown epitaxially on top. (b) SAD pattern of pure hBN (marked in blue in (a)). Four diffraction spots are indexed. (c) SAD pattern of BTS on hBN. All spots observable in (b) are marked in blue. The inner spots that are split up in triangles (marked in pink) can be attributed to the  $\{1\bar{1}00\}$  planes of BTS.

In Chapter 7, we investigated  $\text{Bi}_2\text{Te}_2\text{Se}$  thin films grown epitaxially on hBN. Although there is strong evidence for the growth mechanism depicted in Figure 7.1a, b, an experimental proof is missing. This can be studied by transferring as-grown nanostructures of BTS on hBN onto a TEM grid. One possible approach is to spin-coat a thick layer (300 – 400 nm) of PMMA on the growth substrate and immerse it in water at 90 °C for about 2 h.<sup>150</sup> The PMMA film can be easily peeled off, with the hBN/BTS stack remaining attached to it. The film can be fished with a TEM grid and directly be used for TEM characterization. Figure 10.1a depicts a TEM image where BTS can be seen as dark, triangular-shaped regions on the brighter hBN flake. We performed selected area diffraction (SAD) measurements of pure hBN (Figure 10.1b) and

BTS/hBN (Figure 10.1c). Figure 10.1b clearly reveals the hexagonal structure of hBN. The inner  $\{1\bar{1}00\}$  spots provide a nearest-neighbor distance  $a = 1.41 \pm 0.04 \text{ \AA}$ , very close the value of  $1.44 \text{ \AA}$  reported in literature.<sup>120</sup> Interestingly, the SAD on a BTS flake yields a very complex diffraction image as depicted in Figure 10.1c, where the positions of the reflexes of pure hBN (Figure 10.1b) are highlighted by blue circles. The inner reflexes are split up into triangles (marked in pink) and could be attributed to the symmetry forbidden  $\{1\bar{1}00\}$  reflexes of  $\text{Bi}_2\text{Te}_2\text{Se}$ . Using the centers of these triangles a lattice constant of  $a = 4.24 \text{ \AA}$  is calculated, which again fits well to the theoretical value of  $a = 4.283 \text{ \AA}$ .<sup>123</sup> It is pertinent to mention, that the  $\{1\bar{1}00\}$  reflexes of  $\text{Bi}_2\text{Te}_2\text{Se}$  are tilted by  $30^\circ$  compared to the  $\{1\bar{1}00\}$  reflexes of hBN supporting the validity of the growth mechanism suggested in Figure 7.1b. However, at the present stage we are neither able to fully explain all the observed reflexes, nor to find an explanation for the splitting of the diffraction spots. This strongly motivates future follow up experiments to clarify these points.

### 10.2 Anomalous Aharonov–Bohm oscillations in Kawazulite

In Chapter 8, we investigated the electrical transport behavior of Kawazulite, a natural topological insulator. By investigating narrow ribbons of that material, like the  $280 \text{ nm}$  wide and  $25 \text{ nm}$  thick structure depicted in Figure 10.2a, a very interesting effect was observed. Figure 10.2b shows the magnetoconductance at  $1.4 \text{ K}$  with the  $B$ -field applied along the ribbon axis. The magnetoconductance oscillations can be seen in Figure 10.2c, where a smoothed background is subtracted from the raw data. These oscillations are periodic in  $B$  and can be attributed to the Aharonov–Bohm effect (see Section 3.4.1), which has similarly been observed for nanoribbons of various TI materials.<sup>97, 151, 152</sup> However, theoretical calculations<sup>77, 78</sup> predict that the maxima of these oscillations should be located at fractional flux values and that their position should be tunable using an external gate voltage (see Chapter 3.4.1). We could clearly observe such effect in one device (see Figure 10.2c). These oscillations consist of a prominent AB-part with a wavelength  $\phi_0 = h/e$  and a less prominent contribution due to Altshuler–Aronov–Spivak (AAS) oscillations with a wavelength  $h/(2e)$ , as underscored by FFT in Figure 10.2d. If it would be possible to reproduce this experiment and demonstrate the gate dependence of the AB effect, this would be the first bullet proof demonstration of the existence of a topological surface state in an electrical transport experiment.<sup>78</sup>

### 10.3 Graphene tunnel barrier

Thus far, no report on spin injection in topological insulators has appeared. To efficiently inject spins from a ferromagnetic metal into a semiconductor, the conductance mismatch problem has to be solved. Schmidt *et al.*<sup>153</sup> demonstrated, that the spin injection coefficient  $\gamma$  is proportional to  $\sigma_N/\sigma_F$ , where  $\sigma_N$  and  $\sigma_F$  are the conductivities of the normal (semiconductor) and the ferromagnetic material. Commonly, the conductivity of a metal is much higher than that of a topological insulating film, making the spin injection very inefficient. To overcome

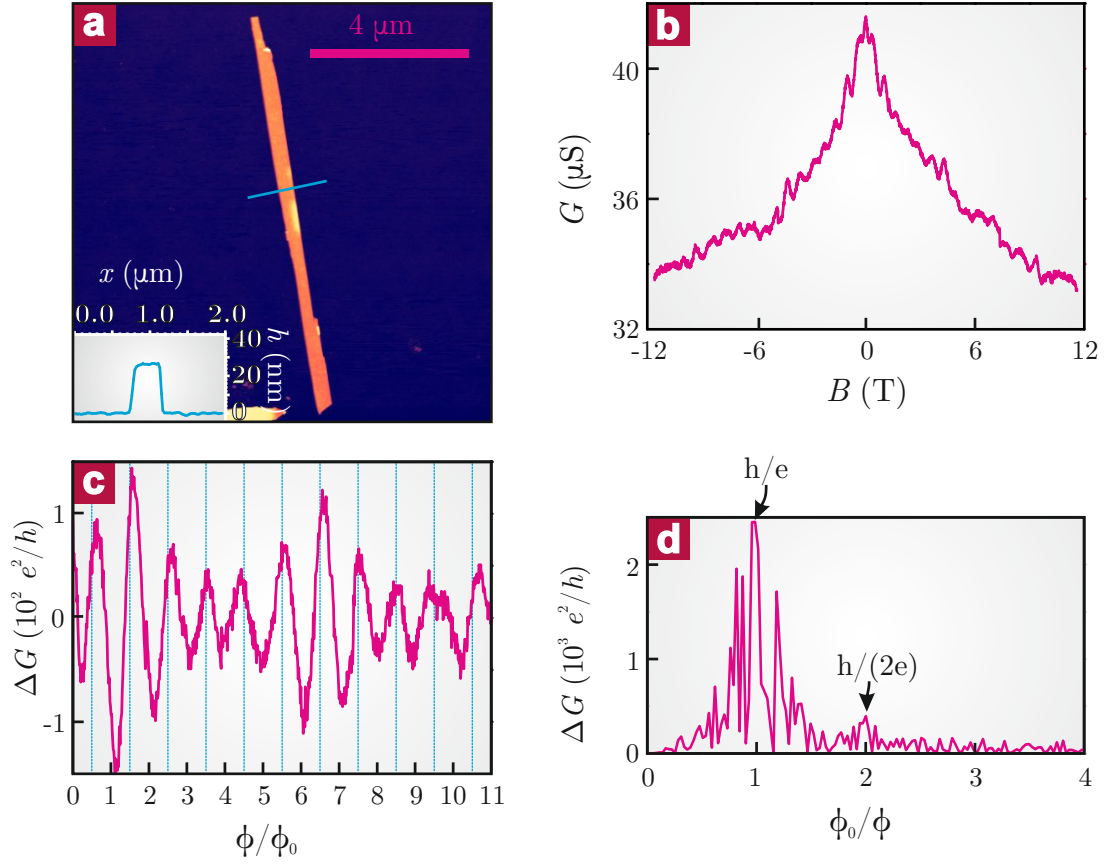


**Figure 10.2: Anomalous Aharonov–Bohm effect in Kawazulite.** (a) AFM image of a ribbon of Kawazulite formed during exfoliation. Inset: height profile. (b) Raw magnetoconductance data with  $B$ -field applied parallel to the ribbon axis. (c) AB oscillations highlighted by subtracting a smoothed background from the magnetoconductance signal. The oscillations are periodic in  $B$  and have maxima at fractional flux values (the maximum at  $B = 0$  can be attributed to the WAL effect). (d) FFT of the data shown in (c). The oscillations consist of two parts with wavelengths of  $h/e$  (Aharonov–Bohm) and  $h/(2e)$  (Altshuler–Aronov–Spivak), respectively.

this problem, Rashba<sup>154</sup> suggested to use tunnel barriers between the ferromagnetic contact and the semiconducting sheet which should dramatically increase the spin injection. It has been recently shown that graphene is an excellent tunnel barrier for spin injection due to its flatness, small thickness, as well as very low conductivity in the direction normal to its surface.<sup>155, 156</sup>

In Chapter 4, we demonstrated the possibility to grow topological insulator nanostructures on various substrates using the CVD method. Thus, by growing TIs epitaxially on graphene we could kill two birds with one stone: firstly, the electrical transport performance is expected to be enhanced due to the high quality of the epitaxial films (see Chapter 7). Secondly, we could directly use the growth substrate (graphene) as a tunnel barrier. A possible strategy to fabricate such devices is depicted in Figure 10.3a. The as-grown TI is covered with PMMA. After putting

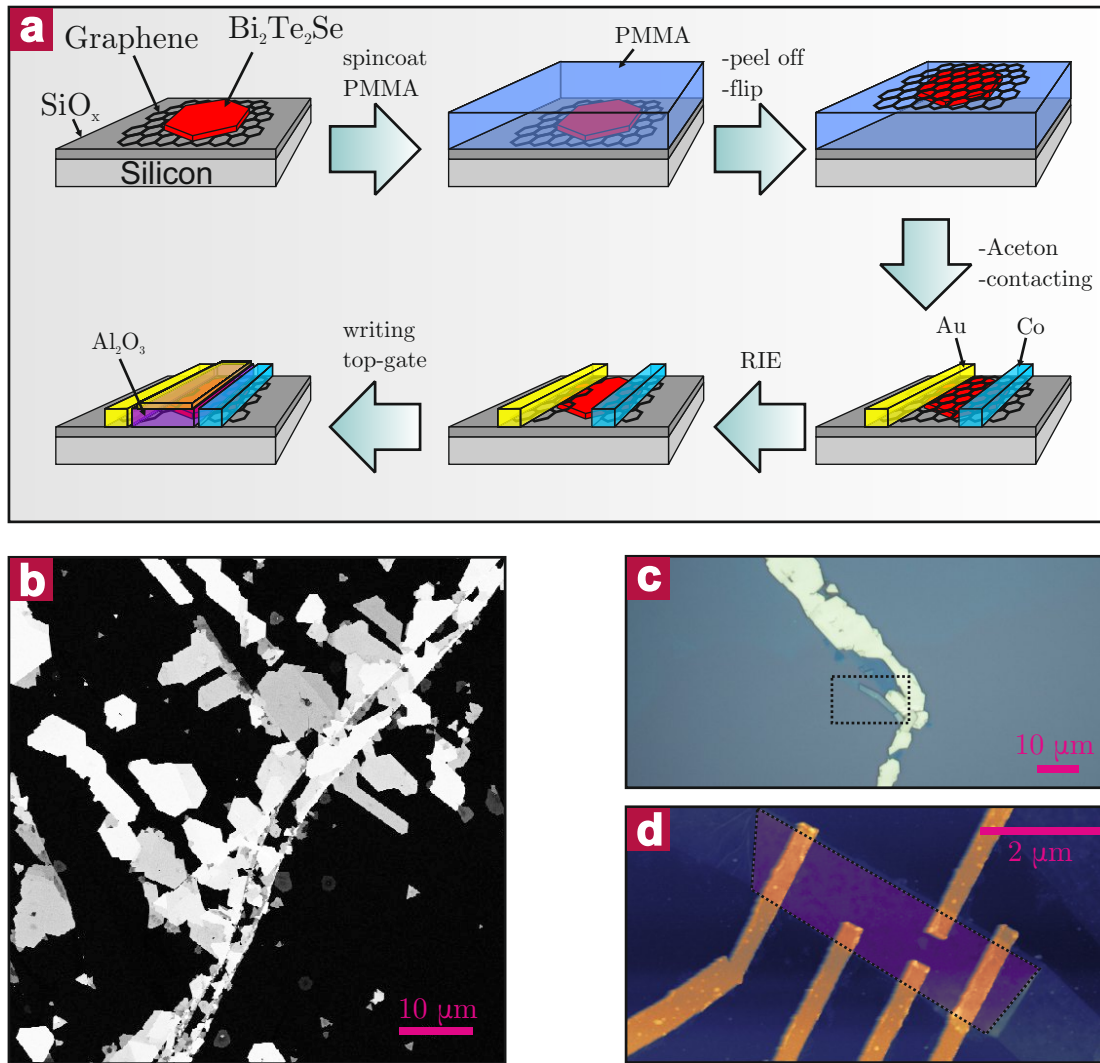


**Figure 10.3: Using graphene as a tunnel barrier.** (a) Schematic depiction of the fabrication of graphene tunnel barriers. BTS is grown on exfoliated graphene, followed by spin-coating of a thick layer of PMMA. This layer can be peeled off (see main text), flipped and used to transfer the graphene/BTS sandwich upside down to a new substrate. The stack can then be electrically contacted using standard e-beam lithography, followed by removing excess graphene by RIE. In a last step, a top gate can be fabricated. (b) SEM image of  $\text{Bi}_2\text{Se}_3$  grown on HOPG. (c) Optical image of graphene (already flipped) on top of  $\text{Bi}_2\text{Se}_3$ . (d) AFM image of the area framed in (c) after electrical contacting.

the substrate in warm water it is possible to peel off the PMMA (with the graphene/TI stack sticking to it),<sup>150</sup> flip the structures and transfer them upside down onto a new substrate. The graphene-on-TI sandwich can then be electrically contacted with magnetic Co or normal Au contacts, or a combination of both.<sup>157</sup> The excess graphene in between the metallic contacts can be removed using reactive ion etching (RIE). The above method also allows for the fabrication of a top gate, in order to individually tune the top and the bottom surface

states of the topological insulator when studying the spin-injection. Figure 10.3b shows a SEM image of a typical epitaxial growth of  $\text{Bi}_2\text{Se}_3$  on HOPG. All platelets on a terrace of HOPG are oriented parallel or tilted by  $60^\circ/120^\circ$ . The same growth can be performed on exfoliated graphene as depicted in Figure 10.3c, which shows an optical image of a graphene/ $\text{Bi}_2\text{Se}_3$  stack that is already flipped using the method proposed in Figure 10.3a. This sandwich, where graphene is on top of  $\text{Bi}_2\text{Se}_3$ , survived all electrical contacting process steps, as apparent from the AFM image of the final device right before RIE in Figure 10.3d. This strategy may lead to the first experimental demonstration of spin injection in TI materials. In this manner access could be gained to the spin-lifetime of the electrons and hence to valuable information about possible spin-polarized surface states contributing to the electrical transport.



## A Supporting linear magnetoresistance data

It is apparent that the bulk state resistance  $R_b(0)$  increases upon cooling from 193 K to 70 K, consistent with thermally activated behavior. However, upon further cooling,  $R_b(0)$  displays a monotonous decrease. As mentioned in Chapter 5, we attribute this unexpected trend to the fact that our model does not account for the weak anti-localization (WAL) effect. The relevance of WAL is evident from the substantial deviation of the  $R$  vs.  $B$  curves (at low temperature and low  $B$ -fields) from the quadratic behavior, see Fig. 5.3c. Unfortunately, there is no straightforward means to include the WAL into our model.

For comparison of the above values of  $R_i(0)$  and  $R_b(0)$  in Table A.1 and A.2, we refer to Figures A.1a and A.1b, where the values derived from fittings of the data in Figure 5.3b and 5.3c are presented. There is a quite good agreement (difference of  $\approx 10\%$ ) between the gap state resistance values determined by the two approaches. Somewhat larger differences can be seen for the bulk state resistance, although the agreement is still reasonable, specifically within a factor of 1.5 for temperatures above 70 K. At lower temperatures, as explained above, the fitting in Fig. 5.3c is not valid any more. Overall, we consider the agreement sufficient to prove our model correct.

## Appendix A. Supporting linear magnetoresistance data

**Table A.1:** Values of the gap state resistance  $R_i(0)$  and bulk state resistance  $R_b(0)$  derived from fitting of the zero field data in Fig. 5.3b for a temperature range from 40 K to 193 K.

Temperature (K)	$R_i(0)$ ( $\Omega$ )	$R_b(0)$ ( $\Omega$ )
40	3.40k	3.0M
50	3.59k	475k
60	3.77k	138k
70	3.95k	57.3k
80	4.14k	29.6k
90	4.32k	17.7k
104	4.58k	10.2k
120	4.88k	6.34k
134	5.13k	4.6k
150	5.43k	3.42k
164	5.69k	2.77k
179	5.96k	2.3k
193	6.22k	1.98k

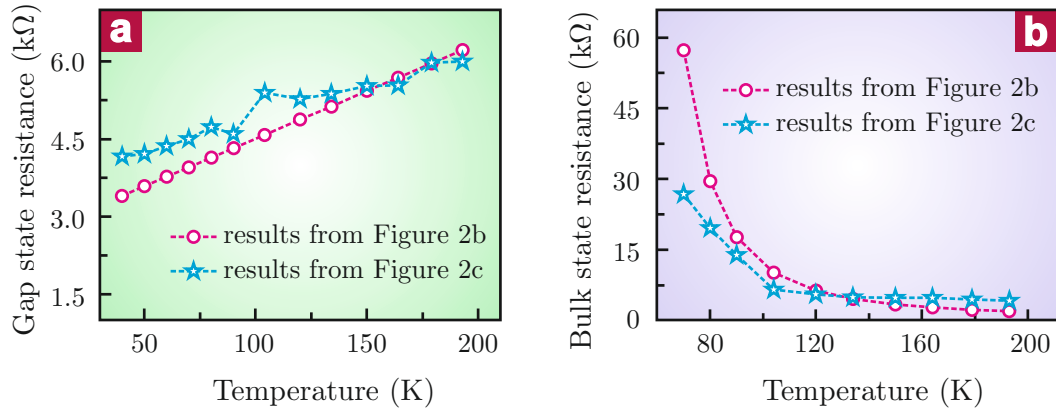


**Figure A.1: Gap and bulk state resistance.** (a) Gap state resistance deduced from the data in Figure 5.3b (pink circle) and Figure 5.3c (blue star). (b) Bulk state resistance deduced from the data in Figure 5.3b (pink circle) and Figure 5.3c (blue star).

**Table A.2:** Values of  $R_i(0)$ ,  $R_b(0)$ ,  $\alpha$  and  $\beta$  extracted from the fitting curves in Fig. 5.3c, complemented by values for various other temperatures. Besides the four parameters provided in Chapter 5, the table includes also the total resistance  $R(0)$  measured at zero  $B$ -field.

Temperature (K)	$R_i(0)$ ( $\Omega$ )	$R_b(0)$ ( $\Omega$ )	$\alpha$ ( $\Omega/T^2$ )	$\beta$ ( $\Omega/T$ )	$R(0)$ ( $\Omega$ )
5	5.95k	6.82k	20.9	1730	3.17k
30	4.84k	9.36k	29.6	710	3.19k
40	4.16k	15.1k	64.4	415.2	3.26k
50	4.21k	18.6k	116.2	365.6	3.44k
60	4.36k	22.7k	367	308.7	3.66k
70	4.50k	26.8k	738.8	271.7	3.85k
80	4.73k	19.6k	406.2	299.8	3.81k
90	4.59k	13.9k	258.1	252.7	3.45k
104	5.39k	6.58k	76.3	288.7	2.96k
120	5.27k	5.50k	59.8	232.9	2.70k
134	5.37k	4.96k	50	190.1	2.57k
150	5.53k	4.80k	48.7	157.9	2.57k
164	5.54k	4.78k	46.6	139.5	2.57k
179	5.97k	4.44k	40.8	120.9	2.55k
193	6.00k	4.20k	36.5	94.6	2.48k



## B Electrical transport data for 12 nm thin platelet grown on hBN

The gate-dependent Hall resistivity and sheet resistance of a 12 nm thick film on a 38 nm thick hBN flake are displayed in Figure B.1a and b, respectively. The Hall curves are seen to become increasingly non-linear upon decreasing the negative back gate voltage. Fitting of the curves with a two-band model (see Chapter 7) yielded the carrier density and mobility for the surface state and the bulk, which are plotted in Figure B.1c and d, respectively. As distinguished from the 45 nm thick sample described in Chapter 7, in this case the bulk carrier density is modulated by the back gate. This finding is in agreement with the similar thickness of the flake and the depletion layer (both  $\approx 10$  nm), which allows for substantial penetration of the electric field into the flake. Reducing the bulk carrier density leads to smaller electron-electron interaction, explaining the observed increase of bulk mobility by about one order of magnitude (see Figure B.1d). By contrast, the surface mobility, which is 1 - 2 orders of magnitude higher than the bulk value, remains almost constant over the entire gate voltage range.

**Table B.1:** Surface carrier mobility of different Bi<sub>2</sub>Te<sub>2</sub>Se nanoplatelets with varying thickness grown on Si/SiO<sub>x</sub> or hBN.

Substrate	$t$ (nm)	$\mu_s$ (m <sup>2</sup> /Vs)	Substrate	$t$ (nm)	$\mu_s$ (m <sup>2</sup> /Vs)
Si/SiO <sub>x</sub>	14	0.062	hBN	12	0.567
Si/SiO <sub>x</sub>	15	0.136	hBN	15	0.329
Si/SiO <sub>x</sub>	21	0.340	hBN	16	0.263
Si/SiO <sub>x</sub>	26	0.100	hBN	44	0.498
Si/SiO <sub>x</sub>	28	0.100	hBN	45	0.723
Si/SiO <sub>x</sub>	38	0.122	hBN	52	0.582
Si/SiO <sub>x</sub>	42	0.140	hBN	107	0.459
Si/SiO <sub>x</sub>	45	0.152			
Si/SiO <sub>x</sub>	68	0.191			

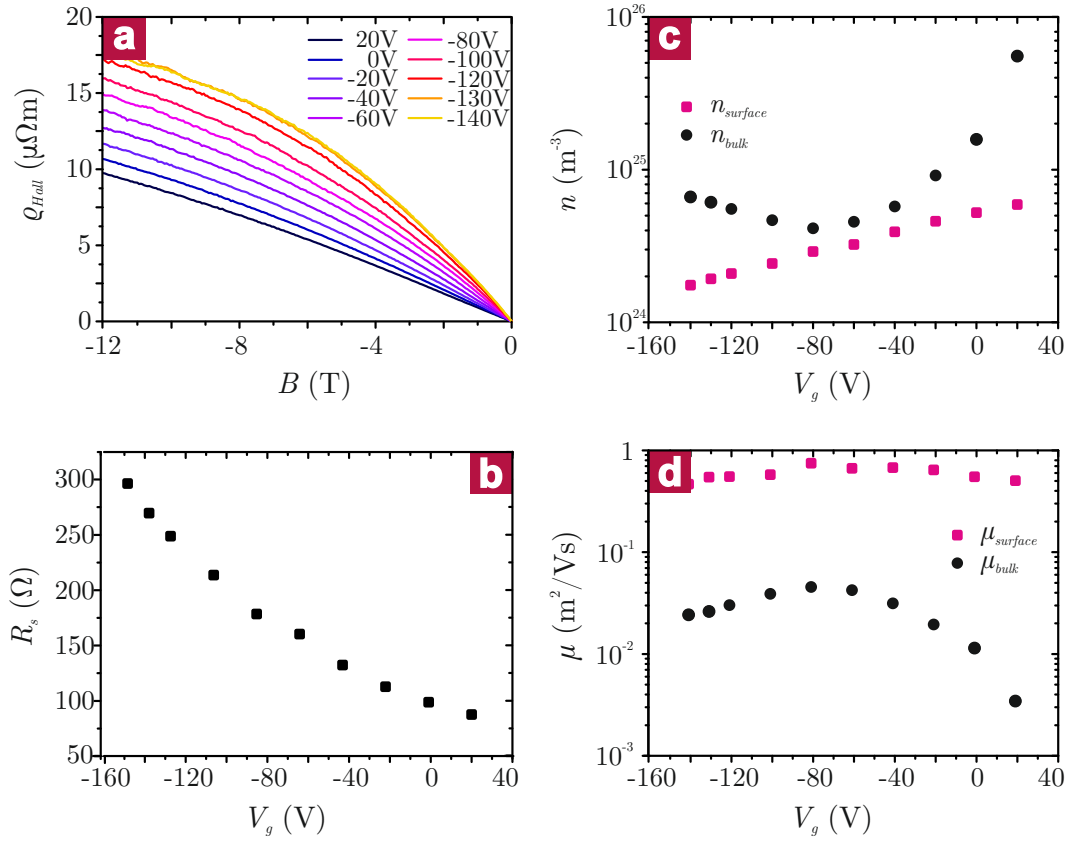


**Figure B.1: Hall measurements of epitaxially grown  $\text{Bi}_2\text{Te}_2\text{Se}$  films on hBN ( $T = 1.5$  K).** (a) Hall resistivity of a 12 nm thick  $\text{Bi}_2\text{Te}_2\text{Se}$  film on a 38 nm thick hBN flake. (b) Sheet resistance as a function of the applied back gate voltage. By fitting the data shown in (a) with the two-band model (Equation 7.6), the surface/bulk carrier density (c) and mobility (d) can be extracted for different back gate voltages.

## C Details of XRD measurements on Kawazulite

Indexing<sup>158</sup> of the recorded spectra led to two similar *R*-centered trigonal unit cells for with lattice parameters given in Table C.1, suggesting the parallel occurrence of two Kawazulite phases with different distribution of elements. The major phase (I) has a slightly smaller unit cell as the minor phase (II). Starting coordinates for both crystal structures of Kawazulite were taken from the literature.<sup>159</sup> Rietveld refinement<sup>160</sup> was performed using the program TOPAS Version 4.2 (Bruker AXS, 2010). The peak profiles and precise lattice parameters were determined by a LeBail fit<sup>161</sup> using the fundamental parameter approach of TOPAS.<sup>162</sup> From elemental analysis, a fully occupied bismuth position could be anticipated, allowing the other occupancies to be correctly refined. A full quantitative Rietveld analysis of the Kawazulite sample revealed a fraction of 89.6(4) wt% for (I) and 10.4(4) of (II). Despite the use of Debye-Scherrer geometry, a small amount of preferred orientation was detected which refined to identical values for both phases using the March-Dollase formalism.<sup>163</sup> Agreement factors (*R*-values) are listed in Table C.1 and the refined coordinates are given in Tables C.2 and C.3.

## Appendix C. Details of XRD measurements on Kawazulite

**Table C.1:** Crystallographic data for the two Kawazulite phases.

	$\text{Bi}_2(\text{Se}_{0.2}\text{S}_{0.74})(\text{Te}_{0.61}\text{Se}_{0.39})_2$	$\text{Bi}_2(\text{Se}_{0.59}\text{Te}_{0.41})\text{Te}_2$
Space group	$R\bar{3}m$	$R\bar{3}m$
Cell parameters (Å)	$a = 4.2537(2)$ $c = 29.704(2)$	$a = 4.3648(8)$ $c = 30.424(8)$
Cell volume (Å <sup>3</sup> )	$V = 465.45(6)$	$V = 502.0(2)$
$Z$	3	3
$T$ (K)	300	300
Formula weight (g/mol)	2038	2340
$\rho_{\text{calc}}$ (g/cm <sup>3</sup> )	7.27(1)	7.74(15)
Radiation source (Å)	0.55941	0.55941
$R_{\text{exp}}$ (%) <sup>[a]</sup>	2.47	2.47
$R_{\text{wp}}$ (%) <sup>[a]</sup>	5.00	5.00
$R_p$ (%) <sup>[a]</sup>	3.83	3.83
$R_{\text{Bragg}}$ (%) <sup>[a]</sup>	3.02	2.00
GoF	2.03	2.03

[a] as defined in TOPAS.

**Table C.2:** Atomic positions and isotropic thermal parameters of Kawazulite phase (I).

Atom	Wyck.	$x$	$y$	$z$	rel. occ.	$U(eq)$ (Å <sup>2</sup> )
Bi	$6f$	0	0	0.41125(4)	1	0.70(4)
S/Se	$3c$	0	0	0	0.70(4)/0.30(4)	0.70(4)
Te/Se	$6f$	0	0	0.19787(9)	0.61(1)/0.39(1)	0.70(4)

**Table C.3:** Atomic positions and isotropic thermal parameters of Kawazulite phase (II).

Atom	Wyck.	$x$	$y$	$z$	rel. occ.	$U(eq)$ (Å <sup>2</sup> )
Bi	$6f$	0	0	0.4083(4)	1	0.70(4)
Te/Se	$3c$	0	0	0	0.4(2)/0.6(2)	0.70(4)
Te	$6f$	0	0	0.1994(8)	1	0.70(4)

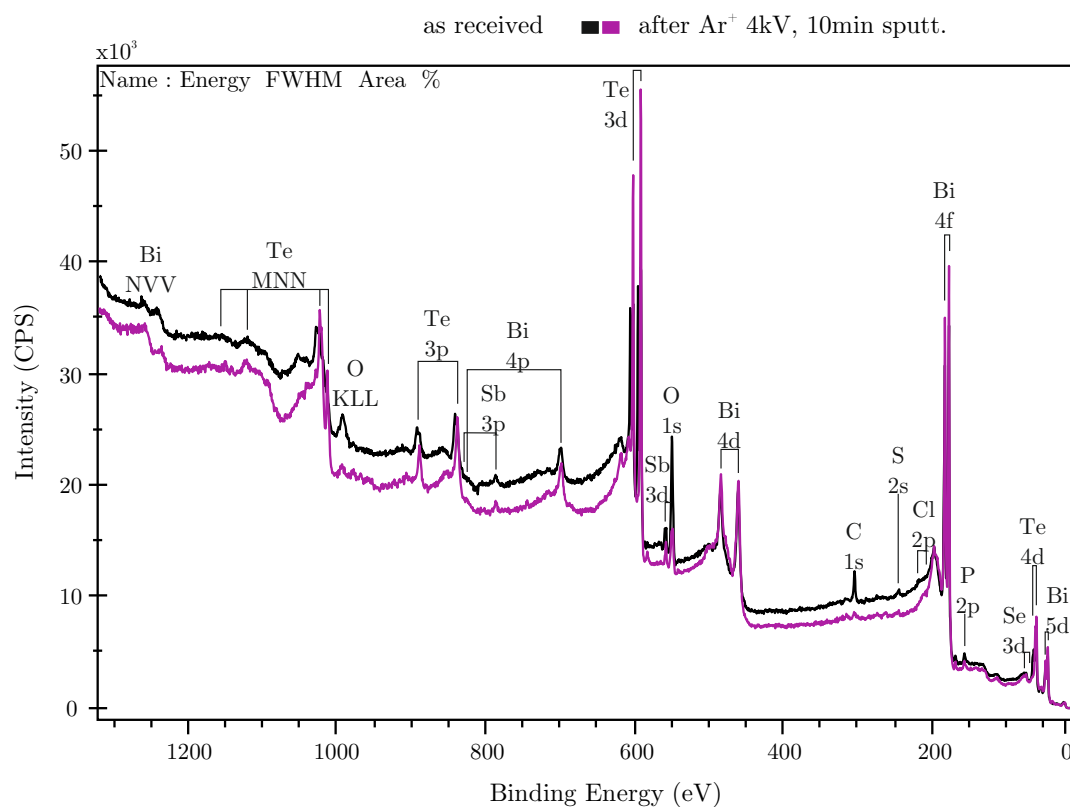


**Figure C.1: Results of the XPS measurements:** As received (black curve) and after 10 min of Ar sputtering (purple curve). The main elements Bi, Te, Se, S and Sb can be detected.



# Bibliography

- [1] Leschke, I. So funktionieren die winzigen Smartphone-Chips. *Die Welt* (05.05.2013).
- [2] Das Sarma, S. Spintronics. *American Scientist* **89**, 516–523 (2000).
- [3] Schmidt, G. Concepts for spin injection into semiconductors - a review. *Journal of Physics D: Applied Physics* **38**, R107 (2005).
- [4] Bianchi, M. *et al.* The electronic structure of clean and adsorbate-covered  $\text{Bi}_2\text{Se}_3$  : an angle-resolved photoemission study. *Semiconductor Science and Technology* **27**, 124001 (2012).
- [5] Jozwiak, C. *et al.* Photoelectron spin-flipping and texture manipulation in a topological insulator. *Nature Physics* **9**, 293–298 (2013).
- [6] Kong, D. & Cui, Y. Opportunities in chemistry and materials science for topological insulators and their nanostructures. *Nature Chemistry* **3**, 845–849 (2011).
- [7] Yazyev, O. V., Moore, J. E. & Louie, S. G. Spin Polarization and Transport of Surface States in the Topological Insulators  $\text{Bi}_2\text{Se}_3$  and  $\text{Bi}_2\text{Te}_3$  from First Principles. *Phys. Rev. Lett.* **105**, 266806 (2010).
- [8] Pan, Z.-H. *et al.* Measurement of an Exceptionally Weak Electron-Phonon Coupling on the Surface of the Topological Insulator  $\text{Bi}_2\text{Se}_3$  Using Angle-Resolved Photoemission Spectroscopy. *Phys. Rev. Lett.* **108**, 187001 (2012).
- [9] Qi, X. L., Li, R. D., Zang, J. D. & Zhang, S. C. Inducing a Magnetic Monopole with Topological Surface States. *Science* **323**, 1184–1187 (2009).
- [10] Linder, J., Tanaka, Y., Yokoyama, T., Sudbo, A. & Nagaosa, N. Unconventional Superconductivity on a Topological Insulator. *Physical Review Letters* **104**, 067001 (2010).
- [11] Xia, Y. *et al.* Observation of a large-gap topological-insulator class with a single Dirac cone on the surface. *Nature Physics* **5**, 398–402 (2009).
- [12] Hyde, G., Beale, H., Spain, I. & Woollam, J. Electronic properties of  $\text{Bi}_2\text{Se}_3$  crystals. *Journal of Physics and Chemistry of Solids* **35**, 1719 – 1728 (1974).

## Bibliography

---

- [13] Wang, G. *et al.* Topological Insulator Thin Films of  $\text{Bi}_2\text{Te}_3$  with Controlled Electronic Structure. *Advanced Materials* **23**, 2929–2932 (2011).
- [14] Kong, D. *et al.* Rapid Surface Oxidation as a Source of Surface Degradation Factor for  $\text{Bi}_2\text{Se}_3$ . *ACS Nano* **5**, 4698–4703 (2011).
- [15] Benia, H. M., Lin, C., Kern, K. & Ast, C. R. Reactive Chemical Doping of the  $\text{Bi}_2\text{Se}_3$  Topological Insulator. *Phys. Rev. Lett.* **107**, 177602 (2011).
- [16] Kim, S. *et al.* Surface Scattering via Bulk Continuum States in the 3D Topological Insulator  $\text{Bi}_2\text{Se}_3$ . *Phys. Rev. Lett.* **107**, 056803 (2011).
- [17] Black-Schaffer, A. M. & Balatsky, A. V. Strong potential impurities on the surface of a topological insulator. *Phys. Rev. B* **85**, 121103 (2012).
- [18] Checkelsky, J. G. *et al.* Quantum Interference in Macroscopic Crystals of Nonmetallic  $\text{Bi}_2\text{Se}_3$ . *Phys. Rev. Lett.* **103**, 246601 (2009).
- [19] Hong, S. S., Cha, J. J., Kong, D. & Cui, Y. Ultra-low carrier concentration and surface-dominant transport in antimony-doped  $\text{Bi}_2\text{Se}_3$  topological insulator nanoribbons. *Nature Communications* **3** (2012).
- [20] Kong, D. *et al.* Ambipolar field effect in the ternary topological insulator  $(\text{Bi}_x\text{Sb}_{1-x})_2\text{Te}_3$  by composition tuning. *Nature Nanotechnology* **6**, 705–709 (2011).
- [21] Wang, Z., Qiu, R. L. J., Lee, C. H., Zhang, Z. & Gao, X. P. A. Ambipolar Surface Conduction in Ternary Topological Insulator  $\text{Bi}_2(\text{Te}_{1-x}\text{Se}_x)_3$  Nanoribbons. *ACS Nano* **7**, 2126–2131 (2013).
- [22] Qu, D.-X., Hor, Y. S., Xiong, J., Cava, R. J. & Ong, N. P. Quantum Oscillations and Hall Anomaly of Surface States in the Topological Insulator  $\text{Bi}_2\text{Te}_3$ . *Science* **329**, 821–824 (2010).
- [23] Zhang, Y. *et al.* Crossover of the three-dimensional topological insulator  $\text{Bi}_2\text{Se}_3$  to the two-dimensional limit. *Nature Physics* **6**, 584–588 (2010).
- [24] Chang, C.-Z. *et al.* Experimental Observation of the Quantum Anomalous Hall Effect in a Magnetic Topological Insulator. *Science* **340**, 167–170 (2013).
- [25] Seo, J. *et al.* Transmission of topological surface states through surface barriers. *Nature* **466**, 343–346 (2010).
- [26] Kandala, A., Richardella, A., Zhang, D., Flanagan, T. C. & Samarth, N. Surface-Sensitive Two-Dimensional Magneto-Fingerprint in Mesoscopic  $\text{Bi}_2\text{Se}_3$  Channels. *Nano Letters* **13**, 2471–2476 (2013).
- [27] Kong, D. *et al.* Few-Layer Nanoplates of  $\text{Bi}_2\text{Se}_3$  and  $\text{Bi}_2\text{Te}_3$  with Highly Tunable Chemical Potential. *Nano Letters* **10**, 2245–2250 (2010).

- 
- [28] Ren, Z., Taskin, A. A., Sasaki, S., Segawa, K. & Ando, Y. Large bulk resistivity and surface quantum oscillations in the topological insulator  $\text{Bi}_2\text{Te}_2\text{Se}$ . *Phys. Rev. B* **82**, 241306 (2010).
- [29] Teo, J. C. Y., Fu, L. & Kane, C. L. Surface states and topological invariants in three-dimensional topological insulators: Application to  $\text{Bi}_{1-x}\text{Sb}_x$ . *Phys. Rev. B* **78**, 045426 (2008).
- [30] Berry, M. V. Robust topological surface states in  $\text{Sb}_2\text{Te}_3$  layers as seen from the weak antilocalization effect. *Scientific American* **259**, 26–34 (1988).
- [31] Bernevig, T. L., B. A.; Hughes. *Topological Insulators and Topological Superconductors*, vol. 1 (Princeton University Press, 2013).
- [32] Thouless, D. J., Kohmoto, M., Nightingale, M. P. & den Nijs, M. Quantized Hall Conductance in a Two-Dimensional Periodic Potential. *Phys. Rev. Lett.* **49**, 405–408 (1982).
- [33] Hasan, M. Z. & Kane, C. L. *Colloquium: Topological insulators*. *Rev. Mod. Phys.* **82**, 3045–3067 (2010).
- [34] Ihn, T. *Semiconductor Nanostructures: Quantum States and Electronic Transport* (Oxford University Press, 2009), 1 edn.
- [35] Ando, Y. Topological Insulator Materials (2013). URL <http://arxiv.org/abs/1304.5693>.
- [36] Kane, C. L. & Mele, E. J.  $Z_2$  Topological Order and the Quantum Spin Hall Effect. *Phys. Rev. Lett.* **95**, 146802 (2005).
- [37] Kane, C. L. & Mele, E. J. Quantum Spin Hall Effect in Graphene. *Phys. Rev. Lett.* **95**, 226801 (2005).
- [38] Fu, L. & Kane, C. L. Time reversal polarization and a  $Z_2$  adiabatic spin pump. *Phys. Rev. B* **74**, 195312 (2006).
- [39] Laughlin, R. B. Quantized Hall conductivity in two dimensions. *Phys. Rev. B* **23**, 5632–5633 (1981).
- [40] Shen, S.-Q. *Topological Insulators: Dirac Equation in Condensed Matters*, vol. 1 (Springer, 2013).
- [41] Fu, L. & Kane, C. L. Topological insulators with inversion symmetry. *Phys. Rev. B* **76**, 045302 (2007).
- [42] Zhang, H. *et al.* Topological insulators in  $\text{Bi}_2\text{Se}_3$ ,  $\text{Bi}_2\text{Te}_3$  and  $\text{Sb}_2\text{Te}_3$  with a single Dirac cone on the surface. *Nature Physics* **5**, 438–442 (2009).
- [43] Fu, L., Kane, C. L. & Mele, E. J. Topological Insulators in Three Dimensions. *Phys. Rev. Lett.* **98**, 106803 (2007).

## Bibliography

---

- [44] König, M. *et al.* The Quantum Spin Hall Effect: Theory and Experiment. *Journal of the Physical Society of Japan* **77**, 031007 (2008).
- [45] Bernevig, B. A., Hughes, T. L. & Zhang, S.-C. Quantum Spin Hall Effect and Topological Phase Transition in HgTe Quantum Wells. *Science* **314**, 1757–1761 (2006).
- [46] König, M. *et al.* Quantum Spin Hall Insulator State in HgTe Quantum Wells. *Science* **318**, 766–770 (2007).
- [47] Roth, A. *et al.* Nonlocal Transport in the Quantum Spin Hall State. *Science* **325**, 294–297 (2009).
- [48] Brüne, C. *et al.* Evidence for the ballistic intrinsic spin Hall effect in HgTe nanostructures. *Nature Physics* **6**, 448–454 (2010).
- [49] Brüne, C. *et al.* Quantum Hall Effect from the Topological Surface States of Strained Bulk HgTe. *Phys. Rev. Lett.* **106**, 126803 (2011).
- [50] Hsieh, D. *et al.* A topological Dirac insulator in a quantum spin Hall phase. *Nature* **452**, 970–974 (2008).
- [51] Olsen, J. L. *Electron Transport in Metals* (Interscience, New York, 1962).
- [52] Kittel, C. *Quantum Theory of Solids* (WILEY, 1987), 2 edn.
- [53] Kapitza, P. The Study of the Specific Resistance of Bismuth Crystals and Its Change in Strong Magnetic Fields and Some Allied Problems. *Proceedings of the Royal Society of London. Series A* **119**, 358–443 (1928).
- [54] Lass, J. S. Linear magnetoresistance of potassium. *Journal of Physics C: Solid State Physics* **3**, 1926 (1970).
- [55] Fickett, F. R. Magnetoresistance of Very Pure Polycrystalline Aluminum. *Phys. Rev. B* **3**, 1941–1952 (1971).
- [56] Tokura, Y. (ed.) *Colossal Magnetoresistive Oxides* (Gordon and Breach Science, New York, 2000).
- [57] Xu, R. *et al.* Large magnetoresistance in non-magnetic silver chalcogenides. *Nature* **390**, 57–60 (1997).
- [58] von Kreutzbruck, M., Lembke, G., Mogwitz, B., Korte, C. & Janek, J. Linear magnetoresistance in  $\text{Ag}_{2+\delta}\text{Se}$  thin films. *Phys. Rev. B* **79**, 035204 (2009).
- [59] Johnson, H. G., Bennett, S. P., Barua, R., Lewis, L. H. & Heiman, D. Universal properties of linear magnetoresistance in strongly disordered MnAs-GaAs composite semiconductors. *Phys. Rev. B* **82**, 085202 (2010).

- 
- [60] Hu, J. & Rosenbaum, T. F. Classical and quantum routes to linear magnetoresistance. *Nature Materials* **7**, 697–700 (2008).
  - [61] Friedman, A. L. *et al.* Quantum Linear Magnetoresistance in Multilayer Epitaxial Graphene. *Nano Letters* **10**, 3962–3965 (2010).
  - [62] Abrikosov, A. A. Quantum linear magnetoresistance. *Europhysics Letters* **49**, 789 (2000).
  - [63] Parish, M. M. & Littlewood, P. B. Non-saturating magnetoresistance in heavily disordered semiconductors. *Nature* **426**, 162–165 (2003).
  - [64] Abrikosov, A. A. Quantum magnetoresistance. *Phys. Rev. B* **58**, 2788–2794 (1998).
  - [65] Shoenberg, D. *Magnetic Oscillations in Metals* (Cambridge University Press, 1984).
  - [66] Bergmann, G. Weak anti-localization - An experimental proof for the destructive interference of rotated spin 1/2. *Solid State Communications* **42**, 815–817 (1982).
  - [67] Hikami, S., Larkin, A. I. & Nagaoka, Y. Spin-Orbit Interaction and Magnetoresistance in the Two Dimensional Random System. *Prog. Theor. Phys.* **63**, 707–710 (1980).
  - [68] Manoharan, H. C. Topological insulators: A romance with many dimensions. *Nature Nanotechnology* **5**, 477–479 (2010).
  - [69] He, H.-T. *et al.* Impurity Effect on Weak Antilocalization in the Topological Insulator Bi<sub>2</sub>Te<sub>3</sub>. *Phys. Rev. Lett.* **106**, 166805 (2011).
  - [70] Gehring, P., Gao, B., Burghard, M. & Kern, K. Two-dimensional magnetotransport in Bi<sub>2</sub>Te<sub>2</sub>Se nanoplatelets. *Applied Physics Letters* **101**, 023116 (2012).
  - [71] Steinberg, H., Laloë, J.-B., Fatemi, V., Moodera, J. S. & Jarillo-Herrero, P. Electrically tunable surface-to-bulk coherent coupling in topological insulator thin films. *Phys. Rev. B* **84**, 233101 (2011).
  - [72] Takagaki, Y., Giussani, A., Perumal, K., Calarco, R. & Friedland, K.-J. Robust topological surface states in Sb<sub>2</sub>Te<sub>3</sub> layers as seen from the weak antilocalization effect. *Phys. Rev. B* **86**, 125137 (2012).
  - [73] Liu, M. *et al.* Crossover between Weak Antilocalization and Weak Localization in a Magnetically Doped Topological Insulator. *Phys. Rev. Lett.* **108**, 036805 (2012).
  - [74] Altshuler, A. G., B.; Aronov. *Electron-electron interaction in disordered conductors*, vol. 10 of *Electron-electron interaction in disordered systems* (North-Holland: Amsterdam, Oxford, New York, Tokyo, 1985).
  - [75] Lee, P. A., Stone, A. D. & Fukuyama, H. Universal conductance fluctuations in metals: Effects of finite temperature, interactions, and magnetic field. *Physical Review B* **35**, 1039 (1987).

## Bibliography

---

- [76] Aharonov, Y. & Bohm, D. Significance of Electromagnetic Potentials in the Quantum Theory. *Phys. Rev.* **115**, 485–491 (1959).
- [77] Bardarson, J. H., Brouwer, P. W. & Moore, J. E. Aharonov-Bohm Oscillations in Disordered Topological Insulator Nanowires. *Phys. Rev. Lett.* **105**, 156803 (2010).
- [78] Bardarson, J. H. & Moore, J. E. Quantum interference and Aharonov-Bohm oscillations in topological insulators. *Reports on Progress in Physics* **76**, 056501 (2013).
- [79] *Lake Shore 7500/9500 Series Hall System User's Manual*.
- [80] Hsieh, D. *et al.* Observation of Time-Reversal-Protected Single-Dirac-Cone Topological-Insulator States in  $\text{Bi}_2\text{Te}_3$  and  $\text{Sb}_2\text{Te}_3$ . *Phys. Rev. Lett.* **103**, 146401 (2009).
- [81] Köhler, H. Conduction Band Parameters of  $\text{Bi}_2\text{Se}_3$  from Shubnikov-de Haas Investigations. *physica status solidi (b)* **58**, 91–100 (1973).
- [82] Deshpande, M. P., Pandya, N. N. & Parmar, M. N. Transport property measurements of  $\text{Bi}_2\text{Se}_3$  crystal grown by Bridgman method. *Turk. J. Phys.* **33**, 139–148 (2009).
- [83] Hsieh, D. *et al.* A tunable topological insulator in the spin helical Dirac transport regime. *Nature* **460**, 1101–1106 (2009).
- [84] Hor, Y. S. *et al.* *p*-type  $\text{Bi}_2\text{Se}_3$  for topological insulator and low-temperature thermoelectric applications. *Phys. Rev. B* **79**, 195208 (2009).
- [85] Wang, Z. *et al.* Tuning carrier type and density in  $\text{Bi}_2\text{Se}_3$  by Ca-doping. *Applied Physics Letters* **97**, 042112 (2010).
- [86] Kasparova, J. *et al.* n-type to p-type crossover in quaternary  $\text{Bi}_x\text{Sb}_y\text{Pb}_z\text{Se}_3$  single crystals. *Journal of Applied Physics* **97**, 103720 (2005).
- [87] Analytis, J. G. *et al.* Two-dimensional surface state in the quantum limit of a topological insulator. *Nature Physics* **6**, 960–964 (2010).
- [88] Zhang, G. *et al.* Quintuple-layer epitaxy of thin films of topological insulator  $\text{Bi}_2\text{Se}_3$ . *Applied Physics Letters* **95**, 053114 (2009).
- [89] Cho, S., Butch, N. P., Paglione, J. & Fuhrer, M. S. Insulating Behavior in Ultrathin Bismuth Selenide Field Effect Transistors. *Nano Letters* **11**, 1925–1927 (2011).
- [90] Atsushi & Koma. New epitaxial growth method for modulated structures using Van der Waals interactions. *Surface Science* **267**, 29 – 33 (1992).
- [91] Li, H. D. *et al.* The van der Waals epitaxy of  $\text{Bi}_2\text{Se}_3$  on the vicinal Si(111) surface: an approach for preparing high-quality thin films of a topological insulator. *New Journal of Physics* **12**, 103038 (2010).

- [92] Song, C.-L. *et al.* Topological insulator Bi<sub>2</sub>Se<sub>3</sub> thin films grown on double-layer graphene by molecular beam epitaxy. *Applied Physics Letters* **97**, 143118 (2010).
- [93] Jiang, Y. *et al.* Fermi Level Tuning of Epitaxial Sb<sub>2</sub>Te<sub>3</sub> Thin Films on Graphene by Regulating Intrinsic Defects and Substrate Transfer Doping. *Phys. Rev. Lett.* **108**, 066809 (2012).
- [94] Zhang, G., Wang, W., Lu, X. & Li, X. Solvothermal Synthesis of V-VI Binary and Ternary Hexagonal Platelets: The Oriented Attachment Mechanism. *Crystal Growth & Design* **9**, 145–150 (2009).
- [95] Xiu, F. *et al.* Manipulating surface states in topological insulator nanoribbons. *Nature Nanotechnology* **6**, 216–221 (2011).
- [96] Kong, D. *et al.* Topological Insulator Nanowires and Nanoribbons. *Nano Letters* **10**, 329–333 (2010).
- [97] Peng, H. *et al.* Aharonov-Bohm interference in topological insulator nanoribbons. *Nature Materials* **9**, 225–229 (2010).
- [98] Cha, J. J. *et al.* Magnetic Doping and Kondo Effect in Bi<sub>2</sub>Se<sub>3</sub> Nanoribbons. *Nano Letters* **10**, 1076–1081 (2010).
- [99] Yan, Y. *et al.* Synthesis and Quantum Transport Properties of Bi<sub>2</sub>Se<sub>3</sub> Topological Insulator Nanostructures. *Scientific Reports* **3**, 1264 (2013).
- [100] Yu, Y. *et al.* Controlled Scalable Synthesis of Uniform, High-Quality Monolayer and Few-layer MoS<sub>2</sub> Films. *Scientific Reports* **3**, 1866 (2013).
- [101] Dang, W., Peng, H., Li, H., Wang, P. & Liu, Z. Epitaxial Heterostructures of Ultrathin Topological Insulator Nanoplate and Graphene. *Nano Letters* **10**, 2870–2876 (2010).
- [102] Gómez-Navarro, C. *et al.* Electronic Transport Properties of Individual Chemically Reduced Graphene Oxide Sheets. *Nano Letters* **7**, 3499–3503 (2007).
- [103] Peng, H. *et al.* Topological insulator nanostructures for near-infrared transparent flexible electrodes. *Nature Chemistry* **4**, 281–286 (2012).
- [104] Tang, H., Liang, D., Qiu, R. L. J. & Gao, X. P. A. Two-Dimensional Transport-Induced Linear Magneto-Resistance in Topological Insulator Bi<sub>2</sub>Se<sub>3</sub> Nanoribbons. *ACS Nano* **5**, 7510–7516 (2011).
- [105] Butch, N. P., Syers, P., Kirshenbaum, K., Hope, A. P. & Paglione, J. Superconductivity in the topological semimetal YPtBi. *Phys. Rev. B* **84**, 220504 (2011).
- [106] Zhang, W. *et al.* Topological Aspect and Quantum Magnetoresistance of  $\beta$ -Ag<sub>2</sub>Te. *Phys. Rev. Lett.* **106**, 156808 (2011).

## Bibliography

---

- [107] He, H.-T. *et al.* High-field linear magneto-resistance in topological insulator  $\text{Bi}_2\text{Se}_3$  thin films. *Applied Physics Letters* **100**, 032105 (2012).
- [108] Richter, W. & Becker, C. R. A Raman and far-infrared investigation of phonons in the rhombohedral  $\text{V}_2\text{-VI}_3$  compounds  $\text{Bi}_2\text{Te}_3$ ,  $\text{Bi}_2\text{Se}_3$ ,  $\text{Sb}_2\text{Te}_3$  and  $\text{Bi}_2(\text{Te}_{1-x}\text{Se}_x)_3$  ( $0 < x < 1$ ),  $(\text{Bi}_{1-y}\text{Sb}_y)_2\text{Te}_3$  ( $0 < y < 1$ ). *physica status solidi (b)* **84**, 619–628 (1977).
- [109] Zhao, S. Y. F. *et al.* Fabrication and characterization of topological insulator  $\text{Bi}_2\text{Se}_3$  nanocrystals. *Applied Physics Letters* **98**, 141911 (2011).
- [110] Checkelsky, J. G., Hor, Y. S., Cava, R. J. & Ong, N. P. Bulk Band Gap and Surface State Conduction Observed in Voltage-Tuned Crystals of the Topological Insulator  $\text{Bi}_2\text{Se}_3$ . *Phys. Rev. Lett.* **106**, 196801 (2011).
- [111] Giraud, S., Kundu, A. & Egger, R. Electron-phonon scattering in topological insulator thin films. *Phys. Rev. B* **85**, 035441 (2012).
- [112] Liu, M. *et al.* Electron interaction-driven insulating ground state in  $\text{Bi}_2\text{Se}_3$  topological insulators in the two-dimensional limit. *Phys. Rev. B* **83**, 165440 (2011).
- [113] Chen, J. *et al.* Gate-Voltage Control of Chemical Potential and Weak Antilocalization in  $\text{Bi}_2\text{Se}_3$ . *Phys. Rev. Lett.* **105**, 176602 (2010).
- [114] Wang, L.-L. & Johnson, D. D. Ternary tetradymite compounds as topological insulators. *Phys. Rev. B* **83**, 241309 (2011).
- [115] Arakane, T. *et al.* Tunable Dirac cone in the topological insulator  $\text{Bi}_{2-x}\text{Sb}_x\text{Te}_{3-y}\text{Se}_y$ . *Nature Communications* **3** (2012).
- [116] Zhang, J. *et al.* Raman Spectroscopy of Few-Quintuple Layer Topological Insulator  $\text{Bi}_2\text{Se}_3$  Nanoplatelets. *Nano Letters* **11**, 2407–2414 (2011).
- [117] Kim, Y. S. *et al.* Thickness-dependent bulk properties and weak antilocalization effect in topological insulator  $\text{Bi}_2\text{Se}_3$ . *Phys. Rev. B* **84**, 073109 (2011).
- [118] Wang, Y. *et al.* Gate-Controlled Surface Conduction in Na-Doped  $\text{Bi}_2\text{Te}_3$  Topological Insulator Nanoplates. *Nano Letters* **12**, 1170–1175 (2012).
- [119] Kou, X. F. *et al.* Epitaxial growth of high mobility  $\text{Bi}_2\text{Se}_3$  thin films on CdS. *Applied Physics Letters* **98**, 242102 (2011).
- [120] Watanabe, K., Taniguchi, T. & Kanda, H. Direct-bandgap properties and evidence for ultraviolet lasing of hexagonal boron nitride single crystal. *Nature Materials* **3**, 404–409 (2004).
- [121] Xiong, J. *et al.* Quantum oscillations in a topological insulator  $\text{Bi}_2\text{Te}_2\text{Se}$  with large bulk resistivity ( $6\Omega\text{cm}$ ). *Physica E: Low-dimensional Systems and Nanostructures* **44**, 917 – 920 (2012).

- [122] Cha, J. J. *et al.* Weak Antilocalization in  $\text{Bi}_2(\text{Se}_x\text{Te}_{1-x})_3$  Nanoribbons and Nanoplates. *Nano Letters* **12**, 1107–1111 (2012).
- [123] Sokolov, O., Skipidarov, S., Duvankov, N. & Shabunina, G. Phase relations and thermoelectric properties of alloys in the  $\text{Bi}_2\text{Te}_3$ - $\text{Bi}_2\text{Se}_3$  system. *Inorganic Materials* **43**, 8–11 (2007).
- [124] Gorbachev, R. V. *et al.* Hunting for Monolayer Boron Nitride: Optical and Raman Signatures. *Small* **7**, 465–468 (2011).
- [125] Dean, C. R. *et al.* Boron nitride substrates for high-quality graphene electronics. *Nature Nanotechnology* **5**, 722–726 (2010).
- [126] Kim, J. S. *et al.* Nonlinear Hall effect and multichannel conduction in  $\text{LaTiO}_3/\text{SrTiO}_3$  superlattices. *Phys. Rev. B* **82**, 201407 (2010).
- [127] Wang, J. *et al.* Evidence for electron-electron interaction in topological insulator thin films. *Phys. Rev. B* **83**, 245438 (2011).
- [128] Snoke, D. W. Density dependence of electron scattering at low density. *Phys. Rev. B* **50**, 11583–11591 (1994).
- [129] Sarikaya, M., Tamerler, C., Jen, A. K. Y., Schulten, K. & Baneyx, F. Molecular biomimetics: nanotechnology through biology. *Nature Materials* **2**, 577–585 (2003).
- [130] Wentorf, R. N. & Bovenkerk, H. P. On the Origin of Natural Diamonds. *Astrophysical Journal* **134**, 995 (1961).
- [131] Shechtman, D., Blech, I., Gratias, D. & Cahn, J. W. Metallic Phase with Long-Range Orientational Order and No Translational Symmetry. *Physical Review Letters* **53**, 1951–1953 (1984).
- [132] Bindi, L. *et al.* Evidence for the extraterrestrial origin of a natural quasicrystal. *Proceedings of the National Academy of Sciences of the United States of America* **109**, 1396–1401 (2012).
- [133] Novoselov, K. S. *et al.* Electric Field Effect in Atomically Thin Carbon Films. *Science* **306**, 666–669 (2004).
- [134] Anthony, J. W., Bideaux, R. A., Bladh, K. W. & Nichols, M. C. *Handbook of Mineralogy* (Mineralogical Society of America, 2012).
- [135] Bland, J. A. & Basinski, S. J. Crystal Structure of  $\text{Bi}_2\text{Te}_2\text{Se}$ . *Canadian Journal of Physics* **39**, 1040 (1961).
- [136] Ren, Z., Taskin, A. A., Sasaki, S., Segawa, K. & Ando, Y. Optimizing  $\text{Bi}_{2-x}\text{Sb}_x\text{Te}_{3-y}\text{Se}_y$  solid solutions to approach the intrinsic topological insulator regime. *Phys. Rev. B* **84**, 165311 (2011).

## Bibliography

---

- [137] Xu, S.-Y. *et al.* Topological Phase Transition and Texture Inversion in a Tunable Topological Insulator. *Science* **332**, 560–564 (2011).
- [138] Neupane, M. *et al.* Topological surface states and dirac point tuning in ternary topological insulators. *Physical Review B* **85** (2012).
- [139] Ji, H. *et al.*  $\text{Bi}_2\text{Te}_{1.6}\text{S}_{1.4}$ : A topological insulator in the tetradymite family. *Phys. Rev. B* **85**, 201103 (2012).
- [140] Li, Z. *et al.* Two-dimensional universal conductance fluctuations and the electron-phonon interaction of surface states in  $\text{Bi}_2\text{Te}_2\text{Se}$  microflakes. *Scientific Reports* **2**, 595 (2012).
- [141] Yang, K., Setyawan, W., Wang, S., Buongiorno Nardelli, M. & Curtarolo, S. A search model for topological insulators with high-throughput robustness descriptors. *Nature Materials* **11**, 614 (2012).
- [142] Kraus, Y. E., Lahini, Y., Ringel, Z., Verbin, M. & Zilberberg, O. Topological States and Adiabatic Pumping in Quasicrystals. *Physical Review Letters* **109**, 106402 (2012).
- [143] Gehring, P. *et al.* A Natural Topological Insulator. *Nano Letters* **13**, 1179–1184 (2013).
- [144] Silkin, I. *et al.* Natural sulfur-containing minerals as topological insulators with a wide band gap. *JETP Letters* **96**, 322–325 (2012).
- [145] Jin, H., Song, J.-H., Freeman, A. J. & Kanatzidis, M. G. Candidates for topological insulators: Pb-based chalcogenide series. *Phys. Rev. B* **83**, 041202 (2011).
- [146] Ereameev, S. V. *et al.* Atom-specific spin mapping and buried topological states in a homologous series of topological insulators. *Nature Communications* **3**, 635 (2012).
- [147] Altshuler, B. L., Aronov, A. G. & Khmelnitsky, D. E. Effects of electron-electron collisions with small energy transfers on quantum localisation. *Journal of Physics C: Solid State Physics* **15**, 7367 (1982).
- [148] Echternach, P. M., Gershenson, M. E., Bozler, H. M., Bogdanov, A. L. & Nilsson, B. Nyquist phase relaxation in one-dimensional metal films. *Phys. Rev. B* **48**, 11516–11519 (1993).
- [149] Cha, J. J. *et al.* Effects of Magnetic Doping on Weak Antilocalization in Narrow  $\text{Bi}_2\text{Se}_3$  Nanoribbons. *Nano Letters* **12**, 4355–4359 (2012).
- [150] Bonaccorso, F. *et al.* Production and processing of graphene and 2d crystals. *Materials Today* **15**, 564 – 589 (2012).
- [151] Lee, S. *et al.* Single Crystalline  $\beta\text{-Ag}_2\text{Te}$  Nanowire as a New Topological Insulator. *Nano Letters* **12**, 4194–4199 (2012).

- 
- [152] Hamdou, B., Gooth, J., Dorn, A., Pippel, E. & Nielsch, K. Aharonov-Bohm oscillations and weak antilocalization in topological insulator  $\text{Sb}_2\text{Te}_3$  nanowires. *Applied Physics Letters* **102**, 223110 (2013).
- [153] Schmidt, G., Ferrand, D., Molenkamp, L. W., Filip, A. T. & van Wees, B. J. Fundamental obstacle for electrical spin injection from a ferromagnetic metal into a diffusive semiconductor. *Phys. Rev. B* **62**, R4790–R4793 (2000).
- [154] Rashba, E. I. Theory of electrical spin injection: Tunnel contacts as a solution of the conductivity mismatch problem. *Phys. Rev. B* **62**, R16267–R16270 (2000).
- [155] Cobas, E., Friedman, A. L., van 't Erve, O. M. J., Robinson, J. T. & Jonker, B. T. Graphene As a Tunnel Barrier: Graphene-Based Magnetic Tunnel Junctions. *Nano Letters* **12**, 3000–3004 (2012).
- [156] van 't Erve, O. M. J. *et al.* Low-resistance spin injection into silicon using graphene tunnel barriers. *Nature Nanotechnology* **7**, 737–742 (2012).
- [157] Burkov, A. A. & Hawthorn, D. G. Spin and Charge Transport on the Surface of a Topological Insulator. *Phys. Rev. Lett.* **105**, 066802 (2010).
- [158] Coelho, A. A. Indexing of powder diffraction patterns by iterative use of singular value decomposition. *Journal of Applied Crystallography* **36**, 86–95 (2003). Part 1 636LK Times Cited:115 Cited References Count:20.
- [159] Nakajima, S. The crystal structure of  $\text{Bi}_2\text{Te}_{3-x}\text{Se}_x$ . *Journal of Physics and Chemistry of Solids* **24**, 479–485 (1963).
- [160] Rietveld, H. M. A Profile Refinement Method for Nuclear and Magnetic Structures. *Journal of Applied Crystallography* **2**, 65 (1969).
- [161] Le Bail, A., Duroy, H. & Fourquet, J. L. Abinitio Structure Determination of  $\text{LiSbWO}_6$  by X-Ray-Powder Diffraction. *Materials Research Bulletin* **23**, 447–452 (1988).
- [162] Cheary, R. W., Coelho, A. A. & Cline, J. Fundamental parameters line profile fitting in laboratory diffractometers. *J. Res. Natl. Inst. Stand. Technol.* **109**, 1 (2005).
- [163] March, A. Mathematical theory on regulation according to the particle shape and affine deformation. *Zeitschrift Fur Kristallographie* **81**, 285–297 (1932).



# Danksagung

Die letzten 3½ Jahre als Doktorand am Max-Planck-Institut für Festkörperforschung in Stuttgart – voller Höhen und Tiefen, Erfolge und Misserfolge – waren unvergesslich. Nun bin ich zwar am Ende meiner Doktorarbeit, doch den Weg dorthin musste ich nicht allein bestreiten. Dass ich mein Ziel erreicht, so viel gelernt und so viel erlebt habe, verdanke ich hauptsächlich den Menschen an meiner Seite, die mich auf meinem Weg begleitet haben. Diesen möchte ich von ganzem Herzen danken.

Als erstes möchte ich Prof. Klaus Kern danken, dass ich meine Doktorarbeit in seiner Forschungsgruppe durchführen durfte. Seine Philosophie war es immer, einem Doktoranden ein größtmögliches Maß an Freiheit zu gewähren, wobei dieser mögliche Chancen erkennen und unverzüglich ergreifen muss. Dies gab mir zu jedem Zeitpunkt die Möglichkeit, mich wissenschaftlich zu entfalten und – wenn nötig – neu zu definieren, was maßgeblich zum Erfolg meiner Arbeit beigetragen hat.

Zu größtem Dank bin ich auch meinem Betreuer Dr. Marko Burghard verpflichtet. Er nahm sich immer Zeit für Diskussionen über Probleme oder Ergebnisse und war neuen Ideen gegenüber nie voreingenommen – egal wie kurios diese auch manchmal waren. Ich schätze Marko sowohl wissenschaftlich als auch menschlich und denke, dass wir uns in unseren Denkweisen perfekt ergänzen konnten. Deshalb könnte ich mir auch keinen besseren Betreuer für meine Doktorarbeit vorstellen.

Ich danke Dr. Eberhard Ulrich Stützel und Dr. Bo Gao, welche sich zu Beginn meiner Arbeit unzählige Stunden Zeit nahmen, um mich in diverse Maschinen und Prozesse einzuarbeiten. Herrn Dr. Gao danke ich zudem für die vielen Diskussionen und Uneinigkeiten in welchen er mir beibrachte, fokussiert und „ergebnisorientiert“ zu denken.

Ich danke Thomas Meisner und Arnold Weible für ihre kompetente Beratung und Hilfe bei allem, das etwas mit Öfen zu tun hatte. Beide nahmen sich immer Zeit, jegliche Art von technischen Problemen zu untersuchen und mit mir gemeinsam zu lösen.

Für ihre technische Unterstützung danke ich auch dem Reinraum-Team: Thomas Reindl, Ulrike Weizmann, Marion Hagel (vielen Dank auch für die unzähligen Proben, die du für mich gebondet hast) und Achim Güth.

Ich danke Ye Weng für die zahlreichen TEM Messungen, die Hilfe bei deren Interpretation und für die Tasse Kaffee, die ich jedes mal bekommen habe, wenn ich in ihr Büro kam. Meinen Gruppenmitgliedern und ehemaligen Kollegen der Gruppe „Quantum Materials“ möchte ich für die gute Arbeitsatmosphäre und die stetige Unterstützung und Hilfe danken: Dr. Bo Gao,

## Danksagung

---

Dr. Ravi Sudaram, Dr. Adarsh Sagar, Dr. Eva Carmen Peters, Dr. Eberhard Ulrich Stützel, Dr. Thomas Dufaux, Robert Preuß, Christian Cervetti, Kristina Vaklinova, Alexander Hoyer, Gaurav Pathak, Frieder Reusch, Roberto Urcuyo.

Ich danke zudem Dr. Christian Ast und Dr. Ralf Vogelgesang für die vielen, äußerst hilfreichen Diskussionen.

Ein ganz besonderer Dank geht an unsere Sekretärinnen Sabine Birtel und Erika Menamkat. Sie waren die „guten Geister“, welche mich des Öfteren an wichtige Fristen erinnert, mich bei undurchsichtigen Formalitäten unterstützt und Unterkünfte und Dienstreisen organisiert haben.

Meine Zeit am MPI wäre nicht annähernd so großartig gewesen, wenn ich meine Bürokollegen nicht gehabt hätte: Dr. Thomas Dufaux, Dr. Moritz Eßlinger, Sören Krotzky, Sina Habibian und Kristina Vaklinova. Vielen Dank für die vielen Stunden innerhalb (und vor allem auch außerhalb) des Büros, die ich mit euch verbringen durfte.

Für die besonderen Arbeitspausen danke ich zudem der Schokoladenpräsidentin Carola und meinen Tischkicker-Trainingspartnern Robert und Thomas.

Zu guter Letzt möchte ich meiner Familie danken und vor allem auch meiner Freundin Michaela für ihre uneingeschränkte Unterstützung, ihr Verständnis und die Kraft, die sie mir all die Jahre gegeben hat.

*Stuttgart, 29. Oktober 2013*

P. G.

# Pascal Gehring

## *curriculum vitae*

date/place of birth    October the 20th, 1984 in Dinkelsbühl, Germany

---

### education

1991–1995    **primary school**, *Christoph-von-Schmid Grundschule*, Dinkelsbühl.

Sep 1995– May 2004    **secondary school**, *Gymnasium Dinkelsbühl*.

specialised courses: Mathematics and Physics

May 2004    **general qualification for university entrance**, *Gymnasium Dinkelsbühl*.

Sep 2004– Jan 2010    **studies of material sciences**, *University of Stuttgart*.

Jul 2009 – Jan 2010    **diploma thesis (with distinction)**, *University of Stuttgart*.

(in cooperation with the Max-Planck-Institute for Metals Research, Stuttgart)

Mar 2010 – Dec 2013    **Doctoral Studies (PhD)**, *Ecole Polytechnique Federale de Lausanne, Switzerland, Doctoral School: Materials Science and Engineering and Max-Planck Institute for Solid State Research Stuttgart, Nanoscale Science Department, Prof. Dr. K. Kern.*

---

### practical work

Jun 2007 – Sep 2008    **research assistant**, *Fraunhofer IPA*, Stuttgart.

luminescence properties of particles

---

### teaching

May 2011 - Dec 2013    **lab course assistant**, *University of Stuttgart*.

Jul 2013    **Funktionsmaterialien**, *University of Stuttgart*.

4 lectures about electronic transport in reduced dimensions

---

### honors and awards

2011    Erster Förderpreis der Willi Dauberschmidt Stiftung

---

### conferences and seminars

Jun 2013    **Invited Talk: University of Stuttgart**, *Group seminar Materials Science, “Topological Insulators”*.

Jun 2013    **Symposium on Quantum Hall Effects and Related Topics**, *Stuttgart, “A Natural Topological Insulator”, (Poster)*.

Jun 2013 **New Trends in Topological Insulators**, *Sant Feliu de Guixols, Barcelona, Spain*, “Growth of High-Mobility Bi<sub>2</sub>Te<sub>2</sub>Se Nanoplatelets on hBN Sheets by van der Waals Epitaxy”, (Poster).

Mar 2013 **DPG Conference, Regensburg**, “Growth of High-Mobility Bi<sub>2</sub>Te<sub>2</sub>Se Nanoplatelets on hBN Sheets by van der Waals Epitaxy”, (Poster).

---

## language skills

German	<b>fluent</b>	<i>native language</i>
English	<b>fluent</b>	<i>school education, language course: Mechanical Engineering English</i>
French	<b>basics</b>	<i>school education</i>

---

## computer literacy

os	Windows, Linux	programming	Visual Basic
word processing	Word, LaTeX	simulation	CRYSTAL (basics)
data analysis	Origin, Excel, Mathematica	image processing	Corel Draw

---

## hobbies

sounddesign  
playing the piano  
sightseeing

---

## publications

1. **Gehring, P.**; Benia, H. M.; Weng, Y.; Dinnebier, R.; Ast, C. R.; Burghard, M. and Kern, K. A Natural Topological Insulator *Nano Letters* **13**, 1179–1184 (2013)
2. **Gehring, P.**; Gao, B. F.; Burghard, M. and Kern, K. Growth of High-Mobility Bi<sub>2</sub>Te<sub>2</sub>Se Nanoplatelets on hBN Sheets by van der Waals Epitaxy *Nano Letters* **12**, 5137–5142 (2012)
3. **Gehring, P.**; Gao, B. F.; Burghard, M. and Kern, K. Two-dimensional magnetotransport in Bi<sub>2</sub>Te<sub>2</sub>Se nanoplatelets *Appl. Phys. Lett.* **101**, 023116 (2012)
4. Gao, B. F.; **Gehring, P.**; Burghard, M. and Kern, K. Gate-controlled linear magnetoresistance in thin Bi<sub>2</sub>Se<sub>3</sub> sheets *Appl. Phys. Lett.* **100**, 212402 (2012)
5. **Gehring, P.**; Weng, Y.; Wu, Z.; and Strunk, H. P. Evidence for resonant energy transfer in terbium-doped (Al,In)N films *IOP Conference Series: Materials Science and Engineering* **15**, 012007 (2010)
6. **Gehring, P.**; Weng, Y.; Wu, Z.; and Strunk, H. P. Photoluminescence from Al<sub>x</sub>In<sub>1-x</sub>N layers doped with Tb<sup>3+</sup> ions *Journal of Physics: Conference Series* **281**, 012014 (2010)